Distribution Agreement

In presenting this thesis or dissertation as a partial fulfillment of the requirements for an advanced degree from Emory University, I hereby grant to Emory University and its agents the non-exclusive license to archive, make accessible, and display my thesis or dissertation in whole or in part in all forms of media, now or hereafter known, including display on the world wide web. I understand that I may select some access restrictions as part of the online submission of this thesis or dissertation. I retain all ownership rights to the copyright of the thesis or dissertation. I also retain the right to use in future works (such as articles or books) all or part of this thesis or dissertation.

Signature:

_____ Date_____

Annie M. Goettemoeller

**Parvalbumin Interneuron Regional Variability and
Vulnerability in Early Alzheimer's Disease**

By

Annie M. Goettemoeller
Doctor of Philosophy

Graduate Division of Biological and Biomedical Science
Neuroscience

_____

Matthew JM Rowan, Ph.D.
Advisor

_____

David Weinshenker, Ph.D.
Committee Member

_____

Shannon Gourley, Ph.D.
Committee Member

_____

Steven Sloan, M.D., Ph.D.
Committee Member

_____

Stephen Traynelis, Ph.D.
Committee Member

Accepted:

_____

Kimberly Jacob Arriola, Ph.D.
Dean of the James T. Laney School of Graduate Studies

_____

Date

**Parvalbumin Interneuron Regional Variability and
Vulnerability in Early Alzheimer's Disease**

By

Annie M. Goettemoeller
B.S., University of Michigan, 2019

Advisor: Matthew J.M. Rowan, Ph.D.

An abstract of a dissertation submitted to the Faculty of the James T. Laney School of
Graduate Studies of Emory University in fulfillment of the requirements for the degree of
Doctor of Philosophy in the Graduate Division of Biological and Biomedical Science's
Neuroscience Program
2024

Abstract

**Parvalbumin Interneuron Regional Variability and
Vulnerability in Early Alzheimer's Disease**

By Annie M. Goettemoeller

Complex functions performed by the brain require dynamic cortical circuits. Awareness of incoming salient stimuli as well as maintenance of homeostasis require strong regulation of neuronal firing, a phenomenon mediated heavily by inhibitory interneurons. Although typically a strength of the circuit, these imperative interneurons also provide a gateway to circuit chaos should they become vulnerable. Unsurprisingly, many diseases which plague humankind arise from the dysfunction of interneurons. In human patients with Alzheimer's Disease, one of the earliest observed pathophysiological correlates to cognitive decline is hyperexcitability. The origin of hyperexcitability in early-stage disease and why it preferentially emerges in specific regions is unclear. Using cortical-region and cell-type-specific assessments across a multitude of studies, we have observed dysregulation of a subgroup of cortical interneurons, parvalbumin+ (PV) interneurons. We have observed that not only does PV interneuron dysfunction arise prior to severe amyloid pathology, it also arises earliest in regions vulnerable to subsequent amyloid pathology. Furthermore, we note altered PV interneuron firing and circuit hyperexcitability without intrinsic alterations of the expectedly vulnerable excitatory cell type in Layer II of the Lateral Entorhinal Cortex. We suggest this vulnerability is a feature inherent to PV interneurons and may be exacerbated in some cortical regions from a regional-related variability in cell type intrinsic features and protein expression profiles. This study suggests early disease interventions targeting PV interneurons may protect regions with early vulnerability to pathological symptoms of Alzheimer's Disease and downstream cognitive decline.

**Parvalbumin Interneuron Regional Variability and
Vulnerability in Early Alzheimer's Disease**

By

Annie M. Goettemoeller
B.S., University of Michigan, 2019

Advisor: Matthew J.M. Rowan, Ph.D.

A dissertation submitted to the Faculty of the James T. Laney School of Graduate Studies of
Emory University in fulfillment of the requirements for the degree of Doctor of Philosophy in
the Graduate Division of Biological and Biomedical Science's Neuroscience Program
2024

Acknowledgements

This work is dedicated to all the individuals who have supported and motivated me throughout this journey.

I would first like to thank my advisor Dr. Matthew Rowan for his exceptional mentorship and guidance throughout my PhD. I can truly say that he has completely altered my trajectory as a scientist and as an individual, both incredibly for the better. His relentless support and tailored mentorship have allowed me to reach goals I never knew I could create. A graduate student might succeed despite a caring mentor, but in my experience, having your mentor as your highest advocate is truly invaluable. The gratefulness I have for Dr. Matthew Rowan cannot be summed into a simple paragraph; it is endless.

Thank you to Dr. David Weinshenker and Dr. Steven Sloan for their continued scientific guidance and mentorship beginning from the first year of my graduate career. Thank you for always giving me confidence in my place as a scientist and for pushing me to think critically. I would like to thank my committee members Dr. Shannon Gourley and Dr. Stephen Traynelis for their expert guidance throughout my dissertation research.

Additionally, I would like to thank members of the Rowan lab for all of the mentorship, guidance, and assistance during my time in the lab. I specifically would like to thank Dr. Viktor Oláh for his guidance in patch-clamp methodology and notably, his mentorship in the basic science literature; there is no doubt that his support has been truly formative in my training. Thank you to Emmie Banks, for her scientific advice, teamwork, and of course, friendship. Thank you to Anna Eaton and Hailian Xiao for your invaluable input, assistance, and friendship throughout your time in the lab. To the Ward Lab, notably, Jordan Owyoung and Tina Tian, your presence in the lab space changed the community and enjoyment of my work. I would also like to specifically thank Dr. Srikant Rangaraju and Dr. Prateek Kumar for their time and commitment to our collaboration, which contributed to a significant portion of this work. Thank you to Dr. James Zheng for his expertise and suggestions to this work.

Thank you to Lydia Farina, Heidi Sommers, Kayla Muschong, Ermioni Carr Clemence, Dr. Tina Lam, Dr. Monique North, Dr. Korin Fletemier, Dominic Becker, Sean Psenka, Josue Toledo, Claire Fendrick, Jennifer Isaac, Sarah Blumenthal, and Brittney Ward for their enduring friendship and support. I would also like to thank Dr. Lou Blanpain as a primary source of encouragement, love, and inspiration. A tremendous thank you as well to our dogs, Finley (mine) and Bruce (Lou's), for never-ending love and emotional support, and reminders to always take a break.

Finally, thank you to my incredible family – my mother, Dr. Melody Campbell; my father, Duane Goettemoeller; my sister, Megan Goettemoeller; my brother and sister-in-law, Drew and Michelle Goettemoeller; and my nephew and niece, Henry and Caroline Goettemoeller. I am immensely appreciative of your unconditional love and support of me throughout this process. It undoubtedly takes a village, and what an incredibly inspiring village I have.

Table of Contents

Figures & Tables

Chapter 1: Introduction

The equality (insomnia) of the powers (wet, dry, cold, hot, bitter, sweet, etc.) maintains health,
but that monarchy among them produces disease.

-Alcmeon (~500-450 BCE)

1   <u>1.1 The *Hegemonikon*</u>

2   Far before the brain was determined to be the *hegemonikon,* or the intellectual seat of the soul,

3   its susceptibility to disease was apparent (Edwin Smith Surgical Papyrus, 17th Century BCE). It

4   wasn't until many centuries later (5th-4th century BCE), that it was suggested to rule the senses,

5   memories, and thoughts (Pythagoras, and his pupil, Alcmaeon). However, this concept was still

6   under dispute by 17th Century AD, when Descartes was still grappling with the disconnect between

7   the physical and the mental, leading to the theory of Dualism. Our understanding of the role of the

8   brain in connecting the physical to the mental can ultimately be attributed in large to the study of

9   diseases and their origins. *On the Sacred Disease* ([putatively] Hippocrates, 400 BCE), represented

10   not only the first recorded observation of epilepsy, but also suggested the disease to arise through

11   naturalistic causes – an impairment of the brain – rather than through divine origin. Although the

12   [contested] author of *On the Sacred Disease* may have been misguided in their description of the

13   etiology of epilepsy, the attribution of an aberrant biological system created a new path for our

14   understanding of neurological diseases. Remarkably, it took over <u>2,000 years</u> for John Hughlings

15   Jackson to understand the electrical basis of epilepsy in many of its forms, including seizures

16   originating from the temporal lobe.

17   Even then, our understanding of the 'basic' unit of neurophysiology – the neuron – was not

18   described until the advent of a novel staining method by Camilla Golgi and the truly elaborate

19   observations and drawings of Santiago Ramón y Cajal (*e.g.,* **Fig. 1.1**). After a long wait of 2,000

20   years of disputes over the role of the brain as a commanding organ of the body, the last 200 years

21   have been remarkably exponential in our understanding of the brain and its operations. Luckily for

22 us, however, the more questions we answer – the more questions arise.
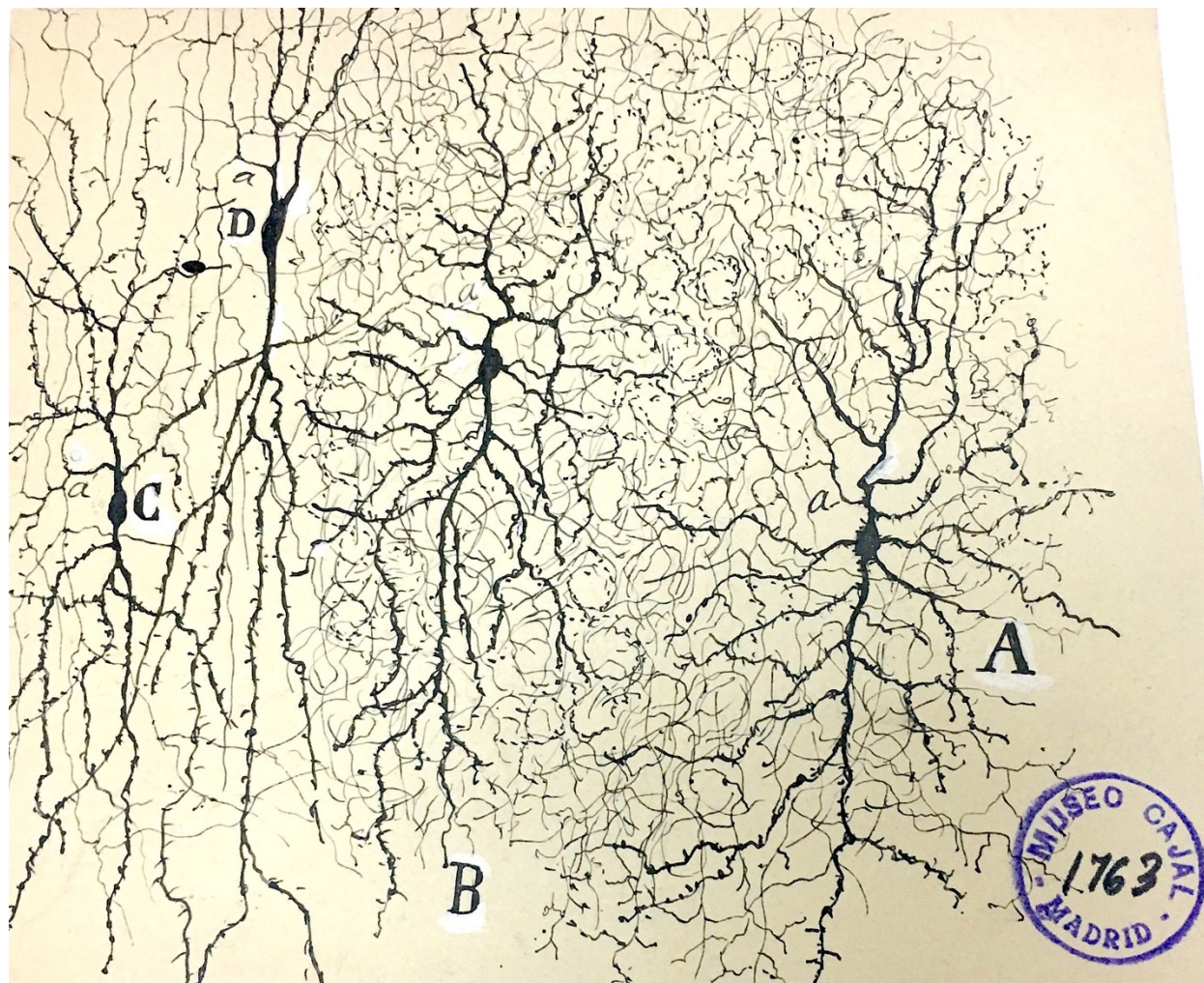
23

24 *Figure 1.1. Neurogliaform cells (class of inhibitory interneuron) as drawn by Ramón y Cajal*
25 *(1899)[3].*

26   Over the past century, the exploration of the brain's electrical properties and our knowledge

27 of neurons as conduits of the electrical signals have been extraordinary fields of study. Through

28 recordings from the squid giant axon (one of my favorite experiments in modern neuroscience[1]),

29 we began to understand the action potential[4,5], the electrical signal neurons use to communicate.

---

[1] I must confess that, as many beginners do, I first presumed squid giant axon was an experiment completed on the
neuronal axon from a Giant Squid. [To my dismay] the axon was simply giant in diameter. Despite this discovery, I
acknowledged my ignorance by subsequently maintaining my laboratory 'Slack' profile name as Giant Squid for my
entire graduate career.

30   This communication between neurons occurs at specialized junctions known as synapses, where

31   neurotransmitters[6] (i.e. Glutamate, GABA, Glycine) facilitate transmission. Many years of

32   research have ensued since, formalizing the field of 'neurophysiology', enabling a deeper

33   understanding of the nervous system in health and disease.

34   1.2 Homeostasis of the circuit

35   It is clear now that neurons (and other cells of the brain, *e.g.,* glia) communicate as separate

36   entities acting together to achieve a single goal. Remarkably, the communication between cells is

37   highly coordinated and dynamic. From development, cells develop specified relationships with

38   each other to form a circuit, the strength of which changes in response to activity and experience.

39   The circuit is an ensemble of neuronal and glial cell types coordinating together for an intended

40   purpose. This dissertation focuses primarily on local cortical circuits. Although different cortical

41   regions serve different functions, it has always been considered that the cell types and their

42   physiological features between cortical regions are quite similar[7,8]. This is likely specific to cortical

43   regions which fall under the umbrella of the 'neocortex', which is the six-layered cortex including

44   sensory and motor cortices, but has not been fully investigated for areas within the allocortex, such

45   as the Entorhinal Cortex.

46   All circuits of the brain must undergo constant alterations to maintain a balance between

47   excitation and inhibition under 'resting' conditions but are also prepared to clearly propagate an

48   important signal when the moment arises. This requires two classes of plasticity: Hebbian and

49   homeostatic. Hebbian plasticity, which includes spike-timing-dependent plasticity (such as long-

50   term plasticity [LTP] and long-term depression [LTD] of a synapse), alters synaptic strength in

51   individual synapses based on input alterations. This concept is often explained as "Neurons wire

52   together if they fire together"[9]. However, across layers of cells in a circuit, signals must propagate

53   across multiple layers without losing vital information from a stimulus and without the signal

54   losing its valence. Despite this need, cortical circuits exhibit high levels of positive feedback,

55   where slight alterations in excitation or inhibition should, in theory, result in either epileptiform

56   activity or full quiescence. However, a healthy circuit manages to compensate for minor changes

57   and maintain balance without noticeable alterations in function. This balance is referred to as

58   homeostasis and requires a multitude of mechanisms to be achieved. These mechanisms prevent a

59   stable circuit from becoming hyper- or hypoactive. This interplay of stability and responsiveness

60   to external stimuli cooperate in an elegant manner without interfering with one another[10].

61   The mechanisms of homeostasis occur across all levels of the circuit, from an individual cell's

62   excitability to connectivity. This includes neuronal action potential firing rates and synaptic

63   transmission strength to ensure overall firing rates remain consistent[11,12]. If individual neurons can

64   detect its own activity level and adjust itself to return to an 'average' set-point, then the circuit

65   itself will remain relatively constant[13]. These changes in intrinsic excitability can be achieved by

66   a cell altering its K^+, Ca^{2+}, or Na^+ conductances by altering the biophysical properties or expression

67   levels of corresponding ion channels[14]. However, if an individual or group of cells is unable to

68   return to its set-point, it may allow the circuit to stray from homeostasis, resulting in an alteration

69   in the excitation/inhibition (E/I) balance.

70   1.3 Interneurons and the circuit

71   While all cells in the circuit contribute to sustaining a balance between excitation and

72   inhibition, inhibitory interneurons stand out as crucial regulators. In contrast to the semi-

73   homogenous group of excitatory cells which comprise the cerebral cortex, the inhibitory

74   interneurons of the cortex comprise a diverse set of cells. These cells are named inhibitory because

75   they synthesize and release the classical inhibitory neurotransmitter, GABA (γ-aminobutyric acid).

76   Even when first described by Ramon y Cajal[3], it was clear that these 'short axon cells' – denoting

77   their ability to make local circuit connections – were comprised of multiple subtypes. Early on in

78   the study of GABAergic interneurons, it was surmised that interneurons belong to different

79   classes[15]. It is difficult to classify these abundantly different cells into discrete groups or 'cell-

80   types' as variance arises across experiments, cortical areas, and individuals. However, it is clear

81   that most inhibitory neurons thus fall into three main groups, according to their specific

82   histological markers: Parvalbumin+ (PV), Somatostatin+ (SST), and 5HT3aR+[16]. In order to

83   achieve clear communication across investigators, The Petilla Interneuron Nomenclature Group

84   convened in and published a set of guidelines in 2008 in order to create a standardized

85   nomenclature of interneuron properties[17]. The determined classifiers allow interneuron groups to

86   be further broken down based on the following features[17]:

87   1. Morphological

88   a. Somata: shape, size, and orientation

89   b. Dendrites: polarity of arborization, branching metrics, spines and beads

90   c. Axons: morphology, origin, branching metrics, bouton size and density,

91   d. Connections: postsynaptic target, location of synapse on post-synaptic cell, pattern

92   of postsynaptic contacts

93   i. Presence of gap junctions

94   2. Molecular

95   a. Transcription Factors

96   b. Neurotransmitters

97   c. Calcium Binding Proteins

98   d. Receptors

99   e. Structural Proteins

100   f. Cell-surface markers

101   g. Ion-channels

102   h. Connexins

103   i. Transporters

104   3. Physiological

105   a. Passive or subthreshold parameters

106   b. Action potential measurements

107   c. Dendritic Backpropagation

108   d. Depolarizing plateaus

109   e. Firing Pattern

110   f. Response to Hyperpolarizing step

111   g. Spiking recorded extracellularly

112   h. Postsynaptic responses

113   These qualifications result in at least 21 classes of interneurons, historically classified as such most

114   notably in CA1 of the hippocampus[18] **(Fig. 1.2)**.

Glutamatergic inputs:

Dentate gyrus

Subiculum, retrosplenial cortex

CA3 dentate gyrus

Pyramidal cells

Thalamus

Stratum lacunosum moleculare

Entorhinal cortex

Stratum radiatum

CA3

Stratum pyramidale

Stratum oriens

Amygdala

CB− CB+ CB−

Subiculum ? CA3 dentate gyrus Subiculum Septum

GABAergic interneurons in the hippocampal CA1 area

1	Axo-axonic	5	Bistratified	9	Apical dendritic innervating	14	Cholinergic	19	Interneuron-specific- I
2	Basket PV	6	Ivy	10	Perforant path–associated	15	Trilaminar	20	Interneuron-specific- II
3	Basket CCK/VIP	7	O-LM	11	Neurogliaform	16	Back-projection	21	Interneuron-specific- III
4	Basket CCK/VGLUT3	8	Schaffer collateral–associated	12	Radiatum-retrohippocampal projection	17	Oriens-retrohippocampal projection		
				13	Large calbindin	18	Double projection		

Figure 1.2. Interneurons of the hippocampus (CA1).

Adapted from Klausberger & Somogyi (2008)[18]

Of these, the PV+ subgroup of interneurons, accounts for ~40% of GABAergic neurons in the neocortex[16]. The PV+ expressing subgroup of inhibitory interneurons are comprised of basket cells (targeting the soma and proximal dendrites of pyramidal neurons as well as other basket cells[19]) and axo-axonic cells (targeting the axon initial segment)[20,21]. PV+ basket cells and axo-axonic cells, although recruited at different phases in both theta oscillations and Sharp Wave Ripples[18], share indistinguishable physiological properties, most notably their fast-spiking phenotypes. Because of this, researchers often use fast-spiking (FS) and parvalbumin+ (PV) interchangeably while generally referring to this population of inhibitory interneurons. This fast-spiking phenotype is made feasible by the fast onset of Nav and Kv3 channels[22-30].

128   Wild-type (WT) fast-spiking PV interneurons display stereotyped intrinsic properties, such

129   as a low input resistance (75-90 MΩ), high rheobase (330-400 pA), high firing frequency at 2-3x

130   threshold (130-180 Hz), a narrow action potential half-width (0.40-0.44 ms), and minimal spike

131   frequency adaptation (0.75-0.85)[31]. However, it is also important to note that the same firing

132   phenotype can be recapitulated by vastly different conductances of the same channels[32].

133   Furthermore, there is a range of firing frequencies within which a cell may still be categorized

134   within the group of 'fast-spiking cell'. For example, although a canonical FS interneuron can be

135   pushed to fire higher than 300 Hz, there are also PV+ cells which fire slower than the canonical

136   FS interneuron. These atypical wild-type PV+ cells have been shown in the subiculum (quasi fast-

137   spiking interneurons)[33], the striatum (fast-spiking-like cells)[34], and the CA1 region of the

138   hippocampus (non-fast-spiking PV+ interneurons, NFS)[31]. The subgroup of NFS PV+

139   interneurons displayed varied intrinsic properties from those canonical FS interneurons, including

140   a low-firing frequency (~96.1 Hz at 3x threshold), high input resistance, and low rheobase[31]. This

141   raises the question: Are these a distinct subgroup of PV+ interneurons, or is this a result idealized

142   discrete group definitions? Perhaps researchers could simplify matters by defining this group of

143   cells as PV+ expressing, rather than concerning themselves with the variability of their intrinsic

144   properties. Unsurprisingly, this definition again falls short. Parvalbumin is a calcium-binding

145   protein which has a high affinity for calcium[35] and is involved in intracellular calcium regulation

146   and trafficking[36]. However, it has been shown that parvalbumin expression correlates with PV+

147   interneuron activity levels[37,38]. It is also known that only a fraction of axo-axonic cells (also known

148   as chandelier cells) display lower parvalbumin positivity[39]. Furthermore, parvalbumin expression

149   is lower in some posterior and association cortical areas, despite cells displaying a stereotyped

150   fast-spiking phenotype[40]. Thus, although the 'fast-spiking, parvalbumin+' interneuron is a widely

151 accepted idealized average interneuron subtype, it is imperative to recognize this group still

152 exhibits a variety of morphological, electrophysiological, and molecular properties across the

153 brain.

154 However, regardless of their variance, these cells maintain strong control over their respective

155 circuits due to their extensive local axonal arborizations. Alterations in inhibitory interneuron

156 function appear responsible for circuit and behavioral dysfunction in several neurological diseases.

157 In particular, dysfunction of fast spiking, parvalbumin-expressing interneurons (PV-INs) are

158 implicated in epilepsy, neurodevelopmental, and neurodegenerative diseases, including

159 Alzheimer's disease (AD)[26,41], a likely consequence of their role in maintaining circuit excitability

160 locally, and brain state more generally, coupled with their substantial energy requirements[42].

161

162 1.4 Alzheimer's Disease

163 Alzheimer's disease (AD) is the most prevalent neurodegenerative disease, constituting 60-

164 90% of dementia cases[43], yet current treatments are unable to prevent its initiation and progression.

165 The development of the disease begins many decades prior to diagnosis. However, it is unclear

166 which factor(s) initiate the development of Alzheimer's Disease. From the initial description by

167 Alois Alzheimer[44], Alzheimer's disease has been characterized by the neuropathological staging

168 of two aggregate proteins: amyloid-beta plaques and tau neurofibrillary tangles. Early studies

169 focused on these two late-stage pathologies as the cause of the associated cognitive decline. This

170 initial focus has left the field to work backwards from the large protein aggregates to consider its

171 precursors as potential causes of the disease. For example, with amyloid pathology: including the

172 amyloid-beta peptide, and the amyloid-beta peptide as it forms dimers and oligomers with itself[45].

173 Despite the progression, each of these hypotheses still falls under the phrase of the "amyloid

174 cascade hypothesis"[46]. This hypothesis posits that the aggregation of amyloid-beta, a protein

175 cleavage product of the amyloid precursor protein (APP), initiates a neurodegenerative cascade

176 which ultimately results in cognitive decline.

177 Interestingly, under normal conditions, the amyloid-beta peptide, alongside APP and its

178 other cleavage products are imperative for synaptic plasticity and development. APP itself is

179 enriched at the synapse[47]. It has been found to function as a cell-adhesion molecule and surface

180 receptor, regulating synaptogenesis[48] and cell division[49]. Furthermore, the absence of APP from

181 certain neurons inhibits neurite outgrowth[50] and impairs short- and long-term plasticity[51].

182 Alternate splicing of APP mRNA can result in 8 different isoforms of the protein, but 3 are

183 the most common: APP 695, APP 751, and APP 770[52]. In the Central Nervous System of a healthy

184 individual, the 695 isoform is predominantly expressed[53]. However, in human AD, the ratio of

185 different APP isoforms shifts from predominantly expressing APP 695 to higher levels of APP 770

186 and 751[54,55]. These longer isoforms show increased expression following aging-related processes

187 (*e.g.,* after reproductive hormonal production decline[56], hypercholesterolemia[57], and

188 atherosclerosis[58]), all of which are also associated with increased AD risk[59-62].

189 APP is generated consistently and metabolized quickly[63]. The APP protein undergoes two

190 'pathways' of cleavage (Fig. 3), determined as such through their production (or lack) of the

191 amyloid-beta peptide: the amyloidogenic and non-amyloidogenic pathways, respectively. The non-

192 amyloidogenic pathway takes place primarily on the cell surface[64]. In the non-amyloidogenic

193 pathway, APP is cleaved first by α-secretases, which include several members of the ADAM

194 family, which releases the ectodomain sAPPα, leaving the membrane-bound α-CTF or C83. The

195 sAPPα fragment alone has been shown to improve synaptic density and memory[65,66]. The C83

196   segment is subsequently cleaved by γ-secretase, which is a complex presenilin, and other proteins,

197   resulting in the soluble p3 segment as well as the APP intracellular domain (AICD).

198   The amyloidogenic cleavage pathway takes place primarily in cellular locations with a

199   lower pH, such as endosomal compartments[67,68]. In fact, preventing surface endocytosis reduces

200   amyloid-beta production by 80%[69]. In the amyloidogenic pathway, APP is first cleaved by β-

201   secretase, also known as BACE1, resulting in the soluble sAPPβ and the membrane bound β-CTF

202   or C99. The neuroprotective effects of sAPPβ are far less than its counterpart, sAPPα[70,71].

203   However, it does induce neural differentiation[72] and axonal outgrowth[73]. The β-CTF has been

204   implicated in lysosomal dysfunction[74] and hyperexcitability[75], independently of Aβ. After the

205   formation of β-CTF, it is cleaved again by γ-secretase forming a similar length AICD and the

206   amyloid-beta peptide. Interestingly, the AICD fragment from both processes has transcriptional

207   activity[76]. Remarkably the amyloid-beta peptide (Aβ) also has a physiological role. Aβ regulates

208   synaptic scaling[77] and vesicle release[78]. The complexity of APP processing and the dual function

209   of its cleavage products underscore the intricate interplay between normal physiological function

210   and pathological processes in Alzheimer's Disease.

"Non-amyloidogenic pathway"   "Amyloidogenic pathway"
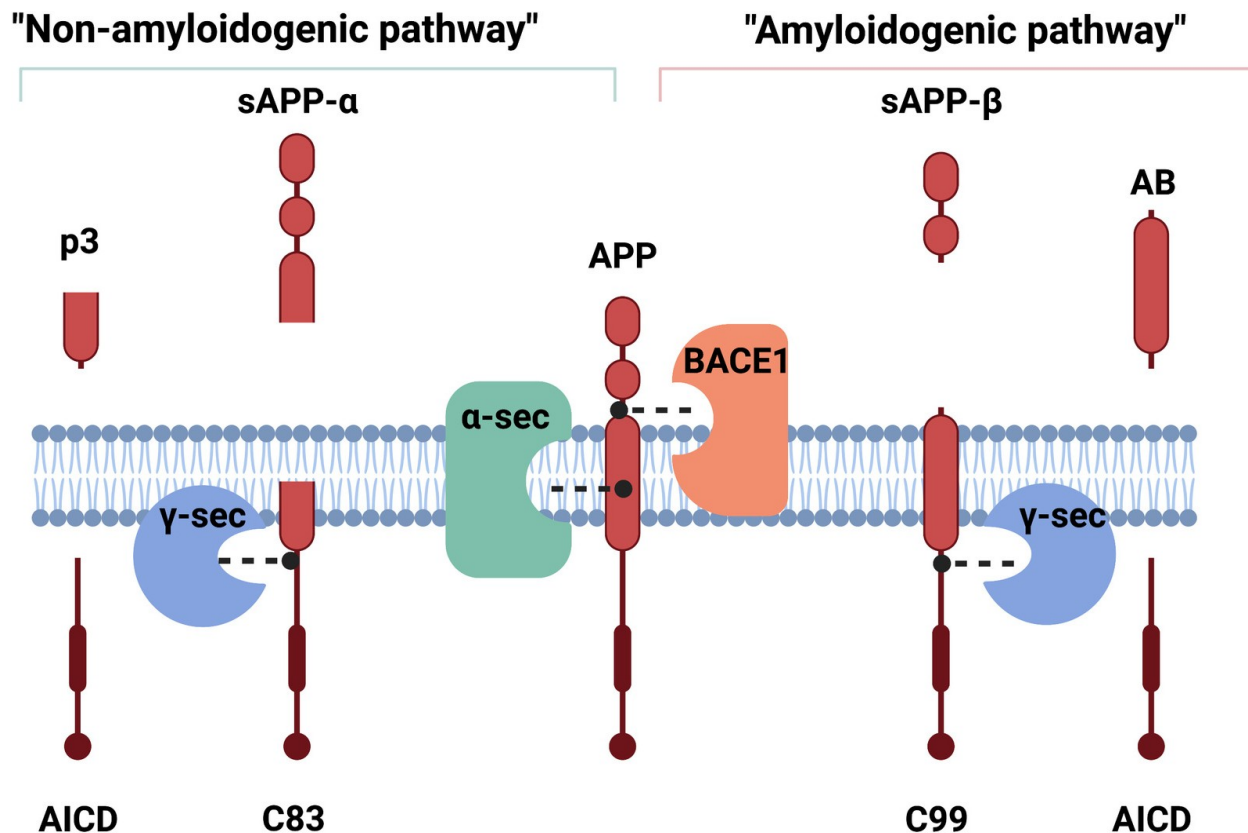
Figure 1.3. APP processing pathways.

Although all cells release Aβ, its levels increase with synaptic activity and its production and release are regulated by synaptic activity[79], and modulated by the sleep-wake cycle[80]. However, it has been suggested that whether Aβ maintains a physiological role or a toxic one is dependent on its biophysical state[81]. Furthermore, in mouse models of AD, the contribution of Aβ may vary from different cell types. For example, in the hippocampus of an APP knock-in model, inhibition of Aβ production specifically from GABAergic interneurons (through inhibition of BACE1) resulted in 75% reduction of the plaque load[82], despite interneurons comprising only 10-15% of the cells in the whole hippocampus[83].

Whether Aβ is truly the initiating factor of AD is highly contested. Of course, many of the causative genes of early-onset Alzheimer's Disease are within APP or associated cleavage proteins. In fact, many other disease mechanisms have been suggested, including inflammation[84,85],

224   oxidative stress and mitochondrial failure[86,87], and glial activation[88]. It is likely that all of these,

225   when combined with aging, are involved in the pathogenesis of Alzheimer's Disease[89].

226   Interestingly, however, these mechanisms – whether they be pathological protein

227   aggregates or inflammation – do not occur ubiquitously across brain regions at the same time.

228   Rather, it is evident that some regions develop Alzheimer's Disease pathology early, while others

229   remain relatively stable until many years later[90,91].

230   The first location of excessive amyloid-beta pathology is slightly contested. Some have

231   asserted amyloid pathology appears first in the Default Mode Network (DMN), which is comprised

232   of the posterior cingulate gyrus, the prefrontal cortex, and the inferior parietal lobule[92,93]. However,

233   it has also been suggested that a subtype of excitatory cells in the Lateral Entorhinal Cortex (LEC)

234   are the first to exhibit intracellular amyloid pathology[94]. Interestingly, the DMN and the

235   hippocampus are dynamically connected, likely through the LEC[95,96]. The entorhinal cortex

236   functionally links the hippocampus to the DMN[96-99]. Importantly, it has been shown that while

237   individual may develop medial temporal tauopathy[90,100], the propagation of tau outside of the

238   medial temporal lobe is dependent upon the presence of $A\beta$[101-103]. This does not help to clarify

239   whether amyloid pathology *truly* begins in the entorhinal cortex or the DMN, but it is apparent

240   that increased amyloid pathology coincidental with tau pathology is imperative for the subsequent

241   propagation of AD-related pathologies throughout the rest of the brain. The propagation of tau

242   pathology outside of the medial temporal lobe is also a differentiating feature for natural aging

243   versus dementia[104]. Furthermore, previous studies have assessed whether aging-related memory

244   decline results from alterations in entorhinal cortex thickness, hippocampal volume, and/or DMN

245   connectivity. It was determined that while both the DMN connectivity and hippocampal volume

246   have direct influences on memory decline, entorhinal cortex thickness is the node which influences

247 both of them[96]. This positions the Lateral Entorhinal Cortex as a pivotal regional in the progression

248 of Alzheimer's Disease, particularly in early phases. Although brain regions of early vulnerability

249 have been known for over 30 years[90], our understanding of what makes certain areas more

250 susceptible remains unknown. Furthermore, how the disease progresses out of these areas to impair

251 the remainder of the cortex is unclear.

252

253 <u>1.5 Vulnerability in Alzheimer's Disease</u>

254 *What does it mean for a region or cell type to be vulnerable?*

255 The formal definition of vulnerability as defined by Merriam-Webster Dictionary is [*as in*

256 *susceptibility*] "the quality or state of having little resistance to some outside agent". In

257 Alzheimer's Disease, the outside agent is considered to pathological accumulation of Aβ/tau or

258 neurodegeneration. This secondary qualification within the field has caused much confusion,

259 particularly in early stages of the disease before severe pathology and neurodegeneration arises. A

260 clear description of the 'outside agent' referred to is particularly salient when discussing the

261 susceptibility of individual cell types.

262 Notably, landmark studies identified Layer II (LII) neurons of the LEC as highly vulnerable

263 to early neurodegeneration with up to 60% cell death in mild AD patients and up to 90% in severe

264 cases[105]. More recently, LII LEC principal neurons were also characterized as a cell population

265 exhibiting amyloid pathology[94]. However, the distinctive features which impart vulnerability to

266 neurons in the LEC AD remain unclear. Uncovering region-specific cellular mechanisms could

267 improve our understanding of the initiating factors in the AD cascade and are imperative in

268 determining potential interventions at a time when subsequent cognitive decline and

269 neurodegeneration might still be prevented.

270   Hyperexcitability, or an increase in the aberrant firing of excitatory neurons, is one of the

271   earliest pathophysiological biomarkers in the human AD brain, and its emergence correlates with

272   severity of cognitive decline in individuals[106]. Hyperexcitability is also observed in recordings

273   from *in vivo* and *in vitro* models of AD pathology[75,107-112], arising prior to amyloid plaque

274   deposition[113] and likely contributing to spine degeneration[114]. Interestingly, hypermetabolism[115]

275   and hyperexcitability[109,116] emerged in the LEC of a sporadic AD mouse model before spreading

276   to other regions[117]. These shifts in circuit activity may result from dysfunctional neuronal firing

277   and neurotransmission[118,119]. It is unclear whether cell-intrinsic changes in principal neuron

278   excitability or other forms of circuit dysfunction are responsible for aberrant LEC activity in early

279   AD.

280   Cognition and memory require carefully balanced excitatory and inhibitory activity[120]. In

281   different AD mouse models, impairments in inhibition precede plaque formation, disrupting brain

282   rhythms associated with memory formation[115,121-123]. Modified inhibitory tone in early AD[107,109,115]

283   is likely related to changes in the intrinsic excitability of local circuit inhibitory interneurons. Most

284   notably, AP firing is altered in PV interneurons in different human APP (hAPP)-expressing

285   mice[108,109,118,121,124,125]. Interestingly, altered PV physiology may occur before changes to other

286   neighboring neuron subtypes[110,126]. Whether the basal properties of PV interneurons confer

287   functional vulnerability to early AD pathogenesis prior to other cell types is unknown. Thus, it is

288   imperative to obtain cell-type-specific measurements across stages of pathogenesis to understand

289   which cell types are vulnerable to early insults, in order to develop preventative treatments.

290   <u>1.6 Cell-type-specific assessment of vulnerability</u>

291   Alzheimer's disease is a complex disease which spans decades, but diagnosis does not occur

292   until the disease is well underway. This delay in diagnosis has posed challenges for developing

293   effective treatments to prevent its progression. While both preventative and disease-modifying

294   treatments remain elusive[127], there is ongoing debate as to whether these therapeutic failures are

295   stem from flawed strategies or if intervention occurs too late into the disease progression.

296   Consequently, it seems imperative to explore implementation of treatment earlier in disease

297   progression, which requires a thorough understanding of disease staging prior to diagnosis.

298   Qualification of AD in the research context relies upon measurement of the levels of $A\beta$

299   plaques and tau (neurofibrillary tangles, NFTs) in the brain, alongside assessments of cognitive

300   dysfunction[128]. However, the difficulty remains in characterizing the progression of AD prior to

301   severe pathology. In order to study these changes on a large scale, many research centers have

302   focused on using 'omics' methods, including genomics, transcriptomics, and proteomics, which

303   enable large-scale measurements of alterations throughout the brain over time. Genomics have

304   discovered genes which put individuals at risk for AD[129]. In the context of basic science,

305   transcriptomic studies have recently provided unparalleled access to the genetic diversity of dozens

306   of unique brain cell classes[7,130]. Functional information is nonetheless limited in transcriptomic

307   studies, due to substantial discordance between mRNA and protein levels, especially in neurons[131-

308   133]. However, recent developments in proteomic studies from AD tissue have correlated proteins

309   with alterations of those proteins in the CSF, and how they change across AD staging, providing

310   notable biomarkers outside of the levels of $A\beta$ and tau pathologies[134]. Importantly, this type of

311   analysis can be performed in healthy individuals and assess their levels of progression toward AD

312   as they age.

313   Although the identified proteins provide specific targets for therapeutics, it is unlikely that

314   they are ubiquitously expressed across the brain or individual cell types. An elegant treatment

315   which hopes to be successful at early phases of the disease must consider the regions and cell types

316   which are vulnerable at that time, to address the problem at its source. Unfortunately, it is difficult

317   to acquire cell-type-specific proteomics in living humans, and until recently, in mice. Previous

318   proteomic studies which relied on physical isolation of individual neuron types are also inadequate,

319   as physical isolation of individual neurons is poorly tolerated, and of those that do survive, the vast

320   majority of their functional surface area (i.e., dendrites and axons) is lost[135,136]. To overcome these

321   limitations, we recently developed an *in vivo* strategy called cell type-specific in vivo biotinylation

322   of proteins (CIBOP). When coupled with mass spectrometry, CIBOP can resolve native state

323   proteomes from physically unaltered cell subtypes *in vivo*[2]. Key technical advancements,

324   especially relating to neuronal subtype-specific targeting across different disease models, are also

325   necessary to fully realize the potential of this method via extension to distinct classes of excitatory

326   and inhibitory neurons. Thorough cross-comparison of these non-overlapping cell-type specific

327   alterations with alterations observed across human AD bulk-tissue staging may provide specific

328   targets for therapeutics to halt disease progression. Furthermore, comparison of cell-type-specific

329   proteomics to ongoing alterations in circuit excitability, such as phases of hyperexcitability

330   observed in AD patients, may provide such targets at a unique point of intervention.

Chapter 2: Methods

I'm not sure yet what I'm going to do for my PhD…
but I know for sure it's not going to be patch-clamp electrophysiology.

-AMG (As a Y1 PhD Student)

331   <u>2.1 Patch-clamp electrophysiology</u>

332   *Acute slice preparation*

333   All animal procedures were approved by the Emory University IACUC. Acute slices from

334   SS cortex and LEC were prepared from a mixture of C57Bl/6J and PV-Cre mice (8-12 weeks old),

335   evenly dispersed between test and control groups. Male and female mice were used for all

336   experiments with data collected from $\geq$ 3 mice per experimental condition. Mice were first

337   anesthetized and then killed by decapitation. The brain was then immediately removed by

338   dissection in ice-cold cutting solution (in mM) 87 NaCl, 25 NaHO3, 2.5 KCl, 1.25 NaH2PO4, 7

339   MgCl2, 0.5 CaCl2, 10 glucose, and 7 sucrose. Brain slices (250 μm) were sectioned in the sagittal

340   plane using a vibrating blade microtome (VT1200S, Leica Biosystems) in the same solution. Slices

341   were transferred to an incubation chamber and maintained at 34°C for ~30 min and then at 23-

342   24°C thereafter. During whole-cell recordings, slices were continuously perfused with (in mM)

343   128 NaCl, 26.2 NaHO3, 2.5 KCl, 1 NaH2PO4, 1.5 CaCl2, 1.5MgCl2 and 11 glucose, maintained

344   at 30.0±0.5°C. All solutions were equilibrated and maintained with carbogen gas (95% O2/5%

345   CO2) throughout.

346

347   *Electrophysiology*

348   PV interneurons and excitatory cells were targeted for somatic whole-cell recording in

349   layer 5 region of somatosensory cortex or layer 2 lateral entorhinal cortex by combining gradient-

350   contrast video-microscopy with epifluorescent illumination on custom-built or commercial

351   (Olympus) upright microscopes. Electrophysiological recordings were acquired using Multiclamp

352   700B amplifiers (Molecular Devices). Signals were filtered at 10 kHz and sampled at 50 kHz with

353   the Digidata 1440B digitizer (Molecular Devices). For whole cell recordings, borosilicate patch

354 pipettes were filled with an intracellular solution containing (in mM) 124 potassium gluconate, 2

355 KCl, 9 HEPES, 4 MgCl2, 4 NaATP, 3 L-Ascorbic Acid and 0.5 NaGTP. For experiments recording

356 spontaneous and miniature events, an intracellular solution containing (in mM) 120 CsMeSO4, 10

357 HEPES, 5 TEA.Cl, 4 Na2ATP, 0.5 Na2GTP, 2 MgCl2, 10 L-Ascorbic Acid, and 3 Qx314. To obtain

358 miniature events, slices were perfused with 1 μM TTX for 10 minutes prior to recording. The same

359 protocol was used for spontaneous and miniature events. Pipette capacitance was neutralized in all

360 recordings and electrode series resistance compensated using bridge balance in current clamp.

361 Liquid junction potentials were uncorrected. Recordings had a series resistance < 20 MΩ.

362 Membrane potentials were maintained near -70 mV during current clamp recordings using constant

363 current bias. Action potential trains were initiated by somatic current injection (300 ms)

364 normalized to the cellular capacitance in each recording measured immediately in voltage clamp

365 after breakthrough[137]. For quantification of individual AP parameters, the 1st AP in a spike train at

366 was analyzed at 12pA/pF for all cells. Passive properties were determined by averaging the

367 responses of several 100 ms long, -20pA steps during each recording. Spontaneous and miniature

368 events were recorded at a holding voltage of -70 and 0 mV, one second each, interleaved for 3-5

369 minutes. For regional comparisons of PV interneurons, combined controls from datasets in each

370 region were used. K$^+$ channel activation curves were calculated as described (Rowan et al. 2016)

371 using chord conductance (g) values from current peaks and fit with a Boltzmann function.

372 Activation time constants were obtained by fitting the rising phase of the K$^+$ current with a single

373 exponential function. Event detection was carried out using Clampfit (Molecular Devices) using a

374 template matching algorithm and were curated manually with a 4 kHz low-pass filter.

375 For optogenetic slice experiments, C1V1 was activated using an unfiltered amber LED (M590L3;

376 Thorlabs) centered on l = 596 nm (±15 nm). ChETA was excited using blue light from an unfiltered

377   LED (M470L3; Thorlabs) centered on $l = 461$ nm ($\pm$ 20 nm). LEDs were rapidly modulated with

378   time-locked TTL pulses from the electrophysiology software using short pulses with a current

379   controller (LEDD1B; Thorlabs). Due to kinetics differences between ChETA and C1V1, 0.15-0.3

380   and 4ms pulses (respectively) were found to be optimal to reliably elicit PV-pyramidal cell IPSCs

381   every trial with minimal jitter. To eliminate potential sources of variation between experiments,

382   these parameters and the amber/blue light power at the objective remained unaltered for all

383   optogenetic control and test experiments.

384

385   <u>2.2 Viral Injections</u>

386

387   *Intracranial viral injections:*

388   <u>Optogenetics Experiments</u>

389   PV-IN-specific optogenetic studies were performed in separate cohorts of WT and 5xFAD

390   mice, or in PV-Cre (Jax strain #:017320) mice for hAPP-AAV studies. For C1V1 experiments in

391   5xFAD (or WT controls), AAV(PHP.eB)-E2-C1V1-eYFP (addgene 135633) was co-injected with

392   AAV1.CamKII(1.3).eYFP.WPRE.hGH (addgene 105622) at a 1:1 ratio. For ChETA experiments,

393   AAV1-Ef1a-DIO-ChETA-EYFP (addgene 26968) was co-injected with an hAPP-expressing virus

394   AAV(PHP.eB).EF1a.hAPP.oPRE (hAPP RefSeq NM_000484.4) or an equivalent amount of sterile

395   saline in controls. Injections were all performed in the SBFI region of S1 cortex. For injections,

396   mice were head-fixed in a stereotactic platform under continuous isoflurane anesthesia (1.8–2.0%).

397   Thermoregulation was provided by a heat plate with a rectal thermocouple for biofeedback, to

398   maintain core body temperature near 37°C. A small incision was made and a craniotomy cut in the

399   skull (<0.5 μm in diameter) to allow access for a glass microinjection pipette. Coordinates (in mm

400   from Bregma) for microinjection were X = ±3.10–3.50; Y = −2.1; α = 0°; Z = 0.85–0.95. Viral

401   solutions (stock titers were ~1.0 × 10^{13} vg/mL, except for AAV.EF1a.hAPP, which was 1.0 x 10^{12}

402   vg/ml) were injected slowly (~0.02 µL min^{-1}) using Picospritzer-directed short pulses (~0.3 µL

403   total). After ejection of virus, the micropipette was held in place (~5 min) before withdrawal. The

404   scalp was closed first with surgical sutures and Vetbond (3M) tissue adhesive thereafter and the

405   animal was allowed to recover under analgesia (carprofen and buprenorphine SR). After allowing

406   for onset of expression (1 or 3 weeks for C1V1/YFP or ChETA/hAPP, respectively), animals were

407   sacrificed, and acute slices harvested for patch clamp studies as detailed above.

408

409   <u>hAPP experiments</u>

410   5-9 week old mice were injected with AAV(PHP.eB).E2.tdTom with saline or

411   AAV(PHP.eB).EF1a.hAPP (0.3 µL total, 1:1) in the SBFI vibrissal region of cortex or the Lateral

412   Entorhinal Cortex. For murine APP experiments AAV(PHP.eB).EF1a.hAPP was replaced with

413   AAV(PHP.eB).EF1a.mAPP. For murine APP/hAβ chimera experiments,

414   AAV(PHP.eB).EF1a.mAPP/hAβ was used. For tau experiments, the four conditions were: Ctrl

415   (CaMKII.eYFP: saline 1:2), hAPP (EF1a.hAPP: CaMKII.eYFP: saline, 1:1:1), hTau

416   (AAV(PHP.eB).EF1a.hMAPT: CaMKII.eYFP: saline, 1:1:1), and hAPP+hTau (EF1a.hAPP:

417   Ef1a.hMAPT: CaMKII.eYFP, 1:1:1). When performing intracranial viral injections, mice were

418   head-fixed in a stereotactic platform (David Kopf Instruments) using ear bars, while under

419   isoflurane anesthesia (1.5 - 2.0%). Thermoregulation was provided by a heating plate using a rectal

420   thermocouple for biofeedback, thus maintaining core body temperature near 37°C. Bupivacaine

421   was subcutaneously injected into the scalp to induce local anesthesia. A small incision was opened

422   5-10 minutes thereafter and a craniotomy was cut in the skull (< 0.5 µm in diameter) to allow

423   access for the glass microinjection pipette. Coordinates (in mm from Bregma) for microinjection

424   in the SS Cortex were X = ± 0.85; Y = −2.5; α = 0°; Z = −0.85, coordinates for the LEC were X =

425   ± 3.39; Y = −4.52; α = 0°, Z= −2.4, −1.5. Viral solution (titer $1x10^{09}$ to $1x10^{13}$ vg/mL) was injected

426   slowly (~0.02 µL min-1) by using a Picospritzer (0.3 µL total). After ejection of virus, the

427   micropipette was held in place (5 min) before withdrawal. The scalp was closed with surgical

428   sutures and Vetbond (3M) tissue adhesive and the animal was allowed to recover under analgesia

429   provided by injection of carprofen and buprenorphine SR. After allowing for onset of expression,

430   animals were sacrificed acute slices were harvested.

431

432   *Retro-orbital (RO) injection:*

433   Male and female mice were given AAV retro-orbital injections as previously described[138].

434   Mice were anesthetized with 1.8-2% isoflurane. AAV(PHP.eB).E2.Cre.2A.GFP virus was titrated

435   to $2.4x10^{11}$ vector genomes total was accompanied by AAV(PHP.eB).Flex.tdTom titrated to

436    $3.1x10^{11}$ and injected in TurboID+ mice[2] (Proteomics), WT littermates (C57B6J), 5xFAD, or

437   TurboID+/5xFAD mice to label PV interneurons throughout cortex. As a control, PV-Cre mice

438   (Jackson Laboratory; stock no. 008069); were injected with AAV(PHP.eB).Flex.tdTom

439   (Addgene).Titrated virus was injected into the retro-orbital sinus of the left eye with a 31G x 5/16

440   TW needle on a 3/10 mL insulin syringe. Mice were kept on a heating pad for the duration of the

441   procedure until recovery and then returned to their home cage. For proteomics experiments in

442   TurboID+ mice, were provided with biotin water continuously starting 3 weeks post-injection.

443   Biotin water was administered for 2 weeks until acute slice sample collection (total of 5 weeks

444   post-RO injection).

445

446   <u>2.3 RNA expression detection techniques</u>

447

448   *Fluorescent cell picking and qPCR:*

449   Manual cell picking was performed for single cell isolation. 12 mice (2 genotypes x 6

450   animals/group) were used for cell picking experiments. Acute slices (300 µm) were acquired from

451   5xFAD mice and their wild-type littermates at 7-8 weeks of age. Acute slices obtained as described

452   above. Slices containing SBFI cortex were placed into cutting solution with 0.5 mg/mL protease

453   (P5147–100MG, Sigma-Aldrich) for 60-minutes with continuous carbogen gas bubbling.

454   Immediately after, slices were returned to room-temperature cutting solution for 10 minutes. Slices

455   were then micro-dissected to isolate the cortical region containing GFP$^+$ or tdTom expressing cells

456   using an epi-fluorescent stereoscope (Olympus SZX12). Samples were then manually triturated in

457   cutting solution with 1% Fetal Bovine Serum (F2442–50 mL, Sigma Aldrich) into a single-cell

458   suspension. The sample was then diluted with ~300 uL of cutting solution, dropped onto a Sylgard

459   (DOW) coated petri dish, and cells were allowed 10 minutes to settle. The remainder of the dish

460   was then filled with pre-bubbled cutting solution. Cells were selected using epi-fluorescent

461   illumination under an inverted microscope (Olympus IX71) using a pulled borosilicate glass

462   pipette connected to a filter-tipped stopcock. ~200 picked cells were stored in RLT buffer (Cat.

463   No. 79216 – 220 mL, Qiagen) with 1% 2-Mercaptoethanol (M6250-100ML, Sigma-Aldrich) at -

464   80°C until cDNA isolation. cDNA was generated from each sample using an RNAseq library prep

465   method. A cDNA library was created with the CellAmp™ Whole Transcriptome Amplification Kit

466   (#3734, Takara Bio) to allow for real-time PCR (qPCR) to be conducted. qPCR was then conducted

467   with the following primers:

468

469   GAPDH (Mm99999915_g1, Taqman), *Pvalb* (Mm.2766, Taqman), *Scn1a* (Mm00450580_m1,

470   Taqman), *Scn8a* (Mm00488119_m1, Taqman), *Kcnc1* (Mm00657708_m1, Taqman), *Kcnc2*

471   (Mm01234232_m1, Taqman), *Kcnc3* (Mm00434614_m1, Taqman), *Kcnc4* (Mm00521443_m1,

472   Taqman). Results of qPCR were analyzed using the Common Base Method with expression

473   normalized to GAPDH. ΔCt values were averaged between triplicate samples from each mouse.

474

475   *RNAscope:*

476   RNAscope was performed for confirmation of viral hAPP and mAPP expression, as well

477   as quantification of viral expression in a cell-type-specific manner. RNAscope was performed as

478   instructed by Advanced Cell Diagnostics (ACD). Tissue was prepared from C57Bl/6J mice (8-12

479   weeks old), evenly dispersed between test and control groups. Male and female mice were used

480   for all experiments with data collected from ≥ 3 mice per experimental condition. Mice were

481   injected with AAV(PHP.eB).E2.tdTom and AAV(PHP.eB).hAPP or AAV(PHP.eB).mAPP (0.3 uL

482   total, 1:1) in one hemisphere and injected contralaterally with AAV(PHP.eB).E2.tdTom and saline

483   (0.3 uL total, 1:1), n=3 each. Hemispheres were randomized. After 2-3 weeks, mice were first

484   anesthetized and then killed by decapitation. The brain was then immediately removed and flash

485   frozen in isopentane on dry ice. Samples were kept at -80°C prior to sectioning. Tissue was

486   sectioned on a cryostat at 16 μm thick, mounted onto Superfrost Plus Slides, and stored at -80°C

487   until use. Samples were fixed and dehydrated according to the RNAscope kit manufacturer

488   (ACDBio) standard protocol. In brief, frozen slides containing tissue sections were immediately

489   dipped in pre-chilled 4% paraformaldehyde (PFA) for 15 minutes at room temperature. After

490   fixation, slides were briefly rinsed with 1× phosphate buffered saline (PBS) two times to remove

491   excess fixative. Tissue sections were then dehydrated in a series of ethanol solution 50%, 70% and

492   100% for 5 min at room temperature. After ethanol washes the slides were transferred into a fresh

493   100% ethanol solution to sit overnight at 4°C. The following day, slides were taken out of the

494   ethanol solution, air dried for 5 minutes, and hydrophobic barriers were drawn around each section.

495   The remainder of the RNAscope assay was then performed following the manufacturer's protocol,

496   multiplexing two different probe groups on two different sections from each animal: 1) human

497   APP (catalog #418321), mouse APP (catalog #519001-C2), and CaMKIIα (catalog #445231-C3),

498   and 2) human APP, mouse APP, and Pvalb (catalog #421931-C3).

499

500   *RNAscope Image Analysis:*

501   Images for analysis of RNAscope sections were taken on a Keyence BZ-X800 microscope

502   (KEYENCE; Osaka, Japan) at 40X magnification. Two images were acquired of each mouse LEC

503   hemisphere, and 4 sections were imaged per mouse (total: ~8 images/experiment for an n=3). The

504   acquisition parameters were kept constant throughout imaging of all sections. Four fluorescent

505   channels were used simultaneously; (1) the green channel was assigned for VIVID 520 dye (human

506   APP probe), (2) the blue channel was used for DAPI nuclear stain, (3) the red channel was assigned

507   for VIVID 570 dye (mouse APP probe), and (4) the far-red channel was assigned for VIVID 650

508   dye (CaMKIIα or Pvalb probes). A z-stack was taken (with 1 μm steps) of each hemisphere, and

509   the full focus feature in the Keyence BZ-X800 analysis software was applied to compress each 10

510   μm z-stack. These compressed z-stacks were then used for image analysis in HALO v3.6 FISH-IF

511   v2.1.4 (Indica Labs). For immunohistochemistry experiments, 2 sections were imaged per

512   antibody per mouse (total: ~4 images/experiment for an n=3-5). The acquisition parameters were

513   kept constant throughout imaging of all sections. Two channels were used simultaneously; (1) the

514   green channel was assigned for CaMKII.eYFP expression, (2) the red channel was assigned for

515   Alexa Fluor™ 647. For each slice, four line scans of 200 thickness were analyze from the pia to

516   the end of the 60x photo (~180-200 μm total) using ImageJ software. Antibody brightness was

517   normalized to CaMKII.eYFP expression for each condition to control for any slight variation in

518   viral expression. The obtained data was then analyzed for figure generation in Prism (GraphPad).

519   The process from sample fixation to image analysis covered a four-day time frame.

520

521   2.4 Protein expression detection techniques

522

523   *Immunohistochemistry:*

524   For Chapter 4: IHC was performed on brain slices obtained from CIBOP studies. Tissue

525   was transferred immediately after euthanizing the animals in 4% PFA or after completion of

526   electrophysiological recordings. Brain tissue/slices were post-fixed in 4% PFA in PBS at 4°C

527   overnight then subsequently transferred into 30% sucrose solution until cryo-sectioning. After

528   embedding in optimal cutting temperature (OCT) compound, the slices were further cut coronally

529   or sagittally into 40-μm-thick sections on a cryostat (Leica Biosystems). IHC and

530   immunofluorescence protocols used were as previously published[2]. The tissue sections were

531   transferred into the cryoprotectant or directly mounted on the charged glass slides and stored at -

532   20°C until use. For immunofluorescence (IF) staining, 40 μm thick free-floating brain sections or

533   glass slides were washed, blocked and permeabilized by incubating in TBS containing 0.30%

534   Triton X-100 and 5% horse serum for 1 h at room temperature. If desired, then the antigen retrieval

535   was performed in Tris-EDTA buffer (10 mM Tris base, 1mM EDTA, 0.05% tween-20) pH9 for 30

536   minutes at 65°C before the blocking and permeabilization step. Primary antibodies were diluted in

537   TBS containing 0.30% Triton TX-100 and 1% horse serum. After overnight incubation at 4°C with

538   primary antibodies, the sections were rinsed 3x in TBS containing 1% horse serum at room

539   temperature for 10 min each. Then, the sections were incubated in the appropriate fluorophore-

540   conjugated secondary antibody at room temperature for 2 h in the dark. The sections were rinsed

541   once and incubated with DAPI (1µg/ml) for 5 min, washed 3x in TBS for 10 min, dried, and cover

542   slipped with ProLong Diamond Antifade Mountant (P36965; ThermoFisher,). All the primary and

543   secondary antibody detail including dilution used are listed in **Supplemental Datasheet 7**. We

544   optimized several existing antibodies to detect Pvalb protein by IHC (**Supplemental Datasheet**

545   **7**). Since the AAV E2.Cre.GFP labels all PV-INs with very high efficiency, cells expressing GFP

546   were used as the reference standard for PV-INs and Pvalb antibodies with highest levels of

547   agreement with GFP-positive PV-INs were used interchangeably for IHC studies, to allow species

548   compatibility of primary antibodies. In addition, the guinea pig Pvalb antibody (195004; Synaptic

549   Systems) preferentially labeled the synapto-dendritic compartment of PV-INs. IHC studies were

550   also performed on experimental animals from CIBOP studies, as well as from non-CIBOP WT and

551   5xFAD mice using sagittal sections of entire hemispheres.

552   Images of the same region across all samples were captured as z-stacks using the Keyence BZ-

553   X810, except for images in **Supp Fig S5** (Parvalbumin IHC quantification). Some of the z-stacked

554   images of entire brain were stitched together to allow regional comparison based on level of

555   biotinylation. Images for quantification of Parvalbumin staining were obtained with a two-photon

556   laser scanning microscope (2pLSM) using a commercial scan head (Ultima; Bruker Corp) fitted

557   with galvanometer mirrors (Cambridge Technology) using a 60x, 1.0 NA objective. Parvalbumin

558   levels were quantified in an analogous fashion to that described previously[139], but at higher

559   magnification to resolve potential differences across different cortical layers. All image processing

560 was performed either using the Keyence BZ-X810 Analyzer or Image J software (FIJI Version

561 1.53).

562

563   For Chapter 5: Acute slices were acquired as previously described at 100 um thickness.

564 Immediately following collection from the vibratome, free-floating sections were placed in 4%

565 paraformaldehyde for fixation at room temperature for 1-2 hours. Sections were then washed three

566 times in 1x Tris Buffered Saline (1xTBS) for 10 minutes. To block nonspecific binding, the

567 sections were then incubated with 5% goat serum (in 1xTBS) for 1 hour at room temperature.

568 Sections were then incubated overnight at 4°C on a shaker plate in the primary antibody solution,

569 which contained 0.2% Triton X-100, 1% goat serum, and a 1:1000 dilution of either the AH36

570 antibody (StressMarq Sciences, #SMC-601) or T22 antibody (Millipore Sigma, #ABN454) in

571 1xTBS. The next day, sections were washed three times for 10 minutes in 1xTBS before incubation

572 with the secondary antibody (Alexa Fluor^{TM} 647 at 1:1000; ThermoFisher Scientific, #A-21245)

573 in 1xTBS for 1 hour at room temperature on a shaker plate. From the point of secondary antibody

574 incubation, sections were protected from light using aluminum foil. Following secondary antibody

575 incubation, sections were washed again three times for 10 minutes in 1xTBS, mounted on slides

576 (Fisher Scientific, #1255015), and coverslipped with Fluoromount containing DAPI

577 (ThermoFisher Scientific, #00-4959-52). Slides were then imaged on a Nikon C2 laser-scanning

578 confocal system with an inverted Nikon ECLIPSE Ti2 microscope. Imaging parameters (*e.g.,* laser

579 power, gain) were defined for each primary antibody and were kept consistent between all sections

580 in that primary antibody group.

581

582 *Flow Cytometry:*

583   Flow cytometry was performed for confirmation of viral hAPP expression. GFP+ PV cells

584   were isolated 2-3 weeks after stereotactic injection at a 1:1 ratio with AAV(PHP.eB).E2.GFP and

585   saline (.3 uL) for 5xFAD and wild-type littermates. GFP+ PV cells were isolated 2-3 weeks after

586   C57Bl/6J were stereotactically injected at a 1:1 ratio with AAV(PHP.eB).E2.GFP and saline or

587   AAV(PHP.eB).hAPP (.3 uL total). Acute slices (250 μm) were acquired from 5xFAD mice and

588   their wild-type littermates at 8-9 weeks of age; slices from C57Bl/6J mice were acquired at 8-10

589   weeks of age. Acute slices obtained as described above. Slices containing SBFI cortex were placed

590   into cutting solution with 0.5 mg/mL protease (P5147–100MG, Sigma-Aldrich) for 60-minutes

591   with continuous carbogen gas bubbling. Immediately after, slices were returned to room-

592   temperature cutting solution for 10 minutes. Slices were then micro-dissected to isolate the cortical

593   region containing GFP$^+$ expressing cells using an epi-fluorescent stereoscope (Olympus SZX12).

594   Samples were then manually triturated in 300 uL of 1% PBS into a single-cell suspension. Cells

595   from both hemispheres were stained with a human-specific APP antibody (SIG-39320, Biolegend).

596

597   2.4a Proteomics

598   *Animals:*

599   C57BL/6J (wildtype[WT]) mice (JAX #000664), Rosa26-TurboID (C57BL/6-

600   Gt(ROSA)26Sortm1(birA)Srgj/J, JAX #037890)[2], Camk2a-Cre-ert2 (B6;129S6-Tg(Camk2a-

601   cre/ERT2)1Aibs/J, JAX #012362)[140], Parvalbumin TdTomato (C57BL/6-Tg(Pvalb-

602   tdTomato)15Gfng/J, JAX #027395), B6 Pvalb-IRES-Cre (B6.129P2 – Pvalb$^{tm1(cre)Arbr}$/J JAX

603   #017320), and 5xFAD (B6.Cg-Tg(APPSwFlLon,PSEN1*M146L*L286V)6799Vas/Mmjax, JAX

604   #034848)[115,141] mouse lines were used for experiments in this study and genotyping was performed

605   using primers and polymerase chain reaction (PCR) conditions listed on the vendor website

606   (Jackson labs). All animals were maintained on the C57BL6/L background, following at least 10

607   serial backcrosses if originally derived from a different or mixed background. Male and female

608   mice were used for all experiments with data collected from ≥ 3 mice per experimental condition

609   for all experiments. Animals were housed in the Department of Animal Resources at Emory

610   University under a 12 h light/12 h dark cycle with ad libitum access to food and water and kept

611   under environmentally controlled and pathogen-free conditions. All experiments involving animal

612   procedures were approved by the Emory University Institutional Animal Care and Use Committee

613   (IACUC, PROTO201700821) and were in accordance with the ARRIVE guidelines.

614

615   *CIBOP studies:*

616   PV-CIBOP studies were performed by single retro-orbital injections of

617   AAV(AAV(PHP.eB).E2.Cre.2A.GFP) as described above to Rosa26TurboID/wt mice and WT

618   littermate animals at 7 weeks of age, as previously described[142]. Briefly, PV-CIBOP studies in WT

619   mice were performed by single retro-orbital injections of AAV (AAV(PHP.eB).E2.Cre.2A.GFP) to

620   Rosa26$^{TurboID/wt}$ mice. Rosa26$^{TurboID/wt}$ (PV-CIBOP) were also crossed with 5xFAD (hemizygous)

621   to derive 5xFAD (hemi)/Rosa26$^{TurboID/wt}$ (5xFAD/PV-CIBOP) and littermate WT/PV-CIBOP)

622   animals. Camk2a-CIBOP experiments were performed in Camk2a-Cre-ert2^{het}/Rosa26$^{TurboID/wt}$

623   mice. Tamoxifen was injected (intraperitoneally or i.p., 75mg/kg/dose in corn oil x for 5

624   consecutive days), followed by 3 weeks to allow Cre-mediated recombination and TurboID

625   expression after which biotinylation (37.5 mg/L in drinking water) was performed for 2 weeks[2].

626   In the case of PV-CIBOP (on WT or 5xFAD backgrounds), AAV injections were followed by 3

627   weeks to allow recombination after which biotinylation was performed as above. For all CIBOP

628   studies, control animals included Cre-only (in the case of Camk2a-CIBOP experiments) or

629   Rosa26[TurboID/wt] mice (for PV-CIBOP experiments). Control groups in PV-CIBOP studies also

630   received AAV E2.Cre injections for fair comparisons. In Camk2a-CIBOP studies, all experimental

631   groups received tamoxifen to account for tamoxifen mediated effects. No tamoxifen was needed

632   for PV-CIBOP experiments (non-inducible Cre). Recombination period (after inducing Cre via

633   tamoxifen or delivery of AAV E2.Cre) and biotinylation period after recombination were kept

634   constant across all studies. CIBOP studies were completed at 12 to 13 weeks of age. After 5 weeks

635   (total), acute slices were acquired as described above, with subsequent microdissection of the SS

636   Ctx or the LEC.

637

638   *Tissue processing for protein-based analysis, including Western Blot (WB):*

639   Tissue processing for proteomic studies, including Mass Spectrometry (MS), were

640   performed in a previous CIBOP studies[2,142]. Frozen brain tissues (whole brain homogenate

641   excluding cerebellum for WB and microdissected cortical regions for Fig 1) either intact or

642   dissected cortex, was weighed and added to 1.5mL Rino tubes (Next Advance) containing

643   stainless-steel beads (0.9-2mm in diameter) and six volumes of the tissue weight in urea lysis

644   buffer (8 M urea, 10 mM Tris, 100 mM NaH2PO4, pH 8.5) containing 1X HALT protease

645   inhibitor cocktail without EDTA (78425, ThermoFisher). Tissues were homogenized in a Bullet

646   Blender (Next Advance) twice for 5 min cycles at 4 °C. Tissue were further sonicated consisting

647   of 5 seconds of active sonication at 20% amplitude with 5 seconds incubation periods on ice.

648   Homogenates were let sit for 10 minutes on ice and then centrifuged for 5 min at 12,000 RPM

649   and the supernatants were transferred to a new tube. Protein concentration was determined by BCA

650   assay using Pierce™ BCA Protein Assay Kit (23225, Thermofisher scientific). For WB analyses,

651   10μg of protein from brain lysates were used to verify TurboID expression (anti-V5) and

652 biotinylation (streptavidin fluorophore conjugate). Standard WB protocols, as previously

653 published, were followed[2].

654 Other proteins detected by WB also included beta actin, Pvalb, and LC3 (see Supplemental

655 Datasheet 7 for antibodies/dilutions). All blots were imaged using Odyssey Infrared Imaging

656 System (LI-COR Biosciences) or by ChemiDoc Imaging System (Bio-Rad) and densitometry

657 was performed using ImageJ software.

658

659 *Enrichment of biotinylated proteins from CIBOP brain:*

660 As per CIBOP protocols previously optimized by our group[2], biotinylated proteins were

661 captured by streptavidin magnetic beads (88817; Thermofisher Scientific) in 1.5 mL Eppendorf

662 LoBind tubes using 83uL beads per 1mg of protein in a 500 µL RIPA lysis buffer (RLB)(50 mM

663 Tris, 150 mM NaCl, 0.1% SDS, 0.5% sodium deoxycholate, 1% Triton X-100). In brief, the beads

664 were washed twice with 1 ml of RLB and 1 mg of protein were incubated in 500 µl of total RPL.

665 After incubation at 4 deg C for 1 h with rotation, beads were serially washed at room temperature

666 (twice with 1 mL RIPA lysis buffer for 8 min, once with 1 mL 1 M KCl for 8 min, once with 1 mL

667 0.1 M sodium carbonate (Na2CO3) for ~10 s, once with 1 mL 2 M urea in 10 mM Tris-HCl (pH

668 8.0) for ~10 s, and twice with 1 mL RIPA lysis buffer for 8 min), followed by 1 RIPA lysis buffer

669 wash 4 final PBS washes. Finally, after placing the tubes on the magnetic rack, PBS was removed

670 completely, then the beads were further diluted in 100 µl of PBS. The beads were mixed and 10%

671 of this biotinylated protein coated beads were used for quality control studies to verify enrichment

672 of biotinylated proteins (including WB and silver stain of proteins eluted from the beads). Elution

673 of biotinylated protein was performed by heating the beads in 30 µL of 2X protein loading buffer

674 (1610737; BioRad) supplemented with 2 mM biotin + 20 mM dithiothreitol (DTT) at 95 °C for

675   10 min. The remaining 90% of sample were stored at -20*C for western blot or mass spectrometric

676   analysis of biotinylated protein.

677

678   *Western blotting:*

679   To confirm protein biotinylation, 10 μg of tissue lysates were resolved on a 4–12% Bris-

680   Tris gel (M00668, GenScript) and transferred onto a nitrocellulose membrane. The membranes

681   were washed once with TBS-T (0.1% tween-20) and then blocked with Start Block (37543,

682   Thermofisher Scientific) and probed with streptavidin-Alexa 680 diluted in Start Block for 1 h at

683   room temperature. After blocking, incubation with primary antibodies was performed overnight at

684   4°C. Further, the membranes were washed 3 times 10 minutes each and incubated with an

685   appropriate secondary antibody conjugated with horseradish peroxidase-conjugated or another

686   fluorophore. Proteins were detected using the enhanced chemiluminescence method (ECL)

687   (1705060; BioRad).Validation of MS enriched protein were performed with 100 ug equivalent of

688   protein eluted with beads. The quantification of each band was performed by densitometric

689   measurement.

690

691   *Protein digestion, MS, protein identification and quantification:*

692   On-bead digestion of proteins (including reduction, alkylation followed by enzymatic

693   digestion by Trypsin and Lys-C) from SA-enriched pulldown samples (1mg protein used as input)

694   and digestion of bulk brain (input) samples (50 μg protein), were performed as previously

695   described with no protocol alterations[2]. In brief, after removal of PBS from remaining 90% of

696   streptavidin beads (10% used for quality control using western blot and silver stain) were

697   resuspended in 225 uL of 50 mM ammonium bicarbonate (NH4HCO3) buffer. Biotinylated

698   proteins were then reduced with 1 mM DTT and further alkylated with 5 mM iodoacetamide (IAA)

699   in the dark for 30 min each on shaker. Proteins were digested overnight with 0.5 µg of lysyl (Lys-

700   C) endopeptidase (127-06621; Wako) at RT on shaker followed by further overnight digestion with

701   1 µg trypsin (90058; ThermoFisher Scientific) at RT on shaker. The resulting peptide solutions

702   were acidified to a final concentration of 1% formic acid (FA) and 0.1% trifluoracetic acid (TFA),

703   desalted with a HLB columns (Cat#186003908; Waters). The resulting protein solution was dried

704   in a vacuum centrifuge (SpeedVac Vacuum Concentrator). Detailed methods for this protocol have

705   been previously published[2]. Lyophilized peptides were resuspended followed by liquid

706   chromatography and MS (Q-Exactive Plus, Thermo, data dependent acquisition mode) as per

707   previously published protocols[2]. MS raw data files were searched using Andromeda, integrated

708   into MaxQuant using the mouse Uniprot 2020 database as reference (91,441 target sequences

709   including V5-TurboID). All raw MS data as well as searched MaxQuant data before and after

710   processing to handle missing values, and uploaded to the ProteomeXchange Consortium via the

711   PRIDE repository[143]. As previously published, methionine oxidation (+15.9949 Da) and protein

712   N-terminal acetylation (+42.0106 Da) were included as variable modifications (up to 5 allowed

713   per peptide), and cysteine was assigned as a fixed carbamidomethyl modification (+57.0215 Da).

714   Only fully tryptic peptides with up to 2 missed cleavages were included in the database search. A

715   precursor mass tolerance of ±20 ppm was applied prior to mass accuracy calibration and ±4.5 ppm

716   after internal MaxQuant calibration. Other search parameters included a maximum peptide mass

717   of 4.6 kDa, minimum peptide length of 6 residues, 0.05 Da tolerance for orbitrap and 0.6 Da

718   tolerance for ion trap MS/MS scans. The false discovery rate (FDR) for peptide spectral matches,

719   proteins, and site decoy fraction were 1 %. Other quantification settings were similar to prior

720   CIBOP studies[2]. Quantitation of proteins was performed using summed peptide intensities given

721   by MaxQuant. We used razor plus unique peptides for protein level quantitation. The MaxQuant

722   output data were uploaded into Perseus (Version 1.6.15) and intensity values were log2

723   transformed, after which data were filtered so that >50% of samples in a given CIBOP group

724   expected to contain biotinylated proteins, were non-missing values. Protein intensities from SA-

725   enriched pulldown samples (expected to have biotinylated proteins by TurboID) were normalized

726   to sum column intensities prior to comparisons across groups. This was done to account for any

727   variability in level of biotinylation as a result of variable Cre-mediated recombination, TurboID

728   expression and/or biotinylation[2]. For Chapter 5: On-bead digestion of proteins (including

729   reduction, alkylation followed by enzymatic digestion by Trypsin and Lys-C) from SA-enriched

730   pulldown samples (1mg protein used as input) and digestion of bulk brain (input) samples (25 µg

731   protein), were performed as previously described with no protocol alterations[2,142]. In brief, after

732   the removal of PBS from remaining 90% of streptavidin beads (10% used for quality control using

733   western blot and silver stain) were resuspended in 90 uL of 50 mM ammonium bicarbonate

734   (NH4HCO3) buffer. Biotinylated proteins were then reduced with 1 mM DTT and further

735   alkylated with 5 mM iodoacetamide (IAA) in the dark for 30 min each on shaker. Proteins were

736   digested overnight with 0.2 µg of lysyl (Lys-C) endopeptidase (127-06621; Wako) at RT on shaker

737   followed by further overnight digestion with 0.4 µg trypsin (90058; ThermoFisher Scientific) at

738   RT on shaker. The resulting peptide solutions were acidified to a final concentration of 1% formic

739   acid (FA) and 0.1% triflouroacetic acid (TFA), desalted with a HLB columns (Cat#186003908;

740   Waters). The resulting protein solution was dried in a vacuum centrifuge (SpeedVac Vacuum

741   Concentrator). Detailed methods for this protocol have been previously published[2]. Lyophilized

742   peptides were resuspended followed by liquid chromatography and MS (Q-Exactive Plus, Thermo,

743   data dependent acquisition mode) as per previously published protocols[2]. As previously

744   published[1,144,145], MS raw data files were searched using SEQUEST, integrated into Proteome

745   Discoverer (ThermoFisher Scientific, version 2.5) using the Uniprot 2020 database as reference

746   (91,441 target 37 sequences including V5-TurboID). Raw MS data as well as searched Proteome

747   Discoverer data before and after processing to handle missing values, will be uploaded to the

748   ProteomeXchange Consortium via the PRIDE repository[143]. The false discovery rate (FDR) for

749   peptide spectral matches, proteins, and site decoy fraction were 1 %. Other quantification settings

750   were similar to prior CIBOP studies[2]. Quantitation of proteins was performed using summed

751   peptide abundances given by Proteome Discoverer. We used razor plus unique peptides for protein

752   level quantitation. The Proteome Discoverer output data were uploaded into Perseus (Version

753   1.6.15) and abundance values were log2 transformed, after which data were filtered so that >50%

754   of samples in a given CIBOP group expected to contain biotinylated proteins, were non-missing

755   values. Protein intensities from SA-enriched pulldown samples (expected to have biotinylated

756   proteins by TurboID) were normalized to sum column intensities prior to comparisons across

757   groups. This was done to account for any variability in level of biotinylation as a result of variable

758   Cre-mediated recombination, TurboID expression and/or biotinylation[2].

759

760   *Analysis of enrichment of cognitive resilience proteins in regional PV interneuron DEPs:*

761   We cross-referenced PV-CIBOP regional proteins (N=207, unadjusted $p<0.05$) with

762   proteins previously found to be associated with cognitive decline in humans (N=55 proteins

763   associated with cognitive slope in the Religious Orders Study and the Rush Memory and Aging

764   Project (ROSMAP), unadjusted $p<0.05$)[142,146]. In this prior study, cognitive slope was estimated in

765   the ROSMAP longitudinal study of aging, and cognitive slope was correlated with post-mortem

766   protein abundances, measured by quantitative MS. Proteins that were associated with stable

767   cognitive function (positive association with cognitive slope) were identified as protein markers

768   of cognitive resilience (or pro-resilience proteins). Conversely, proteins ante-correlated with

769   cognitive stability were labeled as anti-resilience proteins. 55 resilience-associated proteins in

770   ROSMAP were identified as regional DEPs in our PV-CIBOP study. The median correlation with

771   cognitive slope for SS Ctx and LEC PV-CIBOP DEPs was estimated and compared across the two

772   regions (two-tailed Mann-Whitney U test).

773

774   *Integration of PV-CIBOP proteomes with existing human AD proteomic datasets:*

775   We cross-referenced our PV-CIBOP regional proteomes with existing human post-mortem

776   proteomes in which the entorhinal cortex (EC), frontal cortex (FC) and other regions were sampled

777   from AD cases (early BRAAK stages I-III, late BRAAK stages IV-VI) and non-AD/non-pathology

778   controls. Proteins were identified as DEPs if they were significantly different comparing AD

779   versus controls within any given region (total of 737 DEPs identified). PV-CIBOP proteins

780   identified by our current study were further assessed for evidence of regional differences within

781   PV interneurons (SS Ctx vs. LEC).

782

783   *Assessment of human tau/APP protein-protein interactors among PV-CIBOP regional DEPs:*

784   We cross-referenced our PV-CIBOP regional proteomic data with human tau protein

785   interactors, previously identified in a meta-analysis across 12 published tau interactome studies[147],

786   in which 2,084 human tau interactors were identified, and among these, 261 were high-confidence

787   interactors if they were identified by at least 3 studies. PV-CIBOP proteins in our study that were

788   also found among these 216 human tau interactors, were further analyzed for evidence of regional

789   differences (SS Ctx vs. LEC) in PV interneurons. The proportions of tau interactors and non-tau

790   interactors across SS Ctx-enriched, LEC-enriched and non-regional PV interneuron proteins were

791   compared (Chi square test).

792   Using a similar approach, we obtained a list of 243 human APP interactors derived from protein-

793   protein-interaction databases (STRING consortium 2023, Version 12.0, https://string-db.org/)

794   restricting the interactome to physical interactors with medium confidence stringency (confidence

795   scores >0.40, including text mining, experiments and databases). We excluded proteomic studies

796   of extracellular amyloid beta plaques as these are less likely to represent interactions relevant to

797   intra-neuronal APP processing.

798

799   *Quantitative mass spectrometry of mouse brain:*

800   Quantitative mass spectrometry was performed on whole cortex homogenates from WT (n

801    $= 43$) and 5xFAD ($n = 43$) mice (C57BL6J-Jax genetic background, age groups spanning 1.8 to

802   14.4 months of age, including 50% females), using previously published methods (Johnson et al.,

803   2022). Brain tissue was homogenized using a bullet blender and sonication, in 8M Urea lysis buffer

804   with HALT protease and phosphatase inhibitor cocktail (ThermoFisher). Proteins were reduced,

805   alkylated and then digested (Lysyl endopeptidase and Trypsin) followed by peptide cleanup as

806   previously published. Tandem mass tag (TMT, 16-plex kit, A44520) peptide labeling was

807   performed per manufacturer's instructions, with inclusion of one global internal standard (GIS)

808   per batch. Samples were also randomized across six TMT batches, allowing for balanced

809   representation of age, sex and genotype. A detailed description of this work, including methods for

810   sample preparation, mass spectrometry work flow and data processing, are available online

811   (https://www.synapse.org/#!Synapse:syn27023828) and a comprehensive analysis of these data

812   will be published separately. Raw data were processed using Proteome Discover (Ver 2.1) and

813 searched against Uniprot mouse database (2020). Abundances normalized to the maximum total

814 sample reporter ion counts were transformed as $\log_2$ of the within-batch ratio over mean within

815 each protein isoform and within each batch. Missing values were controlled to less than 50% across

816 all batches within each isoform-specific set of measures. After confirming the presence of batch

817 effect, this was adjusted using bootstrap regression modelling genotype, age, sex, and batch but

818 removing covariance with batch only (Wingo et al., 2020) and the batch-corrected data were used

819 for downstream analyses. Within these data (8,535 proteins in total), we extracted information

820 limited to K^+ and Na^+ channel protein subunits of relevance to the current study. We contrasted the

821 $\log_2$-transformed protein abundance means between 5xFAD and WT mice within each age group

822 (1.8, 3.1, 6, 10.2 and 14.4 months) to identify differentially abundant proteins. If peptides mapping

823 to separate isoforms were identified, they were quantified separately. Unadjusted T-test *p* values

824 (two tailed, assuming equal variance), Benjamini-Hochberg adjusted *p* values (5% FDR for

825 determination of significance) and $\log_2$ fold change differences across genotype were computed.

826

827 *Analyses of MS data and bioinformatics analyses:*

828   Within each MS study, we compared bulk proteomes to SA-enriched proteomes to confirm

829 that expected proteins (from either PV-INs or Camk2a neurons) were indeed enriched while non-

830 neuronal proteins (*e.g.,* glial proteins) were de-enriched as compared to bulk brain proteomes. We

831 also identified proteins unique to bulk or SA-enriched pulldown samples. Within SA-enriched

832 biotinylated proteins, we restricted our analyses to those proteins that were confidently biotinylated

833 and enriched (based on statistical significance unadj. P<0.05 as well as 2-fold enrichment in

834 biotinylated vs. non-biotinylated samples). This allowed us to exclude proteins that were non-

835 specifically enriched by streptavidin beads. Within biotinylated proteins, group comparisons were

836 performed using a combination of approaches, including differential abundance analysis,

837 hierarchical clustering analysis (Broad Institute, Morpheus,

838 https://software.broadinstitute.org/morpheus), as well as PCA, (in SPSS Ver 26.0 or R).

839 Differential abundance analyses were performed on log2 transformed and normalized intensity

840 values using two-tailed unpaired T-test for 2 groups assuming equal variance across groups or one-

841 way ANOVA + post-hoc Tukey HSD tests for >2 groups). Unadjusted and FDR-corrected

842 comparisons were performed, although we relied on unadjusted p-values along with effect size

843 (fold-enrichment) to improve stringency of analyses. After curating lists of differentially enriched

844 proteins, gene set enrichment analyses (GSEA) were performed (AltAnalyze Ver 2.1.4.3) using all

845 proteins identified across bulk and pulldown proteomes as the reference (background list).

846 Ontologies included GO, Wikipathways, KEGG, Pathway Commons, as well as prediction of

847 upstream transcriptional and micro RNA regulators (all included in AltAnalyze Ver 2.1.4.3).

848 Ontologies representative of a given group were selected based on enrichment scores (Fisher test

849 $p < 0.05$). We used SynGO to identify the types of known synaptic proteins (in pre- as well as post-

850 synaptic compartments, and different functional classes) identified in CIBOP studies. Protein-

851 protein-interactions between proteins within lists of interest were examined using STRING

852 (https://string-db.org/cgi/input?sessionId=bqsnbjruDXP6&input_page_show_search=on)[148].

853 We also performed GSVA of proteins identified in bulk as well as PV-IN proteomes from WT and

854 5xFAD PV-CIBOP mice to complement GSEA[149,150]. GSVA was performed using the R package

855 GSVA (v1.46.0). As previously published, statistical differences in enrichment scores for each

856 ontology comparing two groups, were computed by comparing the true differences in means

857 against a null distribution which was obtained by 1000 random permutations of gene labels.

858 Benjamini & Hochberg false discovery rate adjusted p values <0.05 were considered significant.

859 The reference gene sets for GSVA were the M5 (Mouse) Ontology Gene Sets from MSigDB

860 (https://www.gsea-

861 msigdb.org/gsea/msigdb/mouse/collections.jsp?targetSpeciesDB=Mouse#M5).

862

863 *Luminex immunoassay for signaling phospho-protein quantification from mouse brain:*

864 Multiplexed Luminex immunoassays were used to measure phosphoproteins in the MAPK

865 (Millipore 48-660MAG) and PI3/Akt/mTOR pathways (Millipore 48-612MAG). The

866 PI3/Akt/mTOR panel included pGSK3α (Ser21), pIGF1R (Tyr1135/Tyr1136), pIRS1 (Ser636),

867 pAkt (Ser473), p-mTOR (Ser2448), p70S6K (Thr412), pIR (Tyr1162/Tyr1163), pPTEN (Ser380),

868 pGSK3β (Ser9), pTSC2 (Ser939) and RPS6 (Ser235/Ser236). The MAPK panel detected pATF2

869 (Thr71), pErk (Thr185/Tyr187), pHSP27 (Ser78), pJNK (Thr183/Tyr185), p-c-Jun (Ser73),

870 pMEK1 (Ser222), pMSK1 (Ser212), p38 (Thr180/Tyr182), p53 (Ser15) and pSTAT1 (Tyr701). We

871 performed adapted Luminex assays as previously described[2] to directly quantify biotinylated

872 proteins in PV-CIBOP samples (from WT and 5xFAD CIBOP animals), whereby the biotinylated

873 phospho-protein of interest is first immobilized on a bead using capture antibodies, and then their

874 biotinylation status is detected using a streptavidin fluorophore (Streptavidin-PE), to directly

875 quantify biotinylated PV-IN-derived phospho-proteins from the bulk homogenate. Luminex assays

876 were read on a MAGPIX instrument (Luminex). As per published protocols, we performed linear

877 ranging for every experiment and sample type prior to full assay runs[2]. Using this approach, any

878 signal arising from non-biotinylated (non-CIBOP) control samples is the background/noise level,

879 which was subtracted from signals derived from CIBOP animals. We also additionally normalized

880 these background-subtracted signals based on TurboID protein levels quantified by MS, to account

881 for any unequal biotinylation across samples. Data were analyzed with and without this TurboID

882 normalization, and no meaningful differences were observed between approaches, therefore the

883 TurboID-normalized data were statistically analyzed and presented in the results.

884

885 *Analysis of existing mouse brain TMT-MS data:*

886 We used a subset of the data from a larger mouse brain TMT-MS study of aging and 5xFAD

887 disease pathology, and a complete description of this mouse TMT-MS study including expression

888 data after batch correction are available online

889 (https://www.synapse.org/#!Synapse:syn27023828); and data relevant to this study are included in

890 the supplemental data (**Supplemental Datasheet 4).** Briefly, TMT-MS was performed on whole

891 cortical brain homogenates from 43 WT and 43 5xFAD mice (ages 1.8 mo. to 14.4 months, n=8,

892 equally balanced based on sex). Standard tissue processing and TMT-MS pipelines were used, as

893 we have previously published[1]. Brain samples were homogenized using a bullet blender with

894 additional sonication in 8M Urea lysis buffer containing HALT protease and phosphatase inhibitor

895 (78425, ThermoFisher). Proteins were reduced, alkylated and digested (Lysyl endopeptidase and

896 Trypsin), followed by peptide cleanup and TMT (16-plex kit) peptide labeling as per

897 manufacturer's instructions. We included one global internal standard (GIS) per TMT plex batch

898 to facilitate normalization across batches. All samples in a given batch were randomized across six

899 TMT batches, while maintaining nearly-equal representation of age, sex and genotype across all

900 six batches. A complete description of the TMT mass spectrometry study, including methods for

901 sample preparation, mass spectrometry methodology and data processing, are available online

902 (https://www.synapse.org/#!Synapse:syn27023828). Mass spectrometry raw data were processed

903 in Proteome Discover (Ver 2.1) and then searched against Uniprot mouse database (version 2020),

904 and then processed downstream as described for human brain TMT mass spectrometry studies

905   above. Batch effect was adjusted using bootstrap regression which modelled genotype, age, sex

906   and batch, but covariance with batch only was removed[151]. From the 8,535 proteins identified in

907   this mouse brain proteome, we analyzed data related to known markers of distinct classes of mouse

908   neurons and glial subtypes, based on published bulk and single cell RNAseq studies, as well as

909   markers of AD-associated pathology (including hAbeta42 peptide and Apoe).

910

911   *Analysis of human brain proteomic data, brain cell type estimates and association with*

912   *neuropathological and cognitive traits:*

913   Single nucleus Allen brain atlas snRNA data was downloaded from

914   https://cells.ucsc.edu/?ds=allen-celltypes+human-cortex+various-cortical-

915   areas&meta=class_label and processed in R to generate a counts per million normalized reference

916   matrix with 47,509 non-excluded cell nuclei assigned to any of 19 cell type clusters[7,152]. The 598

917   sample Banner+ROSMAP consensus proteome protein profiles of bulk dorsolateral prefrontal

918   cortex (BA-9) from postmortem human donors was the bulk brain data for deconvolution, or

919   ultimately, across-sample, within cell type relative abundance estimation[1]. EnsDeconv was run

920   with some adjustment per: https://randel.github.io/EnsDeconv/reference/get_params.html and

921   https://randel.github.io/EnsDeconv/[153]. Briefly, the 5 marker identification methods used to get the

922   top 50 markers by each method were t, wilcox, combined, "none" (i.e., all genes in the snRNA

923   reference as a profile), and regression. All methods were run for both untransformed and log2-

924   transformed data. CIBERSORT was used as the most efficient deconvolution method with a low

925   profile for RAM use and CPU time, and estimates from 9 of 10 successful combinations of the

926   above marker selection and transformation methods with CIBERSORT estimation. The nine

927   individual marker selection methods produced a redundant total of 350 marker genes, and of these,

928 genes present in all 9 of the lists for each respective cell type were kept as a consensus list of

929 markers. These consensus lists (**Supplemental Datasheet 3**) were used as input into the GSVA R

930 package implementation of the ssGSEA algorithm[154]. Finally, ssGSEA estimates of within-cell

931 type relative abundances across the 488/598 samples in the published consensus protein network[1]

932 were correlated to the 44 module eigenproteins (MEs), which are the first principal components of

933 each module in the network, in addition to the ROSMAP cohort specific trait of slope of cognitive

934 decline, a Z score-scaled measure indicating degree of cognitive resilience of an individual

935 compared to the mean age-dependent cognitive decline of the full ROSMAP cohort

936 population[146,155]. Correlation was performed using the WGCNA R package (v1.72-1) function

937 plotEigengeneNetworks. For resilience PWAS enrichment of significance among PV-IN or

938 CAMK2A neuron-enriched protein gene products (**Fig. 2F**), and for PV-IN 5xFAD DEPs (**Fig.**

939 **5O**), permutation-based enrichment of pooled significance from the PWAS was computed as

940 previously published ()[156], Software for this is available from

941 https://www.github.com/edammer/MAGMA.SPA.

942

943 *Other sources of data used for analyses in this manuscript:*

944 MicroRNA affinity purification (miRAP) data from studies of PV-IN and Camk2a neurons

945 was downloaded from supplemental information associated with the original miRAP publication[157]

946 and miRNA species with PV-IN vs. Camk2a neuronal enrichment patterns, were cross-referenced

947 with predicted miRNA regulators in our PV-CIBOP and Camk2a-CIBOP studies.

948

949 *Other statistical considerations:*

950   Specific statistical tests used for individual experiments are detailed in the figure legends.

951   Generally, all continuous variables were analyzed using parametric tests (two-tailed unpaired T-

952   test assuming equal variances when comparing 2 groups, or one-way ANOVA and post-hoc Tukey

953   HSD tests for >2 group comparisons). Power calculations were not performed for individual

954   experiments.

955

956   *Data availability:*

957   The mass spectrometry proteomics data generated by PV-CIBOP studies have been

958   deposited to the ProteomeXchange Consortium via the PRIDE partner repository, and processed

959   data have been provided as supplemental datasheets as well. Camk2a-CIBOP data can be obtained

960   using dataset identifiers PXD027488 and PXD032161. The 2020 mouse Uniprot database

961   (downloaded from https://www.uniprot.org/help/reference_proteome).

962

963   2.5 Modeling (By VJO)

964

965   *PV cell NEURON modeling:*

966   Computer simulations were performed using the NEURON simulation environment

967   (version 7.5 and 7.6, downloaded from http://neuron.yale.edu). For PV interneuron models a single

968   20μm × 20μm compartment was created and was equipped by sodium, potassium and leak

969   conductances. The passive background of the cell was adjusted to recreate passive membrane

970   potential responses of whole-cell recorded PV INs for given stimulus intensities. The sodium

971   conductance was based on the built-in Hodgkin-Huxley model of NEURON with freely adjustable

972   sets of parameters (Oláh et al., 2021). The PV potassium conductance was implemented based on

973   a previous publication (Lien and Jonas, 2003) constrained by our outside-out patch recordings.

974   The steady state activation was governed by the following equation:

975
$$minf = \frac{-1}{\left(1 + \exp\left(\frac{v + 5 + vshift}{12}\right)\right) + 1}$$

976   where v is local membrane potential and *VShift* is the applied voltage shift in order to adjust

977   membrane potential dependence. The steady state inactivation was set as follows:

978
$$hinf = \frac{1}{\left(1 + \exp\left(\frac{v + 30 + vshift}{10}\right)\right)}$$

979   The activation and deactivation time constant was defined as:

980
$$mtau = \left(0.5 + 4 * \exp\left(-0.5 * \left(\frac{v + vshift}{25}\right)^2\right)\right) * scale$$

981   where scale was the parameter by which kinetics were adjusted. Inactivation time constant was set

982   to 1000 ms or 50-1000 ms where noted in figures. Synaptic inputs for examining firing responses

983   under more naturalistic network conditions were supplemented by using NEURON's built-in

984   AlphaSynapse class. During the simulation (1 second), 1000 individual excitatory synapses and

985   500 inhibitory synapses were added with random timing, 10 nS synaptic conductance, and 0 or -

986   90 mV reversal potential, respectively.

987

988   In a subset of experiments, a Kv7 (M-current) conductance (Sekulić et al., 2015) was incorporated

989   into the Kv3 model. Model M-currents (half activation voltage = -27 mV) were incorporated

990   without changes to their kinetic parameters. To calculate the effect of M-current (I_M), square pulse

991   current steps were injected into the single (Kv3-Kv7) compartmental model cell, with gradually

992   increasing amplitude. Kv7 conductance density was set such that noticeable changes in the firing

993   pattern occurred, without completely abolishing spiking during current injections. In subsequent

994   experiments, action potential firing and parameters were measured with upon altered Kv7

995   conductance densities, or adjusted activation voltage dependence.

996

997   *Network simulations (By VJO):*

998   Network simulations were carried out with the class representation of the previously

999   detailed PV model cell, and a newly constructed pyramidal cell (PC) mode, which was a slight

1000   modification of a bursting model cell described by earlier (Pospischil et al., 2008). 200 PC and 20

1001   PV cells were used and connected with accordance to previous publications. Recurrent PC

1002   connectivity was set to 10% (Markram et al., 2015), PV-to-PC connectivity was set to 36% (Packer

1003   and Yuste, 2011), PV cell recurrent connections occurred with 78% probability, and gap junction

1004   connectivity between these cells was 61% (Galarreta and Hestrin, 2002). Finally, PC innervated

1005   PV cells with 80% chance (Hofer et al., 2011). All simulated cells received constant current

1006   injections in order to elicit baseline firing at variable frequencies. The network construction was

1007   done in several consecutive steps. First, PV cells were connected to each other with chemical

1008   synapses constrained to elicit moderate network synchronization (Wang and Buzsáki, 1996). Next,

1009   PV cells were connected with gap junctions, were gap junction conductance was set to a value,

1010   which could synchronize the network further. PV cells inhibited PC cells with less inputs less than

1011   1 mV in amplitude (Packer Yuste 2011), similarly to PC to PV connections (Hofer et al. 2011).

1012   Firing correlations and power spectrum was analyzed in Python. All modeling-related code will

1013   be made available upon publication.

1014

1015 <u>2.6 Dynamic Clamp (By VJO)</u>

1016 The dynamic clamp system was built in-house based on a previous publication (Desai

1017 Johnston 2017), related online available materials (www.dynamicclamp.com). The equations

1018 governing the implemented gKdr were identical to those used in the NEURON model construction.

1019 Synaptic conductances were built-in predefined conductances available from

1020 www.dynamicclamp.com.

1021

1022 <u>2.7 Analysis</u>

1023

1024 *Image Analysis:*

1025 Images for analysis of RNAscope sections were taken on a Keyence BZ-X800 microscope

1026 (KEYENCE; Osaka, Japan) at 40X magnification. Two images were acquired of each mouse LEC

1027 hemisphere, and 4 sections were imaged per mouse (total: ~8 images/experiment for an n=3). The

1028 acquisition parameters were kept constant throughout imaging of all sections. Four fluorescent

1029 channels were used simultaneously; (1) the green channel was assigned for VIVID 520 dye (human

1030 APP probe), (2) the blue channel was used for DAPI nuclear stain, (3) the red channel was assigned

1031 for VIVID 570 dye (mouse APP probe), and (4) the far-red channel was assigned for VIVID 650

1032 dye (CaMKIIα or Pvalb probes). A z-stack was taken (with 1 um steps) of each hemisphere, and

1033 the full focus feature in the Keyence BZ-X800 analysis software was applied to compress each z-

1034 stack. These compressed z-stacks were then used for image analysis in HALO (Indica Labs), and

1035 the obtained data was then analyzed for figure generation in Prism (GraphPad). The process from

1036 sample fixation to image analysis covered a four-day time frame.

1037

1038 *K-means clustering and Principal Component Analysis:*

1039   K-means clustering and Principal component analysis (PCA) were conducted on datasets

1040 from excitatory neurons and PV interneurons, respectively, in the LEC. All passive and active

1041 properties were used for each cell to conduct unsupervised clustering. Post-clustering and analysis,

1042 Ctrl   and   hAPP   identities   were   restored   to   each   cell.

1043

1044 *Analyses of MS data and bioinformatics analyses:*

1045   Within each MS study, we compared bulk proteomes to SA-enriched proteomes to confirm

1046 that expected proteins (from either PV-INTs) were indeed enriched while nonneuronal proteins

1047 (*e.g.,* glial proteins) were de-enriched as compared to bulk brain proteomes. We also identified

1048 proteins unique to bulk or SA-enriched pulldown samples. Within SA-enriched biotinylated

1049 proteins, we restricted our analyses to those proteins that were confidently biotinylated and

1050 enriched (based on statistical significance unadj. $P<0.05$ as well as 2-fold enrichment in

1051 biotinylated vs. non biotinylated samples). This allowed us to exclude proteins that were non-

1052 specifically enriched by streptavidin beads. Within biotinylated proteins, group comparisons were

1053 performed using a combination of approaches, including differential abundance analysis,

1054 hierarchical   clustering   analysis   (Broad   Institute,   Morpheus,

1055 https://software.broadinstitute.org/morpheus), as well as PCA, (in SPSS Ver 26.0 or R).

1056 Differential abundance analyses were performed on log2 transformed and normalized intensity

1057 values using two-tailed unpaired T-test for 2 groups assuming equal variance across groups or one-

1058 way ANOVA + post-hoc Tukey HSD tests for >2 groups). Unadjusted and FDR-corrected

1059 comparisons were performed, although we relied on unadjusted p-values along with effect size

1060 (fold-enrichment) to improve stringency of analyses. After curating lists of differentially enriched

1061   proteins, gene set enrichment analyses (GSEA) were performed (AltAnalyze Ver 2.1.4.3) using all

1062   proteins identified across bulk and pulldown proteomes as the reference (background list). Protein-

1063   protein-interactions between proteins within lists of interest were examined using STRING

1064   ([https://stringdb.org/cgi/input?sessionId=bqsnbjruDXP6&input_page_show_search=on)](https://stringdb.org/cgi/input?sessionId=bqsnbjruDXP6&input_page_show_search=on)[123]. We

1065   also performed GSVA of DEPs identified in bulk as well as PV-IN proteomes from SS Ctx and

1066   LEC to complement GSEA[149,150]. As previously published, statistical differences in enrichment

1067   scores for each ontology comparing two groups, were computed by comparing the true differences

1068   in means against a null distribution which was obtained by 1000 random permutations of gene

1069   labels. Benjamini & Hochberg false discovery rate adjusted p values <0.05 were considered

1070   significant. The reference gene sets for GSVA were the M5 (Mouse) Ontology Gene Sets from

1071   MSigDB

1072

1073   <u>2.8 Statistics</u>

1074

1075   *Statistics and Analysis*

1076   Custom python scripts, Axograph, Graphpad Prism (Graphpad Software), and Excel

1077   (Microsoft) were used for analysis with values in text and figures. Statistical differences were

1078   deemed significant with α values of $p < 0.05$. Two-tailed unpaired and paired t-tests were used for

1079   unmatched and matched parametric datasets, respectively. Where appropriate, group data were

1080   compared with 1 or 2-way ANOVA and significance between groups noted in figures was

1081   determined with Tukey's or Sidak's multiple post-hoc comparison tests. Normality was determined

1082   using D'Agostino & Pearson omnibus or Shapiro-Wilk tests. Specifics for each statistical test used

1083   are found in figure legends, or in the results text where data was not included in a figure.

Chapter 3 : Inhibitory interneuron dysfunction arises in early stages of Alzheimer's Disease models

If you're studying Alzheimer's Disease,
then why are you looking at the Somatosensory Cortex?

-Dr. David Weinshenker, Committee Member
[With a very valid question]

1084   This chapter was adapted from: Olah, V. J., Goettemoeller, A. M., *et al.* Biophysical K(v)3 channel

1085   alterations dampen excitability of cortical PV interneurons and contribute to network

1086   hyperexcitability in early Alzheimer's. *Elife* **11**, doi:10.7554/eLife.75316 (2022).[113]

1087   3.1 Introduction

1088   Unraveling mechanisms that initiate cognitive decline in Alzheimer's disease (AD) is a

1089 central aim in neuroscience. A prevailing model of AD posits that progressive deposition of toxic

1090 protein aggregates spark a neuropathological cascade. However, recent work suggests that early

1091 cognitive dysfunction is uncoupled from these aggregates[115,121,158]. Several alternative models for

1092 early cognitive decline are under consideration[159,160] including abnormal circuit activity[79,161-163].

1093 Circuit hyperexcitability is evident in several mouse models of familial (FAD) and sporadic

1094 AD[115,164,165] including at prodromal stages[166,167]. Furthermore, abnormal brain activity is apparent

1095 in humans with mild cognitive impairment[168-171] and in early FAD[172,173]. These shifts in circuit

1096 activity may result from dysfunctional neuronal firing and neurotransmission[118,119]. However, the

1097 cellular and molecular mechanisms underlying these neuronal deficits are not yet fully understood.

1098   Cognition and memory require carefully balanced excitatory and inhibitory activity[120]. In

1099 different AD mouse models, impairments in inhibition precede plaque formation, disrupting brain

1100 rhythms associated with memory formation[115,121-123]. Modified inhibitory tone in early AD is likely

1101 related to changes in the intrinsic excitability of local circuit inhibitory interneurons. For example,

1102 AP firing is altered in 'fast spiking' PV interneurons in different human APP (hAPP)-expressing

1103 mice[108,109,118,121,124,125]. Interestingly, altered PV physiology may occur before changes to other

1104 neighboring neuron subtypes[110,126]. Altered AP firing in PV cells could result from changes in the

1105 expression of genes that regulate excitability[125]. However, major shifts in gene and protein

1106 expression may only materialize after substantial plaque formation[174] in AD. Thus, a systematic

1107 evaluation of molecular mechanisms contributing to altered firing in PV cells is required.

1108   In this study, we used a viral-tagging method to examine PV interneuron excitability in the

1109 somatosensory cortex of young adult 5xFAD mice. PV interneurons from 5xFAD mice displayed

strongly dampened firing near-threshold and modified action potential (AP) waveforms, indicating

dysregulation of either Na^+ or K^+ channels. Combined examination of several AP firing parameters,

computational modeling, and PV-specific qPCR indicated that changing Na^+ channel availability

was not responsible for changes in AP firing. However, we observed alterations in K^+ channel

activation and kinetics in AD mice, independent of changes in K^+ gene expression. Using dynamic

clamp and additional PV modeling, we found that these shifts in K^+ channel activation could

recapitulate the observed phenotypes in 5xFAD mice. Furthermore, K^+ channel-induced changes

in PV firing were sufficient to induce circuit hyperexcitability and modified gamma output in a

reduced cortical model. Together, these results establish a causal relationship between ion channel

regulation in PV interneurons and cortical circuit hyperexcitability in early AD, independent of

changes in gene expression.

3.2 Results

Near-threshold suppression of AP firing in PV interneurons of young 5xFAD mice

To evaluate physiological phenotypes of PV interneurons in 5xFAD and wild-type control

mice, we implemented an AAV viral-enhancer strategy[175] to specifically label PV interneurons.

Mature animals were injected with this PV-specific vector (referred throughout as 'AAV.E2.GFP')

in layer 5 somatosensory cortex before plaque formation (postnatal day 42-49)[141,174,176]. Acute

slices were obtained ~7 days later and GFP-expressing (GFP^{+}) cells were targeted for patch clamp

using combined differential contrast and epifluorescent imaging (Figure 1A). Current clamp

recordings from wild-type mice displayed high-frequency, non-adaptive repetitive spiking

characteristics of PV cells (Figure 1B). In addition, the expression of several known PV

interneuron genes was confirmed in AAV.E2.GFP^{+} neurons[16,177,178] using qPCR, the levels of

which were indistinguishable from PV interneurons isolated in an identical fashion from PV-Cre

mice (Figure 1-figure supplement 1).
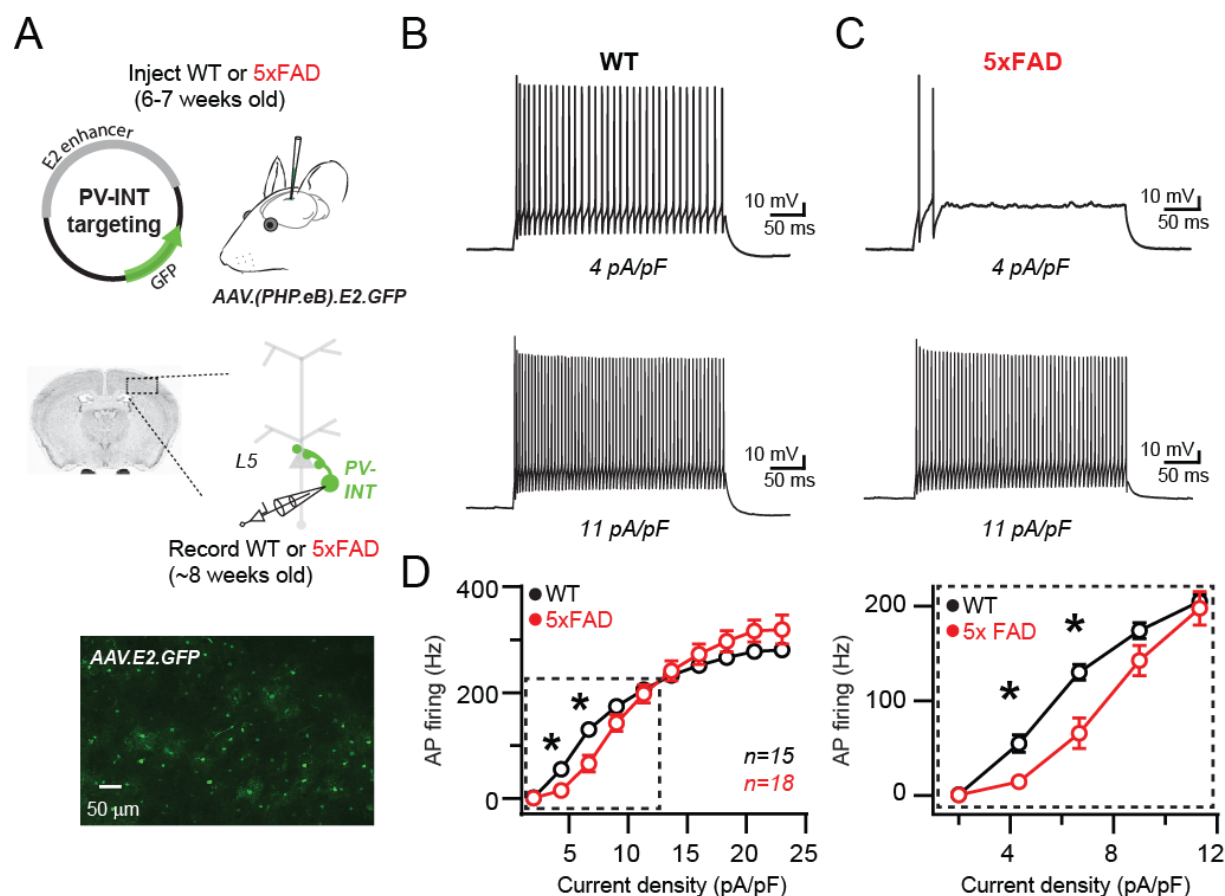
Figure 1. *Reduced AP firing frequency in PV interneurons of young 5xFAD mice*
A. Graphical summary of AAV.E2.GFP stereotactic injection in somatosensory cortex and subsequent whole-cell current clamp recordings from GFP[+] PV interneurons (PV-INT).
B. AP firing elicited in WT mice by square pulse current injections of varying magnitude normalized to cellular capacitance during recordings.

C. AP firing elicited in 5xFAD mice at current density levels matched to WT mice for comparison.
D. Group data summary of AP firing frequency in WT and 5xFAD mice. Significance was defined by RM two-way ANOVA ($p < 0.05$) with Sidak's multiple comparison test.

For all summary graphs, data are expressed as mean ($\pm$ SEM).

1137   Recent studies of several different hAPP-expressing mouse models have demonstrated

1138   abnormal AP firing in GABAergic interneurons at different stages of plaque deposition[75,108-110,126]

1139   . In prodromal 5xFAD mice, we found that continuous spiking was severely dampened in layer 5

1140   PV neurons in the near-threshold range; however, spike-frequency was unaltered near their

1141   maximal firing rate (Figure 1C & D). Passive parameters were unaltered when comparing WT and

1142   5xFAD, including input resistance (94.9 ± 5.9 and 103.5 ± 8.4 MΩ; $p = 0.83$; unpaired t-test) and

1143   holding current immediately after break-in (17.5 ± 7.8 and 19.1 ± 10.5 pA; measured at -60 mV;

1144 $p = 0.41$; unpaired t-test), suggesting that an active mechanism was responsible for the observed

1145   differences in spike-frequency.

1146

1147   *Altered AP waveform and excitability are uncoupled from changes in Nav channels properties and*

1148   *mRNA expression*
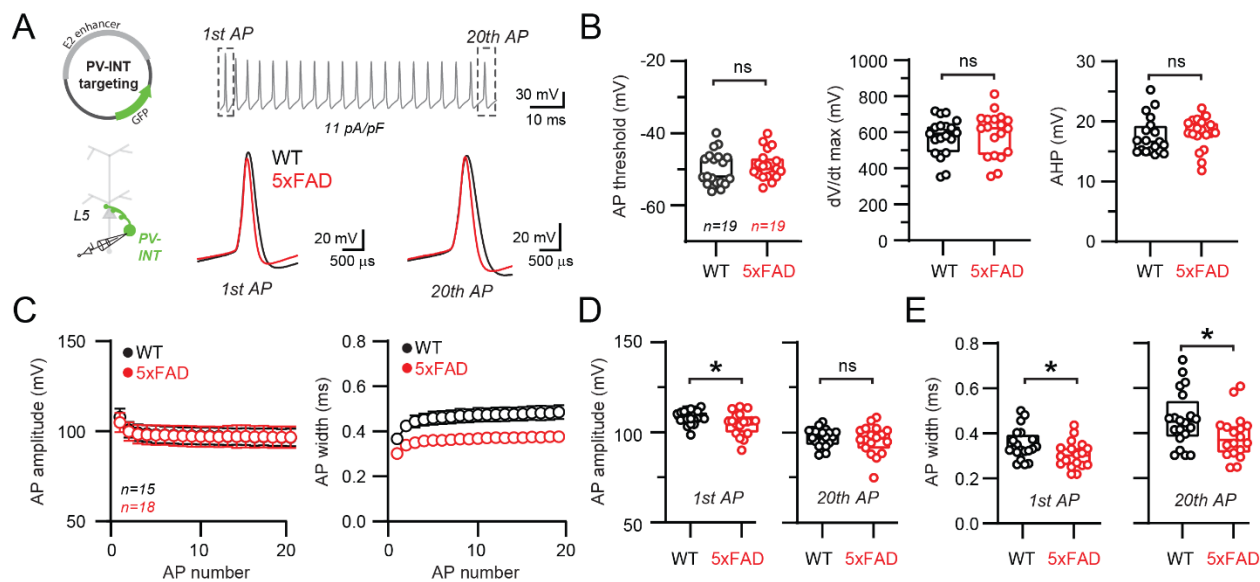
Figure 2. *Altered AP waveforms in PV interneurons of 5xFAD mice*

A. AP waveforms and properties of GFP[+] interneurons were compared at 11 pA/pF square pulse injections in WT and 5xFAD mice. In the enlarged view, APs from the 1st and 20th spike in the train of WT and 5xFAD mice are superimposed for comparison.
B. Summary data of AP properties. No differences in AP threshold, dV/dt maximum, or AHP were observed ($p > 0.05$; unpaired t-test).

C. Relationship between AP amplitude or width in WT and 5xFAD mice and AP # during spike trains elicited with 11 pA/pF current injection. Data are expressed as mean (± SEM).
D. Summary data of AP amplitude for the 1st and 20th APs in WT and 5xFAD mice.
E. Summary data of AP width for the 1st and 20th APs in WT and 5xFAD mice.
For (B,D &E) individual data points and box plots are displayed. Significance was defined as $p < 0.05$; unpaired t-tests.

1149   The extraordinarily rapid onset and repolarization of PV-APs depends on the combined

1150   expression of fast voltage-gated sodium (Na_v) and potassium (K_v) channel families[23-30]. Whether

1151   altered expression of voltage-gated channels emerge before plaque deposition is unclear. Changes

1152   in the expression of channels from the Na_v1 family may contribute to altered spiking in cortical

1153   PV interneurons from hAPP-expressing FAD mice[108,125], but see also[179]. Therefore we examined

1154   parameters associated with fast-activating Na_v channels[180-182], however, found no significant

1155   differences between 5xFAD and control mice (Figure 2A & B). AP afterhyperpolarization (AHP)

1156   amplitude was also unaltered (Figure 2B).

1157 Na_v channel deficits result in reduced AP amplitude and contribute to AP failure during

1158   repetitive firing[25,29,183]. Using a serendipitous current injection step where spike-frequency was

1159   indistinguishable between 5xFAD and control mice (11 pA/pF; Figure 2A), a subtle reduction in

1160   the amplitude of the initial AP was observed (Figure 2D). However, this reduction did not

1161   progressively worsen during continued firing (Figure 2C & 2D) as seen in mouse models where

1162 Na_v1 channels were altered[178,184]. Interestingly, AP repolarization was more rapid across the entire

1163   spike train (quantified as a reduction in full AP width at half-maximal amplitude [half-width];

1164   Figure 2C & E) in 5xFAD mice.

1165   To test whether a Na_v channel mechanism could describe the AP firing phenotypes

1166   observed in 5xFAD mice, we built a simplified PV NEURON model constrained by our

1167   measurement AP parameters. Using the model, we independently simulated how changes in

1168   overall Na_v conductance, activation voltage, and kinetic properties affected relevant AP firing

1169   properties (Figure 3A). Significant reduction of Na_v conductance density (up to 50% of control)

1170   could lessen AP firing at near-threshold current steps (Figure 3B). However, this reduction was

1171   accompanied by complete firing failures at high frequencies[108] (Figure 3B), which was not
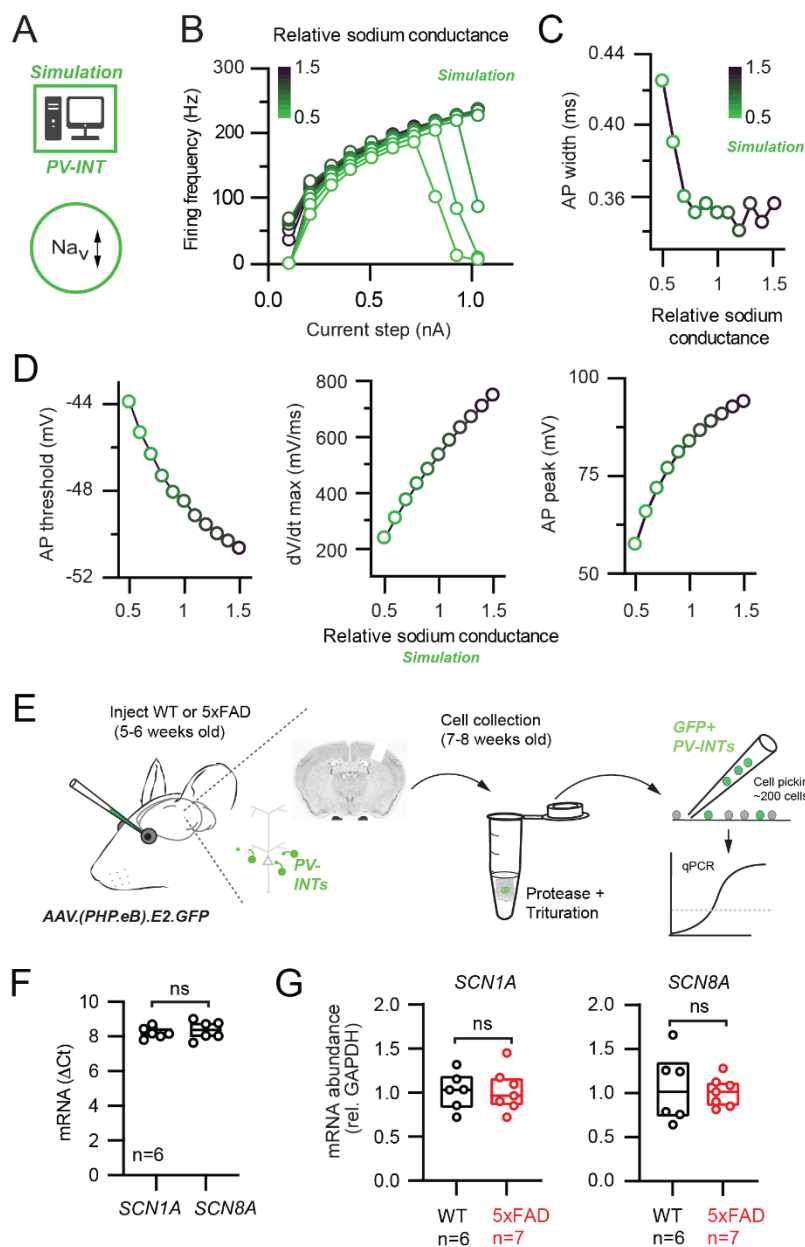
Figure 3. Na_v channel changes do not explain changes in PV interneuron excitability in 5xFAD mice

A. Depiction of PV cell single compartmental model with modified Na_v channel properties.
B. Simulated relationship (S/cm^2) between the magnitude of injected current and AP firing frequency at variable Na_v conductance densities.
C. Summary relationship of AP width and relative Na_v conductance density (± 50% from control Na_v conductance).
D. Summary graphs depicting the effect of changing Na_v conductance density on AP threshold, dV/dt maximum, and AP peak (± 50% from control Na_v conductance).
E. Depiction of cell-type-specific qPCR of *Scn1* genes following retro-orbital AAV injection in 4-6 week old mice. Individual neurons were physically isolated, hand-picked, and pooled after allowing 2-3 weeks for cortical expression.
F. Comparative qPCR expression of *Scn1a* and *ScnN8a* in WT mice.
G. Quantification of *Scn1a* and *Scn8a* mRNA expression between WT and 5xFAD mice.
For (F) and (G) data are expressed as individual data points from each individual mouse with box plots superimposed.

observed in 5xFAD mice. Furthermore, AP width was unaltered over a broad range of Na_v conductance densities (Figure 3C) suggesting that AP width narrowing observed in 5xFAD mice was also due to a Na_v-independent mechanism. In contrast, changing Na_v conductance density was associated with changes in AP threshold and maximal dV/dt (Figure 3D) which were unaltered in our recordings (Figure 2). Shifting Na_v kinetics or activation voltage also could not explain the observed 5xFAD phenotypes (Figure 3-figure supplement 1).

To complement our Na_v modeling, we performed PV interneuron-specific qPCR[7] by isolating and pooling

1195   AAV.E2.GFP^{+} neurons from dissected somatosensory cortex following AAV retro-orbital

1196   injection[138] in 5xFAD and control mice (Figure 3E). Expression of $Na_v1.1$ (*Scn1a*) and $Na_v1.6$

1197   (*Scn8a*) were detected in wild-type PV interneurons (Figure 3F). Relative to control, no changes

1198   in mRNA expression of either subunit in 5xFAD mice were found. (Figure 3G). Together, our

1199   patch clamp recordings, simulations, and gene expression data indicate that

1200   modifications in Na_v channel expression cannot account for the observed changes in PV firing in

1201   our pre-plaque hAPP model.

1202

1203   *Biophysical but not gene expression changes of Kv3 channels in PV interneurons*

1204

1205   The distinct firing phenotype and rapid AP repolarization of fast-spiking PV cells require

1206   expression of fast-activating K_v channels, which complement Na_v1[29]. Thus, by ruling out Na_v

1207   channels as viable candidates for explaining the above differences, we postulated that altered K_v

1208   channel availability could contribute to AP firing differences observed in 5xFAD mice. TEA-

1209   sensitive K_v3 channels are highly expressed in PV cells, and possess extremely fast kinetics which

set AP width and firing rate in different neuron types[27,185-187]. To record K_v conductances from PV interneurons, we obtained outside-out patches from AAV.E2.GFP^{+} neurons in both 5xFAD and control mice. TEA (1mM) was puffed onto isolated patches to block and *post-hoc* evaluation (Figure 4A).

Large TEA-sensitive currents were isolated in patches from PV cells (Figure 4B) displaying characteristic K_v3-like properties, including a relatively depolarized steady-state half-activation voltage (Figure 4D) and submillisecond activation

Figure 4. *Modified K_v3 channel biophysics in 5xFAD mice*
A. Experimental workflow for obtaining outside out patches from PV interneurons in WT and 5xFAD mice.
B. Representative K_v3 currents isolated from outside out patches in WT and 5xFAD mice. Patches were held at -110mV and then stepped from -90 to +50mV using 300 ms, 20mV steps.
C. Data summary of maximal K_v3 conductance in WT and 5xFAD mice (p > 0.05; unpaired t-test). Individual data points from each patch and box and whisker plot summaries are displayed.
D. Summary of activation voltage of K_v3 conductance isolated from patches in WT and 5xFAD mice. Conductance was normalized to the maximal overall conductance (gmax) for each cell. The average dataset was fit with a Boltzmann function with individual values expressed as mean (± SEM).
E. Summary of activation time constant ( ) of K_v3 currents in isolated from patches in WT and 5xFAD mice. Datasets were fit with single monoexponential decay functions and are expressed as mean (± SEM).

1230   kinetics (Figure 4E)[23,24,188]. Substantial changes in K_v channel availability could account for the

1231   observed differences in AP firing in 5xFAD mice (Figure 1). However, the overall TEA-subtracted

1232   conductance was unchanged in 5xFAD (Figure 4C), suggesting that overall Kv channel surface

1233   expression was unaltered. The proportion of TEA-insensitive conductance was also unchanged

1234   (wild-type, $33.1 \pm 2.9\%$; 5xFAD, $33.0 \pm 2.3\%$; $p = 0.98$; unpaired t-test; $n = 9$ and 12; respectively).

1235   Interestingly, we observed differences in the biophysical properties of TEA-sensitive channels in

1236   5xFAD. Channels activated at more hyperpolarized (left-shifted) voltages (Figure 4D; half

1237   activation voltage -6.6 mV wild-type vs -15.5 mV in 5xFAD). Furthermore, activation kinetics

1238   decreased across the observable range in 5xFAD mice (Figure 4E). We also performed recordings

1239   to evaluate steady-state inactivation parameters and kinetics (Figure 4 - Figure supplement 1A-C).

1240   On average, voltage dependence of activation and inactivation from wild-type recordings was in

1241   agreement with the biophysical characteristics of $K_v3.3$ channels[189]. Inactivation kinetics were

1242   highly variable, but on average resembled $K_v3.3$ homomers[190] or $K_v3.1/K_v3.4$ heteromers[24], but

1243   other possible compositions cannot be excluded. In contrast to changes in K_v activation voltage in

1244   5xFAD, half inactivation voltage was slightly right-shifted (half inactivation voltage -19.9 mV in

1245   wild-type vs -13.9 mV in 5xFAD). Inactivation kinetics were indistinguishable in wild-type and

1246   5xFAD (Figure 4 - Figure supplement 1B,C).

1247   Differential mRNA expression of the four known K_v3 channel *Kcnc* subunits in 5xFAD

1248   mice could account for the observed shifts in K_v3 biophysics (Figure 4 D & E). To evaluate this

1249   possibility, we again performed PV interneuron-specific qPCR by isolating AAV.E2.GFP$^+$ cells

1250   (Figure 4F), as described earlier. Expression of all four subunits was confirmed in PV cells from

1251   somatosensory cortex, however, no differences in mRNA expression were found between 5xFAD

1252   and control mice, for any of the four *Kcnc* subunits (Figure 4F). Several studies have demonstrated

1253   a discordance between steady-state mRNA and protein levels[191,192]. To evaluate whether altered

1254   protein levels of ion channels could account for AP firing differences in young 5xFAD mice, we

1255   examined quantitative mass spectrometry data related to K^+ and Na^+ channel proteins obtained

1256   from cortical homogenates from WT and 5xFAD mice (1.8, 3.1, 6.0, 10.2, and 14.4 months old).

1257   Protein levels from nearly all *Kcnc* (K$_v$3), *Kcna* (K$_v$1), *Kcnq* (K$_v$7), *Kcnd* (K$_v$4), *Kcnma1* (BK$_{Ca2+}$),

1258   and *Scn1* (Na$_v$1) subunits, as well as other K$^+$ and Na$^+$ channel families and regulatory subunits,

1259   were quantified (Figure 4 - figure supplement 2).
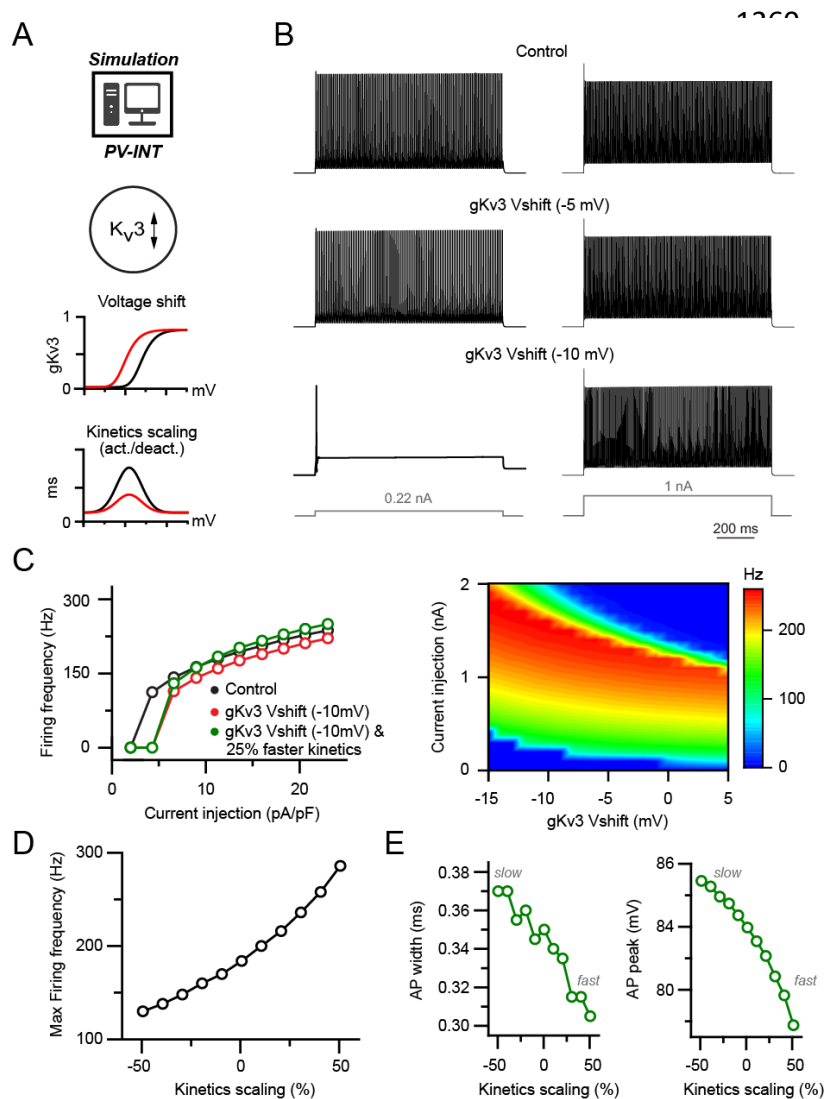
Figure 5. *Effect of biophysical K_v3 dysregulation on AP firing in a PV model*
A. PV cell single compartmental model with modified K_v3 channel properties. K_v3 activation voltage and kinetics were independently or simultaneously modified in the following simulations. When applied, activation and deactivation kinetics were scaled together (± 50% of control).
B. AP firing elicited by square pulse current injections at control and hyperpolarized K_v3 activation voltages. Two example current injection magnitudes are displayed.
C. Summary of firing frequency changes in different simulated K_v3 conditions. Near-threshold AP firing is reduced with hyperpolarized K_v3 activation independent of shifting K_v3 activation kinetics.
D. Effect of modifying K_v3 channel activation kinetics (± 50% of control) alone on maximal firing frequency in PV neuron compartmental model.
E. Effect on K_v3 channel activation kinetics changes on simulated AP width and amplitude.

K_v3 protein ($K_v3.1$, 3.2, and 3.3) levels at the youngest timepoint (7.2 weeks old), which matched our earlier physiological and mRNA evaluations, were again unchanged, while $Na_v1.1$ was slightly increased (Figure 4 - figure supplement 2B; 5.9%; unadjusted $p < 0.05$) in 5xFAD. Protein levels for most other examined channel types and regulatory subunits were unaltered in young 5xFAD mice (Figure 4- figure supplement 2B,C). However, several age-related trends were noted. After showing a slight increase in young 5xFAD mice, $Na_v1.1$ levels were reduced at 10.2 months old (Figure 4 - figure

1280 supplement 2E). Additionally, $K_v3.3$ levels progressively reduced with age (Figure 4- figure

1281 supplement 2B-F). In general, proteomic alterations expanded with increasing age in 5xFAD mice

1282 (see Figure 4- source data 1). Protein levels of PV and CaMKII were unchanged at 1.8 and 3 month

1283 timepoints (p > .05; one-way ANOVA). Together, our combined mRNA and protein-level

1284 evaluations indicate that the modifications responsible for divergent K_v biophysical properties

1285 occur without changes in mRNA or protein levels at this pre-plaque disease stage.

1286

1287 *Modified K_v3 channel biophysics recapitulate the 5xFAD phenotypes in a PV model*

1288

1289   To test whether modifying K_v3 channel biophysics alone could adequately explain the AP

1290 firing phenotypes in 5xFAD mice, we returned to our reduced PV cell simulation (Figure 5A). In

1291 control conditions, our model PV neuron increased firing in relation to the magnitude of current

1292 injection (Figure 5B & 5C). Notably, when the K_v3 activation potential dependence was

1293 hyperpolarized as observed in 5xFAD PV neurons (Figure 5A & 5B; control absolute half

1294 activation voltage = -5.0 mV; absolute test Vshift (-10 mV) = -15.0 mV) we found that AP firing

1295 was strongly dampened in the near-threshold range (Figure 5B & 5C; see also[193]), mirroring

1296 changes in 5xFAD mice. This near-threshold reduction in firing remained stable at differing

1297 inactivation voltage dependences (Figure 4 - Figure supplement 1E). Shifting the K_v3 activation

1298 voltage left-ward also led to a slight reduction in firing frequency at higher current injection levels,

1299 which could be normalized with a concurrent increase in K_v3 activation kinetics (tau) (Figure 5C).

1300   Modulation of K_v3 activation kinetics alone could modify AP firing frequency in either

1301 direction (Figure 5D), likely owing to changing Nav channel use-dependence. In contrast, broadly

1302 shifting K_v3 inactivation kinetics had no effect on either near-threshold or saturating firing

1303 frequencies (Figure 4 - Figure supplement 1F,G). This is likely because extremely rapid PV-APs

1304 (half-width ~350 us) are too brief for K_v3 inactivation to accumulate, even with very rapid (tau =

1305 50 ms) inactivation kinetics ((Figure 4 - Figure supplement 1G). AP repolarization is differentially

1306   shaped by distinct kinetic properties of different K_v subtypes[30,186,194-196]. As AP width in our PV

1307   cell model was uncoupled from changes in Na_v conductance, we hypothesized that AP width was

1308   influenced by changes in K_v3 channel kinetics[24]. Indeed, increased activation kinetics were

1309   correlated with a reduction in AP width, which could also influence AP amplitude (Figure 5E). In

1310   contrast, changes in K_v3 inactivation kinetics had no effect on AP width or amplitude (Figure 4 -

1311   Figure supplement 1H).

1312   Other potassium channel types may also be sensitive to 1mM TEA and thus contribute to

1313   biophysical alterations in patches from 5xFAD mice, in particular, B_K and $K_v7.2$[197]. When

1314   expressed locally, B_K channels can influence AP repolarization[198,199]. However, B_K blockade in

1315   PV-expressing interneurons in cortex or cerebellum did not affect AP width[186,199] or spike-

1316   frequency, likely due to functional confinement of B_K to axonal synapses in PV cells[27,200]. These

1317   factors suggest that TEA-sensitive currents isolated in outside out patches in this study unlikely to

1318   include B_K. To confirm this, we puffed Iberiotoxin[199,200] onto outside out patches from layer 5 PV

1319   interneurons. No changes in outward conductance were identified following IBTX (control, $5.2 \pm$

1320   1.6 nS; IBTX, 5.1 ± 1.5 nS; $p>0.05$, paired t-test; n=5), indicating the absence of active B_K

1321   conductance in our patch recordings.

1322   Although Kv7 kinetics are likely not rapid enough to regulate AP width, if present,

1323   subthreshold activation of K_v7 could contribute to changes in AP firing[201] in 5xFAD mice.

1324   Therefore we supplemented our original K_v3 model with an additional K_v7 conductance[202] (Figure

1325   5- figure supplement 1). Addition of K_v7 ($2mS/cm^2$) could reduce firing across a range of current

1326   injections (Figure 5- figure supplement 1B, C). However, in contrast to K_v3 (Figure 5B),

1327   hyperpolarizing the K_v7 activation voltage had no effect on AP firing frequency (Figure 5- figure

1328 supplement 1C). Furthermore, shifting the supplemented K_v7 conductance density or its voltage-

1329 dependence did not affect AP waveform properties (Figure 5- figure supplement 1D). Hence upon

1330 model exploration of relevant biophysical parameters, we could fully recapitulate the AP firing phenotypes observed in 5xFAD PV cells via biophysical shifts in K_v3 alone.

Introduction of modified K_v3 conductance reproduces near-threshold hypoexcitabilty in PV interneurons
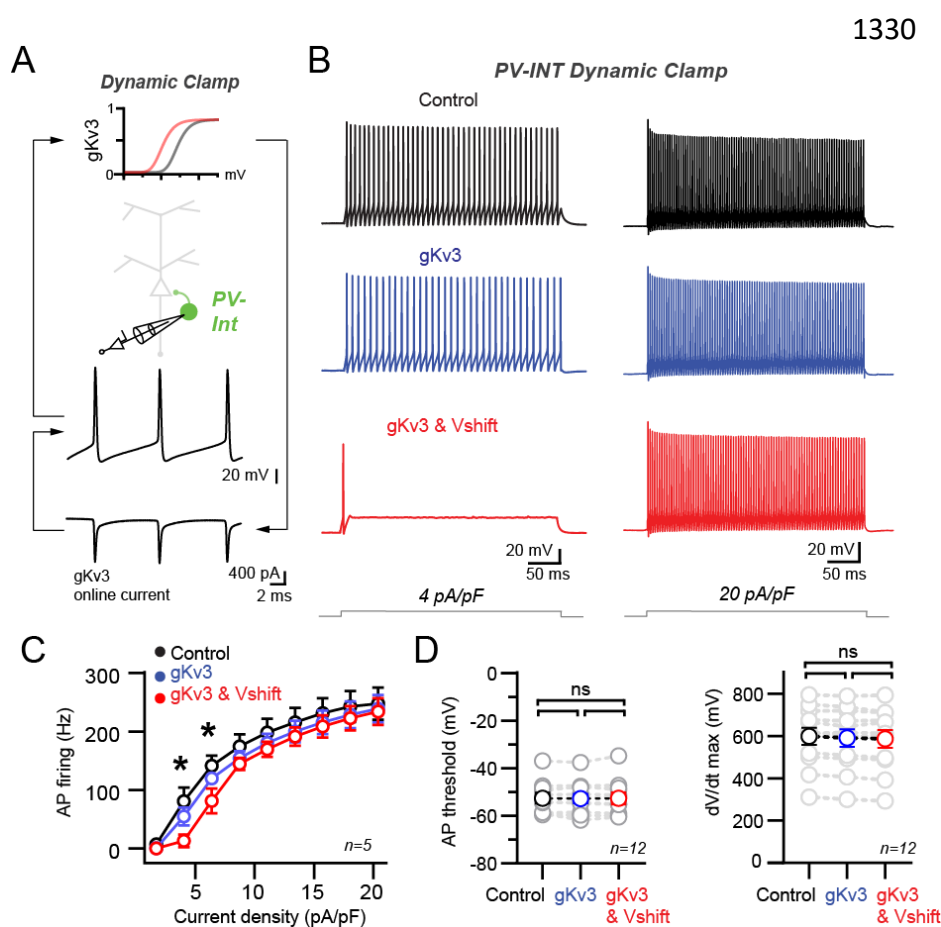
Figure 6. *Recapitulation of the 5xFAD phenotype in PV cells using dynamic clamp*
A. Targeted dynamic clamp recordings from an AAV.E2.GFP[+] neuron. Online K_v3 response (20 nS online gKv3) shown during AP firing in a PV interneuron.
B. AP firing responses to two different square pulse current injection levels in three distinct K_v3 dynamic clamp conditions in the same cell.
C. Summary data plot across a range of current injections from dynamic clamp conditions. Statistical significance was tested between the gKv3 (blue) and gKv3 & Vshift (red) conditions by RM two-way ANOVA (p < 0.05) with Sidak's multiple comparison test.
D. Summary plots for AP threshold and dV/dt maximum in each of the dynamic clamp conditions tested within each cell. No differences were observed in any condition using RM one-way ANOVA (p < 0.05) with Tukey's multiple comparison test.
In all datasets individual values are expressed as mean (± SEM).

1348 While

1349 powerful, model predictions are based on simplified biophysical information. To increase confidence that

1350 altered K_v3 channel properties can explain reduced near-threshold excitability in intact PV neurons, we

1351 employed an Arduino-based dynamic clamp system[203]. Dynamic clamp allows real-time injection of current

1352 constrained by predefined voltage-gated conductances, such as gK_v3, during current clamp recordings

1353   (Figure 6A). Furthermore, distinct properties (*e.g.,* activation voltage) of these conductances can be

1354   adjusted online during recordings. Dynamic clamp recordings were performed in targeted recordings from

1355   AAV.E2.GFP$^+$ neurons in wild-type mice using modeled gK_v3 parameters described earlier. We found that

1356   dynamic clamp introduction of wild-type gK_v3 (absolute half-activation voltage, -5.0 mV) could restore

1357   fast firing after K_v3 blockade (Figure 6 - figure supplement 1A, B).

1358   To model the effect of AP firing in wild-type and AD-like conditions, we examined distinct gK_v3

1359   conditions (Figure 6B; *Control* [no dynamic clamp conductance added, 0.0 nS *gKv3*]; +*gK$_v$3* [absolute half-

1360   activation voltage, -5.0 mV]; and +*gK$_v$3 & Vshift* ['5xFAD' absolute half-activation voltage, -15.0 mV]).

1361   Modest supplementation of additional *Control* K_v3 conductance (+*gK$_v$3*; 20 nS) had no discernable effect

1362   on AP firing across a range of current densities (Figure 6B & 6C). However, introduction of an identical

1363   magnitude of the 5xFAD-modeled K_v3 conductance (+*gK$_v$3 & Vshift*; 20 nS) induced a specific reduction

1364   in near-threshold firing without affecting high-end frequencies (Figure 6B & 6C). This +*gK$_v$3 & Vshift*

1365   induced near-threshold effect could also be replicated in 1mM TEA (Figure 6 - figure supplement 1C, D)

1366   following a left-ward shift in the re-introduced gKv3 conductance. Compared to control, AP threshold and

1367   dV/dt maximum were unchanged in both *gKv3* test conditions (Figure 6D). Together with our NEURON

1368   simulation data, these dynamic clamp recordings indicate that introduction of a biophysically modified K_v3

1369   conductance can reproduce the hypoexcitable firing phenotype observed in PV interneurons in prodromal

1370   5xFAD mice.
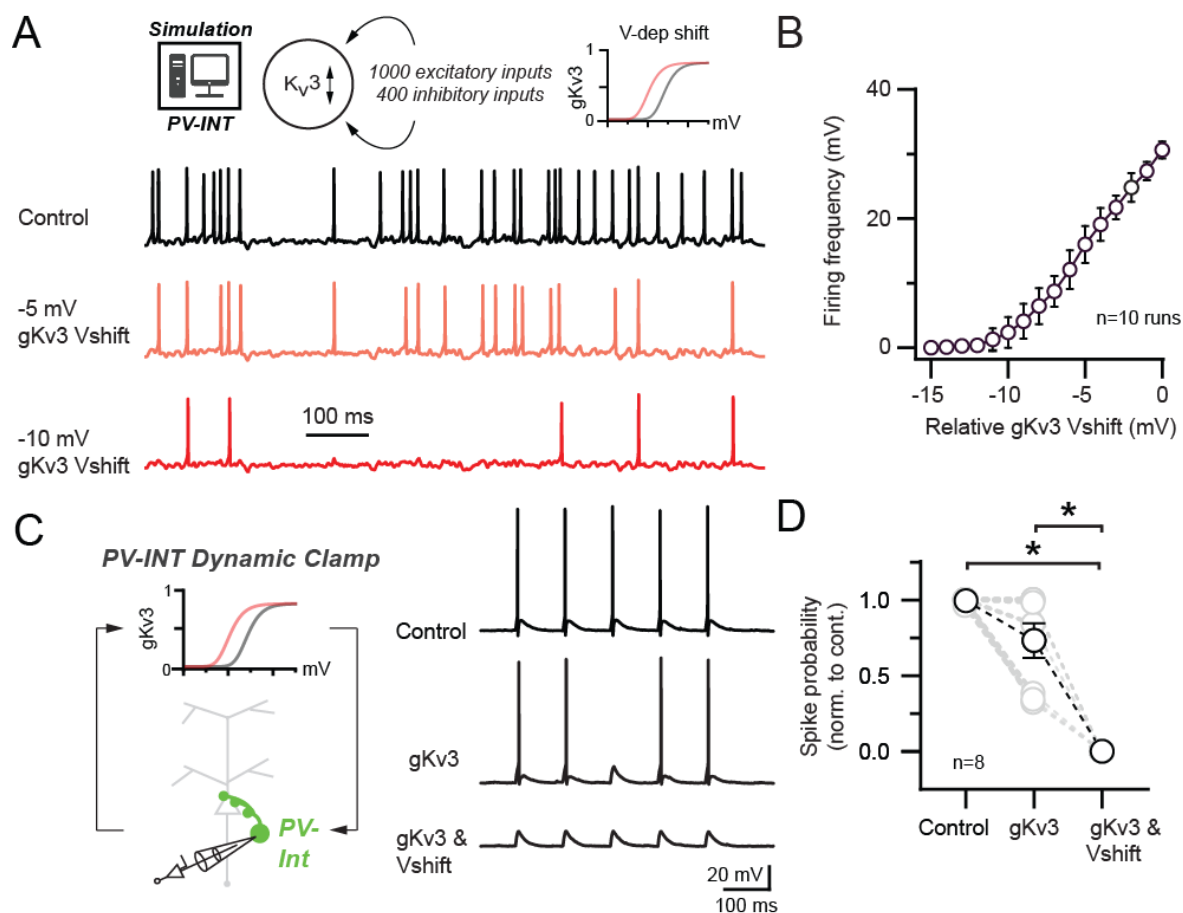
Figure 7. Effect of 5xFAD-related K_v3 channel modulation on synaptically evoked AP firing

A. Simulated responses of PV cell compartmental model with continuous excitatory and inhibitory inputs in control and with hyperpolarized K_v3 activation voltages.
B. Summary graph of PV compartmental model firing frequency in response to continuous synaptic inputs at increasingly hyperpolarized K_v3 activation voltages. 0 mV represents the relative control K_v3 activation voltage.
C. 10 Hz gEPSP-evoked AP firing in dynamic clamp recordings from AAV.E2.GFP+ neurons in acute slice.

In control conditions, gEPSP conductance was calibrated such that the majority of stimuli evoked APs. Within recordings the gEPSP amplitude was constant while the cell was subjected to varying gK_v3 dynamic clamp conditions.
D. Spike probability summary in response to gEPSPs in varying gK_v3 dynamic clamp. Significance was defined by one-way ANOVA ($p < 0.05$) with Tukey's multiple comparison test).

For all summary graphs, data are expressed as mean (± SEM).

1371

1372   *In vivo*, cortical PV neurons often fire at the lower end of their dynamic range[204,205]. To

1373   examine how K_v3 channel modulation affects PV interneuron firing in a realistic network

1374   condition, we imposed several hundred sparsely active (see Methods) excitatory and inhibitory

1375   synapses onto our PV NEURON simulation (Figure 7A). In control conditions, the PV cell fired

1376   regularly (30.64 ± 0.39 Hz). Hyperpolarization of the control K_v3 membrane potential dependence

1377   was inversely correlated with spike-frequency (Figure 7B).

1378   Using dynamic clamp in wild-type mice, we next sought to understand whether K_v3

1379   channel regulation could also diminish synaptically-evoked AP firing in intact PV

1380   (AAV.E2.GFP⁺) interneurons. *In vivo*, single excitatory synaptic inputs can reliably drive AP

1381   firing in PV neurons[206]. Thus, we injected PV neurons with an excitatory conductance

1382   (gEPSP)[11,207,208] to reliably evoke AP firing at 10 Hz (gEPSP, 4.7 ± 1.0 nS; Figure 7C). Dynamic

1383   clamp addition of wild-type K_v3 conductance (+gK_v3; 20 nS) had a non-significant effect on

1384   gEPSP-evoked AP firing (Figure 7C & D). Interestingly, injection of the 5xFAD-modeled K_v3

1385   conductance (+gK_v3 & *Vshift*; 20 nS) strongly reduced gEPSP-evoked firing (Figures 7C and 7D).

1386   While often referred to as high-voltage activating channels, K_v3 channels open in the

1387   subthreshold range in cerebellar GABAergic interneurons[209] and regulate the magnitude of EPSPs

1388   in hippocampal PV cells[210]. In PV NEURON simulations, hyperpolarizing the K_v3 activation

1389   voltage could reduce the amplitude of EPSPs (Figure 7 - figure supplement 1A), thus necessitating

1390   an increase in excitatory synaptic conductance to evoke an AP (Figure 7 - figure supplement 1B).

1391   This modulation was also observed in further dynamic clamp PV recordings with subthreshold

1392   gEPSPs (3.6 ± 0.8 nS; Figure 7 - figure supplement 1C). Together, these data argue that enhanced

1393   subthreshold activation of K_v3 contributes to near-threshold PV hypoexcitabilty during early-stage

1394   AD.

1395

1396   *Modulation of PV K_v3 channels elicits network hyperexcitability in a reduced layer 5 circuit model*
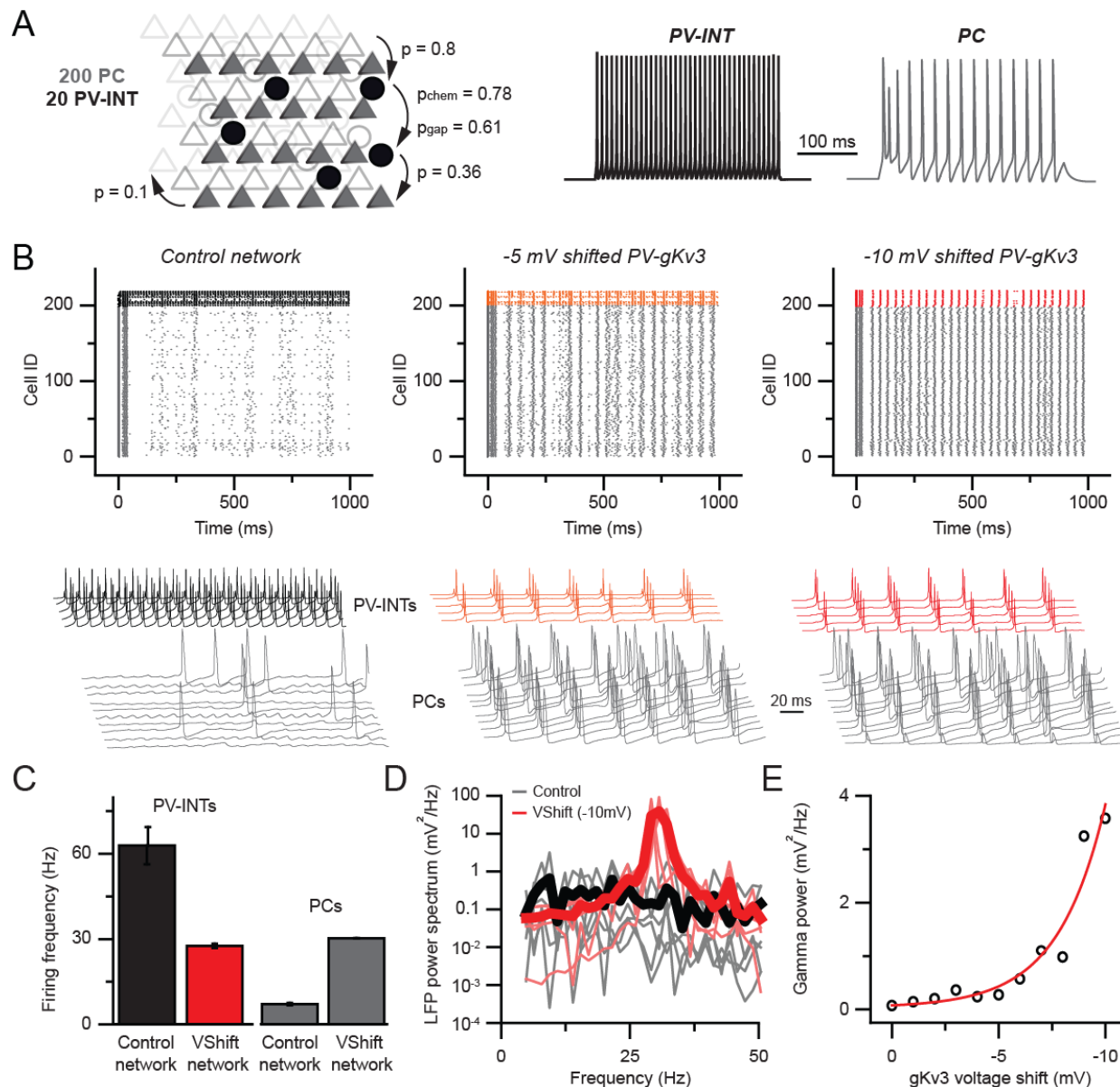
Figure 8. *Hyperexcitability and increased gamma following PV-specific Kv3 modulation*

A. Simplified cortical network consisting of 200 pyramidal cells (PC; triangles) and 20 PV (circle) cells. Connection probabilities between and within cell groups are set based on literature. 300 ms long spiking responses for single PC and PV cells are shown on the right.
B. Raster plots depicting 1 s long network activity of the 220 cells in the network. The top 20 cells correspond to PV cells (black, orange, red), bottom 200 cells show PC activity (grey). The effect of relative -5.0 and -10.0 mV shifts in gK$_v$3 of PV cells are compared to control. Representative traces are shown from 5 PV cells and 10 PC.

C. Mean firing frequency of PV cells and PCs upon -10 mV relative voltage shift of gK$_v$3 in PV cells. Data are expressed as mean (± SEM).
D. Calculated local field potential (LFP) between 5 and 50 Hz, produced by 220 cells in the network. The activity level of individual cells was randomized and network simulations were repeated 5 times in control conditions and with a -10 mV relative shift in gK$_v$3 of PV cells. Individual LFP traces are shown in light grey and light red. Mean LFP traces are shown in bold black and red.
E. Gamma power in relation to the voltage shift of gK$_v$3 in PV cells. Gamma power was calculated by averaging LFP signals between 30 and 50 Hz. Continuous red line depicts the exponential relationship between the two variables.

1397   Precisely timed synaptic inhibition of neuronal circuits provided by PV interneurons is

1398   indispensable for network operations[211-213]. In order to understand the network consequences of

1399   the observed PV phenotype in young 5xFAD mice, we developed a local PV-PC network model

1400   (Figure 8A). Connection strengths and probabilities for the network consisting of 200 PCs and 20

1401   PV cells were based on previous reports[214-218]. The model reproduced key features of local PV

1402   circuit models including gap-junction related firing synchrony[219] and recurrent connection related

1403   synchrony[220].

1404   We found that gradual shifting of the voltage dependence of gK_v3 conductance in PV cells

1405   markedly increased the firing rate of the simulated PCs (Figure 8B, control: 7.07 ± 0.42 Hz, 10

1406   mV; Vshift: 30.3 ± 0.12 Hz, n = 200, $p < 0.0001$, paired t-test). This network hyperexcitability can

1407   be attributed to the altered excitation-inhibition ratio due to the effects of gKv3 biophysical

1408   changes of PV interneuron firing. Specifically, in the control network, PV firing (62.9 ± 6.58 Hz

1409   mean firing, n = 20) was constrained by their recurrent connections, gap junctions and sporadic

1410   entrainment by the PC population's low firing rate. However, when the excitability of PV cells

1411   was dampened by altered gK_v3 voltage-dependence (Figure 8C; n = 20 runs), PCs were released

1412   from the high inhibitory tone resulting in network hyperexcitability, which is a hallmark of

1413   recurrently connected pyramidal cells networks[221,222].

1414   Next, we investigated whether the increase in network excitability resulted in altered

1415   oscillatory behavior. We found that there was a significant increase of gamma power at 30 Hz

1416   (Figure 8D, 0.13 ± 0.08 and 38.7 ± 14.76 mV^2/Hz, n = 5 each, $p < 0.05$, paired t-test; for control

1417   and shifted gK_v3 network respectively) which is in agreement with previous work[213].

1418   Our simulations demonstrate that alterations in the voltage dependence of a single PV

1419   conductance can have substantial effects on local network activity. However, minor deviations

1420   from the ensemble mean can arise from the stochastic nature of channel opening and closing[223,224]

1421 and from interactions with auxiliary channel subunits[225,226]. Therefore, we tested the stability of

1422 the network upon perturbations of gK_v3 gating. Our results showed an exponential relationship (R^2

1423 = 0.93) between the voltage shift of gK_v3 in PV cells (Figure 8E) and network gamma power. This

1424 nonlinearity indicates that although a ~10 mV shift can alter circuit behavior, the network is

1425 protected against expected stochastic ion channel fluctuation-induced alterations in excitability.

1426 Together, our results demonstrate that a hypersynchronous (Figure 8 - figure supplement 1) and

1427 hyperactive network activity can emerge as a consequence of altered PV interneuron K_v3

1428 biophysics.

1429

1430 3.3 Discussion

1431 In this study, we report a novel mechanism contributing to cortical circuit dysfunction in

1432 an early-stage AD mouse model. Our findings indicate that modulation of K^+ channel biophysics

1433 contributes to cortical PV interneuron dysfunction in early AD. In a simplified circuit model, this

1434 K^+ channel mechanism caused cortical network hyperexcitability and modified signaling

1435 specifically in the gamma frequency domain. Our results represent a novel cellular mechanism

1436 with a causal link to overall circuit hyperexcitability, thus presenting a potential therapeutic avenue

1437 to combat AD progression in its early stages.

1438 *PV interneuron pathophysiology in AD models*

1439

1440 PV-positive GABAergic interneurons constitute a substantial proportion (~ 40%) of the

1441 total cortical interneuron population[227]. These interneurons form powerful inhibitory synapses

1442 with local pyramidal neurons, thereby regulating a variety of cognitive functions[204]. In several

1443 different AD mouse models, investigators have observed abnormal PV intrinsic excitability,

1444 however, mechanistic understanding of this phenomenon is incomplete. Here we report reduced

1445 cortical PV firing in the 5xFAD model. In complementary AD mouse models, human APP and

1446 PS1 proteins (*e.g.,* APP/PS1, hAPPJ20) are also expressed at high levels and include mutations

1447 resulting in increased amyloid production. Within these models, PV interneurons display

1448 physiological phenotypes including altered AP firing[108,110]. Notably, PV neurons were found to be

1449 more susceptible to shifts in their excitability with respect to neighboring pyramidal neurons in

1450 these studies. PV-specific vulnerability could manifest as a result of their high metabolic demand[41]

1451 or through abnormal regulation of ion channel subunits necessary for maintaining their fast-spiking

1452 nature[125].

1453   Related changes in PV neuron excitability are evident among the hAPP mouse models. In

1454 layer 5 PV cells, we observed reductions in near-threshold AP firing and AP width, but AP

1455 amplitude and passive properties were largely unaffected. In hippocampal CA1 from 5xFAD mice,

1456 AP firing during synaptic recruitment was also strongly reduced[124]. In layer 2/3 PV neurons of

1457 hAPPJ20 mice, overall AP firing rates were unchanged but a significant reduction in AP amplitude

1458 was observed[108], however, in hAPPJ20 hippocampal CA1, spike frequency was strongly reduced[75].

1459 A CA1 study from APP/PS1 mice observed reduction in AP width but increased AP frequency[110].

1460 In next-generation hAPP KI mice, which express the hAPP at far lower levels with respect to the

1461 aforementioned APP models, PV firing frequency was also reduced in entorhinal cortex before

1462 plaque deposition[109]. Variations among these studies could depend on the disease severity at which

1463 observations were made, regional differences, or genetic differences between models. Nonetheless

1464 the related phenomena evident across these studies suggests that a unifying set of molecular

1465 mechanisms may spark circuit-level dysfunction in early AD.

1466

1467   *Mechanisms of altered PV excitability in AD*

1468

1469   In a hallmark set of studies, differential expression of voltage gated Na^+ channels in PV

1470   neurons was linked with network hyperexcitability in hAPP-expressing AD mice[108,125]. It is

1471   unclear whether other channel types are regulated and contribute to PV neuron dysfunction in AD.

1472   In this study we observed physiological changes in 7-8 week old 5xFAD mice, however, few

1473   proteomic changes are predicted until ~4 months of age in this model[174]. In keeping with this

1474   finding, we did not observe differences in Na_v1 or K_v3 mRNA levels in 7-8 week old mice.

1475   However, steady-state mRNA and protein levels are not always well correlated[191,192]. Therefore,

1476   we compared a significant subset of the relevant cortical voltage-gated channel proteome from

1477   5xFAD and wild-type mice, using mass spectrometry across several ages.

1478   In general, the number of channels showing genotype-associated changes increased with

1479   age in 5xFAD mice[174]. Similar to K_v3 mRNA, K_v3 protein levels ($K_v3.1$-3.3) were unchanged in

1480   ~7 week old mice. Interestingly, $K_v3.3$ protein expression was reduced in more aged 5xFAD mice,

1481   displaying progressive depletion with age. Along with other K_v3 subunits[190], $K_v3.3$ expression is

1482   relatively high in PV neurons[228] and alternative splicing of $K_v3.3$ is associated with temporal lope

1483   epilepsy[229]. Thus network hyperexcitability in intermediate-late AD could be associated with

1484   altered $K_v3.3$ expression.

1485   Unfortunately, $K_v3.4$ protein was not isolated in our mass spec analysis. As $K_v3.4$

1486   upregulation has been shown in humans and animal models[230,231] or following Aβ treatment[232],

1487   future studies should focus on evaluating regional $K_v3.4$ mRNA and protein expression in different

1488   AD models and disease stages, including well before extensive amyloid plaque deposition.

1489   Although K_v3 channels are highly expressed in PV cells, our proteomic analysis was from bulk

1490 homogenates. Thus cell-type-specific proteomic approaches in 5xFAD and other AD models

1491 should be a major focus for future work.

1492 Rather than changes in expression levels, our results indicate that biophysical modulation

1493 of K_v3 channels was responsible for reduced AP firing and AP width in young 5xFAD mice.

1494 Interestingly, reduced AP width was observed in PV cells before other intrinsic alterations in

1495 APP/PS1 mice[110] suggesting that K_v3 modulation could precede that of other channels or

1496 homeostatic responses. Several APP-related cellular processes could explain the biophysical

1497 modulation of K_v3 observed here. The intermediate APP transmembrane protein product C99,

1498 produced following β-Secretase (BACE1)-directed cleavage, can regulate K_v channel activity[233].

1499 One or more of these APP-related interactions could contribute to the K_v3 channel dysregulation

1500 observed in 5xFAD mice here.

1501 Biophysical modulation of K_v3 could also arise through several other well-described

1502 mechanisms without direct hAPP interactions. Changes in K_v3 phosphorylation via PKC, PKA,

1503 nitric oxide phosphatase[203,234-238], or casein kinases[239] as well via K_v3 glycosylation[240] can impart

1504 changes in K_v3 conductance, voltage dependence, or kinetics. Future work to characterize the

1505 phosphorylation and glycosylation state of K_v3 in AD models will be necessary. Differential

1506 surface expression of K_v3 subunits or splice variants could also explain the K_v3 phenotype

1507 described here. For example, $K_v3.4$ subunits can increase K_v3 activation kinetics while also

1508 hyperpolarizing their activation voltage in cerebellar interneurons[24,241]. However, of three $K_v3.4$

1509 splice variants (Kv3.4a-c) only one ($K_v3.4a$) could impart these features *in vitro[24]*. Intriguingly,

1510 increased BACE1 activity in AD[242] may promote surface expression of $K_v3.4$ subunits. BACE1

1511 may also physically associate with K_v3 channel proteins in a beta-subunit-like fashion to modify

1512 their gating properties[243]. Additionally, changes in ancillary protein (*e.g.,* K_v beta subunit *Kcne*)

1513 expression or activity represent another avenue for modulation of K_v3 biophysics. For example,

1514 co-expression of K_v3 channels with *Kcne3* hyperpolarized their activation voltage[244]. While not

1515 well characterized in PV interneurons to date, *Kcne* subunits may be differentially regulated in

1516 AD[232,245]. Cortical single-cell RNAseq datasets from the Allen institute[246] show no expression of

1517 *Kcne*1-3 in cortical PV interneurons, and a variable level of *Kcne4* expression (our analysis).

1518 Intriguingly, the APP cleavage product C99 displays significant sequence homology with *Kcne[233]*

1519 suggesting that K_v3 channels could be biophysically regulated via C99 in a similar manner as with

1520 *Kcne*. Implementing the PV-type-specific viral approach utilized in this study in various AD

1521 models will allow for a deeper evaluation of the possible mechanisms responsible for K_v3

1522 modulation in future work. Additional longitudinal studies at multiple stages of the disease will be

1523 necessary to parse out the emergence of cell-type-specific biophysical mechanisms during the

1524 disease.

1525

1526 *Relationship of PV interneuron dysfunction and circuit-level disruptions*

1527

1528 Circuit hyperexcitability is a prodromal indicator in familial and late-onset AD[115,164,165,167-

1529 170,172,173]. Altered PV interneuron firing occurs at early stages of the disease[109,110], likely

1530 contributing to epileptiform activity and overall circuit hyper-synchrony in cortex. Using a layer

1531 5 cortical circuit model, we found that PV-specific K_v3 channel dysfunction resulted in overall

1532 hyperexcitability[247,248].

1533 Several PV cell-specific cellular and connectivity features, such as short input integration

1534 time window[210], frequent recurrent connections, and extensive gap junction coupling[215] help

1535 regulate cortical circuit operations. PV cells are particularly important for maintaining signaling

1536   in the gamma frequency domain[220]. In our 5xFAD simulation, which produced near-threshold

1537   reduction in PV firing, we observed a sharp increase in gamma power that scaled with the severity

1538   of K_v3 modulation. Similarly, reduced PV excitability can amplify gamma power in different

1539   cortical areas[249] likely through disruption of feedback inhibitory circuits[213]. Notably, increased

1540   gamma power was observed in AD patients during resting states[250]. In the context of these studies,

1541   it is tempting to hypothesize that near-threshold changes in PV firing may disrupt inhibitory

1542   feedback circuits in cortex in times of sparse coding. Conversely, reduction of PV excitability can

1543   also result in reduced gamma power in different contexts[251]. Thus bidirectional, PV-specific

1544   modulation of the gamma range is likely to be circuit and context-dependent[213]. The tendency for

1545   local gamma power to increase or decrease in different circuits in AD should provide insight into

1546   PV-specific cellular pathology.

1547   Further disentanglement of the mechanisms of interneuron dysfunction in distinct AD

1548   models is necessary. Specifically, the relationship of hAPP, amyloid[111,252], and its intermediate

1549   products to PV-related dysfunction and abnormal circuit function. The versatility and efficiency

1550   provided by the cell-type-specific enhancer approach used here can be implemented in future

1551   studies on novel AD mouse models, or by transgene expression through viral delivery[253], as well

1552   as in iPSC derived human neurons.

1553

1554   *Potential therapeutic strategies for amelioration of Kv3-related PV hypofunction in early AD*

1555

1556   Our findings suggest an opportunity for implementation of novel targeted therapies to

1557   improve cortical circuit hyperexcitability in AD. Our biophysical, dynamic clamp, and modeling

1558   experiments here indicate that a specific K_v3 biophysical parameter, altered in 5xFAD mice

1559   (hyperpolarized activation voltage), can strongly alter PV firing and overall circuit activity. Our

1560   data suggest that strategies to increase expression of wild-type K_v3 are unlikely to rescue the AD

1561   firing phenotype, as supplementation of wild-type gK_v3 did not affect near-threshold PV

1562   excitability. However, drugs that depolarize the activation voltage of endogenous K_v3 channels, or

1563   PV-specific genetic therapies[175] to modify K_v3 activation voltage dependence[24,241] present

1564   promising avenues for therapeutic intervention. Firing in our PV model was not highly sensitive

1565   to changes in other K_v3 properties, such as inactivation kinetics. Thus some off-target K_v3 effects

1566   of pilot therapeutics may be acceptable. To better understand the translational scope of our

1567   findings, future work should focus on understanding whether biophysical K_v modifications are

1568   shared across other AD models at early stages of the disease.

1569

1570

1571

1572

1573

1574

1575
1576

1577   3.4 Supplementary Information

1578
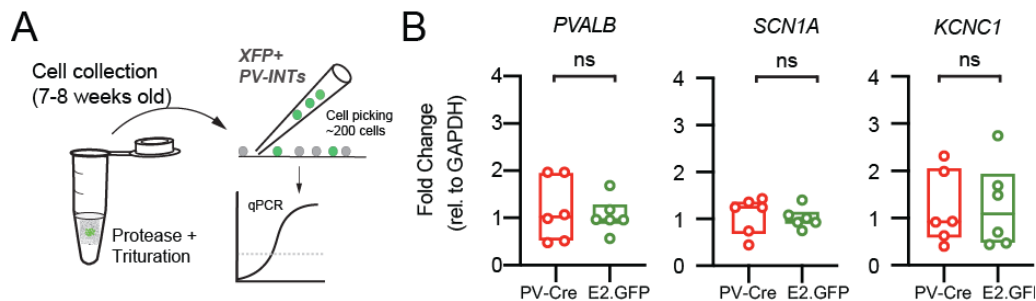
1584

1585

1586   **Figure 1-figure supplement 1**

1587   *Chapter 3. Supplemental Figure 1. Confirmation of PV interneuron gene expression in*
1588   *AAV.E2.GFP+ neurons*

1589   (A) Depiction of cell-type-specific qPCR following stereotactic AAV injection in 5-6 week old mice. ~200

1590   GFP+ neurons were physically isolated and hand-picked from the somatosensory cortex at 7-8 weeks of

1591   age.

1592   (B) PV-specific gene expression was compared in two mouse strains. One cohort of PV-Cre mice (n=6)

1593   acting as the control group were injected with an AAV expressing a floxed tdTomato construct. A second

1594   test cohort (n=6) of WT mice were injected with AAV.E2.GFP. Expression of three known cortical PV

1595   interneuron-specific genes (*Pvalb*, *Scn1a*, *Kcnc1*) were quantified for each cohort. There were no

1596   differences (p > 0.05; unpaired t-tests) between the two groups for any of these genes. Individual data points

1597   and box plots are displayed.

1598

1599

1600
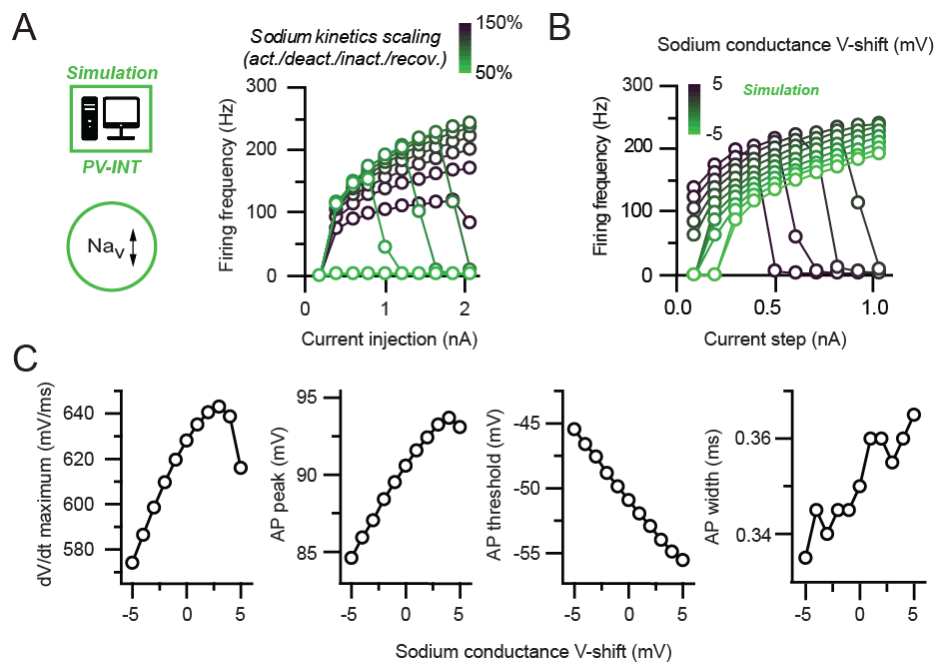
1603 **Figure 3-figure supplement 1**

1604 *Chapter 3. Supplemental Figure 2. Na$_v$ channel changes do not explain changes in PV*
1605 *interneuron excitability in 5xFAD mice*

1606 (A) Depiction of PV cell single compartmental model with modified Na$_v$ channel properties. The

1607 relationship of injected current magnitude and AP firing frequency with varying Na$_v$ kinetics is summarized.

1608 All four kinetic properties (activation, deactivation, inactivation, and recovery from inactivation) were

1609 simultaneously scaled together ($\pm$ 50% of control) in the simulation. Near-threshold dampening of AP firing

1610 was observed with increased kinetics however this was accompanied by an overall reduction in AP firing

1611 rate at higher current injections.

1612 (B) Summary data showing the relationship of injected current magnitude and AP frequency following

1613 shifts in Na$_v$ activation voltage ($\pm$ 5mV from the control). Near-threshold dampening of AP firing was

1614 achieved through a hyperpolarizing shift however this was accompanied by a reduction in firing across all

1615 current injections, which was not observed in recordings from 5xFAD mice.

1616 (C) Additional datasets depicting the effect of shifting Na_v activation voltage on AP properties. Modifying

1617 activation voltage influenced all parameters including dV/dt maximum and AP threshold, which were not

1618 affected in recordings from 5xFAD mice.

1619

1620

1621

1622

1623

1624

1625

1626

1627

1628

1629
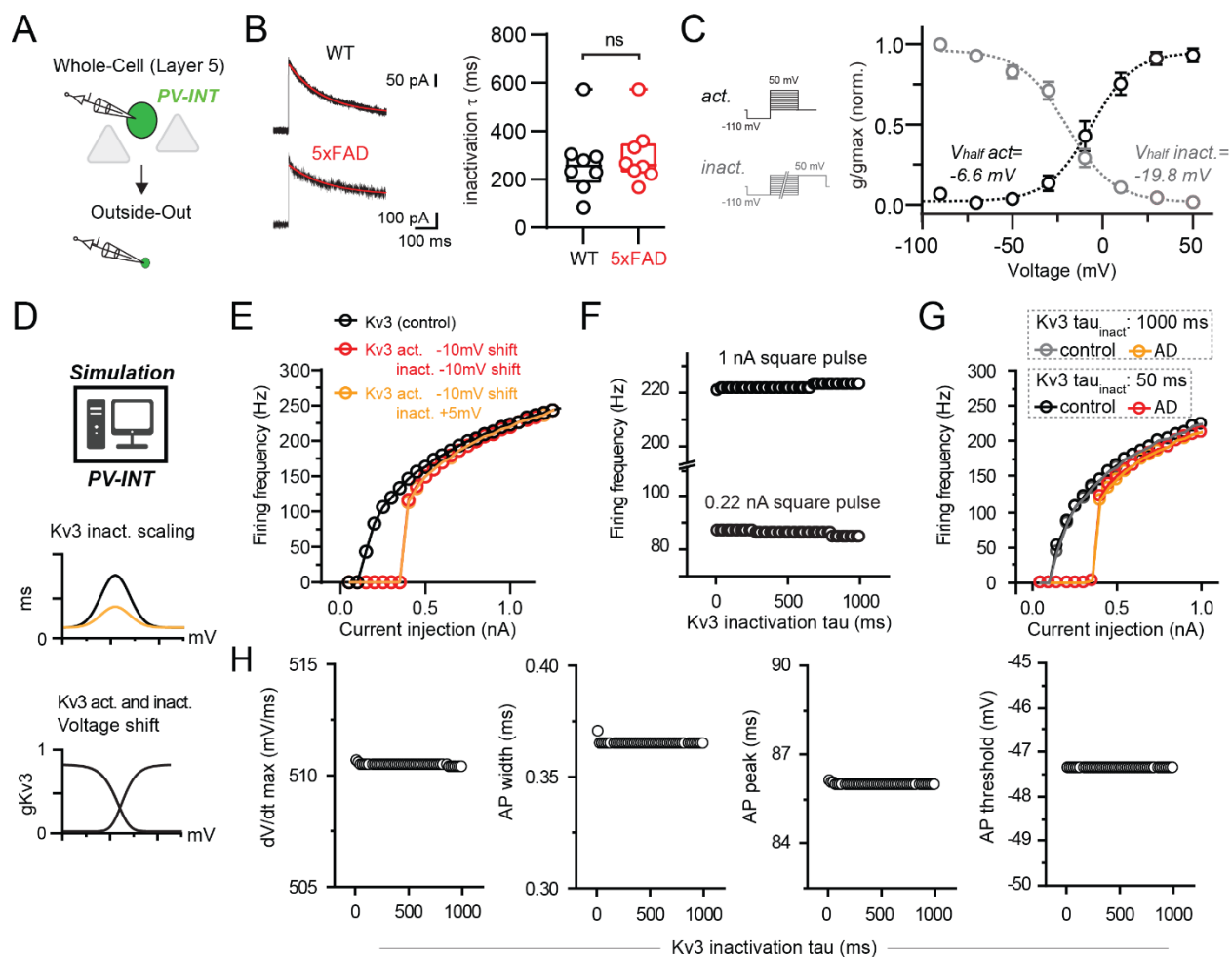
1630

Figure 4 - figure supplement 1

Chapter 3. Supplemental Figure 3. Observed K_v3 inactivation properties and relationship to AP firing in PV interneurons

(A) Experimental workflow for obtaining outside out patches from PV interneurons in WT and 5xFAD.

(B) Representative TEA-sensitive currents (800 ms step; +50 mV holding) from outside out patches in WT and 5xFAD mice. Steady-state inactivation time constants (were determined by fitting traces with a single exponential function (overlaid in red). Summary data of inactivation showed no difference between WT and 5xFAD (p > 0.05; unpaired t-test; n=8 for WT, n=8 and 5xFAD).

(C) Summary of inactivation voltages isolated from patches in WT mice (n=8) overlaid with activation voltage data (from Figure 4). Conductances were normalized to the maximal overall conductance (gmax) for each cell. Datasets fit with Boltzmann functions with individual values expressed as mean (± SEM).

(D) PV cell compartmental model depiction with WT and modified Kv3 channel voltage dependence and kinetics.

(E) Summary data of firing frequency following concurrent shifts in K_v3 activation and inactivation voltage dependence. Near-threshold firing was reduced with hyperpolarized activation voltage (-10 mV relative shift) regardless of negative or positive shifts in inactivation voltage dependence.

(F) Effect of modifying K_v3 channel inactivation kinetics alone on near-threshold (0.22 nA pulse) and saturating (1 nA pulse) firing rates.

(G) Changes to AP firing frequency after simultaneously shifting K_v3 activation voltage dependence and inactivation kinetics. Hyperpolarizing the activation voltage (-10 mV relative shift) reduced near-threshold firing but not high-frequency firing regardless of inactivation kinetics (tau inactivation, 1000 ms [orange trace] or 50 ms [red trace])

(H) Effect on changing K_v3 inactivation kinetics alone on simulated AP waveform parameters.
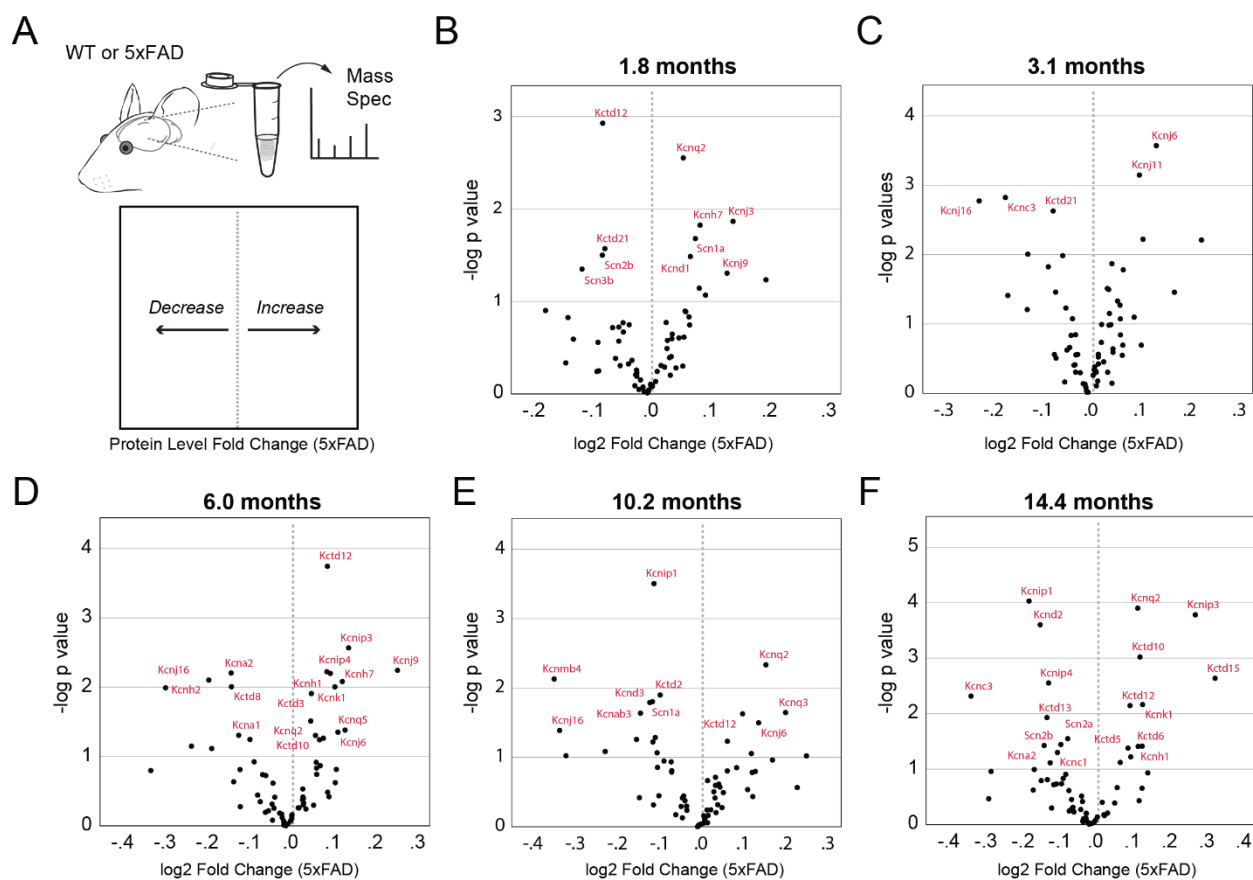
Figure 4 - figure supplement 2

Chapter 3. Supplemental Figure 4. Mass Spectrometry (Mass Spec) of protein levels at varying ages in 5xFAD mice

(A) Cartoon depiction of Mass Spec and data visualization. Rightward shifts indicate increases in protein levels while leftward shifts indicate decreases in protein levels in 5xFAD mice.

(B-F) Differential expression analysis of K^+ and Na^+ channel proteins in 5xFAD mice. Volcano plots summarizing results from differential expression analysis of quantitative mass spectrometry data from WT and 5xFAD mice (age range 1.8 – 14.4 mo, n=4-6 mice per age group with 50% males/females). Proteins demonstrating statistically significant changes at each age (unadjusted p<0.05) are labeled in red. Y axis: -log 10 unadjusted p-value (T test). X axis: log2 transformed fold change (5xFAD vs. WT).
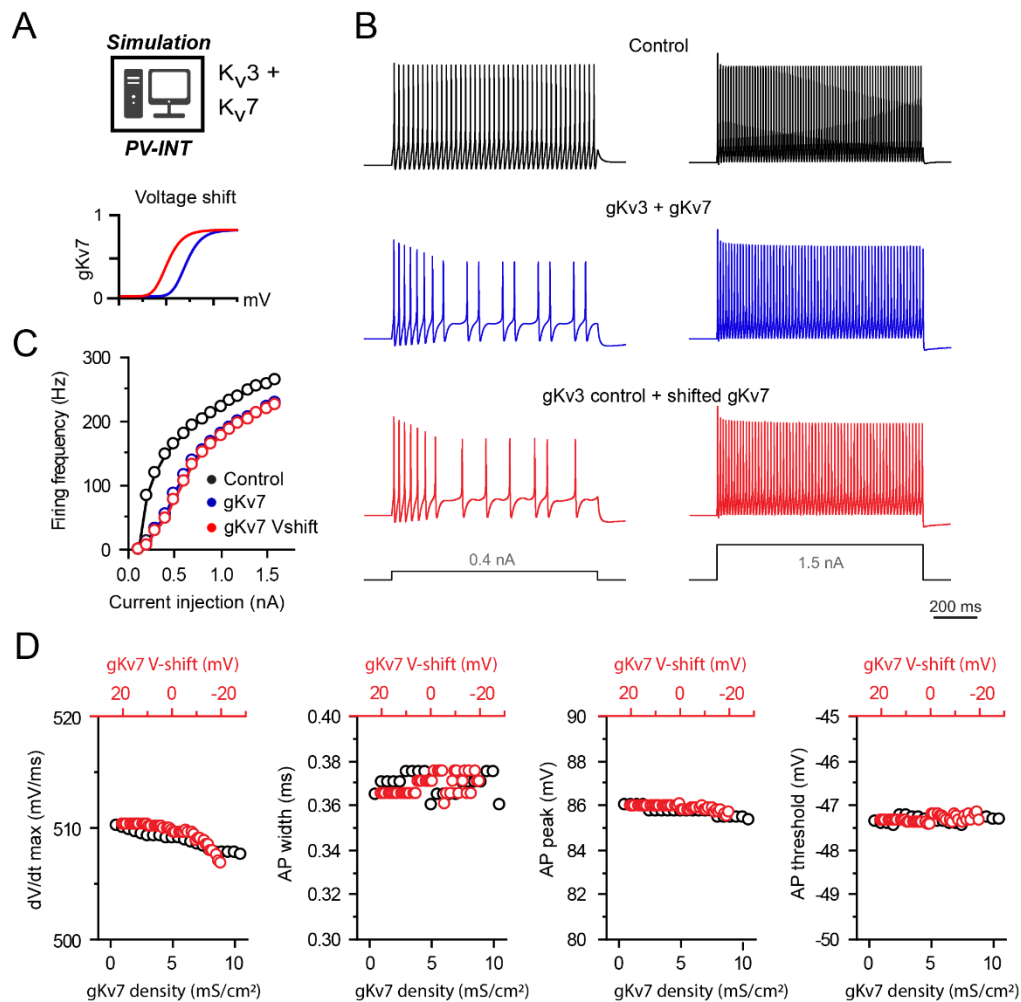
Figure 5 - figure supplement 1

Chapter 3. Supplemental Figure 5. Effects of supplementing different Kv7 conductances on AP firing in a PV model

(A) PV cell single compartmental model with Kv3 and additional Kv7 channels. Kv7 activation voltage and kinetics were independently or simultaneously modified.

(B) AP firing elicited by square pulse current injections in control (gKv3), with supplemented Kv7 (gKv3 + gKv7) and following hyperpolarization (-10mV relative shift) of the supplemented Kv7 activation voltage.

(C) Summary data of firing frequency changes in different conditions. AP firing is unaffected following hyperpolarization of Kv7 voltage dependence.

1688   (D) Effects of Kv7 activation voltage and conductance density on simulated AP parameters.

1689

1690

1691

1692

1693

1694

1695

1696

1697

1698

1699

1700

1701
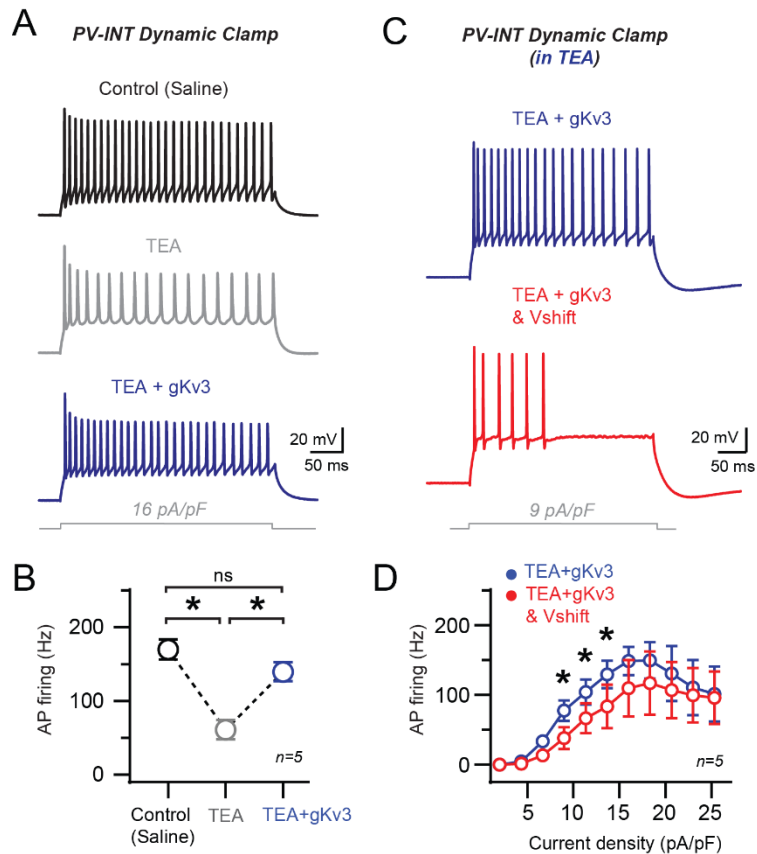
Figure 6 - figure supplement 1

Chapter 3. Supplemental Figure 6. Effects of WT and AD gK_v3 dynamic clamp with endogenous K_v3 channels blocked

(A) Targeted recordings from a representative E2.GFP$^+$ PV interneuron. High-frequency AP firing (current density 16pA/pF) was evaluated in the same cell under control conditions, after bath application of TEA (1mM) and finally after dynamic clamp introduction of (wild-type) gK_v3 conductance in TEA.

(B) Summary data of PV firing (firing rates averaged from 12-20 pA/pF) in control, TEA, and TEA+gK_v3 conditions. gK_v3 (20-50 nS) could partially restore fast firing in TEA. Statistical significance was tested by RM one-way ANOVA (p < 0.05) with Tukey's multiple comparison test.

(C) AP firing responses to square pulse current injection with wild-type- and AD-type K_v3 dynamic clamp conditions in the same cell. Recordings were performed in the presence of 1mM TEA in the bath.

1715   (D) Summary data plot across a range of current injections with wild-type and AD (-10 mV relative shift in

1716   voltage of activation) gK_v3 dynamic clamp conditions, all with bath TEA (1mM). Statistical significance

1717   was tested between the wild-type gKv3 (blue) and AD gKv3-Vshift (red) conditions by RM two-way

1718   ANOVA ($p < 0.05$) with Sidak's multiple comparison test.

1719

1720

1721

1722

1723

1724

1725

1726

1727

1728

1729

1730
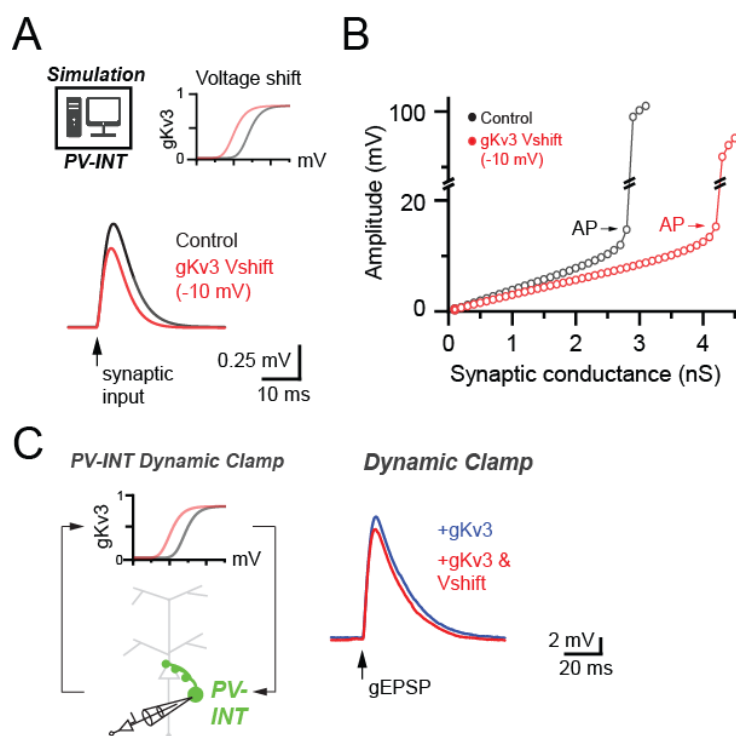
1731

1732

1733   **Figure 7 - figure supplement 1**

1734   *Chapter 3. Supplemental Figure 7. Effect of 5xFAD-related K_v3 channel modulation on*
1735   *synaptically evoked subthreshold events*

1736   (A) Average subthreshold response of PV cell compartmental model following excitatory input in control

1737   conditions and with a relative -10 mV Vshift in K_v3 activation voltage.

1738   (B) Differences in subthreshold excitatory event amplitudes evoked by increasing synaptic conductances.

1739   Simulation was run in control conditions and following leftward K_v3 activation voltage shift.

1740   (C) Subthreshold gEPSPs evoked in dynamic clamp recordings from AAV.E2.GFP^{+} neurons. gEPSP

1741   conductance was calibrated such that stimuli reliably resulted in subthreshold events. For each condition

1742   during recordings, ~10 time-locked gEPSP waveforms were averaged. Comparison of EPSP in +gK$_v$3 (20

1743   nS) and +gKv3 (20nS) with -10 mV Vshift are shown. -10mV K$_v$3 relative Vshift was sufficient to reduce

1744   gEPSP charge (+gK$_v$3, 252.2 ± 38.4 pC.; +gK$_v$3 & Vshift, 221.9 ± 32.7 pC; p = 0.01, paired t-test; n = 5).

1745

1746

1747
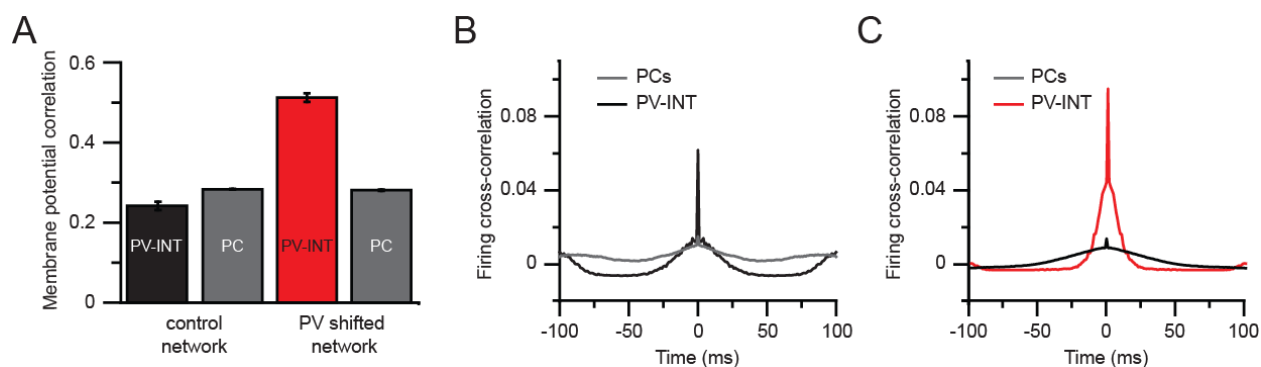
1748

1749

1750 **Figure 8 - figure supplement 1**

1751 *Chapter 3. Supplemental Figure 8. Circuit synchronization following PV-specific Kv3 modulation*

1752 (A) Membrane potential correlations within cell groups in control and -10 mV shifted gK$_v$3 conditions.

1753 Correlations were measured as Pearson correlations coefficient comparing each individual cell. Data are

1754 expressed as mean (± SEM).

1755 (B) Firing cross-correlation of PV cells and PCs in a 200 ms time window.

1756 (C) Same as for panel B but in case of a network with -10 mV shifted gKv3 in PV cells.

1757
1758
1759
1760
1761
1762
1763 All modeling and dynamic clamp included in this chapter were performed by Dr. Viktor Olah.
1764 A great portion of electrophysiological data in this chapter was contributed by Dr. Matthew
1765 Rowan.
1766 Bulk protein analysis in this chapter was run and analyzed by Dr. Prateek Kumar and Dr. Srikant

1767 Rangaraju.

1768

Chapter 4: Native-state proteomics of Parvalbumin interneurons

(and their unique molecular signatures and vulnerabilities in early Alzheimer's)

PV-INs account for less than 10-20% of all neurons in the brain, therefore I'm curious how much impact this cell type alteration could have during early AD Pathology?

-Reviewer #2

This chapter was adapted from:

1769 4.1 Summary

1770   Dysfunction in fast-spiking parvalbumin interneurons (PV-INs) may represent an early

1771 pathophysiological perturbation in Alzheimer's Disease (AD). Defining early proteomic

1772 alterations in PV-INs can provide key biological and translationally-relevant insights. We used

1773 cell-type-specific in-vivo biotinylation of proteins (CIBOP) coupled with mass spectrometry to

1774 obtain native-state PV-IN proteomes. PV-IN proteomic signatures include high metabolic and

1775 translational activity, with over-representation of AD-risk and cognitive resilience-related proteins.

1776 In bulk proteomes, PV-IN proteins were associated with cognitive decline in humans, and with

1777 progressive neuropathology in humans and mouse models of Aβ pathology. PV-IN CIBOP in early

1778 stages of Aβ pathology revealed signatures of increased mitochondria and metabolism, synaptic

1779 and cytoskeletal disruption and decreased mTOR signaling, not apparent in whole-brain

1780 proteomes. Furthermore, we demonstrated pre-synaptic defects in PV-to-excitatory

1781 neurotransmission, validating our proteomic findings. We showcase the first native-state

1782 proteomes of PV-INs, revealing novel molecular insights into their unique roles in cognitive

1783 resiliency and AD pathogenesis.

1784

1785

4.2 Introduction

A major goal in cellular neuroscience is to elucidate how the molecular signatures of unique neuronal subtypes translate to their functional diversity in intact circuits. Single-neuron transcriptomic studies have recently provided unparalleled access to the genetic diversity of dozens of unique brain cell classes[7]. Functional information is nonetheless limited in transcriptomic studies, due to substantial discordance between mRNA and protein levels, especially in neurons[131-133]. Proteomic studies relying on physical isolation of individual neuron types are also inadequate, as physical isolation of individual neurons is poorly tolerated, and of those that do survive, the vast majority of their functional surface area (i.e., dendrites and axons) is lost[135,136]. To overcome these limitations, we recently developed an *in vivo* strategy called cell type-specific in vivo biotinylation of proteins (CIBOP). When coupled with mass spectrometry, CIBOP can resolve native state proteomes from physically unaltered cell subtypes *in vivo*[2]. Key technical advancements, especially relating to neuronal subtype-specific targeting across different disease models, are also necessary to fully realize the potential of this method via extension to distinct classes of excitatory and inhibitory neurons. The recent discovery of highly versatile enhancer-AAVs[254] have the potential to fulfill these requirements, with tools targeting inhibitory interneurons receiving major initial development[255,256].

Inhibitory interneurons account for 10-20% of neurons in the brain[16]. Alterations in inhibitory interneuron function appear responsible for circuit and behavioral dysfunction in several neurological diseases. In particular, dysfunction of fast spiking, parvalbumin-expressing interneurons (PV-INs) are implicated in epilepsy, neurodevelopmental, and neurodegenerative diseases including Alzheimer's disease (AD)[26,41], a likely consequence of their role in maintaining circuit excitability locally, and brain state more generally, coupled with their substantial energy

1809 requirements[42]. Together, this cell class represents a promising locus for designer treatments across

1810 several major neurological disorders. Therapeutic failures are common in brain diseases,

1811 potentially due to unpredictable competing cell-type-specific responses. Thus, to enhance future

1812 therapeutic efficacy, high-resolution native state proteomic signatures of individual cell classes in

1813 wild type and disease models are required. Therefore, we implemented a versatile, systemic AAV-

1814 CIBOP intersectional approach[2,138,255] to characterize and compare native state *in vivo* PV-IN

1815 proteomes from both wild type mice and in a mouse model of early AD pathology. A novel

1816 enhancer-AAV targeting method was used to express Cre recombinase specifically in PV neurons

1817 throughout the cortex and hippocampus of Rosa26[TurboID] mice[2]. Upon Cre-mediated

1818 recombination, TurboID was expressed selectively in PV-INs, leading to robust cellular proteomic

1819 biotinylation. This PV-IN CIBOP approach identified over 600 proteins enriched in PV-INs,

1820 including canonical proteins as well as over 200 novel PV-IN proteins. The PV-IN proteome was

1821 enriched in mitochondrial, metabolic, ribosomal, synaptic, and a large number of

1822 neurodegeneration genetic risk and cognitive resilience-related proteins, suggesting unique

1823 vulnerabilities of PV-INs in AD.

1824 AD is arguably the most impactful and intractable neurodegenerative disease worldwide.

1825 Interestingly, selective alterations in PV-IN physiology are increasingly appreciated across several

1826 distinct *in vivo* models of AD pathology[113,115,119] which may contribute to prolonged cognitive

1827 dysfunction arising during the long-lasting, early stages of the disease[115,257,258]. Using network

1828 analyses of human post-mortem brain proteomes from controls and AD cases, we first identified a

1829 PV protein-enriched co-expression module (M33) strongly associated with cognitive resilience in

1830 longitudinal aging studies. Based on these lines of evidence, we next extended PV-IN CIBOP to a

1831 mouse model of hAPP/Aβ pathology[141,259]. We found that PV-INs in pre-plaque (3 month old)

1832 5xFAD mice exhibited extensive alterations in their mitochondrial and metabolic, cytoskeletal,

1833 and synaptic proteins, coinciding with decreased Akt/mTOR signaling. Several of these changes

1834 were validated using optogenetics, patch clamp, and cell-type-specific biochemistry. Strikingly,

1835 many of the proteomic changes noted in PV-INs in response to early Aβ pathology, were not

1836 resolved in the bulk brain proteome, suggesting that these cell-type-specific alterations are largely

1837 non-overlapping in early AD.

1838 Overall, our studies using the CIBOP approach reveal novel native-state proteomic

1839 signatures and identify potential molecular vulnerabilities of PV-INs to neurodegeneration in AD,

1840 and nominate potentially high-value targets otherwise hidden in the bulk proteome. This enhancer

1841 AAV-CIBOP strategy will also be broadly applicable to understanding molecular complexity of

1842 PV-INs and other neuronal subtypes, across any mouse model of health or disease.

1843

1844 <u>4.3 Results</u>

1845 Proteomic biotinylation of native-state PV-INs (PV-CIBOP) was achieved by retro-orbital

1846 (RO) delivery of PV-IN-specific enhancer-targeting AAV (PHP.eB-E2-Cre-2A-GFP)[255] into

1847 Rosa26$^{\text{TurboID/wt}}$ (PV-CIBOP group) or wild-type (WT) mice (**Fig 1A**)[138]. For acute slice

1848 electrophysiology of PV-INs, we co-injected (RO) an AAV construct containing a floxed

1849 TdTomato sequence to fluorescently-label PV-INs due to non-visualization of GFP in ex vivo

1850 slices. After 3 weeks of Cre-recombination and 2 weeks of biotin supplementation[2], we performed

1851 acute slice current clamp recordings confirming selective targeting and unaltered physiology of

1852 fast-spiking PV-INs by PV-CIBOP (**Fig 1A**, **Supp Figure S1**). To assess potential impacts of PV-

1853 specific TurboID expression and proteomic biotinylation on PV neuron function and overall local

1854 circuit activity, we obtained voltage and current clamp recordings from layer 5 pyramidal neurons

1855 and PV interneurons, respectively, in both WT control and PV-CIBOP mice (**Supp Fig S1A,B,H**).

1856 Fast, spontaneous excitatory and inhibitory synaptic events (EPSCs and sIPSCs) were isolated

1857 during pyramidal cell recordings (**Supp Fig S1B**). The amplitude, frequency and kinetic properties

1858 of both sEPSCs and sIPSCs were unperturbed in PV-CIBOP brains (**Supp Fig S1C-G**). These

1859 results indicate that PV-CIBOP does not affect basal circuit excitability, synaptic receptor

1860 distributions or synaptic properties. In the same slices, neighboring TdTomato+ neurons exhibited

1861 fast, non-accommodating firing with narrow action potentials (**Supp Fig S1H-J**) and passive

1862 properties characteristic of fast-spiking PV-INs (**Supp Fig S1K-M**). No differences in AP firing,

1863 various biophysical features, or passive properties were observed in PV-INs comparing PV-CIBOP

1864 with WT controls (**Supp Fig S1I-M**). Immunohistochemical (IHC) studies from fixed PV-CIBOP

1865 cortices showed widespread biotinylation of PV-positive (PV+) and GFP-positive neurons (**Fig**

1866 **1B-C**), in somatic and axo/dendritic compartments of PV-INs (**Fig 1D**) without off-target

1867 biotinylation or reactive gliosis (**Supp Fig S2**). Western blots (WB) showed strong biotinylation

1868 of a wide array of proteins in PV-CIBOP mice compared to few endogenously biotinylated proteins

1869 in WT control lysates (**Fig 1E**)[2]. Using the N-terminal V5 (V5-TurboID) as a surrogate of Cre-

1870 mediated TurboID expression, we detected V5 in PV-CIBOP mice but not WT controls (**Fig 1E**).

1871 Biotinylated proteins from PV-CIBOP and WT control samples were enriched using

1872 streptavidin (SA) beads followed by silver stain and WB (**Fig 1E**), confirming enrichment of

1873 biotinylated proteins from PV-CIBOP mice, mirroring patterns observed in bulk brain lysates

1874 (inputs). Label-free quantitative MS (LFQ-MS) of SA-enriched samples identified a PV-IN

1875 proteome of 628 proteins enriched in PV-CIBOP samples as compared to controls (≥2-fold

1876 enriched and unadjusted p≤0.05; 192 proteins ≥2-fold enriched at the FDR≤0.05 threshold) (**Fig**

Figure 1. Native-state proteomics of PV-INs by CIBOP.

A. Experimental approach: E2 enhancer Cre AAV was retro-orbitally delivered to WT (Control) or Rosa26TurboID/wt (PV-CIBOP) mice (n=3 per genotype, including males and females) followed by 3 weeks of Cre-mediated recombination, and 2 additional weeks of biotin supplementation (drinking water). The brain is then prepared for cortical slice electrophysiology, immunohistochemistry (IHC) and biochemical studies.

B-D. IHC of fixed brain sections confirmed biotinylation (red) in

PV-INs (Pvalb: green) in the cortex (Ctx) and hippocampal (HC) regions of PV-CIBOP but not control mice (B: 4x and C: 20x magnification; D: Higher magnification (60x) images from HC and Ctx are shown). **E.** Top: Western Blot (WB) of input (bulk brain tissue homogenates) and streptavidin affinity purification (pulldown) samples confirms strong protein biotinylation in PV-CIBOP (labeled) as compared to limited biotinylation (endogenously biotinylated proteins) in control animals. Bottom: Silver stained gels of inputs and pulldown samples corresponding to WB images above.

F. Volcano plot representation of differential abundance analysis of LFQ-MS data obtained from streptavidin pulldown samples, from PV-CIBOP and control mice. Red dots represent proteins biotinylated in PV-INs as compared to control mice. Most highly labeled PV-IN proteins (including TurboID) are highlighted.

G. Top PV-enriched proteins are shown on the left (including TurboID, Cnk1, Kcnc2, Kcnc3, Erbb4, Slc32a1 and GABA-ergic proteins). In contrast, non-neuronal (Mbp, Gfap, Aldh1l1, Cotl1) and excitatory neuronal (Slc17a7) proteins were not enriched (unpaired two-tailed T-test *p<0.05, **p<0.01, ***p<0.005). **H.** Gene Ontology (GO) analyses if PV-enriched proteins (as compared to whole brain proteome lists show enrichment of synaptic vesicle, GTPase binding, cytoskeletal and cell projection related proteins.

I. SynGO analysis of PV-enriched proteins reveals labeling of synaptic proteins in both pre- and post-synaptic compartments.

J. STRING analysis of PV-enriched proteins (>16-fold enriched over control) shows synaptic vesicle and exocytosis related proteins including complexins, ankyrins, synucleins.

K. Venn Diagram representing degree of overlap between proteins enriched in PV neurons, with whole brain proteomes from matched animals. While majority of PV-enriched proteins were also identified in whole brain proteomes, 135 proteins were only identified in PV neurons.

L. Top proteins differentially enriched in PV-INs as compared to the whole brain bulk proteome and those enriched in the bulk as compared to PV-INs, are highlighted.

M. Analysis of protein vs mRNA concordance in PV-INs, using PV-enriched proteins identified by PV-CIBOP and existing single nuclear transcriptomic data from the entire class of adult mouse PV-INs (Allen Brain Atlas). Based on differentials in rank abundances (protein vs. mRNA), discordant and concordant protein/mRNA pairs are highlighted.

Also see Supplemental Figures S1, S2, S3 and Supplemental Datasheet 1 for related analyses and datasets.

1878   **1F**, **Supp Datasheet 1**). These included canonical PV-IN proteins, including Kv3 channels

1879   (Kcnc2, Kcnc3), Gria4, Syt2 and Ank1, while markers of excitatory neurons (Slc17a7), astrocytes

1880   (GFAP), microglia (Cst3), oligodendrocytes (Mbp, Plp1) were not enriched (**Fig 1G**)[113,260-262].

1881   Gene set enrichment (GSEA) (**Fig 1H**) and SynGO (**Fig 1I**) [263] analyses of the PV-IN proteome

1882   showed over-representation of gene ontologies (GO) including synaptodendritic and axonal

1883   localization, neurotransmission, vesicle function, synapse organization, ARF-GTPase signaling,

1884   growth factor receptor signaling, tauopathy/synucleinopathy, and included pre- and post-synaptic

1885   compartments. Some of the most abundant synaptic PV-IN proteins were involved in synaptic

1886   vesicle trafficking, fusion and exocytosis and included complexins (Cplx 1-3), synucleins alpha

1887   and beta (Snca, Sncb), Bin1 and amphiphysin (**Fig 1J**)[264]. In contrast with bulk brain proteomes

1888   (**Fig 1K-L**), PV-IN-specific proteomes including GABAergic and Kv3 channels, proteins involved

1889   in synaptic vesicle function, endocytic/endosomal pathways, GTPase binding proteins,

1890   cytoskeletal proteins (Ank1) [261,265] and ribosomal large subunit proteins (Rpl15, Rpl18, Rpl24).

1891   Non-PV-IN proteins and glial proteins were preferentially enriched in the bulk brain proteome (**Fig**

1892   **1L**). We next contrasted our PV-IN proteome with reference single cell/nuclear RNAseq PV-IN

1893   transcriptomes from mouse brain (**Fig 1M, Supp Fig S3**)[266], revealing modest concordance

1894   between 1,810 mRNA-protein pairs (Spearman's Rho=0.27, p<0.001) (**Supp Datasheet 1)**. Our

1895   PV-CIBOP experiments successfully identified native-state proteomic signatures of PV-INs many

1896   of which are not captured by bulk brain proteomics and are discordant with mRNA-level findings.

1897

1898
1899

1900   *Proteomic signatures of PV-INs in contrast to Camk2a excitatory neurons reveal molecular*

1901   *signatures associated with vulnerability and cognitive resilience*

1902   We contrasted proteomic signatures of PV-INs with Camk2a-positive excitatory neurons

1903   using the CIBOP approach in two independent cellular contexts (**Fig 2A**)[2]. Of 1,841 proteins

1904   enriched in either PV-CIBOP or Camk2a-CIBOP proteomes (**Fig 2A, Supp Datasheet 2**), 1,568

1905   were enriched in Camk2a neurons and 1,408 proteins enriched PV-INs, with 1,135 proteins

1906   enriched in both. 245 proteins were highly-enriched (>4-fold) in PV-INs (including Kv3 channel

1907   proteins) while 163 proteins were highly-enriched in Camk2a neurons (**Fig 2B**). GSEA and

1908   protein-protein-interaction network analyses showed that ribosomal, GABA metabolism, ephrin B

1909   pathway, clathrin-coated vesicle, transport, cytoskeleton, endoplasmic reticulum, calcium binding,

1910   synaptic vesicle exocytosis terms as well as Akt/mTOR signaling were over-represented in PV-IN-

1911   enriched proteins (**Fig 2C, Supp Fig S4**). In contrast, cellular metabolism, fatty acid oxidation,

1912   NAD binding, lipid metabolism, proteasome complex, ER-phagosome and mitochondrial terms

1913   were over-represented in the Camk2a-CIBOP-enriched proteome (**Fig 2C, Supp Fig S4**).

1914   Upstream analyses identified potential microRNA (miRNA) regulators of PV-INs and Camk2a

1915   neurons, including enrichment of microRNAs 133a and 133b targets in the PV-IN proteome (**Supp**

1916   **Fig S4**), in agreement with prior miRNA tagging and affinity purification (miRAP)[157] studies that

1917   identified miRNAs 133a and 133b as highly expressed in PV-INs. Two microRNAs recently

1918   identified as predictors of cognitive decline in humans (miR-29a and miR-132), were also

1919   predicted to specifically regulate PV-IN proteomic signatures[267]. These analyses suggest that

1920   molecular signatures that define PV-INs may be regulated by distinct sets of miRNAs, some of

1921   which have known associations with cognitive decline in humans.

1922   To identify neurodegeneration-relevant proteins in PV-INs, we cross-referenced PV-IN and

1923   Camk2a CIBOP proteomic markers with neurodegeneration-associated risk genes from Multi-

1924   marker Analysis of GenoMic Annotation (MAGMA) analyses (**Fig 2D, Supp Datasheet 2**)[268,269].

1925   We identified 60 PV-IN AD-risk proteins related to synaptic vesicle fusion, docking and recycling

1926   (Bin1, Picalm, Dnm2, Ap1g1, Ap2a2, Sgip1), cytoskeleton and microtubules (Ank1, Actb,

1927   Tubb2a, Mapt), mitochondria (Mtch2, Ndufs3, Ndufb9, Slc25a11), and SNARE complex (Syn2,

1928   Stx1b, Vamp1, Nsf, Stxb1) (**Fig 2E**). In comparison, 24 Camk2a neuron-enriched AD-risk proteins

1929   including oxidoreductases (Sdhb, Idh2, Aldh5a1, Etfb and Acadl), serine/threonine kinase Akt3

1930   and TAR DNA binding protein (Tardbp). We also leveraged data from recent protein-wide

1931   association studies of post-mortem human brains from participants in the Religious Orders Study

1932   and the Rush Memory and Aging Project (ROSMAP) longitudinal study in which proteins

1933   positively-correlated (n=645 pro-resilience proteins) and negatively-correlated (n=575 anti-

1934   resilience proteins) with cognitive slope were identified[146,155]. As compared to the Camk2a-CIBOP

1935   proteome, the PV-IN proteome was significantly enriched in pro-resilience proteins in the PV-IN

1936   proteome, including complexins (Cplx1, Cplx2), Ank1, highly-abundant PV-IN proteins (*e.g.,*

1937   Aak1, Cttn, Bin1, Elfn1, Bsn) as well as ribosomal, mitochondrial, GTP binding, synaptic
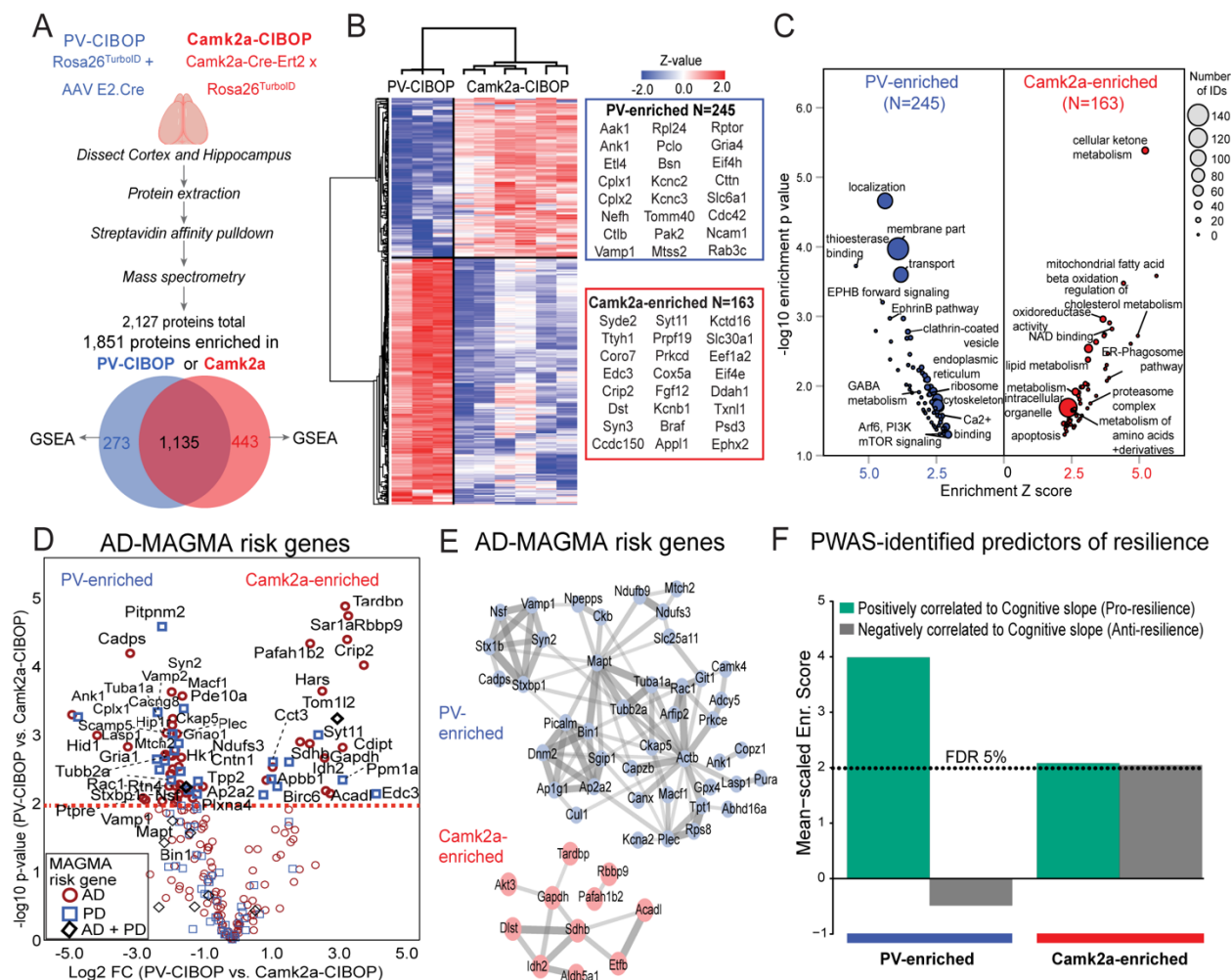
Figure 2. Distinct proteomic signatures and disease vulnerabilities of PV-INs and Camk2a excitatory neurons revealed by CIBOP.

A. Experimental outline for comparative analysis of CIBOP-based proteomics of PV-INs and Camk2a excitatory neurons from the mouse cortex. Camk2a-CIBOP was achieved by tamoxifen-inducible Cre-mediated TurboID expression in Camk2a-Cre-ert2/Rosa26TurboID mice (n=6). PV-IN CIBOP was achieved by E2 enhancer AAV-mediated Cre expression (n=3), as shown in Figure 1. Non-CIBOP negative controls (n=2 per genotype) were also included. Biotinylated proteins from the cortex of Camk2a-CIBOP and PV-CIBOP as well as control mice were enriched by streptavidin pulldown, followed by label-free quantitation MS analyses. 1,841 proteins were quantified above negative samples in either PV-INs or Camk2a neurons.

B. DEA comparing PV-CIBOP and Camk2a-CIBOP proteomes identified proteins with at least 3-fold differential enrichment (signature proteins of each neuronal class), which were then hierarchically clustered. Top proteins (based on fold-change) are shown alongside the heatmap.

C. GSEA of PV-IN (right, blue) and Camk2a (left, red) signature proteins identified over-represented terms (GO, KEGG, Wikipathways, Reactome, Pathway commons) for PV-IN and Camk2a neurons. X-axis represents enrichment Z score for a given term, and Y-axis represents level of statistical significance of enrichment. Size of each data point indicates number of protein IDs in that enrichment term.

D. Volcano plot representation of PV-IN and Camk2a neuron signature proteins which have known genetic risk associations in Alzheimer's disease (AD) and Parkinson's disease (PD) based on MAGMA. Some proteins have shared genetic risk associations with AD and PD.

E. Protein-protein interaction network (STRING) of AD-associated MAGMA risk genes that showed differential enrichment in PV-INs (Top) and in Camk2a neurons (Bottom). Clusters of mitochondrial, synaptic vesicle and endocytosis related proteins were revealed in PV-IN AD MAGMA risk genes.

F. Enrichment of PWAS-identified proteins associated with cognitive slope in PV-enriched and Camk2a-enriched proteomic signatures. Cognitive slope was estimated in ROSMAP cases. Positive slope indicates cognitive stability or resilience while a negative slope indicates cognitive decline. Proteins positively correlated with cognitive slope are referred to as pro-resilience proteins while those negative correlated with cognitive slope are anti-resilience proteins. Enrichment of pro-resilience and anti-resilience proteins in PV-enriched and Camk2a-enriched proteins identified by CIBOP was assessed after weighting based on strength of association between proteins and cognitive slope. FDR 5% threshold is shown.

Also see Supplemental Figure S4 and Supplemental Datasheet 2 for related analyses and datasets.

1939   compartment and vesicle fusion proteins (**Fig 2F**). Our unbiased evaluation PV-IN proteomes, in

1940   contrast to Camk2a neurons, reveal a generalized molecular phenotype showing high translational,

1941   synaptic vesicle transport and fusion (neurotransmission), GTP binding and signaling (Akt/mTOR)

1942   activities, including many AD-related genetic risk factors and proteins associated with cognitive

1943   resilience.

1944

1945

1946   *Network analyses of human post-mortem brain proteomes identify unique associations of PV-IN*

1947   *markers with neuropathology and cognitive dysfunction in AD*

1948   Evidence for unique vulnerability of PV-INs to neurodegenerative disease pathology in AD

1949   may be revealed by analyses of bulk brain proteomes. We interrogated published human post-

1950   mortem bulk brain proteomic studies[156,270-278] which included >500 post-mortem dorsolateral pre-

1951   frontal cortex samples (non-disease controls, Asymptomatic AD, and AD with dementia cases)

1952   from the ROSMAP and Banner Sun Health cohorts[277,278]. Over 8,000 proteins were quantified that

1953   coalesced into 44 modules[128], each with unique correlations to amyloid burden (CERAD),

1954   neurofibrillary tangles (Braak stage), and cognitive function (MMSE or global cognitive function)

1955   (**Fig 3A**)[156,278]. We used the Allen brain atlas of scRNAseq signatures and annotated 1,040 genes

1956   with ≥4-fold enrichment in specific neuronal classes (glutamatergic pyramidal neurons and

1957   GABAergic neurons including PV, Sst, VIP subtypes) (**Supp Datasheet 3**). Pan-

1958   excitatory/glutamatergic proteins (Camk2a, Slc17a7) were enriched in modules M1, M5, M22,

1959   M10 and M4. Pan-inhibitory proteins (Gad1-2, Slc32a1) were enriched in modules M33 and M23.

1960   Among the inhibitory neuron modules, M33 showed enrichment in PV-IN proteins, including

1961   PVALB and KCNC2 [Kv3.2]), while VIP interneuron markers were enriched in M23 (**Fig 3B**).

1962 Therefore, M1 (as well as M22, M5, M10 and M4) is enriched in cellular mechanisms of AD in

1963 excitatory neurons, while M33 represents AD patho-mechanisms impacting PV-INs. Both pan-

1964 excitatory M1 and PV-IN M33 module abundances were lower in AD cases (**Fig 3C, D**) and were

1965 associated with cognitive function (MMSE and global cognitive function) at last clinical visit prior

1966 to   death,   and   negatively   associated   with
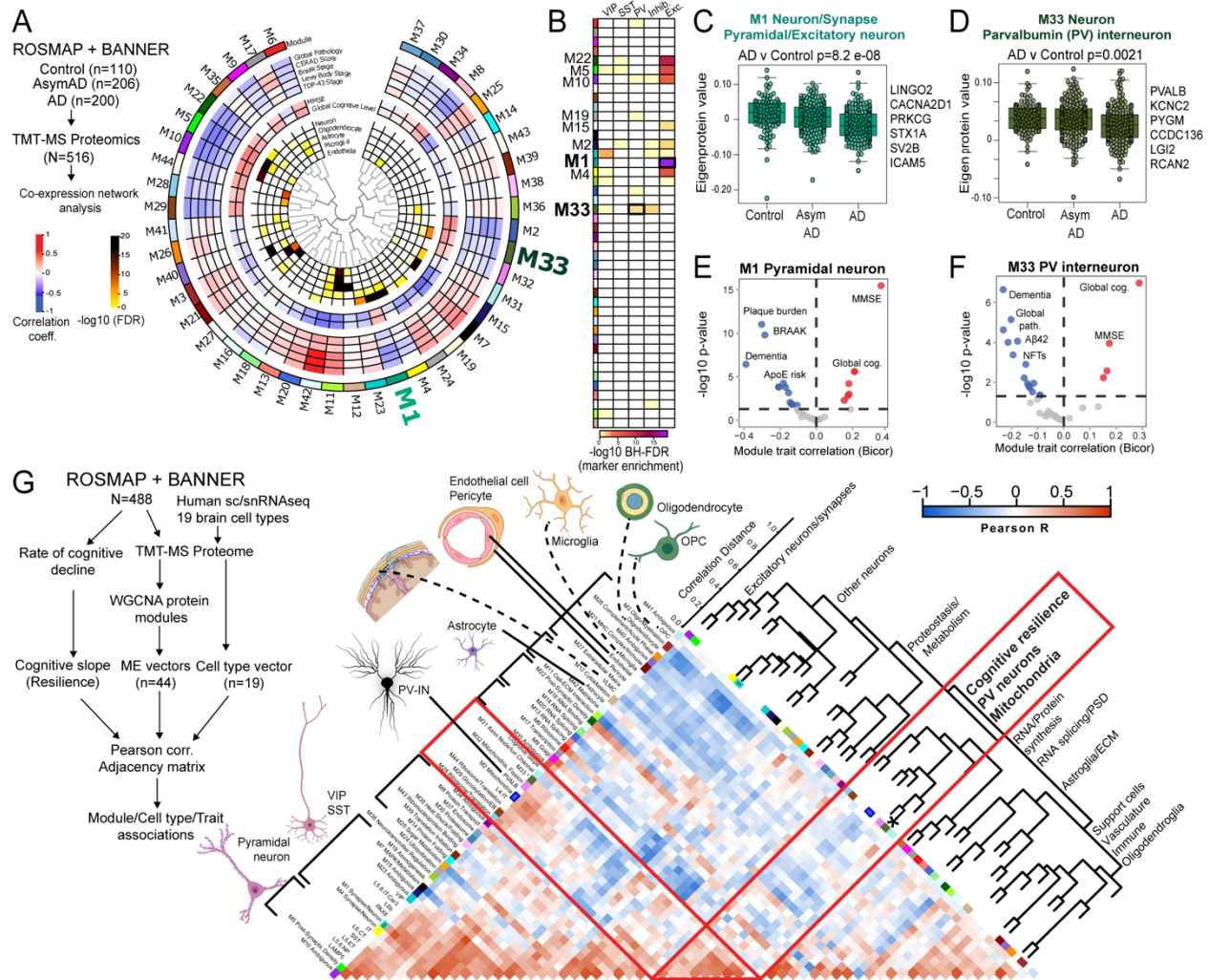
1967

Figure 3. PV-IN molecular signatures are associated with neuropathological traits and cognitive resilience in analyses of bulk human post-mortem brain proteomes.
A. Summary of network-based analysis of human bulk brain proteomes derived from post-mortem frontal cortex samples from controls, AsymAD and AD cases, from ROSMAP and BANNER cohorts (adapted from Johnson et. al.)[1]. Protein co-expression modules (M1-42) are arranged in a circular manner and the central dendrogram indicates module inter-relatedness. Module trait associations are arranged in layers. Inner ring indicates associations with cell type signatures and cell type-enrichment statistical

significance (-log10 FDR) are color coded. The next ring shows module-cognitive trait associations (MMSE and Global cognitive level. The third layer includes module-neuropathological trait associations (red and blue indicating positive and negative correlations). Two neuron-enriched modules of particular interest to this analysis (M1 and M33) are highlighted.
B. Modules that showed over-representation of markers of distinct classes of neurons (pan-excitatory, pan-inhibitory and 3 cardinal IN classes, namely PV-IN, SST-IN and VIP-IN) are shown as a heatmap. Color indicates level of statistical significance of enrichment. M1 was enriched in pan-excitatory neuronal markers,

M33 was enriched in PV-IN markers and M23 was enriched in VIP-IN markers.

C, D. Comparisons of module abundances (eigenprotein value) of M1 (C, pan-excitatory neuronal module) and M33 (D, PV-IN module) across controls, AsymAD and AD cases. Overall ANOVA p value is shown and top neuronal class-specific proteins representative of M1 and M33 are highlighted.

E, F. Volcano plot representations of Module-trait correlations (X-axis: Bicor, Y-axis: -log10 p-value of correlation) for M1 (E) and M33 (F). Top correlated traits (including ApoE genetic risk based on allelic combinations of ApoE ε2, 3 and 4) are labeled. See Supplemental Data x for more details.

G. Adjacency matrix analysis based on correlations between protein co-expression modules (ME vectors), Cell type abundance vectors (based on selected markers of 19 distinct brain cell types identified by sc/snRNAseq) and cognitive slope till time of death (Left: overall outline of the analytical plan). Right: Heatmap representation of Pearson's correlation-based adjacency matrix. Cell type vectors and module ME vectors with representative ontologies of each ME, are shown on the left of the heatmap. Dendrogram on the right indicates relatedness among ME vectors, cell type vectors and cognitive slope, and revealed a cluster of PV-IN module M33, PV-IN vector, mitochondrial module M2 and M32, and cognitive slope (see Supplemental Data x for additional details).

H, I. Associations of module eigenprotein (ME) (H) and cell type vectors (I) with cognitive slope for modules with highest positive correlations with cognitive slope. A higher cognitive slope indicates cognitive stability (or resilience) while a lower (negative) slope indicates faster cognitive decline over time. Color (reg, light blue and dark blue represent controls, AsymAD and AD cases respectively).

J. Module eigenprotein associations with cognitive slope (resiliency) after adjustment for neuropathological features. This shows that module M33, followed by excitatory neuron modules (M5, M10) and mitochondrial modules (M2) had the highest correlation with cognitive resilience.

See Supplemental Datasheet 3 for related analyses.

1968

1969   severity of dementia and neuropathology (both Aβ and tau) (**Fig 3E,F**) although APOE

1970   genetic risk was associated with M1, but not M33.

1971   We next assessed whether excitatory and inhibitory neuronal signatures in bulk brain

1972   proteomes, are associated with rate of cognitive decline (cognitive slope) in longitudinal studies

1973   of aging and AD[146,279](**Fig 3G-I**). Using consensus marker lists of cell types from reference human

1974   brain single cell/nuclear RNAseq studies, we applied single-sample GSEA (ssGSEA) to estimated

1975   vectors proportionate to abundances of 19 classes of excitatory and inhibitory neurons, glia and

1976   vascular cells, in proteomic data from 488 DLPFC post-mortem human DLPFC samples from

1977   ROSMAP/BANNER studies (**Fig 3G**)[1,7,152,154]. Eigenprotein abundances of each protein co-

1978   expression module (ME vectors) were also estimated. The associations between different cell type

1979   abundances, module eigenproteins and rate of cognitive decline were assessed using a correlation-

1980   based adjacency matrix. We found that the PV-IN cell type abundance, modules M33 (PV-IN), M2

1981   and M32 (mitochondria) as well as cognitive slope (cognitive resiliency) were highly inter-

1982   correlated in one cluster (**Fig 3G**). In addition to PV-INs, the layer 4 IT neuronal vector was also

1983   positively correlated with cognitive slope (**Fig 3H, I**). The abundances of these two cell types are

1984   therefore mostly strongly linked to cognitive resilience. In contrast, excitatory pyramidal neurons

1985   such as layer 5/6 IT and CT neurons, were weaker correlates of cognitive trajectory. Furthermore,

1986   the association between PV-IN module M33 and cognitive resilience remained significant after

1987   adjusting for several co-existent neuropathologies (including amyloid, tau, synuclein) (**Fig 3J**)[146].

1988   Overall, these analyses demonstrate the ability of bulk brain proteomic network analysis to

1989   indirectly resolve AD mechanisms at the level of individual neuronal classes, and support the idea

1990   that integrity of PV-INs and/or their proteins, may be determinants of cognitive resilience in AD.

1991

1992   *Neuron-specific molecular signatures resolve vulnerability of PV neurons to progressive Aβ*

1993   *pathology in a mouse model*

1994   Human post-mortem brain proteomic studies have limited ability to resolve the impact of

1995   aging and disease progression on neuronal protein changes in AD because sampling is performed

1996   post-mortem. Thus, we examined bulk brain proteomes from a mouse model of Aβ pathology. We

1997   analyzed TMT-MS data from 43 WT and 43 5xFAD mice (age span 1.8-14.4 mo., 50% male, 50%

1998   female), from which over 8,500 proteins were quantified (**Fig 4A**). We report a sub-analysis of

1999   neuron-enriched markers from this proteomic dataset (**Fig 4A-C, Supp Datasheet 4**). As expected

2000   in 5xFAD mice, age-dependent increase in Aβ pathology was associated with concomitant increase

2001   in levels of Apoe, microglial proteins (Trem2, Msn, C1qb) and astrocyte proteins (Gfap) (**Fig 4A**).

2002   Using canonical markers of different neuronal classes from mouse scRNAseq reference datasets,

2003   we identified distinct patterns of change of neuronal proteins with aging and genotype (5xFAD vs

2004   WT), as well as biological interaction between aging and genotype. Excitatory neuronal proteins

2005   (Camk2a, Slc17a7) showed an age-dependent decrease, although genotype had no effect on this

2006   process. In contrast, Pvalb and Sst proteins (found in PV-INs and SST GABAergic INs,

respectively) increased with age in WT mice, but this trend was significantly blunted by 5xFAD genotype, particularly at 6 months of age (**Fig 4B**). Kcnc3, which encodes a Kv3 channel highly expressed by PV-INs, showed an age-dependent decrease in 5xFAD mice while Vip, a marker of VIP-positive INs, did not show changes related to either age or genotype. We also observed a strong positive correlation between PV-IN proteins (Pvalb and Kcnc3) and myelin proteins (Plp1 and Mbp) (**Fig 4A**) consistent with cell-cell interactions between PV-INs and oligodendrocytes[280].

Using lists of markers highly expressed in excitatory or inhibitory neurons, as well as in PV-INs, SST-INs and VIP-INs from single neuronal RNAseq datasets (**Supp Datasheet 4**)[266] which were also identified at the protein level in our proteomic dataset, we calculated composite cell-type-specific abundance scores to identify age and genotype (5xFAD vs. WT) effects in the bulk proteomic data (**Fig 4C**). When grouped, composite excitatory markers decreased with aging, and were minimally higher in abundance in 5xFAD brains as compared to WT, regardless of age. Inhibitory composite markers also showed an age-dependent decrease in abundance which became more pronounced in 5xFAD mice. Among major IN classes, PV-IN markers showed a gradual increase with age in WT mice, although this was suppressed in 5xFAD brain (**Fig 4B**). In contrast, SST-IN and VIP-IN markers were unaffected by genotype (**Fig 4C**).

To determine whether PV-IN protein changes in 3-6 month-old 5xFAD mice are related to changes in PV-IN cell numbers[281], we performed IHC studies on an independent set of 3 and 6 month-old WT (n=7-8) and 5xFAD (n=7-8) brains, and assessed Pvalb protein levels along with detection of peri-neuronal nets (PNNs) by Wisteria floribunda agglutinin (WFA) in the cortex and subiculum (**Fig 4D-G**). PNNs are known to disproportionately encapsulate PV-INs in the brain and are key regulators of PV-IN excitability[282-284]. The number of Pvalb protein-positive neurons in the cortex and subiculum were not impacted by genotype (5xFAD vs WT) at 3 or 6 months of

2030   age (**Fig 4D, E, Supp Fig S5**) although the proportion of PNN-positive PV-INs was significantly

2031   lower in 5xFAD mice (**Fig 4G**).

2032   Overall, our analyses of mouse brain proteomic data identify novel age and Aβ-dependent

2033   changes that appear to differentially impact neuronal sub-classes, where PV-INs may be selectively

2034   vulnerable in early stages of pathology in 5xFAD mice[41]. Our histological studies suggest that

2035   observed proteomic changes in PV-IN proteins in 5xFAD brain is not explained by changes in the

2036   abundance of PV-INs[285] although the health of PV-INs may be perturbed, as indicated by loss of

2037   PNNs around PV-INs in early stages of Aβ pathology. To better understand the molecular basis for

2038   differential vulnerability of PV-INs to AD pathology with spatiotemporal resolution, neuron class-

2039   specific native state proteomic investigations using CIBOP are warranted.

2040

2041   *Unique molecular signatures of PV-IN proteome in early stages of Aβ pathology in vivo*

2042   To identify molecular events specifically occurring in PV-INs as a result of early AD

2043   pathology, we applied the PV-CIBOP strategy to achieve PV-IN-specific TurboID expression,

2044   biotinylation and fluorescent labeling in WT and 5xFAD mice (**Fig 5A**). Three weeks after RO

2045   AAV injection and 2 weeks of biotinylation, mice were euthanized at 3 months of age. This early

2046   stage of Aβ pathology (i.e., significant Aβ burden but prior to plaque formation) was chosen

2047   capture potentially-modifiable disease mechanisms. IHC confirmed PV-IN-specific biotinylation

2048   in the cortex of WT and 5xFAD PV-CIBOP mice (**Fig 5B**). Flow cytometry of enzymatically-

2049   dissociated cortex[136] confirmed equal efficiency of PV-IN targeting across all groups (**Fig 5C**).

2050   Consistent with early stage of pathology, we observed minimal extracellular Aβ plaque pathology

2051   in the subiculum and cortex of 5xFAD mice, while total Aβ42 levels measured by ELISA were

2052   substantially increased in 3 month-old 5xFAD mice (**Fig 5D**). WBs of cortical lysates showed
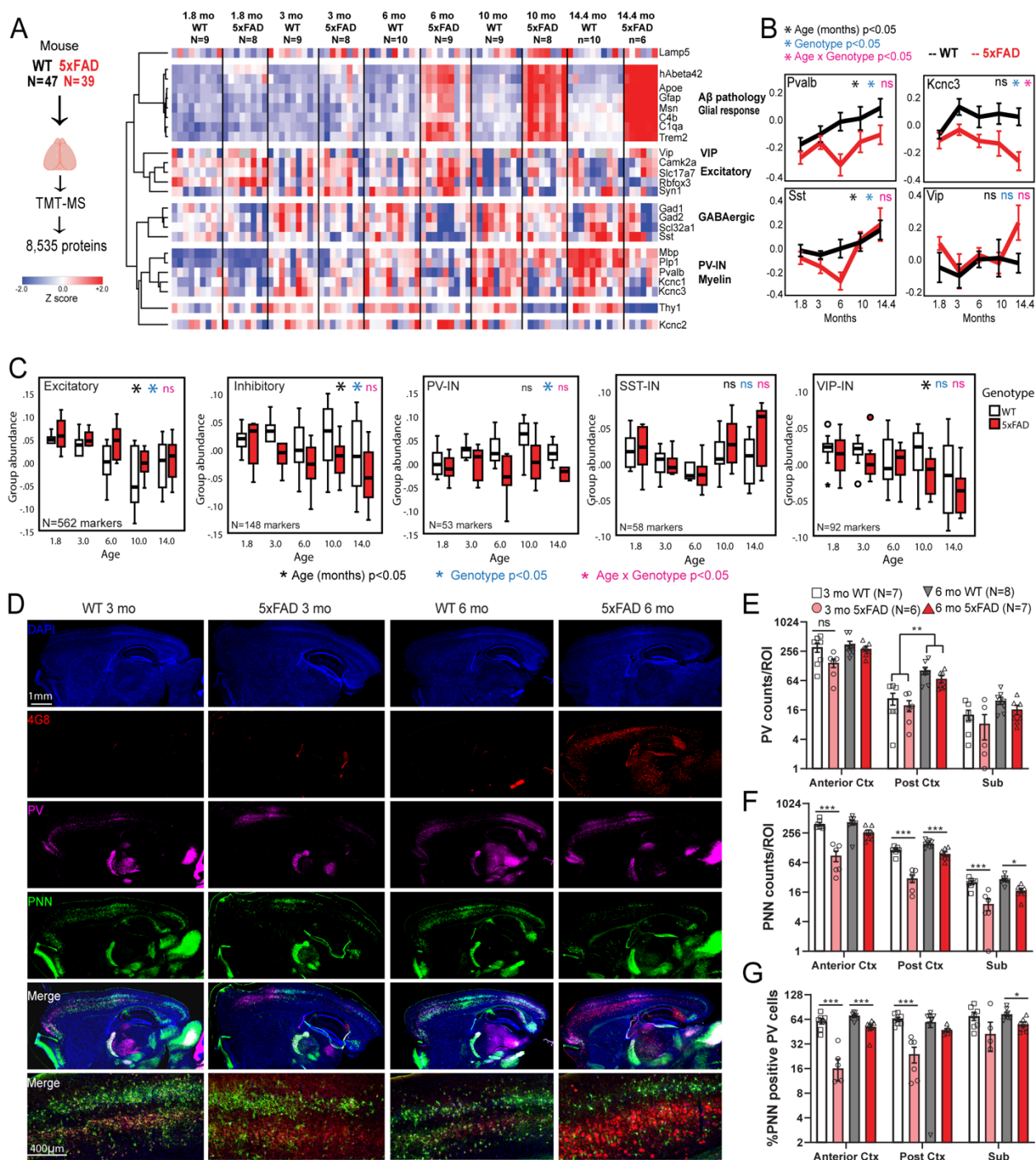
Figure 4. Bulk tissue proteomics of mouse brain reveals differential effects of Aβ pathology and aging on PV-INs and their peri-neuronal nets

A. Study outline for analysis of mouse bulk brain (cortex) TMT-MS proteomics data. 8,535 proteins were quantified by TMT-MS from 43 WT and 43 5xFAD mouse brains (including age ranges 1.8-14 months and 1:1 sex-distribution). From these, selected proteins reflective of Aβ pathology (hAβ42 peptide), resultant glial activation (Apoe, C1qa, C4b, Gfap, Trem2, Msn) and markers of excitatory and inhibitory neuronal subclasses (based on curated lists obtained from sc/snRNAseq mouse brain studies), were visualized as a heatmap

after hierarchical clustering based on protein IDs.
B. Trajectories of change in levels of PV-IN proteins (Pvalb, Kcnc3), SST-IN (Sst) and VIP-IN (Vip) based on age and genotype. Error bars represent SEM. Statistical tests included linear regression analyses including age, genotype and 'age x genotype' interaction terms as covariates. Levels of significance of each are indicated.
C. Trajectories of change in overall levels of pan-excitatory, pan-inhibitory, as well as PV-IN, SST-IN, and VIP-IN proteins, based on age and genotype. We used lists of transcriptomic markers of these classes of neurons (from sc/snRNAseq datasets) that were at

least 4-fold enriched in the class of interest over all other neuronal types. After normalizing and z-transforming proteomic data, neuronal class-based group abundance scores were calculated and compared across ages and genotypes. Linear regression analyses were performed using age, genotype, and age x genotype interaction term as covariates. Levels of significance of each, are indicated.

D. Representative images from immunofluorescence microscopy studies of mouse brain (sagittal sections, WT and 5xFAD, ages 3 and 6 months, animals used for TMT-MS studies in A), to detect PV-INs (Pvalb protein), perineuronal nets (using WFA lectin), Aβ pathology (4G8) and DAPI. 4x tiled images and 20x images from cortex are shown.

E, F, G. Quantitative analysis of Pvalb protein, PNNs, and proportion of Pvalb+ INs that have PNNs in the cortex (anterior and posterior to bregma) and subiculum of WT and 5xFAD mice are 3 and 6 mo (post-hoc Tukey pairwise comparisons were performed). Y axes are log2 transformed. Error bars represent SEM (Post-hoc Tukey HSD *p<0.05, **p<0.01, ***p<0.005).

See Supplemental Figure S5 and Supplemental datasheet 4 for related analyses.

2055

2056 robust biotinylation and V5 protein signals in all PV-CIBOP mice (**Fig 5E**). WB of SA-enriched

2057 samples showed enrichment of biotinylated proteins in PV-CIBOP animals compared to controls,

2058 regardless of 5xFAD or WT genotype (**Fig 5F, Supp Fig S6A**).

2059 LFQ-MS of bulk brain samples (inputs) and SA-enriched (i.e., PV-specific) samples

2060 quantified 3,086 proteins and 2,149 proteins respectively (**Supp Datasheet 5**). PCA of bulk

2061 proteomes indicated minimal effects of biotinylation on the overall brain proteome (**Supp Fig 6B**).

2062 1,973 proteins were enriched in the PV-IN proteome from both WT and 5xFAD PV-CIBOP groups

2063 as compared to negative control SA-enriched proteomes. Top PV-IN enriched proteins identified

2064 in WT/PV-CIBOP tissues in this experiment agreed with findings in the first PV-CIBOP run (**Supp**

2065 **Fig 6C**). PCA of SA-enriched proteomes resolved differences between negative control and PV-

2066 CIBOP proteomes, and revealed further distinction between PV-CIBOP proteomes from WT and

2067 5xFAD mice (**Fig 5G**). Thus, we next contrasted the PV-CIBOP proteomes from Turbo-expressing

2068 WT and 5xFAD mice and identified 248 differentially enriched proteins (DEPs) in PV-INs (134

2069 increased and 114 decreased in 5xFAD, unadjusted p-value <0.05, **Fig 5H, Supp Datasheet 5**).
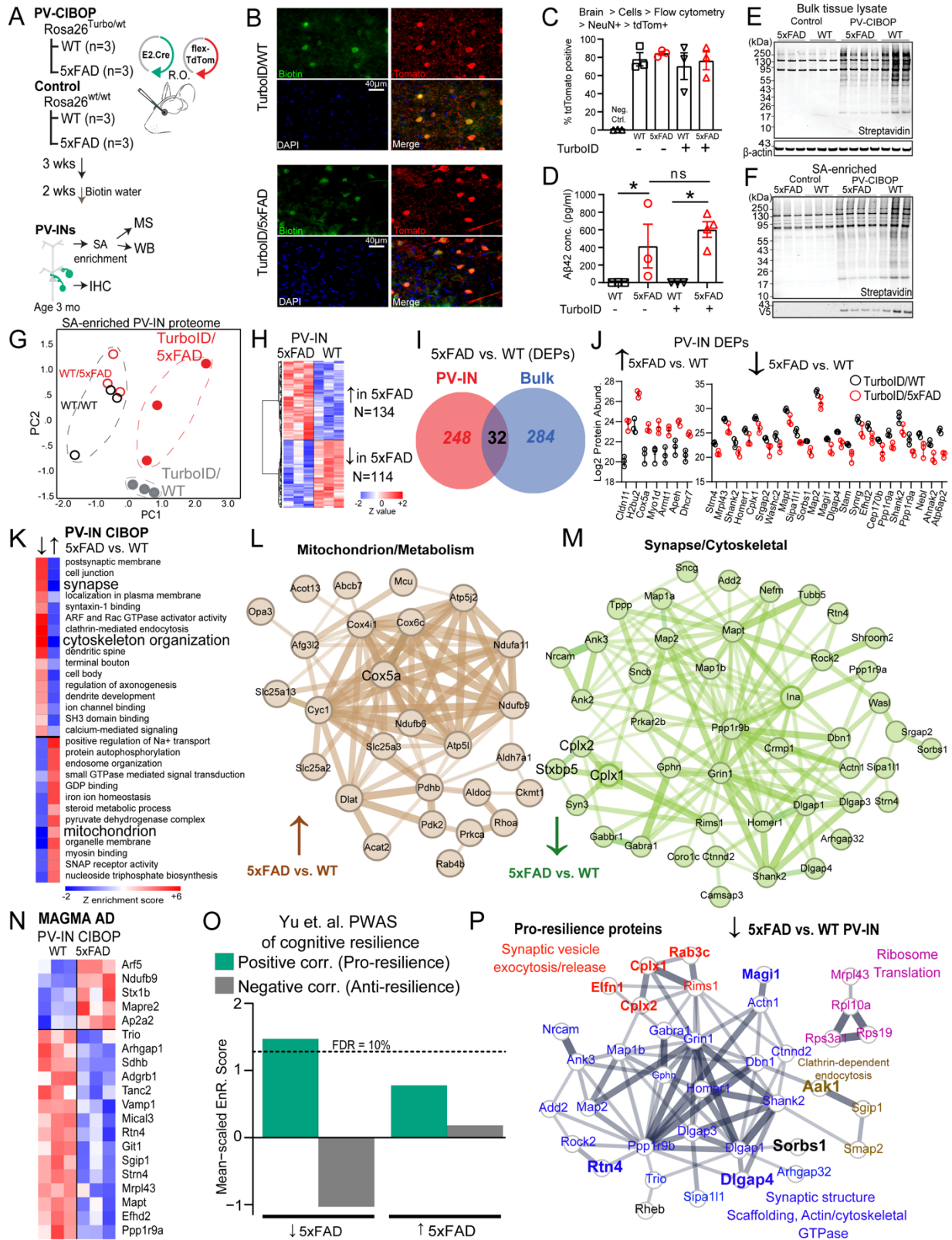
Figure 5. PV-IN proteomic alterations in early stages of Aβ pathology in the 5xFAD model.

A. Experimental outline: PV-IN CIBOP was achieved via co-injection (R.O.) of E2.Cre + flex-TdTomato AAVs into TurboID mice with either WT or 5xFAD genotypes. Non-CIBOP controls involved AAV co-injected non-TurboID mice (WT and 5xFAD). Mice were euthanized at age 3 months after Cre-mediated recombination and biotinylation. Tissues were used for biochemical studies (WB + MS) and IHC.

B. IHC studies confirming PV-IN specific biotinylation in both WT and 5xFAD PV-CIBOP mice. In the cortex, majority of PV-INs (based on Pvalb immunoreactivity) were biotinylated (streptavidin) and/or expressing TdTomato.

C. Flow cytometry analyses comparing AAV-mediated targeting efficiency of PV-INs across experimental animals. Following enzymatic digestion of cortical slices, single cell suspensions were fixed, permeabilized and labeled for live/dead indicator and NeuN. Single and live cells were further sub-gated based on NeuN positivity and proportion of tdTomato+ neurons were quantified and compared across groups. One-way ANOVA across all AAV injected groups was not significant.

D. Aβ42 ELISA measurements (pg/mL/mg protein) from bulk brain (cortex) homogenates from all mice studied in this experiment, confirming that total Aβ42 levels were not impacted by TurboID-biotinylation status (*p<0.05, unpaired two-tailed T-test).

brain proteomes were observed. In SA-enriched proteomes (Right), all PV-IN proteomes clustered away from control samples, and further distinction was observed between 5xFAD and WT PV-IN proteomes.

E,F. WB from bulk cortical tissue lysates as well as from SA-enriched (pulldown) biotilylated fractions from all experimental mice. As compared to minimal biotinylation in control (WT and 5xFAD) mice, robust biotinylation was observed in all PV-CIBOP tissues (top). SA-enriched proteins were probed with streptavidin to confirm enrichment of biotinylated proteins in all PV-CIBOP animals. Inputs and SA-enriched proteins were analyzed by LFQ-MS.

G. PCA of bulk brain proteomes (inputs, Left) and of SA-enriched PV-IN proteomes (Right). In the inputs, minimal-to-no effects of biotinylation on bulk.

H. Heatmap representation of DEPs comparing WT/PV-CIBOP and 5xFAD/PV-CIBOP SA-enriched proteins.

I. DEPs identified comparing 5xFAD and WT SA-enriched PV-IN proteomes minimally overlapped with DEPs identified in the bulk brain proteomes. Within the shared 32 DEPs, concordant directions of change were limited to x proteins.

J. Top DEPs (showing at least 4-fold differential enrichment) comparing 5xFAD to WT PV-IN proteomes are shown.

K. GSEA of DEPs comparing 5xFAD to WT PV-IN proteomes (panel G) identified clear differences based on ontology terms. While cytoskeletal, synaptic/dendritic, and synaptic signaling related proteins were decreased, mitochondrial, oxphos and steroid metabolism terms were increased in 5xFAD PV-INs compared to WT PV-INs.

L, M. STRING protein-protein-interactions (PPI) within DEPs identified in Mitochondrial (L, increased in 5xFAD PV-IN) and Synaptic/Dendritic/Cytoskeletal (M, Decreased in 5xFAD PV-IN) ontologies. Thickness of edges indicate strength of known functional or physical interactions.

N. Heatmap representation of DEPs comparing 5xFAD to WT PV-IN proteomes, limited to proteins encoded by genes with known genetic risk associations in AD (AD-MAGMA).

O. Analysis of enrichment of PWAS-identified proteins within DEPs (5xFAD vs. WT PV-IN proteomes) associated with cognitive resilience in PV-enriched and Camk2a-enriched proteomic signatures (as in Fig 3, pro-resilience proteins are positively correlated with cognitive slope; and anti-resilience proteins are negatively associated with cognitive slope in the ROSMAP cohort). Enrichment of pro-resilience and anti-resilience proteins in PV-IN proteomes, comparing 5xFAD vs. WT PV-INs was assessed after weighting based on strength of association between proteins and cognitive slope. FDR 10% threshold is shown.

P. STRING PPIs of PWAS-nominated proteins positively associated with cognitive resilience (pro-resilience) that are decreased in 5xFAD PV-INs based on PV-CIBOP studies. Colors of proteins are based on shared functions and/or ontologies. Of these, proteins that are also selectively enriched in PV-INs as compared to Camk2a neurons (from CIBOP studies in Fig 3) are highlighted (larger font, and bold).

See Supplemental Figure S6 and Supplemental Datasheet 5 for related analyses.

2071 To establish whether PV-INs display unique cell-type-specific vulnerabilities in response to early

2072 Aβ pathology, we compared DEPs (5xFAD vs. WT) from PV-INs with those identified from the

2073 bulk proteome. Surprisingly, very little overlap was observed between DEPs in PV-INs and those

2074 found in the bulk proteome (**Fig 5I, Supp Datasheet 5**). Only 32 DEPs in the bulk tissue were

2075 identified as DEPs in the SA-enriched PV-CIBOP proteomes, and these shared DEPs also showed

2076 poor concordance (**Supp Fig S6D**). Gene set variation analyses (GSVA) also identified 210

2077 ontologies differentially enriched in the PV-IN proteome in contrast with only 16 ontologies in the

2078 bulk proteome, within minimal agreement between PV-IN and bulk proteomic changes (**Supp**

2079 **Datasheet 5**). As an example of stark discordance between bulk and PV-IN proteomic changes,

2080   oxidative phosphorylation and aerobic respiration gene sets were increased in PV-INs but

2081   decreased in the bulk proteome (5xFAD vs. WT). In contrast, synaptic proteins were decreased in

2082   both bulk and PV-IN proteomes, but the magnitude of this decrease was larger in PV-INs compared

2083   to bulk proteomes (**Supplemental Datasheet 5**). Together, this indicates a lack of concordance

2084   between the effects of 5xFAD genotype on the bulk brain proteome and on PV-IN proteome,

2085   suggests unique metabolic/respiratory perturbations in PV-INs, that are masked in bulk tissue

2086   analyses.

2087   Among DEPs identified in the PV-IN proteome, top proteins showing at least 4-fold

2088   increase in 5xFAD PV-INs included Cox5a, Dhcr7 and Apeh (**Fig 5J**). Cox5a is a Complex IV

2089   mitochondrial protein involved in ATP synthesis[286]. Dhcr7 encodes 7-dehydrocholesterol

2090   reductase that catalyzes final rate limiting steps of cholesterol biosynthesis[287]. Apeh encodes

2091   acylaminoacyl-peptide hydrolase that hydrolyses terminal acetylated residues in small acetylated

2092   peptides, including degradation of monomeric and oligomeric Aβ[288]. Synaptic structural proteins

2093   including Shank2, Homer1, Map2 were conversely decreased by at least 4-fold in 5xFAD PV-INs

2094   (**Fig 5J**). GSEA of DEPs, as well as GSVA of proteins identified in PV-IN proteomes showed

2095   proteins involved in mitochondrial function, steroid biosynthesis, small GTPase signaling, and

2096   GDP binding were increased in 5xFAD PV neurons (**Fig 5K, L, Supplemental Datasheet 5**). In

2097   contrast, proteins associated with structural/cytoskeletal, synaptic, axonal and dendritic ontologies

2098   were generally decreased in 5xFAD PV-INs (**Fig 5K**). GSEA of bulk and PV-IN proteomes also

2099   verified 36 post-synaptic proteins (post-synapse GO:0098794) that showed decreased levels in

2100   5xFAD PV-INs, including structural constituents of the post-synapse (Dlgap1, Homer1, Gphn, Ina,

2101   Shank2, Git), enzymes with kinase activity or binding (Ppp1r9b, Bcr, Rtn4, Rheb, Prkar2b, Map2),

2102   neurotransmitter receptors (Grin1, Gabra1, Gabbr1), dendritic spine proteins (Grin1, Homer1,

2103   Dlgap3, Shank2, Dbn1, Bai1, Tanc2, Ncam1) and ribosomal subunits (Rps19, Rpl10a). Pre-

2104   synaptic proteins involved in synaptic vesicle fusion and exocytosis, including complexins (Cplx1,

2105   2 and 3), showed decreased levels in 5xFAD PV-INs (**Fig 5M**). Of note, Cplx1 and 2 (but not

2106   Cplx3) were more also abundant in PV-INs as compared to Camk2a neurons in our CIBOP studies

2107   (**Supp Fig S6**). Several MAGMA-identified AD genetic risk factors showed differential

2108   abundances in 5xFAD PV-INs as compared to WT PV-INs (*e.g.,* decreased- Ppp1r9a, Mapt, Git1;

2109   increased- Arf5, Ndufb9, Stx1b (**Fig 5N**).

2110   To predict whether changes in the PV-IN synaptic protein landscape would result in

2111   detrimental or protective consequences, we cross-referenced the 5xFAD vs. WT PV-IN DEP list

2112   against pro-resilience and anti-resilience proteins (**Supp Datasheet 5**). We found that pro-

2113   resilience proteins were over-represented while anti-resilience factors were under-represented in

2114   proteins that decreased in 5xFAD PV-INs (**Fig 5O**). The pro-resilience proteins which were

2115   decreased specifically in PV-INs in early 5xFAD pathology included synaptic structural, synaptic

2116   scaffolding, actin/cytoskeleton (Dlgap13/4, Shank2, Homer1, Dbn1, Map1b, Map2, Ank3),

2117   ribosome (Rpl10a, Rps19, Mrpl43), mTOR-C1 regulating protein (Rheb), clathrin-dependent

2118   endocytic (Aak1, Sgip1, Smap2) and synaptic vesicle fusion/exocytosis/release related proteins

2119   (Cplx1, Cplx2, Elfn1, Rab3c, Rims1) (**Fig 5P**). Many of these pro-resilience proteins that were

2120   decreased in 5xFAD PV-INs (*e.g.,* Cplx1, Cplx2, Elfn1, Rab3c, Rtn4, Dlgap4, Sorbs1, Magi1)

2121   were also highly enriched in PV-INs as compared to Camk2a neurons (**Fig 5P, Supp Fig S6E-F**),

2122   indicating that these changes in early AD pathology may indeed be specific to PV-INs.

2123   Overall, these mouse-human integrative analyses indicate that altered levels of PV-IN

2124   bouton and dendritic proteins at early stages of Aβ pathology may have detrimental synaptic

2125   effects, representing a proteomic signature of decreased cognitive resilience in AD pathology.

2126 However, these changes may also represent an early homeostatic response more associated with

2127 resilience. Thus, we next aimed to understand the functional impact of these PV-specific synaptic

2128 proteomic alterations.

2129

2130 *Early Aβ pathology impacts PV-pyramidal cell neurotransmission and network activity*

2131 We leveraged the 'E2' enhancer to express optogenetic actuators in PV-INs (**Fig 6**, **Supp**

2132 **Fig S7)** to measure PV-specific neurotransmission properties, where postsynaptic pyramidal cell

2133 recordings represent an integrated response to PV-specific, action potential-evoked

2134 neurotransmission. C1V1 (AAV.E2.C1V1) was injected in both WT and 5xFAD mice

2135 simultaneously with AAV.Camk2.YFP, which served to confirm accurate viral targeting (**Fig 6A**).

2136 Acute slices were taken from two separate age cohorts (~2 or ~3 months old, 7 or 14 weeks

2137 respectively) and voltage clamp recordings were obtained from postsynaptic L5 pyramidal neurons

2138 (**Fig 6B**). Short (~0.2 ms) LED-light pulses (590 nm) reliably evoked IPSCs every trial (0.1 Hz

2139 inter-trial interval) in both WT and 5xFAD recordings with minimal temporal jitter. The amplitude

2140 of the first IPSC amplitude was unchanged in both 2- and 3-month-old 5xFAD mice *(e.g.,* 2-month-

2141 old WT: 133.5 ± 25.90 pA, n=10; 3-month-old 5xFAD: 163.7 ± 30.55 pA, n=7; p=0.46, unpaired

2142 t-test), suggesting that $GABA_A$ receptor availability was similar in the postsynaptic pyramidal

2143 cells. As several synaptic vesicle fusion/exocytosis/release related proteins (Cplx1, Cplx2, Stx1b,

2144 Elfn1, Rab3c, Rims1) were altered in our 5xFAD PV-IN proteome, we more closely evaluated

2145 presynaptic   properties
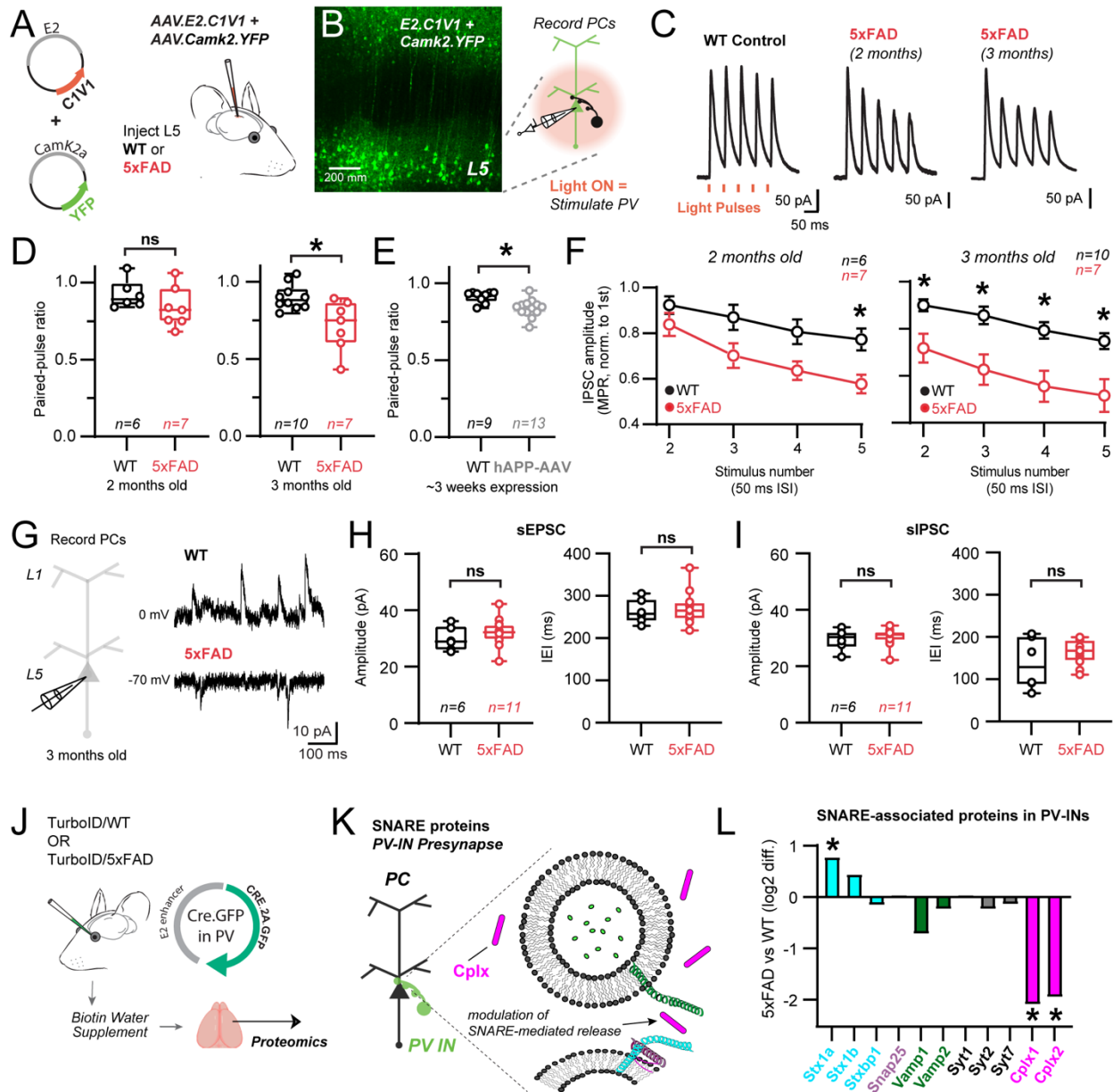
Figure 6. Progressive dysfunction of PV-pyramidal cell neurotransmission in young 5xFAD mice.

A. PV-INs were targeted for optogenetic activation in WT and 5xFAD mice using E2-driven AAV expression of C1V1 in S1 cortex. AAV.Camk2.YFP was also co-injected simultaneously as a volume label in these experiments.

B. 2-photon z-stack image showing successful targeting of L5 following ~1 week after stereotactic surgery. Pyramidal neuron somas and apical dendrites are evident. Patch clamp cartoon depicts the experimental workflow to stimulate PV interneurons and record their synaptic properties in post-synaptic pyramidal cells.

C. Examples of averaged voltage clamp traces from postsynaptic WT and 5xFAD pyramidal cells in layer 5 in response to short amber light pulses. PV-IN IPSCs are shown as time-locked to amber light pulses in a 20 Hz train.

D. Quantification of paired-pulse ratios of C1V1-evoked IPSCs in pyramidal cell recordings for 2- and 3-month-old WT and 5xFAD mice (ns signifies p>0.05, unpaired two-tailed T-test) (*p<0.05, unpaired two-tailed T-test).

E. Quantification of paired-pulse ratios of ChETA-evoked IPSCs in pyramidal cell recordings ~3 weeks following hAPP-AAV injections in L5 cortex (*p<0.05, unpaired two-tailed T-test).

F. Quantification of changes in PV inhibitory synapse dynamics as measured via multiple pulse ratio (MPR) in both 2- and 3-month-old WT and 5xFAD mice. (*p<0.05 Two-way ANOVA with Sidak's posthoc comparisons for each stimulus in WT and 5xFAD experiments).
G. Voltage clamp experiments were performed examining spontaneous synaptic activity in separate cohorts of 3-month-old WT and 5xFAD mice. The holding voltage was interleaved between -70 and 0 mV throughout recordings to resolve spontaneous EPSCs and IPSCs, respectively.

H. Quantification of spontaneous EPSC amplitude and frequency (ns signifies p>0.05, unpaired two-tailed T-test) in 3-month-old 5xFAD and WT mice. Each data point indicates an average value from all spontaneous events from individual recordings.
I. Quantification of spontaneous IPSC amplitude and frequency (ns signifies p>0.05, unpaired two-tailed T-test) in the same recordings as in (H). Data points indicate an average value from all spontaneous events from individual recordings.
See Supplemental Figure S7 for related analyses.

2147 (i.e., release probability) of PV-pyramidal synapses.

2148   To examine whether modification of vesicle fusion and association proteins affected

2149 release probability and presynaptic dynamics at PV-pyramidal synapses, we measured the paired

2150 pulse ratio (PPR)[289] and multiple pulse ratio (MPR) of optogenetically-evoked IPSCs at 20 Hz

2151 (**Fig 6C**)[290,291]. Evaluation of the paired-pulse ratio showed modest depression (PPR ~0.9) in WT

2152 mice at both age timepoints. In 2 month old 5xFAD mice, no difference in PPR was observed (**Fig.**

2153 **6D**) although synaptic depression did intensify in 5xFAD mice during repetitive stimuli (MPR) at

2154 this age (**Fig. 6F**). However, in 3-month-old 5xFAD mice, an decrease in PPR emerged (**Fig. 6D**)

2155 and this more robust depression was now maintained throughout the stimulus train (**Fig. 6F**).

2156 Together these results show progressive presynaptic dysfunction in PV-pyramidal synapses

2157 following early Aβ pathology, likely due to changes in proteins regulating vesicular release

2158 probability (**Fig. 5**). Other mechanisms, such as proteins involved with vesicular docking and

2159 replenishment, axonal action potential signaling, and Ca^{2+} dynamics could also contribute. For

2160 example, changes in presynaptic parvalbumin expression may affect short-term plasticity and

2161 release probability[292]. However, we did not observe a change in bulk parvalbumin protein by MS

2162 (**Fig 4B**) or IHC (**Supp Fig S5**) at 3 months of age.

2163   We next asked whether the signature of synaptic dysfunction observed in 5xFAD mice

2164 could be recapitulated in an independent model of APP/Aβ pathology. We packaged the human

2165 APP gene (variant NM_000484.4) into an AAV (AAV.Ef1a.hAPP). This particular APP isoform

2166 was chosen as it has been shown to proportionally increase with aging and is associated with

2167 increased AD risk[54,55]. 5-11 week old PV-Cre mice were co-injected with hAPP-AAV and

2168 AAV.DIO.CAG.ChETA for PV-specific optogenetic control **Supp Fig S7A**. Control mice only

2169 received AAV.DIO.CAG.ChETA with saline. After 2-3 weeks expression, voltage clamp

2170 recordings were obtained from postsynaptic pyramidal neurons. Brief (~4 ms) LED-light pulses

2171 (470 nm) could reliably evoke IPSCs on every trial (0.1 Hz inter-trial interval) in both control and

2172 hAPP-AAV groups, with minimal temporal jitter **Supp Fig S7B,C**. Similar to 3-month-old 5xFAD

2173 mice, the amplitude of the first PV-PC IPSC was unchanged after hAPP expression (Control: 68.18

2174 $\pm$ 38.37 pA, n=9; hAPP-AAV: 72.70 $\pm$ 44.49 pA, n=13; p = 0.82, unpaired t-test). Optogenetic

2175 stimulation with ChETA also showed modest PV-pyramidal synaptic depression in controls (**Fig.**

2176 **6D vs 6E**). However, similar to 5xFAD, synaptic depression measured via PPR and MPR was

2177 enhanced following adult-onset hAPP-AAV expression (**Fig. 6E**; **Supp Fig S7D**). Together these

2178 results complement our findings in 5xFAD mice, highlighting the early emergence of presynaptic

2179 dysfunction at PV-pyramidal synapses following early Aβ pathology.

2180 Alterations in release probability and other presynaptic dysfunction in PV-INs are expected

2181 to affect basal network excitability by disrupting excitatory/inhibitory balance. Thus, we next

2182 examined whether changes in the amplitude and frequency of spontaneous EPSCs and IPSCs were

2183 apparent in pyramidal cell recordings from 3 month old 5xFAD mice (**Fig. 6G**). Interestingly, no

2184 changes were observed in either the amplitude or frequency of excitatory and inhibitory

2185 spontaneous synaptic events (**Fig. 6 H, I**). This overall lack of network effect echoes recent work

2186 from 3-month-old 5xFAD mice in the hippocampus, where local circuit behavior and oscillations

2187 were also largely resilient to change[293]. The extensive cell-type-specific proteomic alterations we

2188 observed in PV-CIBOP and bulk proteomes thus may be reflective of early homeostatic responses

2189   to maintain overall circuit functionality, which should necessarily induce some degree of metabolic

2190   stress[160]. Therefore, we next sought to explore the extent of changes to mitochondrial proteins and

2191   associated metabolic pathways specifically in PV-INs in early stages of Aβ pathology.

2192

2193   *Evidence for extensive mitochondrial protein changes in PV-INs in response to early Aβ pathology*

2194   Of 300 mitochondrial proteins (MitoCarta 3.0) biotinylated in PV-INs[294], 30 proteins were

2195   increased (*e.g.,* Cox5a, Mpst, Ndufa11, Ckmt1) and 4 proteins that were decreased (Mrpl43,

2196   Septin4, Sdhb, Bphl) in 5xFAD compared to WT PV-IN proteomes (**Fig 7A**). Proteins involved in

2197   complex III, complex IV, complex V, amino acid metabolism and protein homeostasis were

2198   differentially enriched in 5xFAD PV-IN proteomes, while mitochondrial structural (central

2199   dogma), complex II and detoxification related proteins were unaffected (**Fig 7B**). In contrast to the

2200   PV-IN proteome, only 26 mitochondrial proteins were differentially enriched in the bulk brain

2201   proteome, which included only 4 shared DEPs (**Fig 7C**). Furthermore, the overall level of

2202   concordance between bulk brain and PV-IN mitochondrial protein levels was negligible

2203   (R^2=0.0001). The increase of Cox5a levels in 5xFAD PV-INs but not in the bulk brain tissue was

2204   validated by Western Blot, using both bulk brain homogenates and PV-specific enriched proteins

2205   (**Fig 7D**). In bulk brain MS proteomes, Cox5a showed age-dependent decrease in 5xFAD mice

2206   (**Fig 7E**), a pattern in stark contrast to increased levels in PV-INs at 3 months. This overall pattern

2207   of increased abundances of mitochondrial proteins belonging to most mitochondrial

2208   compartments, is likely to represent increased mitochondrial biogenesis to meet increased energy

2209   demands needed to sustain PV-IN firing to maintain circuit homeostasis, particularly in the setting

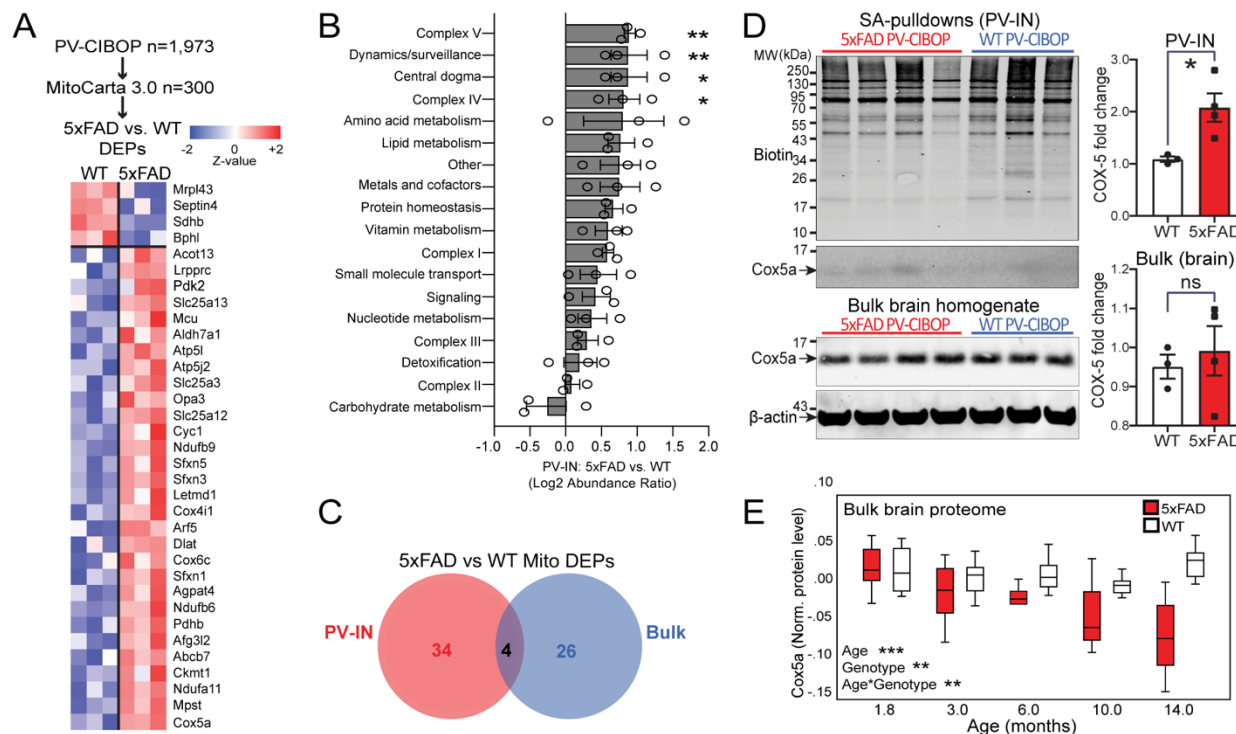2210   of emerging synaptic defects in early Aβ pathology.

Figure 7. Distinct mitochondrial alterations in PV-INs at early stages of Aβ pathology.

A. Heatmap representation of mitochondria-localized proteins that were also identified as DEPs comparing 5xFAD to WT PV-IN proteomes. Of 1,973 biotinylated proteins identified in PV-INs, 300 mitochondrial proteins were identified (based on mouse MitoCarta 3.0 list of over 1,000 mitochondrial proteins). Majority of these mitochondrial DEPs showed increased levels in 5xFAD PV-INs.

B. Differential abundance analysis of distinct mitochondrial functional groups, comparing 5xFAD to WT PV-IN proteomes. The 300 mitochondrial proteins identified in PV-INs were categorized based on known functional and localization-related annotations (from MitoCarta 3.0). Protein levels were normalized and them group-wise abundances were estimated and compared across WT and 5xFAD genotypes (*p<0.05, **p<0.01 for unpaired two-tailed T-test, error bars represent SEM).

C. Venn diagram of mitochondrial proteins that were identified as DEPs in either PV-IN proteomes or bulk brain cortical proteomes, comparing 5xFAD and WT mice. Minimal overlap in DEPs were observed, highlighting unique mitochondrial effects of Aβ pathology in PV-INs, not visible at the bulk tissue level.

D. WB verification of increased Cox5a protein levels in PV-INs in 5xFAD as compared to WT mice. SA-enriched pulldowns were independently performed from samples used for LFQ-MS studies. Cox5a protein band intensity was normalized to total biotinylation signal in the SA-enriched pulldowns, and to beta-actin in the bulk brain homogenates, and then compared across genotype (5xFAD vs. WT) (*p<0.05, unpaired two-tailed T-test).

E. Cox5a protein levels, quantified by TMT-MS, from an independent set of cortical brain homogenates obtained from WT and 5xFAD mice, spanning ages 1.8 to 14 months (equal numbers of male and female mice per group, total N=86). Using linear regression modeling, age, genotype, and age x genotype interaction terms were tested for associations with Cox5a protein levels. As compared to WT brain where Cox5a levels were relatively constant with aging, Cox5a levels in 5xFAD brain showed age-dependent decrease after 6 months of age. This pattern was discordant with increased Cox5a in PV-INs in 5xFAD mice at 3 months.

F. Volcano plot representing proteins that belong to the Akt/mTOR and/or MAPK signaling pathways (curated from HGNC) that were also identified as biotinylated proteins in PV-IN-specific CIBOP proteomes.

G. Among biotinylated Akt/mTOR and MAPK proteins in PV-INs, few were identified as DEPs comparing 5xFAD to WT PV-IN proteomes.

H. Heatmap representation of Akt/mTOR and MAPK DEPs in PV-IN proteomes and their corresponding changes in bulk brain proteomes. PV-IN proteomic changes in these pathways were not observed at the bulk tissue level (with the exception of Rheb).

I. Cartoon representation of adapted Luminex immunoassay to measure levels of phospho-proteins belonging to Akt/mTOR and MAPK signaling pathways. As published previously[2], analytes of interest at first captured onto beads using a capture antibody. If this analyte is biotinylated (by PV-CIBOP), it can be detected using a streptavidin fluorophore. If not biotinylated, no signal is detected. This provides a direct estimation of phosphoproteins that reflect signaling pathway activity, with PV-IN-specific resolution.

2211

2212

2213

J. Heatmap visualization of phospho-proteins from Akt/mTOR and MAPK signaling pathways measured using the adapted Luminex assay in cortical brain lysates from WT/PV-CIBOP and 5xFAD/PV-CIBOP mice (n=3 mice per group). Adapted signal obtained from non-CIBOP brain lysates was used a background signal and subtracted from signal obtained from CIBOP adapted Luminex values. These were further normalized to TurboID abundance (as estimated by LFQ-MS from the same samples) (p<0.05, unpaired two-tailed T-test).

K. Summary of results indicative of an overall decreased activity in mTOR signaling (particularly via mTORC1) in 5xFAD PV-INs as compared to WT PV-INs. This summary was constructed using total protein levels estimated by LFQ-MS of PV-IN proteomes, as well as phospho-protein levels by the adapted Luminex approach. mTORC1 signaling is expected to suppress autophagy, increase ribosome biogenesis and translational efficiency, decreased protein degradation and increase synaptic activity/plasticity.

L. Comparison of proteins that positively regulate autophagy (GO 0010508) as a group, in 5xFAD and WT PV-IN proteomes (levels of 23 proteins were normalized, z-transformed and then averaged across biological replicates before group comparisons using T-test (*p<0.05).

M. Western blot analysis of PV-IN (SA-enriched) samples and bulk brain lysates from 5xFAD and WT PV-CIBOP samples, to measure LC3-II and LC3-I bands, to estimate autophagic activity. LC3-II and I bands were separately quantified and LC3-II/I ratios were calculated and compared across the two groups. Quantitative analysis is shown below (error bar represents SEM, *p<0.05, independent two-tailed T-test).

N. Analysis of DEPs (5xFAD vs. WT PV-IN proteomes) based on published protein half-lives in mouse brain. Proteins with increased levels in 5xFAD PV-INs were skewed towards proteins with longer half-lives (>13.7 days which represents the 75th percentile of protein half-lives in brain). This pattern is consistent with decreased translational efficiency and/or increased protein degradation, which would disproportionately impact the relative abundances of short-lived proteins.

O. Comparison of proteins that regulate synaptic plasticity (GO 0048167) as a group, in 5xFAD and WT PV-IN proteomes (levels of 102 proteins were normalized, z-transformed and then averaged across biological replicates before group comparisons using T-test (***p<0.005).

See Supplemental Datasheet 6 for related analyses.

Evidence for decreased mTOR-C1 signaling in PV-INs in early Aβ pathology

The mitochondrial and synaptic derangements occurring in PV-INs in 5xFAD mice suggest that upstream signaling pathways may be dysregulated in PV-INs. Metabolic signaling pathways, including Akt/mTOR, are important regulators of mitochondrial biogenesis and turnover, as well as synaptic function in neurons while several MAPKs (ERK, p38 MAPK, Jnk) impact cell proliferation, synaptic function and survival[295-298]. We found that PV-CIBOP labeled 75 proteins involved in Akt/mTOR (*e.g.,* Mtor, Rptor, Eif4b) and MAPK (*e.g.,* Map2k1, Ras proteins, Pak2, Akt3, Mapk3, Mapk10) signaling pathways (**Fig 7F**). Of these, few proteins showed increased (Rhoa, Prkca, Hras, Cacna2d1) and decreased levels (Eif4b, Mapt, Rheb) in 5xFAD PV-INs (**Fig 7G**). Interestingly, these differential effects of Aβ pathology were only observed in PV-IN proteomes, and not in the bulk brain proteome with the exception of Rheb, highlighting the specificity of these alterations in PV-INs in early AD pathology (**Fig 7H**).

Based on the ability of CIBOP to biotinylate signaling proteins in PV-INs, we performed adapted Luminex assays to detect MAPK (Erk, P38 Mapk and Jnk) and Akt/mTOR signaling phospho-proteins, specifically derived from PV neurons[2]. In this approach, the biotinylated

2229 phospho-protein is immobilized on beads using capture antibodies, and then their biotinylation

2230 status is detected by streptavidin-fluorophore, to directly measure PV-IN-derived phospho-

2231 proteins from brain homogenates (**Fig 7I, Supplemental Datasheet 5**). We found that mTOR

2232 signaling (via phosphorylation of mTOR and down-stream target p70 S6K), was decreased in

2233 5xFAD PV-INs while MAPK pathway activation was not altered (**Fig 7J**). This pattern of

2234 decreased mTOR signaling was consistent with lower levels of Rheb (a direct activator of mTOR-

2235 C1 function), higher levels of RhoA (a known inhibitor of Rheb function) and lower levels of Eif4b

2236 (involved in translation initiation) in 5xFAD PV-INs (**Fig 7K**)[299]. Collectively, our MS PV-IN

2237 CIBOP and adapted Luminex analyses indicate decreased mTOR-C1 activity in 5xFAD PV-INs.

2238   To assess functional relevance of decreased mTOR-C1 in 5xFAD PV-INs, we assessed

2239 three composite measures of mTOR-C1 signaling, including autophagy (mTOR-C1 inhibits

2240 autophagy)[298], translational efficiency/protein degradation (mTOR-C1 increases translational

2241 efficiency and decreases protein degradation)[300,301] and synaptic plasticity (mTOR-C1 facilitates

2242 synaptic plasticity) (**Fig 7K**)[297]. 23 GO-annotated positive regulators of autophagy (GO-0010508)

2243 were labeled in PV-INs and collectively, this group showed increased levels in 5xFAD PV-INs

2244 (**Fig 7L**). Western blot analyses of biotinylated proteins as well as bulk brain samples from WT

2245 and 5xFAD PV-CIBOP mice found increased LC3-II (relative to LC3-I) in 5xFAD PV-INs as

2246 compared to WT PV-INs, consistent with increased autophagy in 5xFAD PV-INs but not in bulk

2247 brain lysates (**Fig 7M**). Interestingly, all PV-IN (WT or 5xFAD) systematically showed higher

2248 levels of LC3-II as compared to bulk brain samples (**Fig 7M, Supp Fig S8**). These patterns suggest
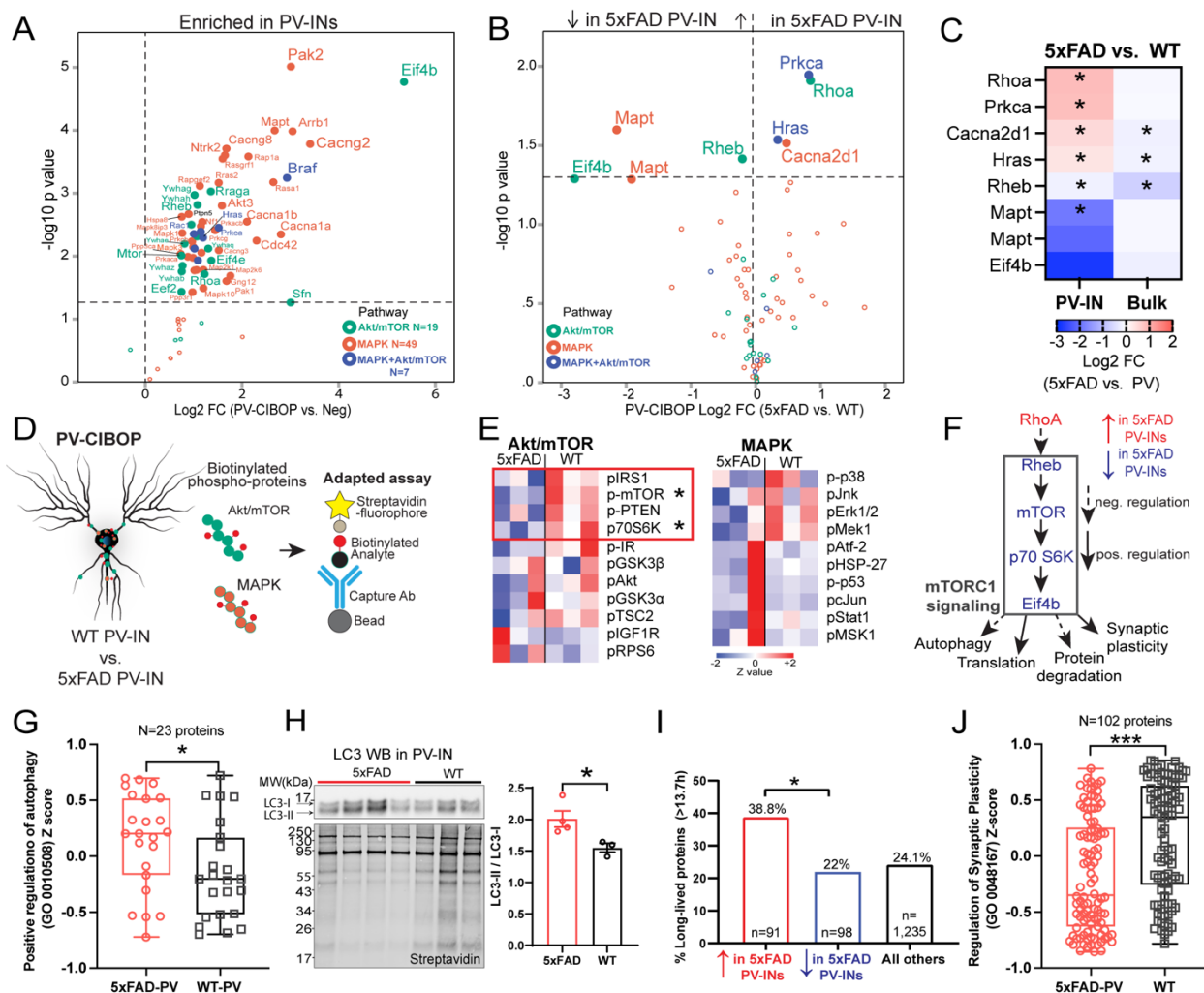
Fig. 8 PV-IN-specific decrease in mTOR signaling in early Aβ pathology.

A. Akt/ mTOR and/or MAPK signaling proteins biotinylated in PV-IN CIBOP proteomes (as compared to non-CIBOP mice).

B. Akt/mTOR and MAPK proteins identified as DEPs comparing 5xFAD to WT PV-IN proteomes.

C. Heatmap representation of Akt/ mTOR and MAPK DEPs in PV-IN proteomes and their corresponding bulk brain proteomes (*p < 0.05, two-tailed unpaired T-test).

D. Cartoon representation of adapted Luminex immunoassay to measure levels of PV-IN-derived phospho- proteins belonging to Akt/mTOR and MAPK proteins from bulk tissue.

E. Heatmap visualization of Akt/mTOR and MAPK phospho-proteins in PV-INs measured by adapted Luminex assay from WT and 5xFAD mice (n = 3 mice/group, p < 0.05 unpaired two-tailed T-test).

F. Summary: Decreased activity in mTOR signaling in 5xFAD PV-INs as compared to WT PV-INs, based on total protein levels estimated by PV-CIBOP MS, and phospho-protein levels by the adapted Luminex approaches.

G. Comparison of proteins that positively regulate autophagy (GO:0010508), in 5xFAD and WT PV-IN proteomes (protein levels were normalized, z-transformed and then group-averaged across biological replicates before group comparisons;

unpaired two-tailed T-test,*p < 0.05).

H. Top: WB of PV-IN (SA-enriched) samples from 5xFAD and WT PV-CIBOP brain. LC3-II/I ratio was compared across the two groups. Bottom: Biotinylated protein from samples corresponding to WB images above. Data are displayed as mean values +/- SEM. (n = 3 (WT), 4 (5xFAD), *p < 0.05, independent two-tailed T-test).

I. Analysis of DEPs (5xFAD vs. WT PV-IN proteomes) based on published protein half-lives in mouse brain. Proteins with increased levels in 5xFAD PV-INs were skewed towards proteins with longer half-lives (> 13.7 days which represents the 75th percentile of protein half-lives in brain). This pattern is consistent with decreased translational efficiency and/or increased protein degra- dation, which would disproportionately impact the relative abundances of short-lived proteins. J. Comparison of proteins that regulate synaptic plasticity (GO:0048167) as a group, in 5xFAD and WT PV-IN proteomes (levels of 102 proteins were normalized, z-transformed and then averaged across biological replicates before group comparisons using unpaired two-tailed T-test (***p < 0.005). See Supplementary Data 6 for related analyses. Source data are provided as a Source Data file.

2250   that PV-INs have high autophagic flux in general[135] and this phenotype is exaggerated in early AD

2251   pathology. To determine whether decreased mTOR-C1 signaling in 5xFAD PV-INs impacts

2252   translational efficiency and/or increased protein degradation, we assessed the relative abundances

2253   of long-lived and short-lived proteins in 5xFAD and WT PV-IN proteomes. Using a reference

2254   dataset of protein half-life estimates derived from *in vivo* isotopic labeling studies in adult mice[302],

2255   we found that DEPs that were increased in 5xFAD PV-INs were biased towards longer-lived

2256   proteins, as compared to non-DEPs as well as compared to DEPs with decreased levels in 5xFAD

2257   PV-INs (**Fig 7N, Supplemental Datasheet 6**). This molecular footprint of relatively-increased

2258   abundance of longer-lived proteins in 5xFAD PV-INs is consistent with decreased translational

2259   efficiency and/or increased protein degradation in 5xFAD PV-INs. Lastly, we found that proteins

2260   involved in regulation of synaptic plasticity (GO-0048167, n=102 proteins) were also decreased

2261   in 5xFAD PV-IN proteomes (**Fig 7O**), consistent with observed synaptic protein changes and

2262   physiological defects presented earlier (**Fig 5,6**). These analyses provide congruent lines of

2263   evidence for decreased mTOR signaling at various levels of the signaling axis (upstream and

2264   downstream of mTOR-C1 function), that are associated with increased autophagic flux, decreased

2265   translational efficiency and decreased synaptic plasticity in PV-INs at early stages of Aβ pathology.

2266

2267   4.4 Discussion

2268   We describe a versatile intersectional method[2,138,255] allowing quantitative *in vivo* neuron-

2269   type-specific proteomics. We leveraged this approach to isolate the native-state PV-IN proteome,

2270   and examine changes in this cell type in an early-stage mouse model of Aβ pathology. In principle,

2271   our approaches are readily adaptable to other neuron types, due to the recent expansion of novel

2272   cis-element-directed AAV approaches[303,304] with unparalleled cell-type-specificity. A secondary

advantage to our workflow is the ability to seamlessly translate the technique across different mouse models of disease, without the need for complex and expensive cross-breeding strategies.

Comprehensive molecular characterization of neuronal subtypes can provide critical insights into the function and modifiable pathogenic mechanisms of neurological diseases. Ideally, this should be performed at the proteomic level, while retaining the native state of neuronal proteome (i.e., protein samples from intact soma, dendrites, and axons), overcoming limitations of transcriptomic studies which rely on isolation of intact neurons or neuronal nuclei. Despite the modest concordance between mRNA and functionally-relevant protein particularly in neurons[131-133,305], proteomic studies of neurons and neuronal subtypes in the *in vivo* context have lagged behind transcriptomic advances due to several technical barriers. However, recent advances in cell type-specific *in vivo* proteomic labeling approaches, involving proximity-dependent biotinylation by biotin ligases included TurboID (CIBOP), and bio-orthogonal amino acid tagging approaches[306-308], provide exciting opportunities to investigate neuronal subtype-specific molecular signatures and disease mechanisms. For the CIBOP approach described in this study, proximity-based biotinylation of proteins in the cytosol and several cellular compartments (*e.g.,* synaptic boutons or postsynaptic densities) can be achieved by TurboID expression selectively in brain cell types of interest, by driving Cre recombinase expression via transgenic or AAV approaches, in the Rosa26[TurboID] mouse line[2]. CIBOP with TurboID mice has thus far been successfully applied in specific brain cell types by crossing with cell-selective Cre mouse lines (Camk2a-Cre for excitatory neurons and Aldh1l1-Cre for astrocytes) and is thus well positioned to be extended to other neuronal subtypes and glial cells[2,308,309]. Universal extension of cell-specific CIBOP across mouse models of disease would provide unparalleled resolution to pathological mechanisms. However, the need for further time-consuming and expensive cross-

2296   breeding represents a significant barrier. Thus, we developed an enhancer-AAV method to deploy

2297   CIBOP more rapidly in PV-INs of both WT and disease model mice. Further development of

2298   intersectional AAV approaches should also allow CIBOP to be expanded in other model species as

2299   well as to cell types outside the brain[310].

2300   Among neuronal subtypes, PV-INs represent a unique class of inhibitory interneurons with

2301   fast-firing properties and high metabolic activity[41,311]. Selective dysfunction of PV-INs contributes

2302   to a variety of neurological insults, including in neurodegenerative diseases such as AD,

2303   neurodevelopmental disorders, and catastrophic early-life epilepsy[108,312,313]. We applied CIBOP to

2304   PV-INs throughout the forebrain by subcloning a Cre-expressing cassette into a PV-specific

2305   enhancer-AAV[255] (AAV.E2.Cre) delivered systemically using the PHP.eB serotype, which readily

2306   enters the brain[138]. Delivery of AAV.E2.Cre in Rosa26[TurboID] mice lead to PV-specific proteomic

2307   biotinylation. When coupled with MS of affinity-purified biotinylated proteins, we obtained the

2308   PV-IN-specific proteome while retaining their native functional state without need for cell isolation

2309   and without physiological disruption. Taken together, the PV-CIBOP approach identified unique

2310   proteomic signatures of PV-INs complementing existing transcriptomic data, serving as an

2311   important resource to the neuroscience research community.

2312   The PV-IN proteomic signature includes hundreds of proteins that are either exclusive to,

2313   or highly-enriched in PV-INs over the bulk brain proteome, including canonical PV-IN markers

2314   (*e.g.,* Kv3.1-3.3, Erbb4, Ank1, Syt2)[16] as well as 200 proteins not predicted by PV-IN scRNAseq

2315   databases (*e.g.,* Tnpo3, Htt, Synrg, Cplx3, Mtor, Gria1). PV-CIBOP also labeled proteins with

2316   predicted subcellular targets in the cell body, axons and dendrites of PV-INs, including pre- and

2317   post-synaptic compartments. The PV-IN proteome was suggestive of high metabolic activity,

2318   protein translation, signaling and vesicle functions, consistent with the fast-firing and rapid

2319   neurotransmission[42] properties of these cells. The PV-CIBOP proteome was also highly-enriched

2320   in proteins with causal associations to neurodegenerative disease risk, including AD (BIN1)[314],

2321   pure tauopathies (MAPT)[315], and synucleinopathies (SNCA, SNCB)[316,317]. Several lines of

2322   evidence now suggest that interneuron dysfunction leads to altered circuit excitability in early-

2323   stage models of APP/Aβ pathology[75,109]. Stx1b and Gat1, among others, are examples of proteins

2324   enriched in the PV-IN dataset linked to both epileptiform activity and AD[318]. Furthermore, other

2325   neurodevelopmental and autism implicated molecules (Shank2, Syngap1, ErbB4)[319-323] were also

2326   highly enriched in PV-INs. When contrasted to CIBOP-derived proteomes from the

2327   (predominantly pyramidal neuron) Camk2a-Cre mice, PV-IN proteomes exhibited clearly higher

2328   levels of ribosomal, endocytic, Akt/mTOR signaling, synaptic cytoskeletal, endocytic and synaptic

2329   vesicle-related proteins. The proteomic contrast between PV-IN and Camk2a neurons in mice,

2330   integrated with recently-identified proteomic correlates of cognitive resilience in humans, revealed

2331   a disproportionate enrichment of pro-resilience proteins in the PV-IN proteome, suggesting a link

2332   between cognitive resilience and PV-INs.

2333   To look for evidence of PV-IN-associated vulnerability in human AD, we assessed existing

2334   human post-mortem bulk brain proteomic data from controls and AD cases (with and without

2335   dementia prior to death)[1]. We identified a module of co-expressed proteins (M33) that was enriched

2336   in PV-IN markers (*e.g.,* Pvalb, Kcnc2), that was distinct from modules enriched in excitatory

2337   neuronal (pyramidal cell) markers. The PV-IN proteomic module was less abundant in AD cases,

2338   compared to both asymptomatic AD and control patients, and this decrease in M33 was also

2339   correlated with AD neuropathological features (Aβ pathology, neurofibrillary tangles), severity of

2340   cognitive dysfunction, and rate of cognitive decline although independent of APOE genetic risk.

2341   After accounting for neuropathological hallmarks of neurodegenerative diseases, M33 still

2342   remained associated with cognitive resilience, suggesting that links between PV-INs and cognitive

2343   resilience may be independent of neurodegenerative pathology. Using a complementary approach

2344   to estimate abundances of different neuronal classes, we found that PV-IN cell type abundance was

2345   strongly associated with cognitive resiliency in longitudinal studies of aging. Our findings suggest

2346   that preservation of PV-IN function in the brain may be generally protective in AD, and link PV-

2347   INs with cognitive resilience and vulnerability in AD.

2348   To directly capture longitudinal impacts of aging and disease progression, we analyzed

2349   mouse bulk brain proteomes from WT and 5xFAD mice spanning a wide age range and found that

2350   PV-IN proteins (but not excitatory neuronal proteins) showed unique age-dependent increases in

2351   expression although this was suppressed in 5xFAD mice, starting as early as 3 months of age.

2352   Albeit a snapshot from bulk tissue, this suggests that of PV-IN protein levels, but not other neuronal

2353   markers, may change in early stages of APP/Aβ pathology. Somatostatin (Sst), a protein primarily

2354   expressed in cortical dendrite-targeting (non-PV fast spiking)[324,325] inhibitory interneurons, was

2355   similarly reduced starting at 3 months of age. As both Pvalb and Sst expression are linked to the

2356   level of circuit activity[38,326] these changes may reflect a differential dysregulation of interneuron

2357   activity levels at a stage where substantial plaque formations are just arising in 5xFAD mice. At

2358   the histological level, no measurable differences in PV-IN density were observed between 3 month

2359   old wild-type and 5xFAD mice, arguing against early overall cell loss of PV-INs at this early stage,

2360   but rather suggesting changes to their proteomic profile.

2361   To evaluate PV-IN proteomic changes in response to early Aβ pathology, we compared PV-

2362   CIBOP-derived proteomes from 3 month old Rosa26[TurboID] WT and 5xFAD mice. Over 450 DEPs

2363   were found. Proteins involved in mitochondrial function, cholesterol biosynthesis (*e.g.,* Dhcr7),

2364   and metabolism were generally increased in PV-INs. In contrast, cytoskeletal, structural, and

2365   synapse-associated proteins were generally decreased in PV-INs. Surprisingly, alterations found in

2366   the PV-IN proteome were almost completely non-overlapping with those changes resolved from

2367   bulk brain. Since the majority of intra-neuronal APP/Aβ was detected in non-PV-INs at this stage

2368   of pathology, the observed changes in PV-INs are most likely due to Aβ from other neurons rather

2369   than due to dysfunctional Aβ processing in PV-INs. Based on these specific effects of Aβ pathology

2370   on PV-INs, extending CIBOP to other interneuron and excitatory neuron subclasses, and capturing

2371   the effects of brain region and age in future studies will be necessary to resolve whether PV-IN

2372   protein levels are profoundly affected in early AD models, or rather, are part of a continuum of

2373   emerging cell-type autonomous alterations across different brain regions.

2374   Initial PV-CIBOP studies in WT mice found substantial enrichment of proteins encoded by

2375   MAGMA-identified AD genetic risk factors, as well of pro-resilience proteins in the PV-IN

2376   proteome in contrast to Camk2a neurons[1,146,155]. Therefore, we asked whether MAGMA AD

2377   proteins would also be disrupted in our early AD model PV proteome, and indeed, cross-referenced

2378   DEPs in 5xFAD matched with 20 MAGMA AD genes. Furthermore, proteins associated with

2379   cognitive resilience were systematically reduced in 5xFAD PV-INs, particularly proteins involved

2380   in presynaptic vesicle fusion/exocytosis/release (Cplx1, Cplx2, Stx1b, Elfn1, Rab3c, Rims1)[146].

2381   To examine the functional implications of this pre-synaptic signature, we used PV-IN-specific

2382   optogenetic approaches in two independent models of early APP/Aβ pathology. At cortical PV-to-

2383   pyramidal synapses, both studies clearly point to disturbances in presynaptic function. In

2384   particular, changes in vesicular release probability appear likely. Beyond pre-synaptic dysfunction,

2385   several studies have also shown an emergence of inhibitory post-synaptic dysfunction across a

2386   number of APP/Aβ models[118,327-329]. Future mechanistic investigations are warranted to examine

2387   the roles of resiliency-related pre-synaptic and post-synaptic proteins in PV-INs and other

inhibitory cell synaptic mechanisms in AD models. Importantly, these early alterations identified at PV synapses may represent opportunities for early therapeutic intervention.

Despite minimal plaque burden in 3 month-old 5xFAD mice[141], the significant shifts in the 5xFAD PV-IN proteome may represent a homeostatic response to prior changes in neuronal and circuit behavior and organization[160,330,331] known to occur in young, pre-plaque APP/Aβ models, including in younger (<3 month-old) 5xFAD mice[109,113,332,333]. Relatedly, a signature of circuit instability is also present in human patients with mild cognitive impairment and AD[168,169,257]. To compensate for this early circuit dysfunction, PV-INs are well-suited to homeostatically respond[334], but this process could impose a higher metabolic demand to sustain this compensation. Indeed, mitochondrial impairments have been observed prior to extensive pathology in APP/Aβ model mice[335,336]. In our PV-CIBOP proteomes, we found a signature of stress-responsive proteins (Armt1, Rhob, Gstm1, RhoA, Tmco1, Akr1b3, Gcn1, Hras, Cul3, Pdk2, Rap2a, Flot1) in 5xFAD as compared to WT. Of note, RhoA activation increases Aβ and tau pathology and co-localizes with NFTs in human brain[337,338]. In contrast to the overall synaptic effects of early AD pathology in PV-INs, we observed a marked increase in mitochondrial and metabolic proteins in PV-INs. This increase could be reflective of a protective or compensatory responses (via increased mitochondrial biogenesis to sustain higher metabolic demand). Other compensatory signatures observed in 5xFAD PV-INs included increased Dhcr7 for de-novo cholesterol biosynthesis in neurons, increased Apeh to process Aβ oligomers along with increased autophagy as supported by increased levels of positive regulators of autophagy and increased lipidated form of LC3 (LC3-II). Conversely, a detrimental/dysfunctional response (*e.g.,* accumulation of dysfunction mitochondria) is also possible. We noted that mitochondrial functional proteins and Complex I, III, IV, V proteins were selectively increased in 5xFAD PV-INs while a smaller group of

2411 mitochondrial structural, dogma, and Complex II proteins were not. Therefore, follow-up studies

2412 focusing on mitochondrial structure and function specifically in PV-INs are warranted to better

2413 understand the basis and consequences of these mitochondrial alterations. Taken together, the

2414 molecular phenotype of 5xFAD PV-INs is indicative of a significant cellular stress response

2415 occurring in 3 month old PV-INs, comprising both compensatory and maladaptive events, which

2416 is not evident in the bulk proteome at this age. Furthermore, we present several lines of evidence

2417 from bulk brain and PV-IN-specific experiments, and human brain proteomic analyses, that PV-

2418 IN proteomic signatures and cognitive resiliency are linked. Therefore, understanding the

2419 mechanisms for this compensation could provide therapeutic insights for future studies.

2420 Metabolic shifts and mitochondrial biosynthesis are regulated by signaling pathways such

2421 as Akt/mTOR and MAPK[295-298]. We also observed high levels of proteins involved in both

2422 Akt/mTOR (*e.g.,* Mtor, Eif4b) and MAPK (*e.g.,* Erk and Mek proteins) signaling pathways in PV-

2423 INs. Therefore, we hypothesized that mTOR signaling may be altered in 5xFAD PV-INs. We

2424 directly measured biotinylated phospho-proteins indicative of levels of activity of these pathways

2425 specifically in PV-INs by leveraging an adapted Luminex immunoassay method recently validated

2426 for CIBOP-based studies[2]. Our MS-based and Luminex-based analyses provide evidence of

2427 decreased mTOR (mTOR-C1) signaling in PV-INs, but not in bulk brain tissue, that appear to

2428 augment autophagic flux, decrease translational efficiency or increased protein degradation, and

2429 impair synaptic plasticity. Collectively, our results indicate early dysregulation of mTOR signaling

2430 in PV-INs as a potential upstream mechanism for mitochondrial and metabolic alterations as well

2431 as synaptic dysfunction occurring selectively in PV-INs in early stages of AD pathology in 5xFAD

2432 mice.

Limitations of our work relate to technical considerations of both AAV-based PV-IN targeting, and potential proteomic biases of the CIBOP approach. Currently, CIBOP leads to cell type-specific expression of TurboID-NES, which contains a nuclear export sequence for preferential proteomic labeling outside the nucleus. This may bias the PV-IN proteome away from nuclear proteins as well as from proteins present within the lumen of organelles (*e.g.,* ER/Golgi, mitochondria, lysosomes)[2,309]. Whether removal of the NES impacts the nature of the PV-IN proteome, remains to be determined Another consideration is that our AAV.E2.Cre strategy targets PV-INs as a whole, although several PV-IN subtypes have been identified by scRNAseq studies[7] (i.e., chandelier cells and several basket cell PV types). It is therefore possible that the proteomic signatures of these different PV-IN subtypes are non-uniform. Thus, our initial PV-CIBOP derived proteome may not accurately describe the proteomic granularity which may further exist within PV-IN interneuron classes. Further studies with increased PV subtype-specificity or physiological and morphological studies using CRISPR or related methods to examine individual proteins may be useful in this regard.

In summary, our integrative PV-CIBOP approach revealed a novel native-state proteomic signature for a single, highly-important interneuron class in the mouse brain. Comparison of PV-CIBOP proteomic signatures with human post-mortem data suggests selective synaptic and metabolic PV-IN vulnerabilities in early AD pathogenesis that may be linked to cognitive dysfunction. These findings provide a strong rationale to investigate and target early proteomic changes occurring in PV-INs and other inhibitory neuron types in mouse models of AD and other neurological diseases.

2457   <u>4.5 Supplementary Information</u>
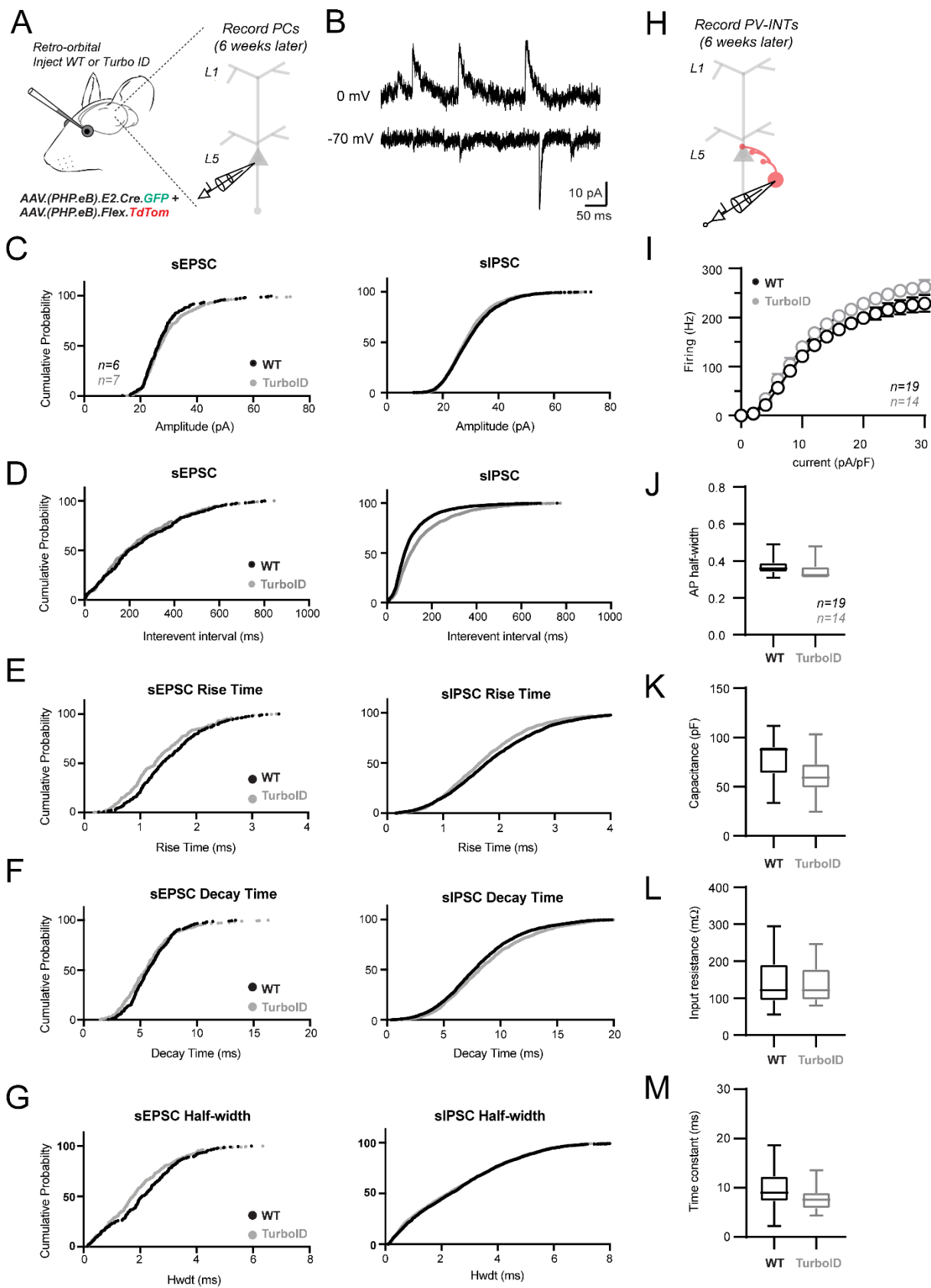
Chapter 4. Supplementary Figure 1. PV-CIBOP does not disrupt PV-IN or local circuit properties (related to Figure 1)

A. During procurement of CIBOP tissues from RO-injected Rosa26$^{TurboID/wt}$ (TurboID) and WT mice, a subset of the brain (SBFI region of S1 cortex) was used to immediately prepare acute slices for patch clamp recordings of unlabeled pyramidal neurons in layer 5.

B. Example traces from a voltage clamp recording in a pyramidal neuron in layer 5 cortex. -70 and 0 mV holding potentials were interleaved throughout the recording to sample spontaneous EPSCs and IPSCs, respectively.

C-G. Cumulative probability distribution curves for the amplitudes, frequency, and kinetic properties from all spontaneous EPSC and IPSC events recorded in pyramidal neurons of TurboID and WT mice.

H, I. In the same experiments as depicted in **A** and **B**, fluorescent-targeted current clamp recordings were performed in TdTomato+ neurons as identified using combined video-epifluorescent illumination. The GFP signal from the E2.Cre.GRP construct was not used, as it was generally much dimmer. Current injections (300 ms) of varying amplitude (0-30 pA/pF) were normalized to the individual cellular capacitance to control for potential variability between passive features.

J. Narrow action potential widths at half-maximal amplitude (half-width) quantified in TdTomato+ between WT and Turbo ID mice. Half-width was measured from the 1st spike elicited by current injection. Action potentials were generally ~0.35 ms, characteristic of fast-spiking cortical PV-INs.

K-M. Passive features measured in recordings from TdTomato+ PV-INs.

For synaptic properties recorded in pyramidal neurons in **C-G,** average values from all spontaneous events from individual recordings were used for statistical analysis comparing TurboID (n=7) and WT (n=6) mice. All comparisons were p>0.05, unpaired two-tailed T-test.

For PV-IN recording data in **J-M**, all TurboID (n=19) and WT (n=14) comparisons were p>0.05, unpaired two-tailed T-test.
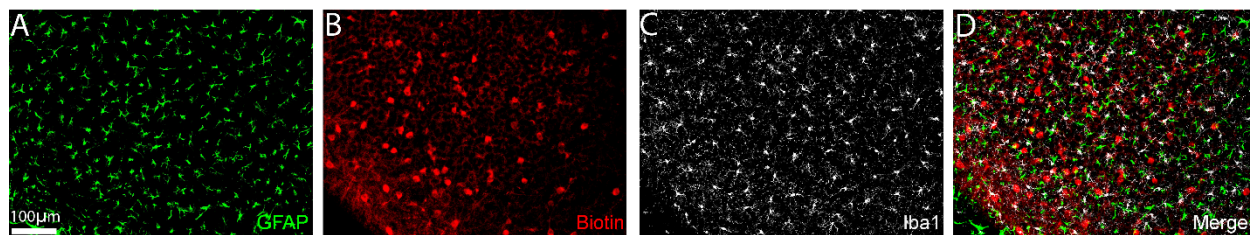
Chapter 4. Supplementary Figure 2. PV-CIBOP specifically labels PV-INs without off-target labeling of astrocytes or microglia (related to Figure 1)

Representative immunofluorescence images (20x) from PV-CIBOP brain, confirming that biotinylation was not detected either in in astrocytes (GFAP+) or in microglia (Iba1+ positive). Furthermore, microglial and astrocyte morphology was qualitatively similar in labeled and non-labeled animals.

Mann Whitney p=0.16
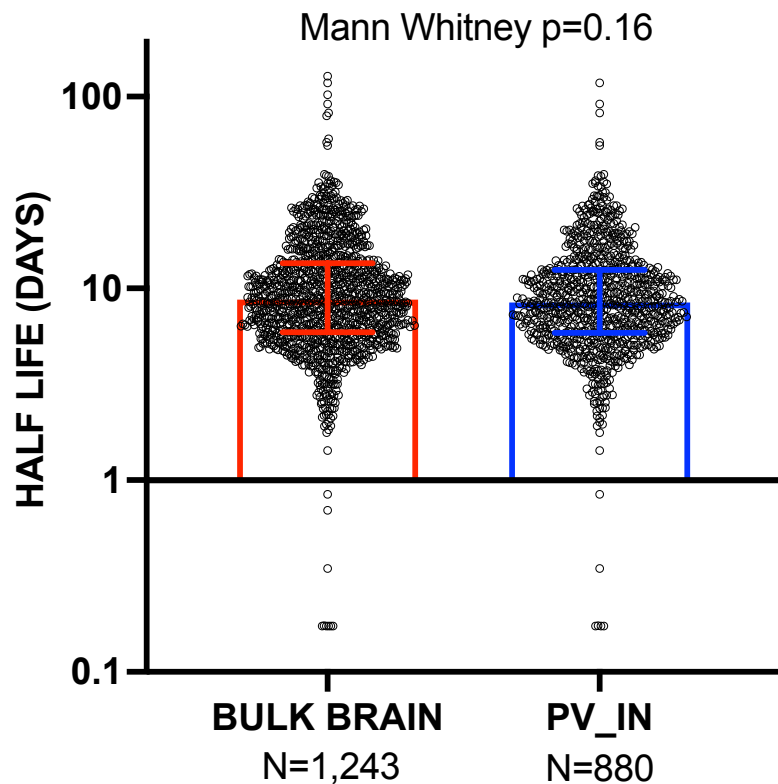
Chapter 4. Supplementary Figure 3. PV-IN CIBOP-derived proteomes are not biased towards shorter or longer-lived proteins

Using brain-specific protein half-live estimates (in days) from Fornasiero et. al. Nature Communications 2018 (also see Supplementary Data 6), we compared half-life distributions of bulk brain proteins and PV-IN-enriched proteins from our CIBOP studies. The median half-life of proteins comparing PV-IN CIBOP proteomes and bulk brain proteomes were not statistically different, indicating that the CIBOP approach does not seem to be impacted by the rate of protein turnover (see Supplementary Data 1 sub-sheet 7 for source data related to protein half-life analysis).

Summary Table: Distribution of proteins based on RiboSeq_Neuropil vs. Soma (Glock et. al. PNAS 2021)

PV-IN proteins	Neuropil enriched	Soma enriched	Other	Total
N	64	397	181	642
%	9.97	61.84	28.19	100.00
Bulk brain proteins	Neuropil enriched	Soma enriched	Other	Total
N	95	520	265	880
%	10.80	59.09	30.11	100.00
All 7,350 proteins (Glock et al.)	Neuropil enriched	Soma enriched	Other	Total
N	807	2945	4098	7850
%	10.28	37.52	52.20	100.00

PV-IN vs. Bulk: Chi Square p = 0.56

2508

2509 *Chapter 4. Supplementary Figure 4. PV-IN CIBOP does not preferentially label neuronal*
2510 *proteins based on somatic or axon/synapse/dendritic localization*

2511 Comparison of distributions of soma-enriched, neuropil-enriched proteins in PV-IN proteomes,
2512 bulk brain proteomes as well as the reference Ribo-seq dataset by Glock et. al. PNAS 2021.
2513 Ribo-seq was used to measure mRNAs that were actively translated (translatome) in neurons,
2514 and classified as being enriched in somatic or neuropil (axon/dendrite/synapse) neuronal sub-
2515 compartments. Using these classifications of neuronal proteins, we assessed distributions of
2516 proteins identified in PV-INs by CIBOP, in the bulk brain proteomes from corresponding
2517 animals, and in the Glock et. al. reference Ribo-seq translatome. Chi-square statistics were used
2518 to compare distributions (see Supplementary Data 1 sub-sheet 6 related to protein localization
2519 analysis).

2520

A. Analysis of protein vs mRNA concordance in PV-INs, using PV-enriched proteins identified by PV-CIBOP and existing single nuclear transcriptomic data from the entire class of adult mouse PV-INs (Allen Brain Atlas). Based on differentials in rank abundances (protein vs. mRNA), discordant and concordant protein/mRNA pairs are highlighted. Spearman's Rho for protein vs. mRNA correlation is shown.

B-D. Three groups of protein/mRNA pairs were further analyzed: **B.** Group 1-Highly abundant and concordant: Protein rank differential between -0.25 and 0.49 and overall abundance >80th

percentile in both protein and mRNA datasets). **C.** Group 2: Discordance with mRNA greater than protein abundance (Protein vs. mRNA rank differential < -0.5). **D.** Group 3: Discordance with protein greater than mRNA abundance (Protein vs. mRNA rank differential > +0.5). Top gene symbols/protein IDs, top GSEA terms representative of each group, and STRING PPI diagrams (with colors indicating each ontology), are shown in each panel. Higher mRNA/protein concordance was observed in ontologies including oxidative-reduction processes, ATP generation, synaptic transmission, glucose metabolism, endocytosis and protein transport. Low abundance proteins with high mRNA abundance were enriched in ontologies related to complex I respiratory chain, proteasome, cytosolic and vesicle-mediated transport terms. Proteins with high abundance but low mRNA expression were enriched in neurogenesis, ion channel function and transporters, cytoskeletal/cell projection and translation-related proteins. Please see Supplementary Data 1 sub-sheet 5 for related source data and analyses.

2547 *Chapter 4. Supplementary Figure 6. GSEA of PV-IN and Camk2a neuronal CIBOP proteomes*
2548 *(related to Figure 2)*

2549 **A-D.** Heatmap representation of (**A**) Gene Ontology (GO) terms, (**B**) GOSlim terms, (**C**)
2550 PathwayCommons terms as well as (**D**) predicted upstream microRNA (miRNA) regulators that
2551 are over-represented in proteomic signatures of PV-INs and Camk2a neurons, using the CIBOP
2552 approach.

2553   **E**. Normalized miRNA levels as measured using the miRAP method (He et. al. Neuron 2012)
2554   that identified miRNAs that were differentially abundant in PV-INs and Camk2a neurons. The
2555   miRNAs enriched in PV-INs that are represented in this graph (particularly miR-133a and miR-
2556   133b), were also predicted as up-stream regulators of PV-IN proteomic signatures. Therefore,
2557   miR-133a and miR-133b are highly likely miRNA regulators that may be functionally important
2558   regulators of PV-INs.
2559   **F.** Venn Diagram representing shared and distinct target genes that are regulated by miR-133a
2560   and miR133-b in PV-IN proteomes.
2561   **G.** 54 proteins were identified as shared down-stream targets of both miR-133a and miR-133b in
2562   PV-INs, and these are represented as a STRING PPI network. Top GO terms emerging from this
2563   analysis include synaptic vesicle, vesicle transport and clathrin-dependent endocytosis terms.
2564   This indicates that miR-133a and miR-133b may be regulators of synaptic vesicle related
2565   function in PV-INs. Also see Supplementary Data 2 for related analyses.
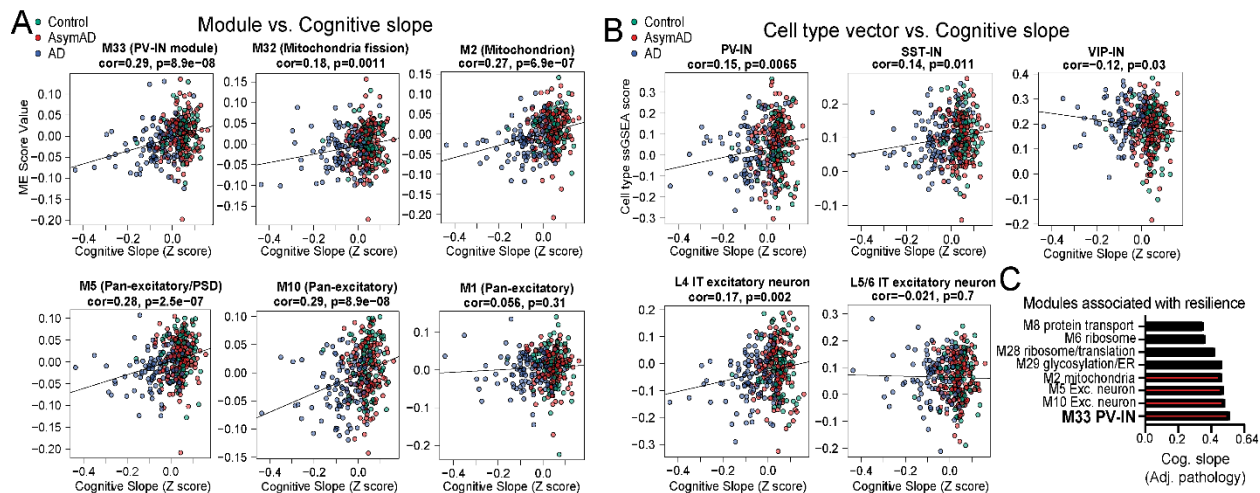
Chapter 4. Supplementary Figure 7. Associations between brain protein co-expression modules and cell type abundance vectors with cognitive slope in humans (related to Figure 3)

A, B. Associations of module eigenprotein (ME) (**A**) and cell type vectors (**B**) with cognitive slope for modules with highest positive correlations with cognitive slope. A higher cognitive slope indicates cognitive stability (or resilience) while a lower (negative) slope indicates faster cognitive decline over time. Color (reg, light blue and dark blue represent controls, AsymAD and AD cases respectively).

C. Module eigenprotein associations with cognitive slope (resiliency) after adjustment for neuropathological features. This shows that module M33, followed by excitatory neuron modules (M5, M10) and mitochondrial modules (M2) had the highest correlation with cognitive resilience.

See Supplementary Data 3 for related analyses and source data.
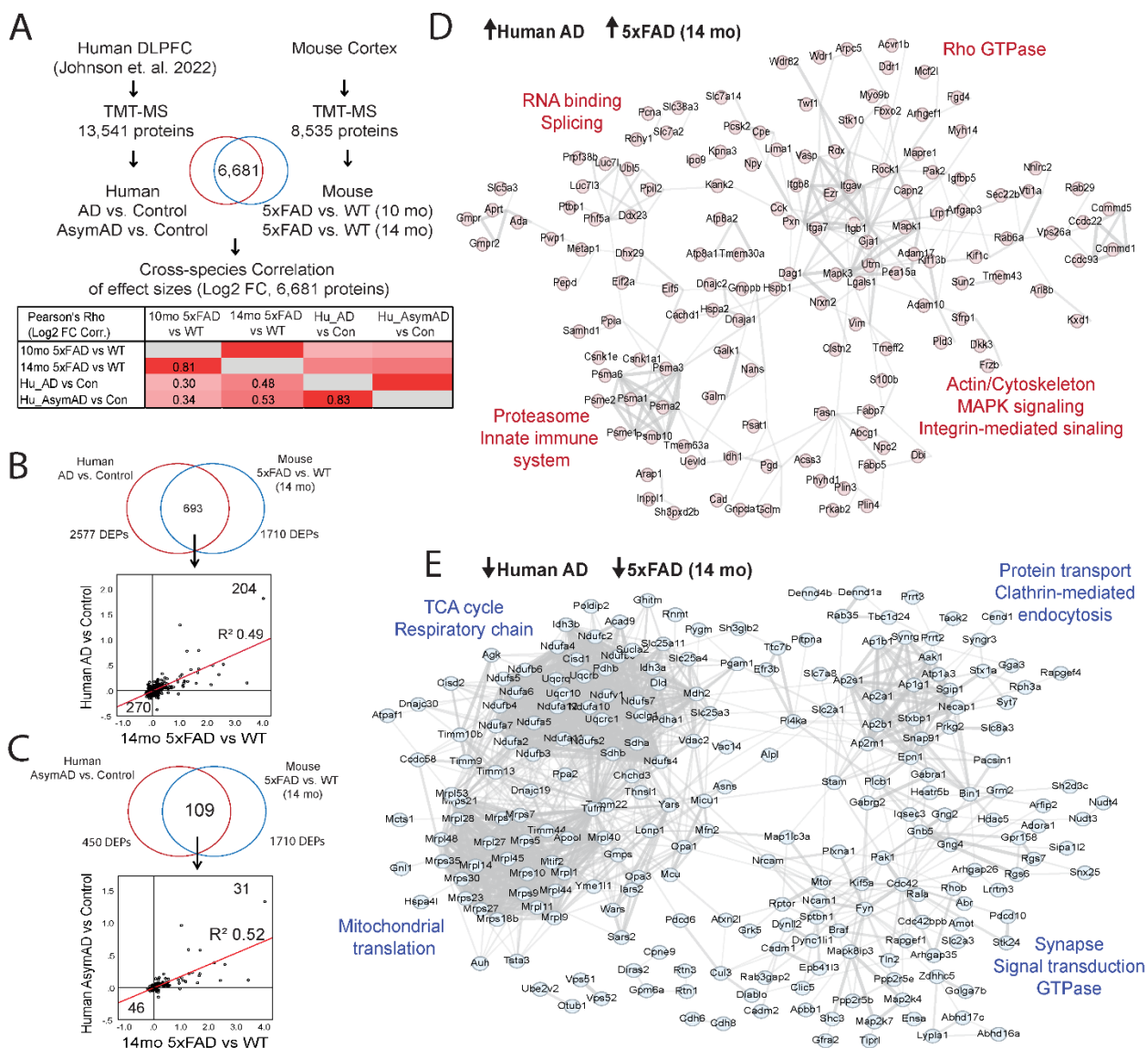
Chapter 4. Supplementary Figure 8. Analysis of concordance between human AD and mouse 5xFAD pathological changes using MS-based proteomics

A. Post-mortem brain proteomic data were obtained from Johnson et. al. (Nat. Neuroscience 2022) in which >13,500 proteins were quantified by TMT-MS. This dataset was derived from post-mortem dorsolateral pre-frontal cortex from subjects with AD+dementia (AD), asymptomatic AD (AsymAD) and from controls (no evidence of AD or other neurodegenerative disease by pathology). Of these, 6,681 proteins were also quantified in our mouse bulk proteomic TMT-MS dataset (also see **Supplementary Data 4**). Pearson's correlation coefficients were calculated, correlating log2-transformed fold changes (Log2FC) (Humans: AD vs. Control, AsymAD vs. Control; Mice: 14 mo 5xFAD vs. Control; 10 mo 5xFAD vs. Control). Pearson's was appropriate given the normal distribution and continuous nature of log2-transformed FC data. These were summarized as a heat-map (deep red indicating a Pearson's Rho =1, 0 indicating Rho =0).

2594   **B.** Log2FC correlations between humans (AD vs. Control) and mice (14 mo 5xFAD vs. WT)
2595   limited to DEPs in both datasets. Pearson R2 values are shown. Number is each quadrant
2596   represent number of proteins.
2597   **C.** Log2FC correlations between humans (AsymAD vs. Control) and mice (14 mo 5xFAD vs.
2598   WT) limited to DEPs in both datasets. Pearson R2 values are shown. Number is each quadrant
2599   represent number of proteins.
2600   **D, E.** STRING protein-protein-interaction networks highlighting pathways/mechanisms that are
2601   conserved across both species. Panel **D** represents concordant proteins and pathways that are
2602   increased in both human AD and in 5xFAD mice at 14 months of age. Panel **E** represents
2603   concordant proteins and pathways decreased in both human AD and 5xFAD mice at 14 months
2604   of age.
2605   Please see Supplementary Data 4 sub-sheet 4 for related source data and analyses.
2606
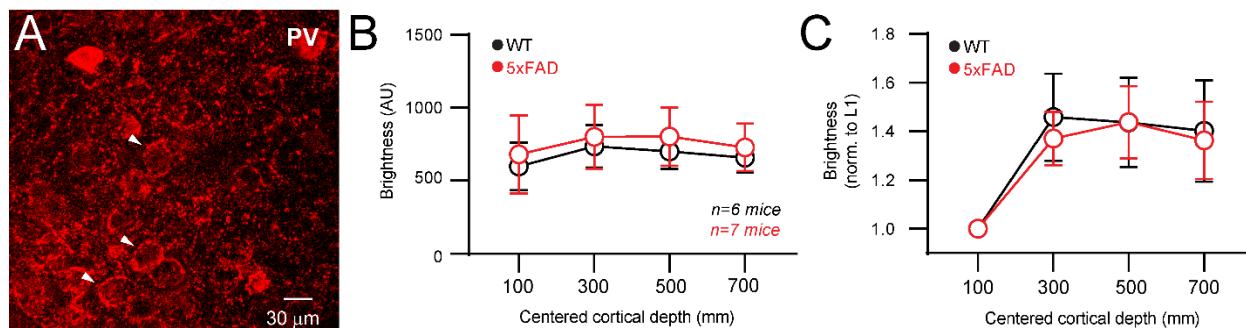
Chapter 4. Supplementary Figure 9. Parvalbumin IHC in WT and 5xFAD mice (related to Figure 4D-G)

A. Representative IHC image of anti-parvalbumin staining in the L5 region of S1 cortex. White arrows denote examples of basket structures surrounding putative pyramidal and other neuron types. Extensive staining of PV-IN presynaptic basket structures was evident using this antibody staining method.

B. Quantification of integrated fluorescence (in arbitrary units) from Alexa-594 secondary directed against Parvalbumin. Z-stacks were obtained from thin slices cortical WT and 5xFAD tissues. An ~200 μm FOV 60X objective allowed for images centered at 100, 300, 500, and 700 (± 100) micron cortical depths. Background fluorescence measured at an offset location was subtracted from all images.

C. Same quantification as in (B) but normalized to the FOV centered at 100 μm cortical depth. Reduced expression was apparent at this superficial depth, likely due to lack of extensive Parvalbumin-labeled structures with respect to deeper layers. Staining was consistent across all deeper areas corresponding to Layers 2/3, 4, and 5 and did not differ between WT and 5xFAD cortices.

A. SA-enriched — Silver Stain

B. Bulk Brain proteome

Group
- TurboID/5xFAD (filled red)
- WT/5xFAD (open red)
- TurboID/WT (filled gray)
- WT/WT (open black)

C. Exp2 Log2FC (PV-IN enriched) vs Exp1 Log2FC (PV-IN enriched)

D. 5xFAD vs. WT (DEPs)
PV-IN 248 — 32 — Bulk 284

E. 5xFAD vs. WT PV (Log2 diff)
- PV WT
- PV 5xFAD

F. Normalized log2 abund.
- PV CIBOP
- Camk2a CIBOP
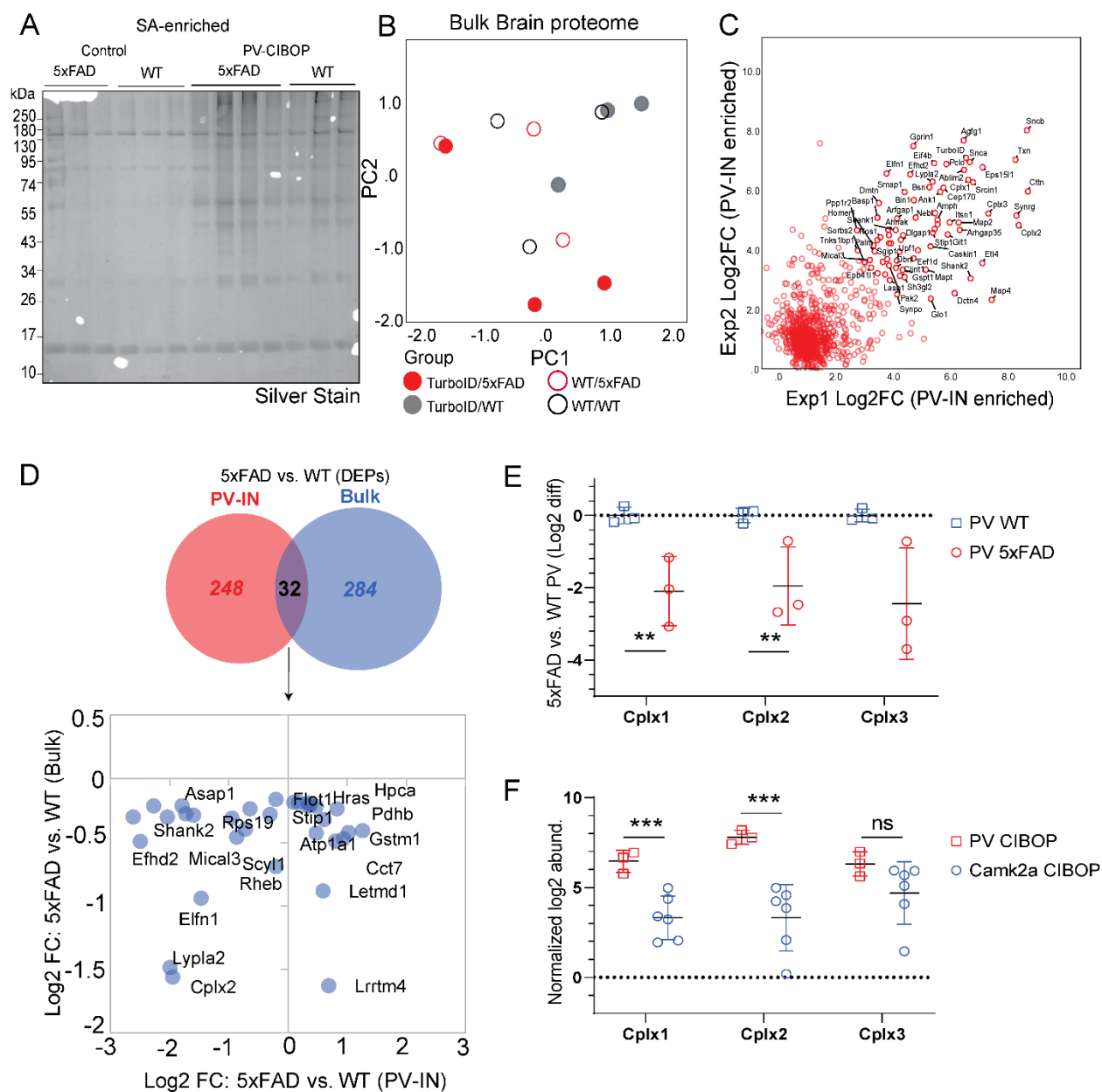
Chapter 4. Supplementary Figure 10. PV-CIBOP identifies proteomic changes occurring in PV-INs in early stages of Aβ pathology (related to Figure 5)

A. Silver-stained gel of SA-enriched PV-IN proteins from experimental animals (in Figure 5) confirming higher protein enrichment from PV-CIBOP animals as compared to control animals.
B. PCA of bulk brain (input) proteomes showing lack of an observable group-based clustering based on genotype (WT vs 5xFAD) or biotinylation (CIBOP vs controls). This contrasts with genotype differences observed in PV-IN proteomes presented in Figure 5 (see Source data file for PCA results).
C. Level of agreement between two independent PV-IN proteomes using the CIBOP approach. Experiment 1: PV-CIBOP in WT mice presented in Figure 1. Experiment 2: PV-CIBOP in WT mice presented in Figure 5. Log2 fold changes (CIBOP vs control) of proteins that were labeled in both datasets, are shown. Overall correlation between two studies was moderate (Pearson's

2638 Rho =0.61, p<0.001). Top PV-IN proteins identified by both studies, were similar (including
2639 Snca, Sncb, Cplx1, Cplx2, Cplx3, Elfn1, Bsn, as well as TurboID).
2640 **D.** DEPs (comparing 5xFAD vs. WT) identified at the level of the bulk proteome and PV-IN
2641 proteome were distinct except for 32 proteins (intersect). Agreement in level of differential
2642 abundances (log2 FC 5xFAD vs WT) between bulk and PV-IN proteomes was modest with the
2643 exception of some proteins (*e.g.,* Cplx2, Lypla2, Elfn1) which shown concordant decreased
2644 levels in both bulk and PV-IN proteomes.
2645 **E.** Protein levels of three complexins in the PV-IN proteome, comparing 5xFAD vs. WT
2646 genotypes (*p<0.05, **p<0.01, ***p<0.005).
2647 **F.** Protein levels of three complexins in PV-IN vs. Camk2a CIBOP proteomes (*p<0.05,
2648 **p<0.01, ***p<0.005).
2649
2650
2651
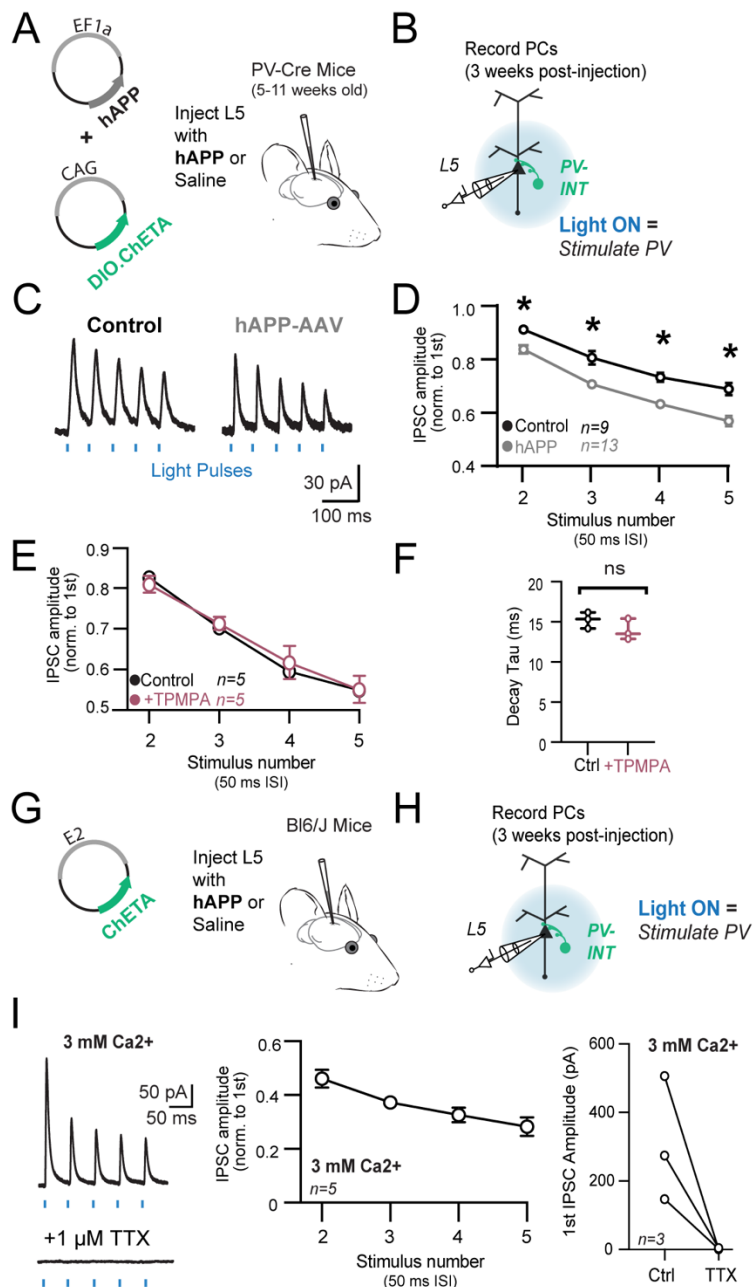
2653 *Chapter 4. Supplementary Figure 11. hAPP-AAV effect on PV neurotransmission (related to*
2654 *Figure 6)*

2655 **A.** Experimental outline: PV-Cre mice were injected with AAV.CAG.DIO.ChETA and either with
2656 or without AAV.EF1a.hAPP in the somatosensory cortex at 5-11 weeks of age.
2657 **B.** Three weeks post-injection, PV interneurons were stimulated at 20 Hz and nearby pyramidal
2658 cells were patched to examine the PV-PC paired-pulse ratio (PPR) and the multiple-pulse ratio
2659 (MPR). For **B-D**, 1.5mM external Ca^{2+} was used.
2660 **C.** Example traces of optogenetically-evoked PV inhibitory post-synaptic currents on pyramidal
2661 cells for saline-injected (left) and hAPP-AAV injected (right) cortices using 1.5mM external
2662 Ca^{2+}.

2663 **D.** IPSCs in AAV-hAPP injected mice displayed a significant change in synaptic dynamics as
2664 measured using MPR across all measured stimuli at 20 Hz. (*$p<0.05$ Two-way ANOVA with
2665 Sidak's posthoc comparisons for each stimulus between hAPP and saline control experiments).
2666 **E.** IPSCs in AAV-hAPP injected mice display no change when post-synaptic $GABA_C$ channel is
2667 blocked. (*$p<0.05$ Two-way ANOVA with Sidak's posthoc comparisons for each stimulus
2668 between hAPP and saline control experiments).
2669 **F.** IPSCs in AAV-hAPP injected mice display no change in kinetics when post-synaptic $GABA_C$
2670 channel is blocked.
2671 **G.** Experimental outline: AAV.E2.ChETA was injected in WT mice in the somatosensory cortex.
2672 **H.** Three weeks post-injection, as depicted in panel **E**, PV interneurons were stimulated with
2673 blue light pulses at 20 Hz and nearby pyramidal cells were patched to examine the PV-PC PPR
2674 and MPR at 3mM external Ca^{2+}.
2675 **I.** AAV.E2.ChETA-driven IPSCs were strongly depressing with 3mM external Ca^{2+}. IPSCs in
2676 these conditions were completely abolished after the application of 1mM TTX in the bath
2677 solution.

2678 Proteomics included in this chapter were run and analyzed by Dr. Prateek Kumar and Dr. Srikant

2679 Rangaraju.

2680

Chapter 5: Entorhinal Cortex Vulnerability to human APP expression promotes hyperexcitability and tau pathology

I don't know, it's your PhD.

-Dr. Matthew Rowan
[When I asked if I should try injecting hAPP into the LEC,
or any similar type of question for that matter.]

This chapter was adapted from: Goettemoeller, A. M. *et al*. Entorhinal cortex vulnerability to human APP expression promotes hyperexcitability and tau pathology. *bioRxiv*, doi.org/10.1101/2023.11.06.565629 (2023).[339]

2681 <u>5.1 Summary</u>

2682 Preventative treatment for Alzheimer's Disease is of dire importance, and yet, cellular

2683 mechanisms underlying early regional vulnerability in Alzheimer's Disease remain unknown. In

2684 human patients with Alzheimer's Disease, one of the earliest observed pathophysiological

2685 correlates to cognitive decline is hyperexcitability. In mouse models, early hyperexcitability has

2686 been shown in the entorhinal cortex, the first cortical region impacted by Alzheimer's Disease. The

2687 origin of hyperexcitability in early-stage disease and why it preferentially emerges in specific

2688 regions is unclear. Using cortical-region and cell-type-specific proteomics and patch-clamp

2689 electrophysiology, we uncovered differential susceptibility to human-specific amyloid precursor

2690 protein (hAPP) in a model of sporadic Alzheimer's. Unexpectedly, our findings reveal that early

2691 entorhinal hyperexcitability may result from intrinsic vulnerability of parvalbumin (PV)

2692 interneurons, rather than the suspected layer II excitatory neurons, despite both cell types similarly

2693 expressing hAPP. This vulnerability of entorhinal PV interneurons is specific to hAPP, as it could

2694 not be recapitulated with increased murine APP expression. However, partial replication of the

2695 findings could be seen after introduction of a murine APP chimera with a humanized amyloid-beta

2696 sequence. Furthermore, the Somatosensory Cortex showed no such vulnerability to adult-onset

2697 hAPP expression, potentially resulting from PV interneuron variability between the two regions

2698 based on physiological and proteomic evaluations. Interestingly, entorhinal hAPP-induced

2699 hyperexcitability was quelled by co-expression of human Tau at the expense of increased

2700 pathological tau species. This study suggests early disease interventions targeting non-excitatory

2701 cell types may protect regions with early vulnerability to pathological symptoms of Alzheimer's

2702 Disease and downstream cognitive decline.

2703

2704   5.2 Introduction

2705   Alzheimer's Disease (AD) is the most prevalent neurodegenerative disease, yet current

2706   treatments are unable to prevent its initiation and progression. Although brain regions of early

2707   vulnerability have been known for over 30 years[90], our understanding of what makes certain areas

2708   more susceptible remains unknown. The first cortical region to display pathology and degeneration

2709   in AD is the Lateral Entorhinal Cortex (LEC)[90,94,105,117]. Notably, landmark studies identified Layer

2710   II (LII) neurons as highly vulnerable to early neurodegeneration with up to 60% cell death in mild

2711   AD patients and up to 90% in severe cases[105]. More recently, LII LEC principal neurons were also

2712   characterized as a cell population exhibiting amyloid pathology[94]. However, the distinctive

2713   features which impart vulnerability to neurons in the LEC AD remain unclear. Uncovering region-

2714   specific cellular mechanisms could improve our understanding of the initiating factors in the AD

2715   cascade and are imperative in determining potential interventions at a time when subsequent

2716   cognitive decline and neurodegeneration might still be prevented.

2717

2718   Hyperexcitability is one of the earliest pathophysiological biomarkers in the human AD

2719   brain, and its emergence correlates with severity of cognitive decline in individuals[106].

2720   Hyperexcitability is also observed in recordings from *in vivo* and *in vitro* models of AD

2721   pathology[75,107-112], arising prior to amyloid plaque deposition[113] and likely contributing to spine

2722   degeneration[114]. Interestingly, hypermetabolism[115] and hyperexcitability[109,116] emerged in the LEC

2723   of a sporadic AD mouse model before spreading to other regions[117]. It is unclear whether cell-

2724   intrinsic changes in principal neuron excitability or other forms of circuit dysfunction are

2725   responsible for aberrant LEC activity in early AD. Hyperexcitability may also arise due to changes

2726   in local circuit inhibition from GABAergic interneurons, with several lines of evidence

2727 demonstrating impaired inhibitory tone[107,109,115], most notably from fast-spiking parvalbumin+

2728 (PV) interneurons[108,110,113]. Whether the basal properties of PV interneurons in the LEC confer

2729 functional vulnerability with respect to PV cells in other regions is unknown. Thus, observing

2730 baseline cellular and regional differences coupled with adult-onset, region-specific APP or Tau

2731 expression is imperative to properly dissect inherent vulnerabilities underlying susceptibility of

2732 the LEC to early AD pathology.

2733

2734 <u>5.3 Results</u>

2735 *PV interneurons in an AD-vulnerable region are functionally and molecularly distinct*

2736 We first compared active and passive features of excitatory neurons in AD-vulnerable and

2737 non-vulnerable cortical regions. Excitatory neurons in LII of Lateral Entorhinal Cortex (LEC)

2738 (highly vulnerable to early AD pathology[94]) and L5 pyramidal cells (PCs) in Somatosensory

2739 Cortex (SS Ctx) of wild type (WT) mice were chosen for comparison, as each represent projection

2740 output neurons and are innervated by similar dominant inhibitory networks[340]. Despite differences

2741 in their dendritic anatomy, axonal projections, and overall local circuit operations, these two cell

2742 types showed striking overlap in their firing capacity, AP waveforms, and most other biophysical

2743 features (Fig 1a-c), with only slight biophysical differences noted (Extended Data Table 1).

2744 Because different cortical regions perform operations over non-overlapping frequency domains,

2745 we hypothesized that differences in the intrinsic excitability of inhibitory interneurons might help

2746 tune circuit activity locally. Thus, we assessed physiological phenotypes of 'fast-spiking' PV

2747 interneurons in each region, using an unbiased, PV-specific enhancer-AAV fluorescent targeting

2748 approach[175]. In the LEC, the E2 enhancer displayed high overlap (92.62±5.7%) with PV+ somas

2749 from the previously established mouse model, PV-tdTom (Extended Data Fig. 7a,b). Surprisingly,

2750   PV interneurons in the LEC maximally fired at only half the rate of SS Ctx PV interneurons (Fig.

2751   1d,e), likely due to their far broader action potentials with respect to PV interneurons recorded

2752   from SS Ctx (Fig. 1f-h)[340]. The first action potential of each AP train was also larger in amplitude

2753   in the LEC PV interneurons (Fig. 1f-h). Furthermore, resting membrane potential and AP threshold

2754   were significantly different for PV cells when compared by region (Extended Data Table 1,

2755   bottom). Despite expressing similar passive features in LEC and SS Ctx (*e.g.,* membrane

2756   capacitance; 70.17 ± 5.46 pF vs. 71.91 ± 9.51 pF; LEC vs SS respectively, Extended Data Table

2757   1), their starkly divergent excitability suggests unique molecular signatures which may also

2758   underlie differential vulnerability in AD and other diseases.
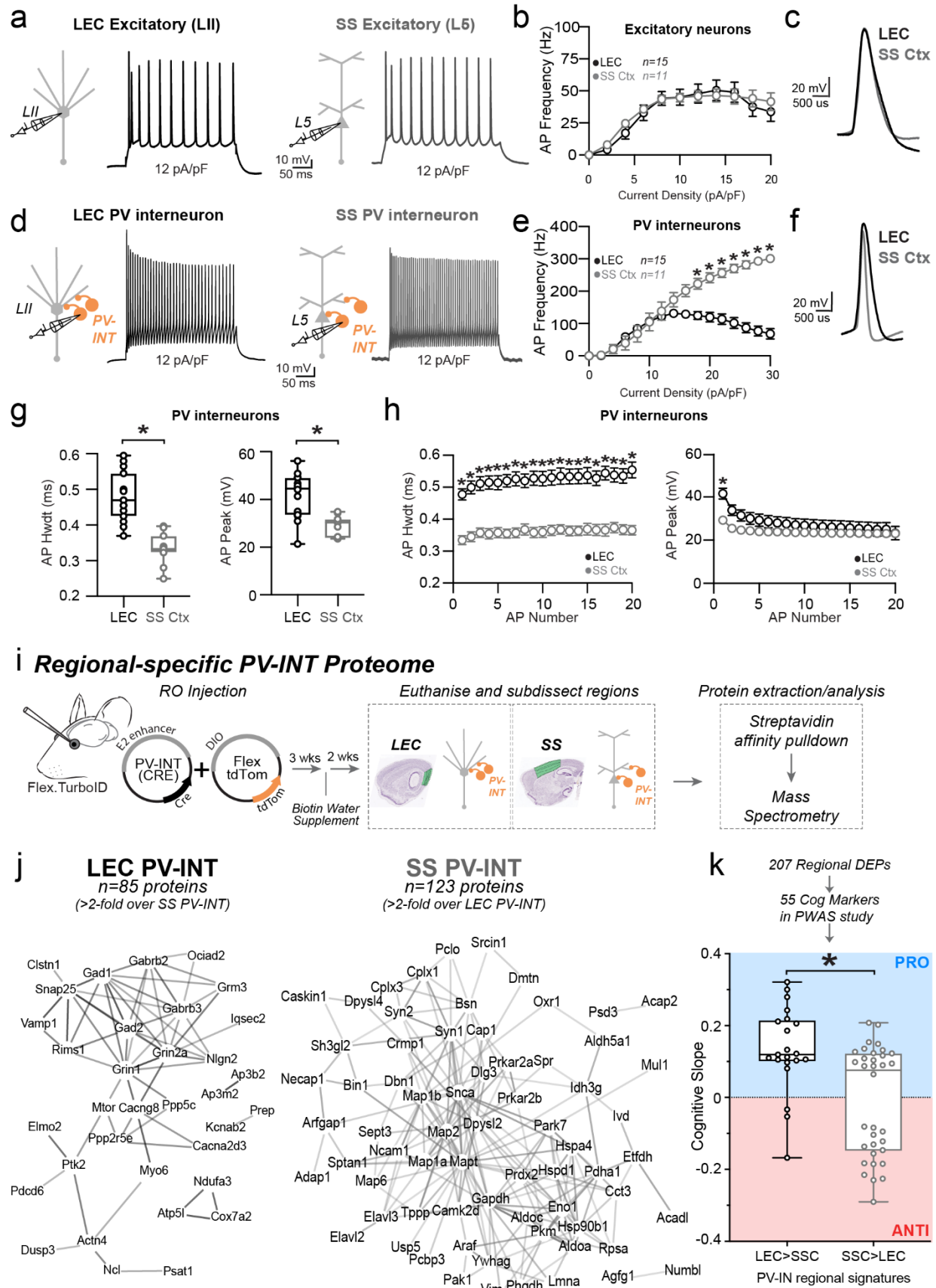
2759

Figure 1. PV-INTs in an AD vulnerable region display reduced baseline firing
(Caption continued onto next page…)

Figure 1. PV-INTs in an AD vulnerable region display reduced baseline firing

a,d. Graphical summary of AAV.E2.tdTom stereotactic injection in either the Lateral Entorhinal Cortex or Somatosensory cortex. PV-interneurons were fluorescently targeted for whole-cell current clamp recordings (d) as well as nearby excitatory cells (a). AP firing elicited by square pulse current injections of varying magnitude normalized to cellular capacitance during recording in excitatory cells (a) and PV-interneurons (d) mice from L2 LEC (left) and L5 SS Ctx (Right) at 12 pA/pF.
b. Group data summary of AP firing frequency in WT mice. Excitatory cells between LEC and SS Ctx showed no difference in AP Frequency (Hz) Ctx (LEC: Max: 50.42±5.63 Hz, SS Ctx: Max: 46.35±5.51 Hz, p=0.46).
c. AP waveforms of excitatory cells were compared at 12 pA/pF square pulse injections in WT mice from L2 LEC and L5 SS Ctx. Aps from the 1st spike in the train are superimposed for comparison.
e. Group data summary of AP firing frequency in WT mice. PV interneurons in L2 LEC show a strong reduction in AP max firing frequency at higher current densities when compared to PV interneurons of L5 SS Ctx (LEC: Max: 131.6±11.48 Hz, SS Ctx: Max: 301.1±27.59 Hz, p=<0.0001 for 16 pA/pF and above).
f. AP waveforms of tdTom+ PV interneurons were compared at 12 pA/pF square pulse injections in WT mice from L2 LEC and L5 SS Ctx. Aps from the 1st spike in the train are superimposed for comparison.
g. Summary data of AP properties. L2 LEC PV interneurons display a significantly increased AP peak (LEC: 41.86±2.66 pA, SS: 28.75±1.30 pA, p=0.0002, t= 4.83, df=24, two-tailed unpaired t-test) and AP Hwdt (LEC: 0.48 ± 0.02 ms, SS: 0.33 ± 0.01 ms, p=<0.0001, t=6.10, df=25) for the first AP of the spike train. Individual data points and box plots are displayed. Significance is defined as p<0.05, unpaired t-tests.

h. Relationship between AP peak or width, in WT mice and AP # during spike trains elicited with a 12 pA/pF current injection.
i. Experimental approach for Regional-specific PV-interneuron Proteomes: E2 enhancer Cre AAV was retro-orbitally delivered to WT (Control) or Rosa26TurboID/wt (PV-CIBOP) mice (n=3 per genotype, including males and females) followed by 3 weeks of Cre-mediated recombination, and 2 additional weeks of biotin supplementation (drinking water). The brain was then microdissected into LEC and SS Ctx and prepared for biochemical studies.
j. STRING analysis of PV-enriched proteins for LEC PV-INTs (left) and SS Ctx PV-INTs (right) (>2-fold enriched over other region) shows synaptic receptors, synaptic vesicle and exocytosis related proteins including GAD1/2, GABAb2/3, and complexins.
k. Enrichment of PWAS-identified proteins associated with cognitive slope in LEC (left) or SS Ctx (right) PV-enriched proteomic signatures. Cognitive slope was estimated in ROSMAP cases. Positive slope indicates cognitive stability or resilience when proteins are present while a negative slope indicates cognitive decline when proteins are present. Proteins positively correlated with cognitive slope are referred to as pro-resilience proteins while those negative correlated with cognitive slope are anti-resilience proteins. Enrichment of previously identified 'pro' and 'anti' resilience proteins within the PV protein dataset identified by CIBOP were assessed after weighting based on strength of association between proteins and cognitive slope. (LEC: 0.13± 0.03 and SS Ctx: -0.01±0.03; p=0.001, t=3.71, df=53, two-tailed Mann Whitney test).
For b, e, and h: For all summary graphs, data are expressed as mean (± SEM). Statistical significance is denoted as *=p<0.05, as determined by Two-way ANOVA with Sidak's multiple comparison test. For all summary graphs, data are expressed as mean (± SEM).

Also see Extended Data Figure 1 for related analyses and datasets.

2761 these regions. Single-neuron transcriptomics is a sound method for uncovering molecular

2762 diversity between different brain cell types. Nonetheless, the functional relevance of these studies

2763 is limited by substantial discordance between mRNA and protein in neurons[341]. Thus, we opted to

2764 isolate the native-state proteomes of PV interneurons from each region using our recently

2765 developed neuron-type-specific TurboID method[2] (Fig. 1i). This was achieved through systemic

2766 AAV injections to achieve whole-cortex expression of a PV-specific, Cre-expressing enhancer-

2767 AAV in Flex.TurboID mice[142] followed by region-specific microdissection (Fig. 1i; Extended Data

2768 Fig. 1a). Over 800 proteins were biotinylated in PV interneurons in each region, of which nearly

2769 two hundred proteins showed region-specific differential abundances (unadjusted p<0.05 n=207;

2770 n=185 below the permFDR 0.05 threshold; Extended Data Datasheet 1; Fig. 1j). Generally, LEC

2771 PV interneuron proteomes showed biased enrichment in transmembrane and synaptic ion channels

2772 and transporters, while SS PV interneuron proteomes showed biased enrichment in microtubule

2773 binding, glycolysis, and fatty acid metabolism-related proteins (Extended Data Fig. 1b).

2774

2775 *Relationships between PV interneuron proteomic signatures with cognitive resilience in human*

2776 *AD*

2777 We next considered whether PV interneuron proteins differentially expressed by region

2778 (Fig. 1j) were representative of proteins associated with cognitive stability during aging. To

2779 achieve this, we used data from a protein-wide association study of cognitive resilience from

2780 human brain samples (Religious Orders Study and the Rush Memory and Aging Project;

2781 'ROSMAP'[146]). In this study, rate of cognitive decline (cognitive slope) was correlated with post-

2782 mortem brain protein levels quantified by mass spectrometry, identifying proteins positively

2783 associated with cognitive stability (pro-resilience proteins) and those negatively associated with

2784 cognitive stability (anti-resilience proteins) (Fig. 1k). We found that wild-type LEC PV

2785 interneurons displayed significantly more 'pro-resilience'-associated proteins as compared to SS

2786 Ctx PV interneurons (p=0.0011; Mann-Whitney test; Fig. 1k). As nearly all the LEC PV

2787 interneuron enriched proteins associated with cognitive stability during aging, we next explored

2788 whether expression of these enriched proteins was perturbed throughout stages of AD pathology.

2789

2790 We next explored whether expression of these enriched proteins was perturbed throughout

2791 stages of AD pathology in humans. While several proteomics surveys of post-mortem brain tissues

2792 from AD and control brain have been performed, few studies have published data comparing the

2793 entorhinal cortex (EC) to neocortical regions, such as the frontal cortex (FC). This is true

2794 particularly regarding disease staging. In a recent study[342], EC and FC regions from post-mortem

2795   brains of control and AD cases (BRAAK stages I-III [early] and IV-VI [late]) were analyzed by

2796   quantitative MS. This yielded 737 differentially-enriched proteins (DEPs) comparing AD to

2797   control, at either early (BRAAK I-III) or late (BRAAK IV-VI) stages, which were significant in

2798   either EC or FC regions. Among these, 93 human DEPs were observed in our PV-CIBOP proteome

2799   (Extended Data Fig. 2a, Extended Data Datasheet 2). Of these, 23 proteins showed differential

2800   levels in SS Ctx PV interneurons as compared to LEC PV interneurons (Extended Data Fig. 2b).

2801   Surprisingly, of the regional PV interneuron proteins that were altered in human AD brain, many

2802   were pro-resilience proteins. Importantly, the LEC-enriched PV interneuron proteins (including

2803   pro-resilience proteins) showed decreased levels in the EC of human AD cases (Extended Data

2804   Fig. 2b). Thus, resilience factors in PV interneurons of the entorhinal cortex may be lost as AD

2805   pathology increases.

2806

2807   Based on observed associations between regional proteomic signatures of PV interneurons

2808   with cognitive resilience and with early changes occurring in human AD brain, we further assessed

2809   relationships between regional proteomic signatures of PV interneurons with APP and Tau protein-

2810   protein interactomes. Many APP-interacting proteins have been identified. Of 243 APP interactors

2811   identified from physical protein-protein interactors listed in the STRING database, 31 APP

2812   interactors were identified in PV-CIBOP proteomes. From these, 14 proteins were highly enriched

2813   regionally in PV interneurons. 10 proteins were highly enriched in SS Ctx PV interneurons

2814   (including Numbl, Snca, Mapt, Bin1, Hspd1, Hspa4, Hspa8, Eno1, Gapdh, Mapk3) (Extended

2815   Data Fig. 3a) and 4 were enriched in LEC PV interneurons (Apoo, Grin1, Clstn1, Grin2a)

2816   (Extended Data Fig. 3a, Extended Data Datasheet 3). However, these physical associations may

2817   be altered in AD with either altered APP expression or mutations in the APP gene.

2818

2819   In a consensus analysis of tau protein interactors[147], over 2000 tau protein interactors were

2820   identified across seven human post-mortem proteomics studies. Of these, 261 proteins were

2821   identified consistently as interactors (represented in at least three of the studies), comprising a

2822   high-confidence list of tau interactors. These proteins, as previously described[147], were enriched

2823   in proteins involved in protein translation, mRNA processing and splicing, protein folding,

2824   intracellular transport, proteasome assembly, and glycolysis. In our work, 107 of these were

2825   labeled by CIBOP in PV interneurons (Extended Data Datasheet 3,4). Of these, 32 proteins had

2826   higher levels in SS Ctx PV interneurons, 8 with higher levels in LEC PV interneurons, while 67

2827   did not show regional differences (Extended Data Fig. 3b). In contrast, non-tau interactors were

2828   more evenly distributed across SSC and LEC PV interneurons. This result suggests that tau

2829   interactors are present at higher levels in PV interneurons located in the SS Ctx as compared to

2830   those in the LEC (Chi square statistic 20.7, p=0.00032). This seems to be consistent with higher

2831   levels of MAPT in SS Ctx PV interneurons as well. Tau interactors in SS Ctx PV interneurons

2832   included 14-3-3 proteins, heat shock proteins, extracellular vesicle proteins, actin/cytoskeletal

2833   proteins and RNA binding proteins. Whether the higher abundance of MAPT and tau interactors

2834   in SS Ctx PV interneurons influences the circuit's resilience to hyperexcitability at early time

2835   points is unclear. To further explore differential responses of PV interneurons between the LEC

2836   and neocortex, we utilized a model of adult-onset induction of AD-related pathology which could

2837   be regionally and temporally controlled.

2838

2839   **Adult-onset human APP expression reduces PV interneuron excitability specifically in LEC**

2840   Traditional rodent models of AD express various (typically mutant) forms of hAPP (and

2841   related processing proteins), with transgene expression beginning while neuronal circuits are still
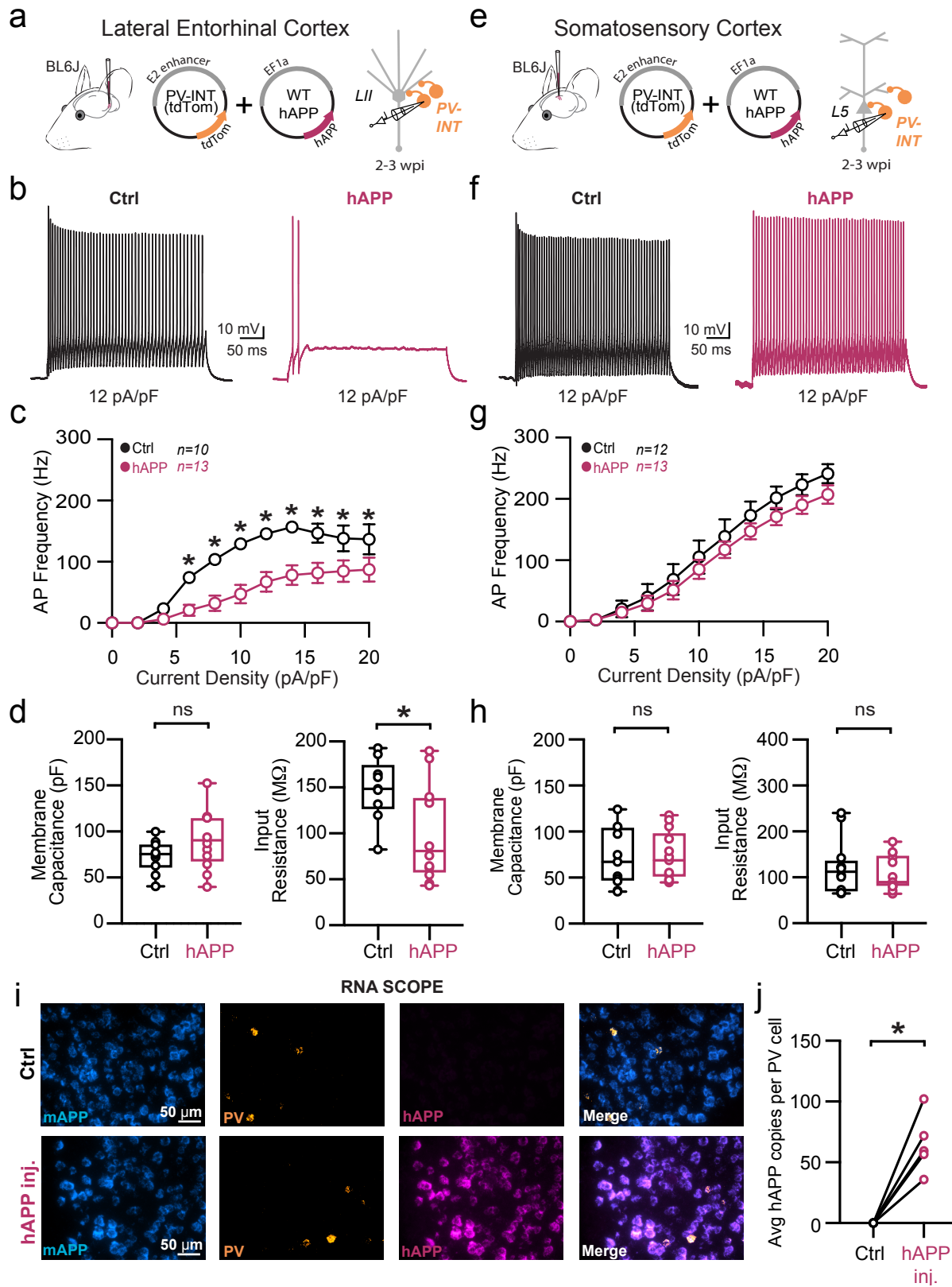
Figure 2. Adult-onset human APP expression reduces LEC PV interneuron excitability
(Caption continued onto next page…)

Figure 2. Adult-onset human APP expression reduces LEC PV interneuron excitability

a. Graphical summary of AAV.E2.tdTom and AAV.EF1a.hAPP (or for Ctrl, saline) stereotactic injection in the Lateral Entorhinal Cortex. PV-interneurons were fluorescently targeted (tdTom+) for whole-cell current clamp recordings.
b. AP firing elicited by square pulse current injections of varying magnitude normalized to cellular capacitance during recording in tdTom+ PV-INT from L2 LEC at 12 pA/pF.
c. Group data summary of AP firing frequency in L2 LEC from Ctrl (black) and hAPP injected mice (magenta). LEC PV interneurons from hAPP injected mice show a significant reduction in AP Frequency (Hz) when compared to Ctrl(Ctrl: Max: 156.6 ±13.52 Hz, hAPP: Max: 91.84± 8.74 Hz).
d. Summary data of AP properties. L2 LEC PV interneurons after hAPP injection display a significantly decreased input resistance (Ctrl: 145.7 ± 11.61 MΩ, hAPP: 88.78 ± 15.11 MΩ, p=0.01, t=2.73, df=21) and an insignificant increase in membrane capacitance (Ctrl: 68.83 ± 5.34 pF, hAPP: 90.21 ± 9.77 pF, p=0.07, t=1.92, df=21).
e. Graphical summary of AAV.E2.tdTom and AAV.EF1a.hAPP (or for Ctrl, saline) stereotactic injection in the Somatosensory Cortex. PV-interneurons were fluorescently targeted (tdTom+) for whole-cell current clamp recordings.
f. AP firing elicited by square pulse current injections of varying magnitude normalized to cellular capacitance during recording in tdTom+ PV-INT from L5 SS Ctx at 12 pA/pF.

g. Group data summary of AP firing frequency in L5 SS Ctx from Ctrl (black) and hAPP injected mice (magenta). SS Ctx PV interneurons from hAPP injected mice show no significant change in AP Frequency (Hz) when compared to Ctrl (Ctrl: Max: 301.1 ±27.59 Hz, hAPP: Max: 257.2± 24.06 Hz).
h. Summary data of AP properties. SS Ctx interneurons after hAPP injection display an unchanged Membrane Capacitance (Ctrl: 71.91 ± 9.514, hAPP: 73.14 ± 7.327, p=0.9180, t=0.1041, df=23) and input resistance (Ctrl: 121.2 ± 17.14, hAPP: 109.1 ± 10.56, p=0.5475, t=0.6106, df=23).
i. RNAscope representative images at 40x magnification for Ctrl injected (top) and hAPP injected mice (bottom): mAPP mRNA (cyan), Parvalbumin mRNA (gold), human APP mRNA (magenta), and a final merged image.
j. RNAscope quantification for hAPP copies per PV+ cell comparing control to hAPP injected. hAPP injected show a significant increase in hAPP copies per PV+ cell (p=0.0039, t=5.987, df=4; two-tailed paired t-test).

For all summary graphs, data are expressed as mean (± SEM). For c, g, and i: Statistical significance is denoted as *=p<0.05, as determined by Two-way ANOVA with Sidak's multiple comparison test. For d, h: Individual data points and box plots are displayed. Statistical significance is denoted as *=p<0.05, as determined by two-tailed unpaired t-test.

2844   maturing, and also in a brain-wide fashion. To eliminate the substantial network effects of hAPP

2845   during development[333] and to assess inherent vulnerability of individual areas independently, we

2846   used an adult-onset, region-specific AAV approach. To explore whether differences in basal

2847   excitability and proteomic signatures of PV interneurons described early conferred region-specific

2848   vulnerability in an AD pathology context, we virally expressed wild-type hAPP in either the LEC

2849   or SS Ctx in 8-12 week old (adult) mice. Full length hAPP (hAPP 770) (NM_000484.4), an isoform

2850   with increased expression in human AD[54,55] was expressed using the pan-neuronal EF1a promoter

2851   (Figure 2a; AAV.Ef1a.hAPP). We assessed the impact of this hAPP isoform on PV interneurons in

2852   the LEC and SS Ctx independently after 2-3 weeks of expression.

2853

2854   In LEC PV interneurons, we observed a dramatic reduction in PV interneuron firing (Fig.

2855   2b,c) likely related to a reduction in input resistance (Fig. 2d), as no other relevant factors (*e.g.,*

2856   AP waveform, RMP, AP threshold, Membrane capacitance) (Fig. 2d; Extended Data Fig. 4) were

2857   affected. By contrast, PV interneurons in the SS Ctx displayed no change in firing rate (Fig. 2g)

despite an increase in AP threshold and AHP (Extended Data Fig. 5d). All other active and passive features were unchanged (Fig. 2h; Extended Data Fig. 5b-e). Using unsupervised clustering of LEC 'fast-spiking' interneuron biophysical features, control- and hAPP-expressing PV interneurons clustered separately (Extended Data Fig. 12b). The presence of hAPP mRNA and protein was confirmed in PV neurons 2-3 weeks after injection (Fig. 2i-j; Extended Data Fig. 6) with RNAscope and PV-specific flow cytometry. Together, the intrinsic excitability of PV interneurons was significantly reduced in the LEC, but not SS Ctx, following hAPP expression.

Adult-onset murine APP expression does not affect PV interneuron physiology

Several studies of different mouse models of APP-related pathology report altered intrinsic excitability in GABAergic interneurons[75,108-110,113]. Whether this is simply a result of hAPP overexpression[343] during development or effects of its downstream cleavage products remain controversial. To address this, we next injected a virus containing full-length murine APP (mAPP) (NM_001198823.1) (Fig. 3a; AAV.Ef1a.mAPP) into the LEC. Despite a significant increase of mAPP expression over endogenous background levels (Extended Data Fig. 8d,e), the robust changes in PV interneuron firing and input resistance seen following hAPP expression (Fig. 2) were lacking following 2-3 weeks of viral mAPP expression (Fig. 3b,c; Extended Data Fig. 8b,c). Importantly, RNAscope studies confirmed that the magnitude of AAV-induced mAPP expression was similar to that of hAPP in earlier experiments (Figure 3d), indicating that the differential physiological effects were not due to variability in APP expression levels. Furthermore, as we saw no alterations in the somatosensory cortex PV interneurons after hAPP expression, we conclude this differing response is not due to a specific inflammatory effect of the human protein alone.

2880   Thus, hAPP-induced dysfunction of LEC PV interneurons cannot be explained by over-expression

2881   of APP alone.

2882

2883   *Adult-onset murine APP expression with a humanized amyloid-beta sequence impairs PV*

2884   *interneuron excitability, but does not recapitulate findings from full-length hAPP*

2885   As the responses of PV interneurons to human APP and murine APP was so dichotomous,

2886   we next investigate whether this effect could be mediated solely by humanizing the amyloid-beta

2887   sequence of APP. To address this, we created a virus containing full-length murine APP (mAPP)

2888   (NM_001198823.1) but humanized the three differing amino acids in the amyloid-beta sequence,

2889   G676R, F681Y, and R684H (Fig. 3e; AAV.Ef1a.mAPP/hAβ Chimera) into the LEC. Remarkably,
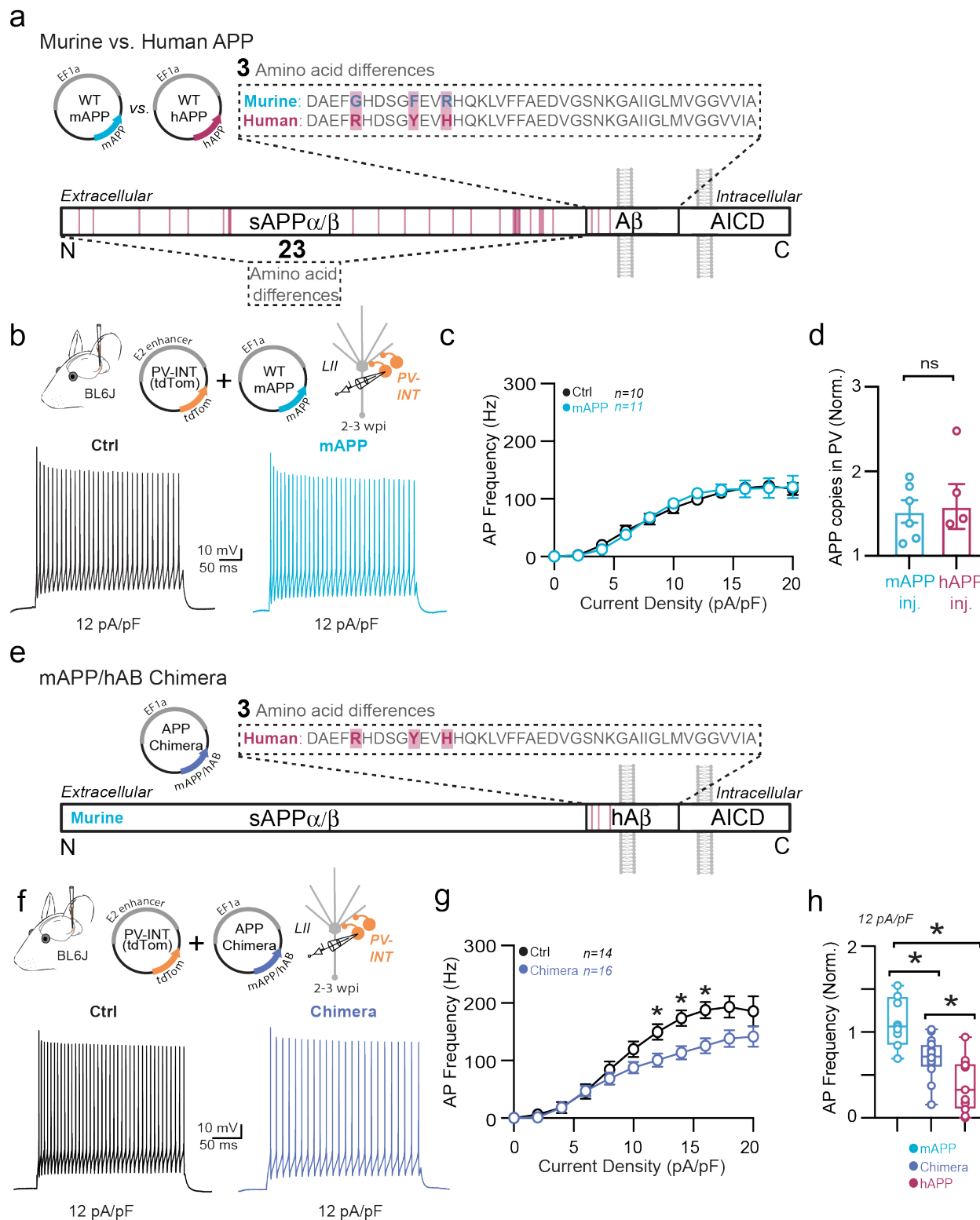
Figure 3. Murine APP does not affect PV interneuron physiology, but mAPP/hAB chimera replicates partial findings of hAPP-induced deficits
(Caption continued onto next page…)

Figure 3. Murine APP does not affect PV interneuron physiology, but mAPP/hAB chimera replicates partial findings of hAPP-induced deficits

a. Pictorial representation of differing amino acids between murine APP and human APP proteins; 26 different amino acids in total, 3 of which are in the amyloid-beta segment of the protein.

b. Graphical summary of AAV.E2.tdTom and AAV.EF1a.mAPP (or for Ctrl, saline) stereotactic injection in the Lateral Entorhinal Cortex. PV interneurons were fluorescently targeted for whole-cell current clamp recordings. AP firing elicited by square pulse current injections of varying magnitude normalized to cellular capacitance during recording in PV interneurons from Ctrl (left) and mAPP injected (right) L2 LEC at 12 pA/pF.

c. Group data summary of AP firing frequency in Ctrl and mAPP injected mice. PV interneurons between Ctrl and mAPP injected showed no difference in AP Frequency (Hz) (Ctrl: Max: 122.3 ±11.11 Hz, mAPP: Max: 120.6 ± 11.50 Hz, p=0.95). Statistical significance is denoted as *=p<0.05, as determined by Two-way ANOVA with Sidak's multiple comparison test.

d. RNAscope quantification for APP copies per PV+ cell with APP injected (mAPP or hAPP) each normalized to their contralateral hemisphere average endogenous murine APP copy per PV+ cell. mAPP injected and hAPP injected mice show similar increases in increased APP expression. copies per PV+ cell (p=0.84, t=0.21, df=9; two-tailed unpaired t-test).

e. Pictorial representation of the resultant Chimera protein; murine APP with a humanized amyloid-beta segment.

f. Graphical summary of AAV.E2.tdTom and AAV.EF1a.mAPP/hAB Chimera (or for Ctrl, saline) stereotactic injection in the Lateral Entorhinal Cortex. PV interneurons were fluorescently targeted for whole-cell current clamp recordings. AP firing elicited by square pulse current injections of varying magnitude normalized to cellular capacitance during recording in PV interneurons from Ctrl (left) and Chimera injected (right) L2 LEC at 12 pA/pF.

g. Group data summary of AP firing frequency in Ctrl and Chimera injected mice. PV interneurons between Ctrl and mAPP injected showed no difference in AP Frequency (Hz) (Ctrl: Max: 193.6 ±19.47 Hz, mAPP: Max: 145.4 ± 14.05 Hz, p<0.0001; for 12 pA p=0.0378, for 14 pA p=0.0368, for 16 pA p=0.0426). Statistical significance is denoted as *=p<0.05, as determined by Two-way ANOVA with Sidak's multiple comparison test.

h. Comparison of PV interneuron firing frequencies expressing mAPP, mAPP/hAB Chimera, or hAPP normalized to their dataset controls at 12 pA/pF. Statistical significance is denoted as *=p<0.05, as determined by Ordinary one-way ANOVA with Tukey's multiple comparisons test. (mAPP vs. Chimera: p=0.0011, mAPP vs. hAPP: <0.0001, Chimera vs. hAPP: p=0.0335; df=35).

2891   after expressing the APP Chimera in the LEC for 2-3 weeks, we again saw a reduction in PV

2892   interneuron firing (Fig. 3f,g). Interestingly, however, the reduction was not significant across

2893   current densities as with hAPP, and similarly did not show as great a reduction as hAPP (Fig. 3h;

2894   Extended Data Fig. 9d). Furthermore, the only alteration which could cause this reduction would

2895   be related to the increase in AP half-width (Extended Data Fig. 9e,f), rather than an alteration in

2896   input resistance or other relevant factors (Extended Data Fig. 9b,c,g) Thus, the contribution of the

2897   human amyloid-beta sequence contributes to the impaired PV interneuron physiology but was not

2898   sufficient to induce the drastic changes seen after full-length human APP expression.

2899

2900   *Adult-onset human APP expression does not affect excitatory cell intrinsic properties*

2901   Because recent studies using different mouse models of APP/Aβ pathology report altered

2902   intrinsic excitability of excitatory neurons[333,344], we also assessed the effects of 2-3 weeks of hAPP

2903   expression on principal excitatory cells in the LEC and SS Ctx (Fig. 4a,e). Consistent with

2904   unaltered PV firing in SS Ctx, no change in intrinsic firing frequency or passive properties were

2905   noted in pyramidal cells in the SS Ctx (Fig. 4f-h; Extended Data Fig. 11). Surprisingly, we also

2906   observed no impact of hAPP on intrinsic AP firing of LII LEC excitatory neurons (Fig. 4b,c).

2907   Further, membrane capacitance was unperturbed (Fig. 4d) suggesting no major alterations to LII

2908   cellular morphology. A modest, but significant increase in dV/dt max was noted in LEC LII

2909   principal cells (Extended Data Fig. 10d), potentially via an hAPP-dependent modulation of Na$_v$

2910   channels in these cells. All other active and passive properties were unaltered (Fig. 4d; Extended

2911   Data Fig. 8). Importantly, RNAscope experiments confirmed increased hAPP expression in

2912   CaMKIIa+ cells (Fig. 4i-j), indicating that our AAV also targeted excitatory neurons as expected.

2913   Using principal component analysis (PCA) of several excitatory cell biophysical features from

2914   LEC recordings, clusters could be separated based on input resistance, membrane time constant,

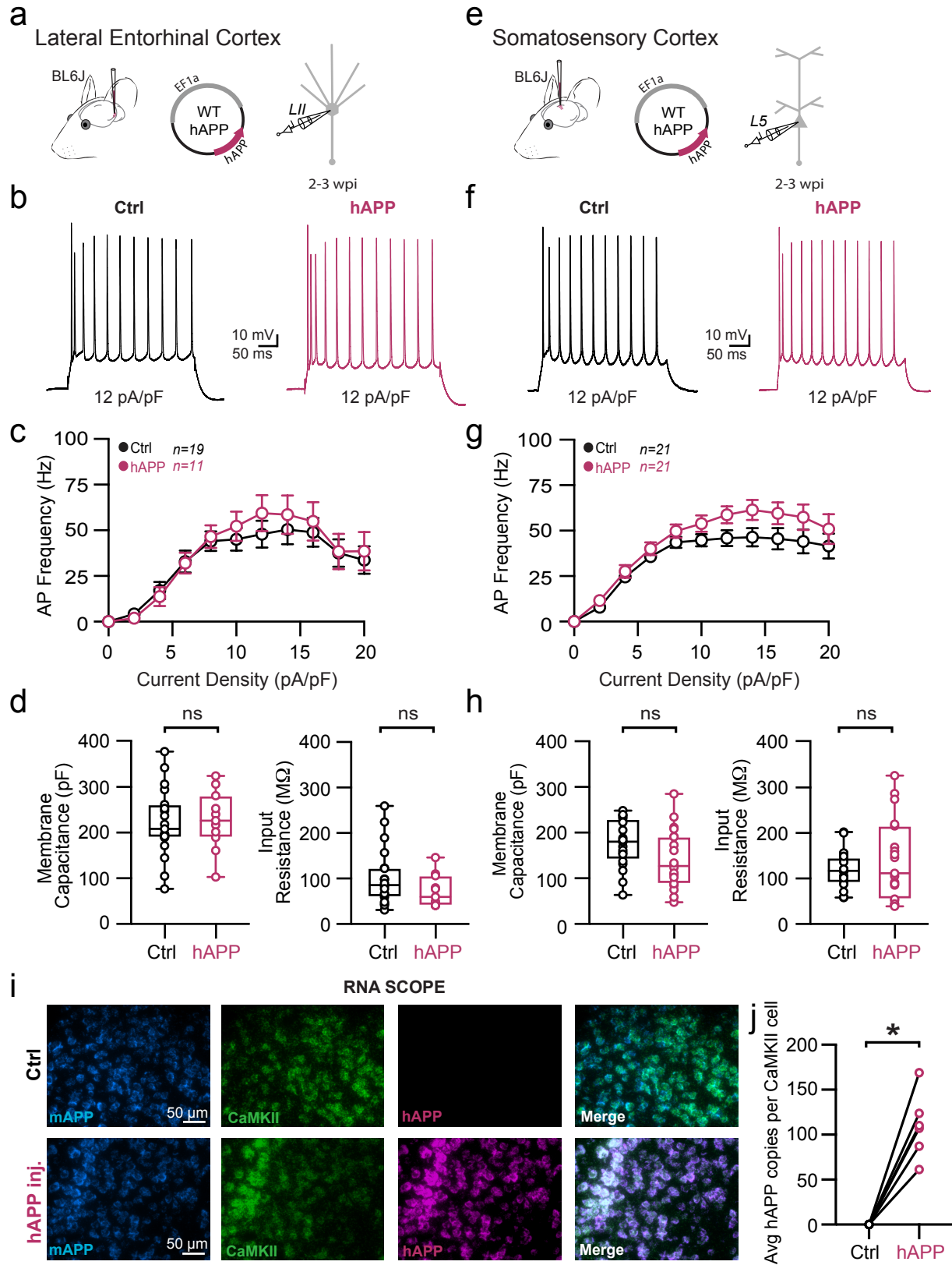2915   and resting membrane potential. These clusters likely arise due to sampling of both LII fan cells

Figure 4. Adult-onset human APP expression does not alter excitatory neuron physiology
(Caption continued onto next page…)

2916

Figure 4. Adult-onset human APP expression does not alter excitatory neuron physiology

a. Graphical summary of AAV.EF1a.hAPP (or for Ctrl, saline) stereotactic injection in the Lateral Entorhinal Cortex. Excitatory cells were targeted for whole-cell current clamp recordings.
b. AP firing elicited by square pulse current injections of varying magnitude normalized to cellular capacitance during recording in Ctrl and hAPP injected L2 LEC excitatory cells from at 12 pA/pF.
c. Group data summary of AP firing frequency in L2 LEC from Ctrl (black) and hAPP injected mice (magenta). Excitatory neurons in L2 LEC from hAPP injected mice show no alteration in AP Frequency (Hz) when compared to Ctrl (Ctrl: Max: 50.42 ± 5.63 Hz, hAPP: Max: 59.43 ± 6.56 Hz, p=0.99, df=28).
d. Summary data of AP properties. L2 LEC excitatory cells after hAPP injection display an unchanged Membrane Capacitance (p=0.83, t=0.27) as well as an unchanged input resistance (p=0.15, t=1.50, df=28).
e. Graphical summary of AAV.EF1a.hAPP (or for Ctrl, saline) stereotactic injection in the Somatosensory Cortex. Excitatory neurons in L5 were targeted for whole-cell current clamp recordings.
f. AP firing elicited by square pulse current injections of varying magnitude normalized to cellular capacitance during recording in excitatory cells from L5 SS Ctx at 12 pA/pF.

g. Group data summary of AP firing frequency in L5 SS Ctx from Ctrl (black) and hAPP injected mice (magenta). SS Ctx excitatory neurons from hAPP injected mice show no significant change in AP Frequency (Hz) when compared to Ctrl (Ctrl: Max: 46.35 ± 5.38 Hz, hAPP: Max: 61.43 ± 6.78 Hz, p>0.05, df=40).
h. Summary data of AP properties. SS Ctx interneurons after hAPP injection display an unchanged Membrane Capacitance and input resistance (Ctrl: 176.9 ± 11.58, hAPP: 140.5 ± 14.31, p=0.06, t=1.98, df=40, two-tailed unpaired t-test).
i. RNAscope representative images at 40x magnification for Ctrl injected (top) and hAPP injected mice (bottom(: mAPP mRNA (cyan), CaMKIIa mRNA (green), human APP mRNA (magenta), and a final merged image.
j. RNAscope quantification for hAPP copies per CaMKIIa+ cell comparing control to hAPP injected. hAPP injected show a significant increase in hAPP copies per CaMKIIa+ cell (p=0.0007, t=7.42, df=5; two-tailed paired t-test).
For all summary graphs, data are expressed as mean (± SEM). For c, g: Statistical significance is denoted as *=p<0.05, as determined by Two-way ANOVA with Sidak's multiple comparison test. For d, h: Individual data points and box plots are displayed. Statistical significance is denoted as *=p<0.05, as determined by two-tailed unpaired t-test.

2917 and LII pyramidal cells[345], suggesting our population of principal cells likely included both cell

2918 types (Extended Data Fig. 12a). When assessed, these excitatory populations showed no

2919 differential clustering following hAPP expression (Extended Data Fig. 12a). Together, these results

2920 indicate that principal neurons are more resistant to changes in their intrinsic excitability following

2921 adult-onset hAPP expression compared to PV interneurons.

2922

2923 *hAPP expression induces basal hyperexcitability in the LEC but not SS Ctx*

2924 Although we observed no alterations in the intrinsic excitability of excitatory cells in either region

2925 following hAPP expression, we wanted to assess whether the changes in PV interneuron

2926 biophysics in LEC had an impact on local circuit activity. To examine this at population level, we

2927 continuously acquired spontaneous post-synaptic currents from principal cells in either region

2928 (Fig. 5a,d). In the LEC, spontaneous inhibitory event (sIPSC) frequency was significantly

2929 decreased (increase in the mean inter-event interval [IEI]) after 2-3 weeks of hAPP expression

2930 (Fig. 5b,c). Furthermore, we analyzed the LEC sIPSCs for differences in the frequency in small

2931 and large amplitude events (cutoff 40 pA derived from a previously published method[118]), to

2932 determine if the increase in sIPSC IEI was related to distal inhibition (small amplitude) or

2933 proximal, peri-somatic inhibition (large amplitude). We observed that while the frequency of small

2934 amplitude events was unchanged (p=0.52, two-tailed unpaired t-test, t=0.65, df=18; Ctrl:

2935 1.66±0.36 Hz, hAPP: 1.33±0.35 Hz), the frequency of large amplitude events was significantly

2936 decreased in the LEC (p=0.02, two-tailed unpaired t-test, t=2.51, df=18; Ctrl: 4.66±1.1 Hz; hAPP:

2937 1.74±0.49 Hz). In layer II of the entorhinal cortex, the Reelin+ excitatory cells receive peri-somatic

2938 inhibition primarily from PV interneurons, rather than CCK basket cells[340,346]. This was consistent

2939 with changes in intrinsic PV excitability observed earlier. In an apparent response to this reduced

2940 inhibitory tone, spontaneous excitatory event (sEPSC) frequency increased in the LEC following

2941 hAPP expression (Fig. 5b,c). In contrast to the LEC, recordings from SS Ctx (Fig. 5d,e) revealed

2942 no change in sIPSC or sEPSC frequency following hAPP expression (Fig. 5f), in agreement with

2943 the lack of changes in intrinsic excitability in the SS Ctx shown earlier. Spontaneous and miniature

2944 (excitatory or inhibitory) synaptic amplitudes in the LEC and SS Ctx were unchanged in either

2945 region (Extended Data Fig. 13), indicating that postsynaptic receptor alterations did not arise in

2946 excitatory neurons following short-term adult-onset hAPP expression. mIPSC and mEPSC

2947 frequencies were also unaltered, suggesting no change in the number of inhibitory or excitatory

2948 synapses at this point (Extended Data Fig. 13b). Together, these results indicate that following

2949 adult-onset hAPP expression, basal circuit activity in the LEC, but not SS Ctx, becomes

2950 hyperexcitable, likely resulting from a region-specific PV interneuron vulnerability.

2951

2952 *hTau co-expression with hAPP quells LEC hyperexcitability at the cost of increased pathological*
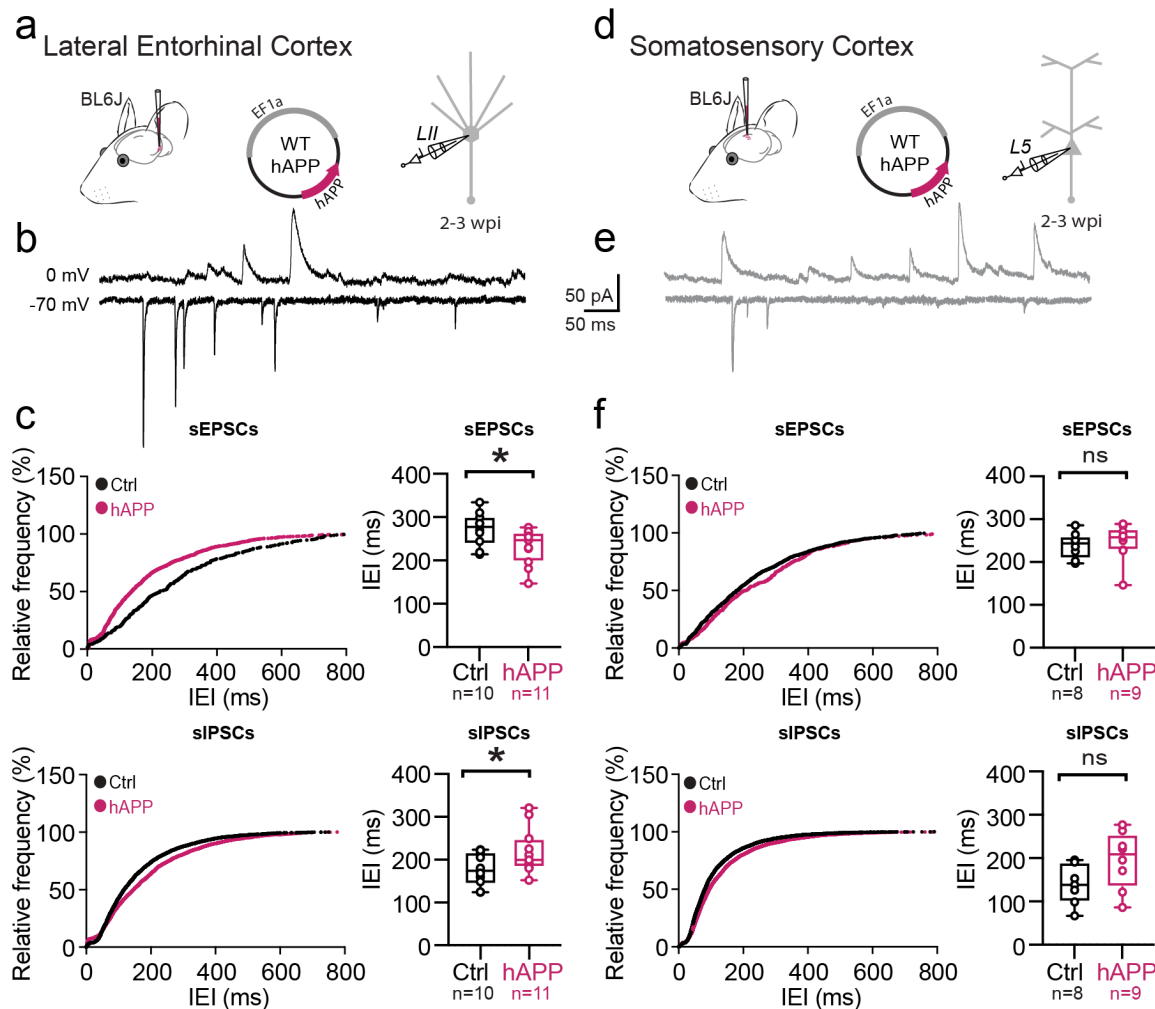
2953 *tau species*

Figure 5. Human APP expression induces hyperexcitability in the LEC but not SS Ctx

a. Graphical summary of AAV.EF1a.hAPP (or for Ctrl, saline) stereotactic injection in the Lateral Entorhinal Cortex. Excitatory cells were targeted for whole-cell voltage-clamp recordings.

b. Spontaneous events obtained by holding cell voltage at 0 mV (inhibitory post-synaptic currents, IPSCs [top]) and -70 mV (excitatory post-synaptic currents, EPSCs [bottom]), interleaved.

c. Top: Cumulative distribution curve for spontaneous EPSCs in the LEC showing the relationship of relative frequency of events to the inter-event interval (IEI) (left). Quantified averages of IEIs are displayed for each cell as individual data points and compared between Ctrl (black) and hAPP injected (magenta) conditions (right). L2 LEC sEPSCs show a significant reduction in the IEIs (231.7 ± 12.25 ms, 272.7 ± 12.24 ms, hAPP and Ctrl respectively, p=0.029, t=2.361, df=19, two-tailed unpaired t-test). See Extended Data Fig. 13 for mEPSC data. **Bottom:** Cumulative distribution curve for spontaneous IPSCs in the LEC showing the relationship of relative frequency of events to the inter-event interval (left). Quantified averages of IEIs are displayed for each cell as individual data points and compared between Ctrl (black) and hAPP injected (magenta) conditions (right).

L2 LEC sIPSCs show a significant increase in the IEIs (219.9 ± 15.84 ms, 177.3 ± 12.02 ms, hAPP and Ctrl respectively, p=0.047, t=2.097, df=19, two-tailed unpaired t-test).See Extended Data Fig. 13 for mIPSC data.**d.** Graphical summary of AAV.EF1a.hAPP (or for Ctrl, saline) stereotactic injection in the Somatosensory Cortex. Excitatory cells were targeted for whole-cell voltage-clamp recordings.

e. Spontaneous events obtained by holding cell voltage at 0 mV (IPSCs [top]) and -70 mV (EPSCs [bottom]), interleaved.

f. Top: Cumulative distribution curve for spontaneous EPSCs in the SS Ctx showing the relationship of relative frequency of events to the IEIs (left). Quantified averages of IEI are displayed for each cell as individual data points and compared between Ctrl (black) and hAPP injected (magenta) conditions (right). L5 SS Ctx sEPSCs show no change in the IEIs (p=0.7372, t=0.3450, df=15; two-tailed unpaired t-test). See Extended Data Fig. 13 for mEPSC data. **Bottom:** Cumulative distribution curve for spontaneous IPSCs in the SS Ctx showing the relationship of relative frequency of events to the inter-event interval (left). Quantified averages of IEIs are displayed for each cell as individual data points and compared between Ctrl (black) and hAPP injected (magenta) conditions (right). L5 SS Ctx sIPSCs show no change in the IEIs (p=0.0812, t=1.890, df=15; two-tailed unpaired t-test). See Extended Data Fig. 13 for mIPSC data.

2954   Beyond hyperexcitability, the LEC is also the first cortical region to develop tau pathology[90,91,347-]

[349]. Although Alzheimer's is characterized by early hAPP/Aβ and later Tau pathology, respectively, the relationship between hAPP, hyperexcitability, and Tau remains unclear. It has previously been established that artificially increasing neuronal activity can accelerate tau pathology[163,350,351]. However, long-term transgene expression of human Tau (hTau) may act to dampen circuit excitability[116,165,352] (but see[353]). Thus, we sought to assess the interplay of hAPP-induced circuit hyperexcitability and hTau expression in the LEC. To achieve this, we packaged full-length wild-type human Tau (hTau) into a separate AAV to induce Tau expression locally in the entorhinal cortex. Spontaneous post-synaptic currents were then recorded from LII principal cells, 3 weeks after hAPP alone, hTau alone, or hAPP + hTau co-injection (Fig. 6a). With hAPP, we again observed an elevated E:I frequency ratio (sEPSC frequency/sIPSC frequency, normalized to the Control dataset) as described earlier (Fig. 6b). We hypothesized that hTau would result in a reduced E:I ratio with respect to the control baseline. Although the E:I ratio with hTau alone was less than hAPP alone, E:I balance surprisingly remained unchanged with respect to the Control (Fig. 6b). However, hAPP + hTau resulted in an intermediate effect, which abolished the hyperexcitable phenotype seen with hAPP alone (Fig. 6b). These results agree with a homeostatic role for Tau in maintaining circuit excitability. Beyond synaptic event frequencies, all other spontaneous event properties (i.e., amplitude) were statistically similar between all groups (Extended Data Fig. 14a,b).

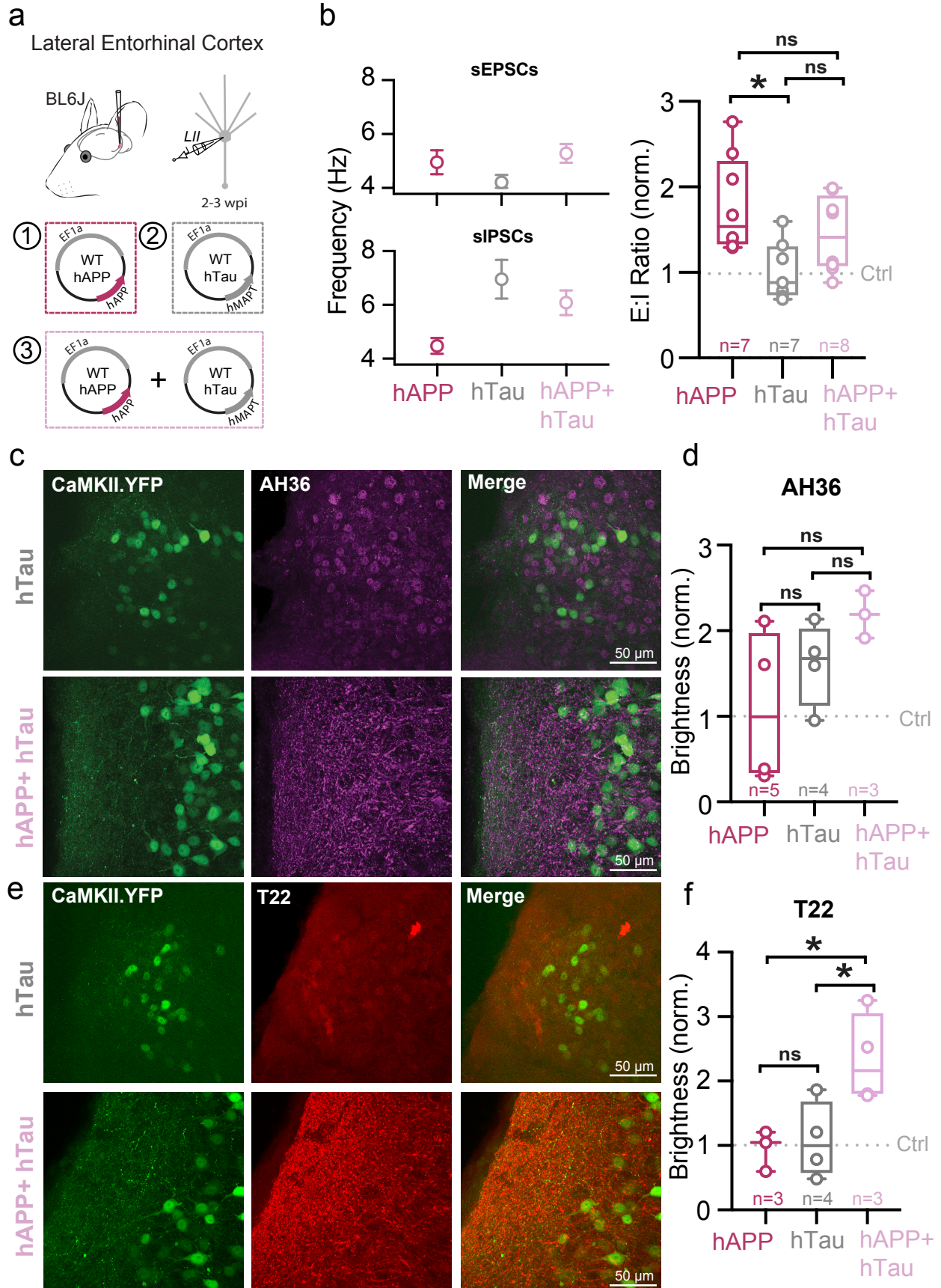**Figure 6. hTau co-expression with hAPP quells hyperexcitability but increases pathological tau**
(Caption continued onto next page…)

2973

Figure 6. hTau co-expression with hAPP quells hyperexcitability but increases pathological tau

a. Graphical summary of AAV.EF1a.hAPP, AAV.EF1a.MAPT (hTau), or co-injected AAV.EF1a.hAPP with AAV.EF1a.MAPT stereotactic injection in the Lateral Entorhinal Cortex. Excitatory cells were targeted for whole-cell voltage-clamp recordings.
b. Spontaneous events obtained by holding cell voltage at -70 mV (excitatory post-synaptic currents, EPSCs [top]) and 0 mV (inhibitory post-synaptic currents, IPSCs [bottom]), interleaved. Quantified averages of event frequency are displayed for each cell normalized to Ctrl values as a ratio of EPSC Frequency to IPSC frequency and compared between hAPP injected (magenta), hTau injected (gray) and hAPP + hTau co-injected (pink) conditions. L2 LEC injected with hAPP showed a significantly elevated E:I ratio compared to hTau injected (p=0.0136, df=20). hAPP and hTau co-injected E:I ratio was not significantly different from hAPP injected (p=0.3323, df=20) or hTau injected (p=0.2175, df=20). For all summary graphs, data are expressed as mean (± SEM). Statistical significance is denoted as *=p<0.05, as determined by an Ordinary one-way ANOVA with Multiple comparisons.

c,e. IHC representative images at 60x magnification for hTau (top) or hAPP+hTau (bottom) injected mice (for Ctrl or hAPP injected, see Extended Data Fig. 14) with staining for either AH36 (c) or T22 (e).
d. hAPP, hTau, and hAPP+hTau were analyzed for AH36 brightness in the first 100 um of every slice. AH36 brightness was normalized to CaMKII.eYFP brightness to control for any potential variability in viral expression. All groups were then normalized to the Ctrl injected condition. hAPP+hTau showed the highest level of AH36 brightness, although it was not significant over hAPP (p=0.1267) or hTau (p=0.4900) (df=8, One-Way ANOVA with Multiple Comparisons). hAPP and hTau were also not significantly different (p=0.5328).
e. hAPP, hTau, and hAPP+hTau were analyzed for T22 brightness in the first 100 um of every slice. AH36 brightness was normalized to CaMKII.eYFP brightness to control for any potential variability in viral expression. All groups were then normalized to the Ctrl injected condition. hAPP+hTau showed a significantly higher level of T22 brightness, above both hAPP (p=0.0350) and hTau (p=0.0.0389) (df=8, One-Way ANOVA with Multiple Comparisons). hAPP and hTau were not significantly different (p=0.9526).

We next assessed whether the moderating effect of hTau on circuit activity came at the cost of increased pathology, using antibodies for pSer202/pThr205 phosphorylated tau (AH36) or oligomeric tau (T22). Both Control and hAPP-injected conditions showed low levels of AH36 positivity, likely due to labeling endogenous murine tau (Extended Data Fig. 14c,d). While both hTau and hAPP+hTau induced high levels of AH36-positive staining (Fig. 6c,d), it appeared that hTau alone injected mice had mostly somatically located staining. In contrast, hAPP+hTau co-injected mice displayed dendritic-based staining (Fig. 6c) suggesting an interaction with hAPP which promotes Tau translocation in entorhinal neurons. Oligomeric tau (T22) (Fig. 6e), which has recently been shown in human tissue as a tau species that may spread transsynaptically from axons to other regions[354], displayed a surprisingly robust increase, but only when hAPP+hTau were co-expressed (Fig. 6e,f; Extended Data Fig. 14e,f). Thus, it appears that co-expression of human Tau might restore human APP-induced circuit hyperexcitability, but consequentially results in increases in known pathological tau species.

5.4 Discussion

Here we demonstrate that PV interneurons within the LEC are biophysically distinct from

2990   other neocortical PV interneurons. Furthermore, differences in the native-state proteomes of PV

2991   interneurons from the LEC and SS Ctx regions were marked. Although the WT PV firing frequency

2992   in our LEC recordings is consistent with previous observations[340], the striking biophysical

2993   differences (i.e., AP waveform) with respect to PV cells in other cortical regions had not been

2994   systematically evaluated. Interestingly, these LEC PV interneurons do resemble a previously

2995   observed PV+ interneuron in other regions, such as the 'quasi fast-spiking interneurons' of the

2996   subiculum[33], the 'fast-spiking-like cells' of the striatum[34], and the 'non-fast-spiking interneurons'

2997   of the CA1[31]. However, where these cells represent a small subset of the PV+ interneurons of these

2998   regions (~20% in CA1)[31], the majority of our recorded PV+ interneurons displayed this low-firing

2999   phenotype. Whether the baseline low-firing frequency of PV+ interneurons in the LEC confers

3000   vulnerability to hAPP-induced pathophysiology remains unclear. In addition to their different

3001   intrinsic features, PV interneurons of the LEC displayed a multitude of differentially expressed

3002   proteins in comparison to SS Ctx PV interneurons. Interestingly, compared to SS, we found that

3003   PV interneurons residing in the LEC were significantly enriched in proteins associated with

3004   cognitive resilience in humans. However, many of these LEC PV interneuron pro-resilience

3005   proteins were altered in the entorhinal cortex of AD patients. This suggests a regional and cell-

3006   type-specific susceptibility to the progression of AD pathophysiology. Although a comparison of

3007   PV-CIBOP regional proteomes with bulk human brain proteomes gives further insight into

3008   potential cell-type-specific alterations in phases of AD, it is still limited by the inability to verify

3009   PV interneuron-specificity of observed changes in human brain. As we only recently established

3010   the first, to our knowledge, PV interneuron-specific proteome[142], we look forward to the

3011   advancement of techniques to come in order to complete such a level of analysis in human tissue.

3012   Future studies at the single-cell level in humans with early-stage AD will be necessary to confirm

3013   this assertion.

3014   Recent work shows that APP expression moves outside of normal homeostatic levels in

3015   models of late-onset AD risk alleles[355,356]. The ratio of different APP isoforms also shifts in human

3016   AD, from mainly APP 695 to increasing levels of APP 770 and 751[54,55]. These longer isoforms

3017   show increased expression following aging-related processes (*e.g.,* after reproductive hormonal

3018   production decline[56], hypercholesterolemia[57], and atherosclerosis[58]), all of which are also

3019   associated with increased AD risk[59-62]. Thus, here we induced adult-onset expression of hAPP 770

3020   to model these phenomena. Adult-onset expression of hAPP allowed us to avoid any alterations to

3021   neurodevelopment which may arise with expression of a transgene early in development, as many

3022   mouse models of AD exhibit. However, we acknowledge that this model does not encapsulate all

3023   alterations which may arise throughout aging and early Alzheimer's Disease. Thus, further studies

3024   must be conducted assessing these mechanisms in aging mice. At this time point, we found that

3025   shortly after hAPP expression (2-3 weeks), LEC PV interneuron firing became severely disrupted.

3026   Although both excitatory and inhibitory cells expressed hAPP, we observed no alteration to

3027   intrinsic firing of excitatory cells in LEC LII. Despite this, there was a significant disruption in the

3028   E:I balance of the LEC circuit. Thus, we propose the basal network hyperexcitability observed

3029   arises as a result of decreased PV interneuron firing, resulting in increased firing of the excitatory

3030   neurons. Interestingly, this hAPP-induced pathophysiology could not be recapitulated following

3031   expression of the full-length mouse mAPP gene analogue. Of the 26 amino acids differentiating

3032   our hAPP and mAPP proteins, only 3 are situated within the amyloid-beta region. Of note, of the

3033   'wild-type' versions of newly designed hAPP knock-in mouse models[357,358] now in wide use, only

3034   the 3 amino acids within the amyloid region are humanized. It has been shown that increasing

3035   expression of WT hAPP does result in a substantial increase in amyloid-beta[359], which may suggest

3036   that this phenotype is a result of increased amyloid-beta. Thus, we investigated if humanizing only

3037   the 3 amino acids could recapitulate our findings of hAPP-induced impaired PV interneuron

3038   physiology. Interestingly, the mAPP/hAβ Chimera did result in impaired PV interneuron firing but

3039   was not sufficient to fully replicate the drastic alterations seen after full-length hAPP expression.

3040   This suggests amyloid-beta is not the sole cause for early phase interneuron dysfunction, and may

3041   suggest a role for either full-length APP or its other cleavage products in this stage of the

3042   neurodegenerative cascade.

3043   GABAergic interneurons require homeostatic APP levels for proper physiological function

3044   and circuit activity control[360]. Furthermore, APP[361], as well its cleavage proteins[362-364] and

3045   products[233,365], can modulate neuronal biophysics and alter the expression of ion channels, many

3046   of which are essential for maintaining the 'fast-spiking' phenotype of PV interneurons.

3047   Modifications to Na_v1 or K_v3 channel availability in different constitutive hAPP-expressing mice

3048   have recently been linked to reduced PV excitability[108,113]. Although short-term full-length hAPP

3049   expression in this study could significantly reduce PV firing, we observed no biophysical

3050   indicators implicating changes to either Na_v1 or K_v3 availability which may underlie altered PV

3051   firing in the LEC. Although the SS Ctx PV interneurons did not observe reduced firing, we did

3052   note alterations in their AP threshold and AHP, which could be attributed to alterations in Na_v1 or

3053 K_v3 availability, respectively. It is possible that if left longer, hAPP expression in the SS Ctx may

3054   result in impaired PV interneuron excitability[108,113]. Thus, alternative biophysical mechanisms

3055   must be responsible for our observations following more short-term hAPP expression in adult

3056   mice. Notably, we observed a substantial decrease in input resistance in LEC PV cells expressing

3057   hAPP. This could be due to enhanced availability of leak channels or potentially low-voltage

3058   activating K^+ conductances, such as KCNQ (K_v7), which curiously have been shown to be

3059   regulated by APP cleaving proteins[362] and cleavage products[233,366]. However, the reduction in PV

3060   interneuron firing after expression of the mAPP/hAβ chimera is likely due to the widening AP

3061   half-width, which may similarly be due to Kv3 alterations. Whether these differences in

3062   mechanisms underlying altered PV firing is related to model systems, different cleavage product

3063   and accompanying protein effects, or different time points through the disease will be necessary

3064   to further understand mechanisms of PV and excitatory cell dysfunction. We cannot rule out that

3065   longer hAPP expression times *in vivo* may induce other changes through distinct pathological or

3066   homeostatic processes.

3067   The LEC is also the first cortical region to develop tau pathology[90,91,347-349]. Yet, the

3068   relationship between hAPP, hyperexcitability, and Tau remains unclear. It has previously been

3069   established that artificially increasing neuronal activity can accelerate tau pathology[163,350,351].

3070   However, the expression of hTau has been suggested to strongly dampen circuit

3071   excitability[116,165,352] (but see[353]). Here we observed that hTau co-expressed with hAPP results in an

3072   intermediate circuit excitability level when compared to hAPP or hTau injected alone. Trans-

3073   synaptic spread of tau has been shown from the entorhinal cortex to other brain regions[367,368], and

3074   most recently this spread has been suggested to occur in human patients via the oligomeric tau

3075   species (T22+)[354]. Remarkably, here we show that although hTau co-injection with hAPP

3076   somewhat normalized circuit excitability, it also caused a significant increase in this oligomeric

3077   tau species. Further research is necessary to determine if this resultant oligomeric species displays

3078   a similar trans-synaptic spread to downstream regions, such as the dentate gyrus.

3079   The LEC is the first cortical region to undergo end-stage cellular neurodegeneration[90] in

3080   AD, specifically, Layer II[105] excitatory cells[94]. Conversely, one of the earliest pathophysiological

3081   alterations seen in both humans with AD, and in mouse models of early- and late-onset AD

3082 pathology[109,115,116] is altered local circuit excitability[117,369,370]. In agreement with our *ex vivo*

3083 mechanistic cellular findings here, hyperactivity has been shown to preferentially emerge in the

3084 LEC region *in vivo[117]*. We recognize that our findings of circuit hyperexcitability *ex vivo* represent

3085 only one state in which the circuit may exist *in vivo,* and thus further studies are necessary to

3086 determine the exact mechanism of early hyperactivity in the LEC *in vivo*. However, slice

3087 electrophysiology assessments of circuit excitability have been observed as good predictors of *in*

3088 *vivo* hyperexcitability in AD pathology studies[108,114,124]. Our study suggests that hAPP-induced

3089 hyperexcitability in the LEC arises not from alterations in the intrinsic or synaptic properties of

3090 AD-vulnerable LII excitatory cells, but rather from an initial alteration in intrinsic excitability of

3091 surrounding PV interneurons. The fact that short-term hAPP expression in SS cortex caused no

3092 changes in PV firing or overall basal circuit excitability also supports this notion. Circuit

3093 hyperexcitability is likely an influential factor in the neurodegenerative cascade, as it has been

3094 shown to exacerbate release of amyloid-beta[371], and also promotes tau pathology and subsequent

3095 trans-synaptic tau spreading[163], which ultimately induces spine degeneration[114] and cell death[372].

3096 Ultimately, regions that first undergo hyperexcitability may also be among the earliest to display

3097 these pathological markers as the disease progresses[163,373].

3098   5.5 Supplementary Information

Table 1

Principal cells in LEC and SS Ctx

Features	Average±SEM LEC EXC	Average±SEM SS Ctx EXC	p-value	t-value	Degrees of Freedom
AHP (mV)	9.66±0.75	6.33±0.64	<0.01	3.41	40
Threshold (mV)	-41.97±1.18	-44.61±1.26	0.14	1.53	40
dV/dt Max	353.40±13.97	469.60±31.50	<0.01	3.37	40
Input Resistance (MΩ)	103.60±14.51	117.80±8.93	0.40	0.86	40
Resting Membrane Potential (mV)	-63.39±1.18	-71.31±1.50	<0.01	4.00	40
Membrane Capacitance (pF)	205.40±14.68	183.30±12.73	0.26	1.14	40
Membrane Tau (ms)	19.65±1.84	20.64±1.74	0.70	0.39	40
Accomodation Ratio	2.52±0.47	2.93±0.28	0.45	0.77	40

All were Unpaired t-tests, Two-tailed

PV Interneurons in LEC and SS Ctx

Features	Average±SEM LEC PV-IN	Average±SEM SS Ctx PV-IN	p-value	t-value	Degrees of Freedom
AHP (mV)	20.68±1.01	19.47±1.19	0.44	0.78	25
Threshold (mV)	-40.02±1.14	-46.14±0.55	<0.01	2.47	25
dV/dt Max	553.70±29.76	571.60±20.48	0.65	0.46	25
Input Resistance (MΩ)	147.30±16.44	121.20±17.14	0.29	1.08	25
Resting Membrane Potential (mV)	-60.38±1.60	-65.71±1.89	0.04	3.15	25
Membrane Capacitance (pF)	70.17±5.46	71.91±9.51	0.87	0.17	25
Membrane Tau (ms)	9.98±0.62	7.39±0.47	<0.01	3.181	25
Accomodation Ratio	2.14±0.24	1.71±0.09	0.154	1.470	25

All were Unpaired t-tests, Two-tailed

3099

3100   *Chapter 5. Supplementary Table 1. Passive and active features of LEC and SS Ctx neurons*

3101   (Extended Data Table 1)

3102   Passive and active properties of principal excitatory cells (top) or tdTom+ PV interneurons

3103   (bottom) in L2 LEC and L5 SS Ctx.

3104

a

b

GO terms enriched in SS Ctx vs. LEC PV-IN proteomes
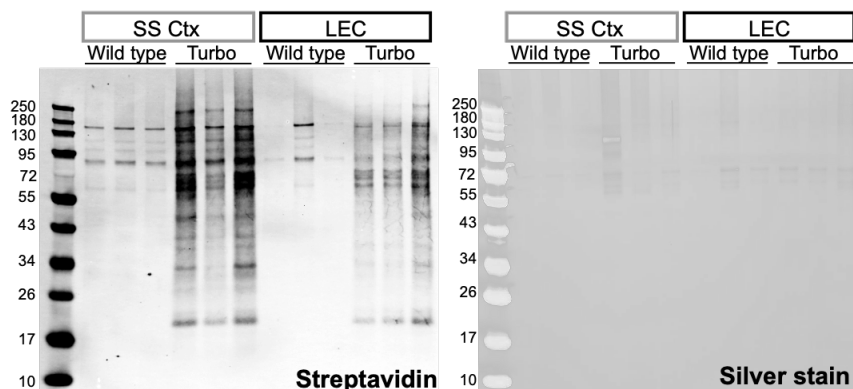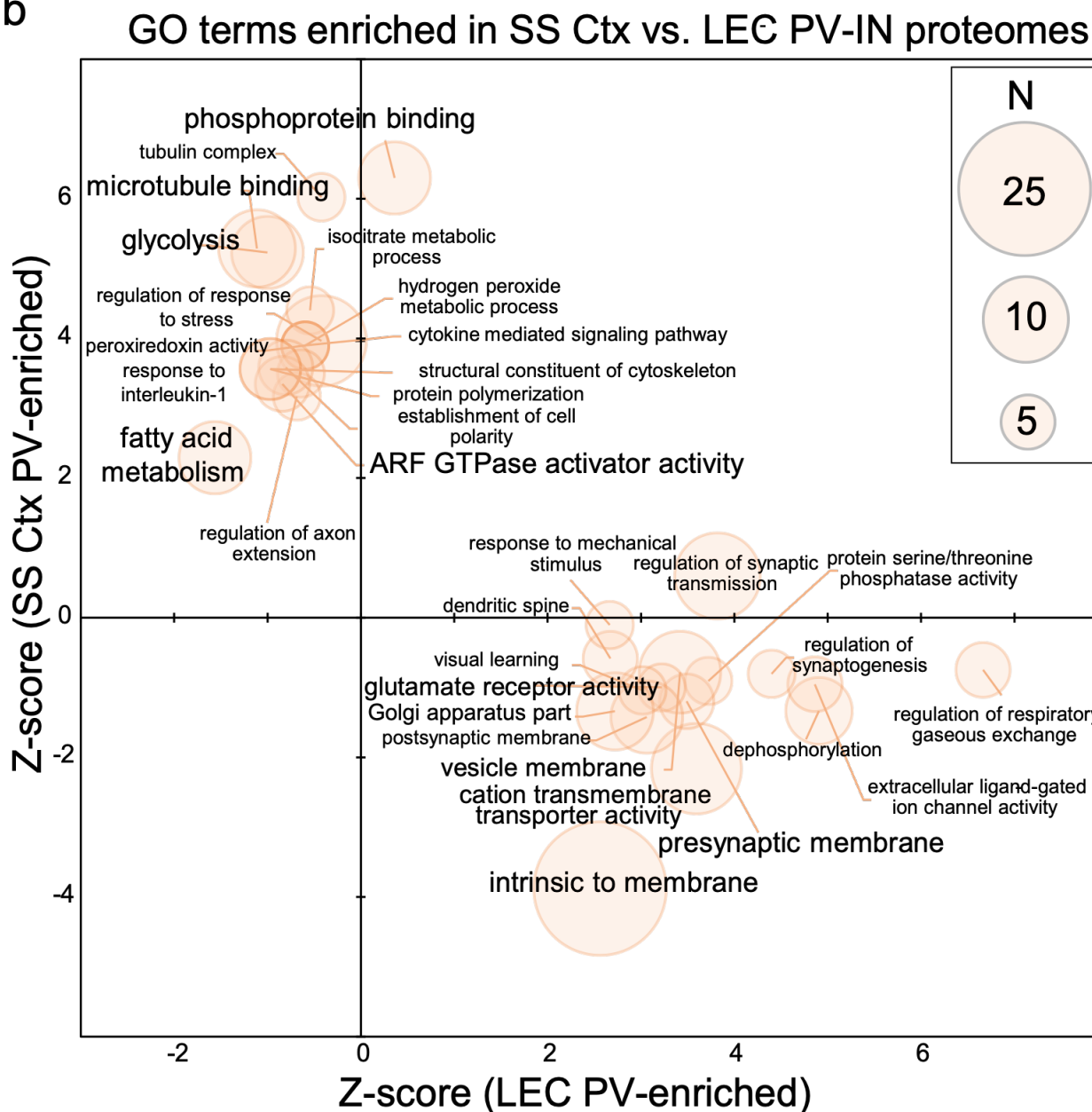
3106 *Chapter 5. Supplementary Figure 1. Enriched biotinylated PV interneuron proteins from the SS*
3107 *Ctx and LEC are neuron-specific*

3108 (Extended Data Figure 1)

3109 **a.** Western blot (left) and silver stain (right) visualization of enriched biotinylated proteins in PV

3110 interneurons (IN) from the SS Ctx and LEC after streptavidin-pulldown and elution of biotinylated

3111 proteins from a 10% aliquot of beads.

3112 **b.** GSEA of $\geq$ 2-fold enriched biotinylated PV interneuron proteins from the SS Ctx and LEC from

3113 PV-CIBOP mice, as compared to a reference protein list of both regions (n = 807) showed

3114 enrichment of synaptic and neuronal proteins confirming neuronal labeling. The orange dot size

3115 represents the number of gene symbols represented in each GO term. WT (Control) or

3116 Rosa26TurboID/wt (PV-CIBOP) mice (n=3 per genotype, including males and females).

3117

3118

3119
3120
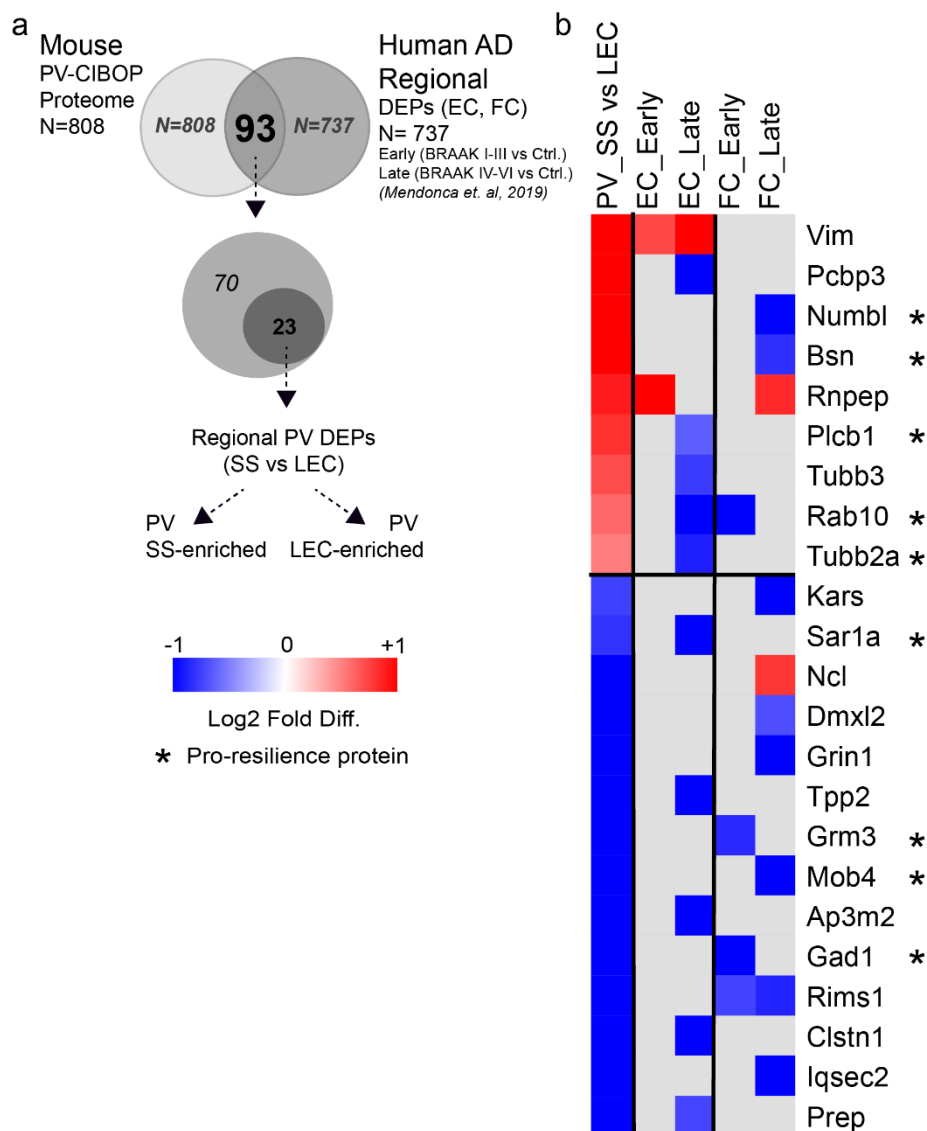
3121
3122 *Chapter 5. Supplementary Figure 2. PV-CIBOP regional proteins that also demonstrate region-*
3123 *specific changes in human AD brain (related to Figure 1)*

3124 (Extended Data Figure 2)
3125 **a.** Mouse PV-CIBOP regional proteins (SS Ctx vs. LEC) that were also identified as regional DEPs

3126 (AD vs. Ctrl) from human post-mortem brain regions (EC and FC)[342]. (EC: Entorhinal Cortex; FC:

3127 Frontal Cortex; Early: Braak I-III vs. Ctrl; Late: Braak IV-VI vs. Ctrl).

3128 See also Extended Data Datasheet 2 for related data and analyses.

3129

a Protein interactors with hAPP

b Protein interactors with Tau
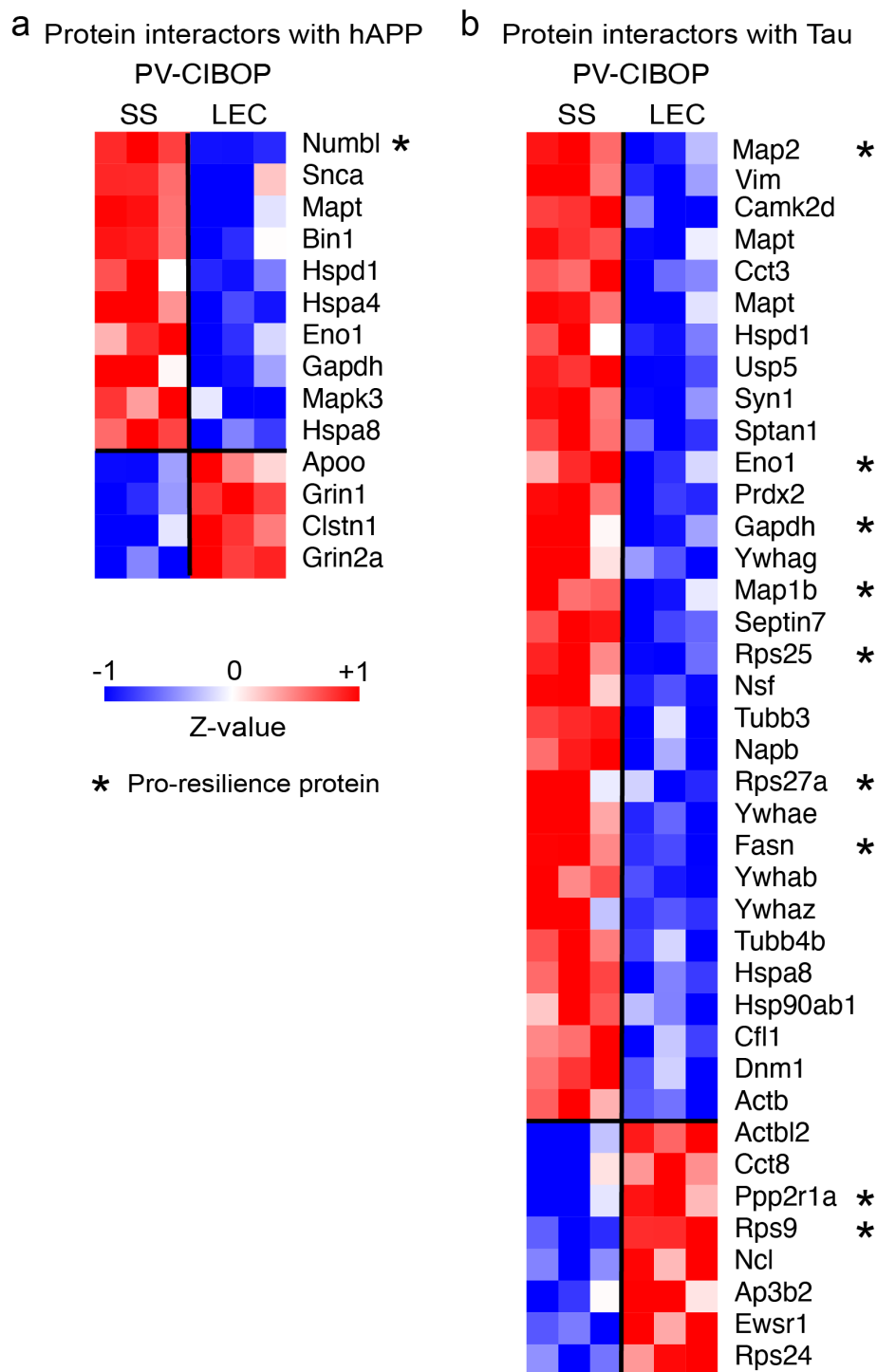
Chapter 5. Supplementary Figure 3. PV-CIBOP identified regional proteins with known
interactions with human APP and Tau (Related to Figure 1)

(Extended Data Figure 3)

a. Heatmap representation of PV regional DEPs (SS Ctx vs. LEC) that are known protein-protein

interactors with human APP (from 243 known APP interactors derived from the STRING

database). Proteins marked with * indicate those that are also known pro-resilience proteins. As expected, the APP interactors were enriched in proteins involved in lipid binding, amyloid beta processing, cholesterol metabolism, and complement and coagulation cascade.

b. Heatmap representation of PV interneuron regional DEPs (SS Ctx vs. LEC) that are known protein-protein interactors with Tau from human brain. Proteins marked with * indicate those that are also known pro-resilience proteins.

Also see Extended Data Datasheets 3 and 4 for related results and analyses.

3154
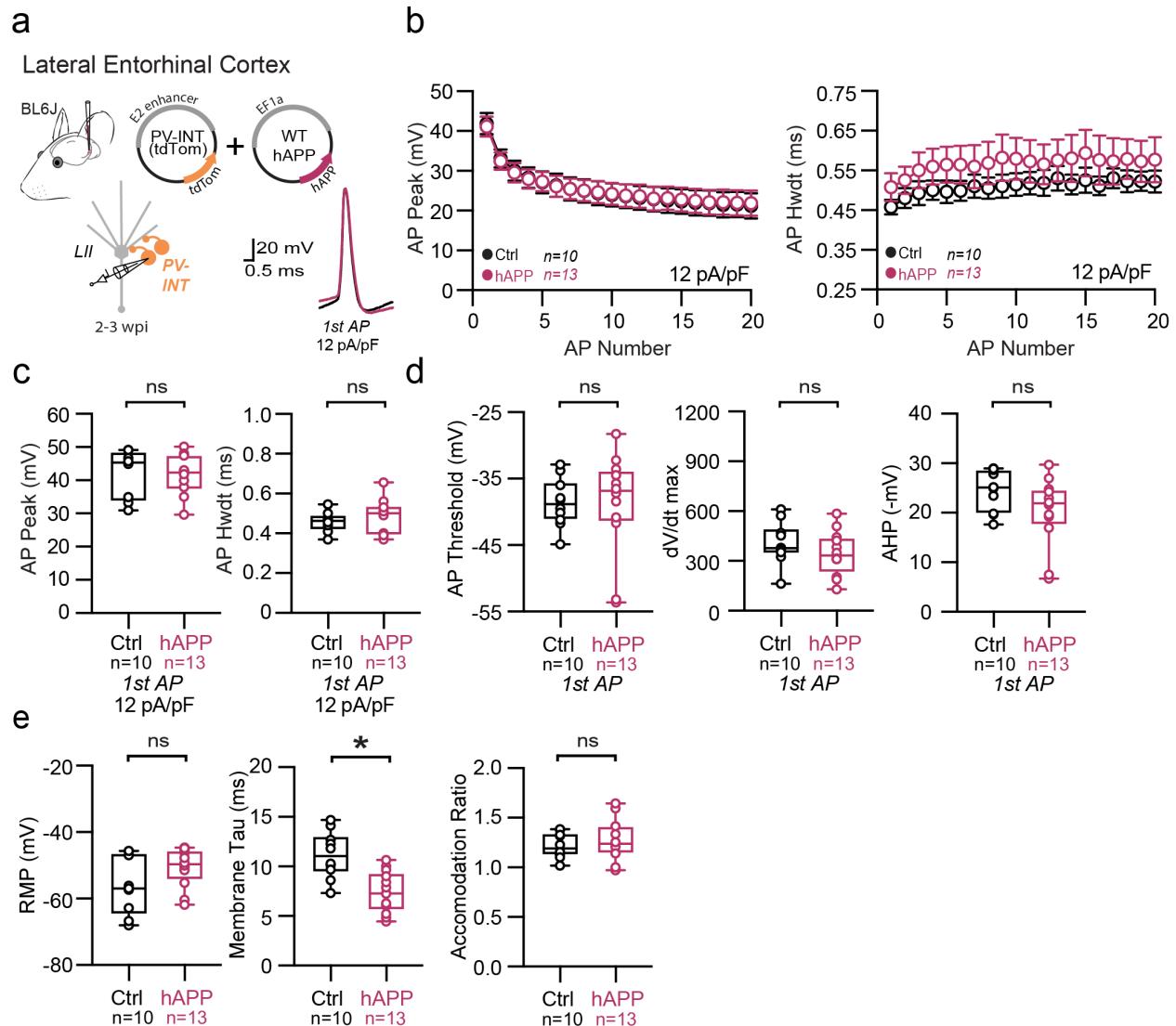
Chapter 5. Supplementary Figure 4. Passive and active properties of LEC PV interneurons after hAPP injection

(Extended Data Figure 4)

a. Graphical summary of AAV.E2.tdTom and AAV.EF1a.hAPP (or for Ctrl, saline) stereotactic injection in the Lateral Entorhinal Cortex. tdTom+ PV interneurons were fluorescently targeted for whole-cell current-clamp recordings. AP waveforms of tdTom+ PV interneurons were compared at 12 pA/pF square pulse injections in WT mice from Ctrl and hAPP injected. Aps from the 1st spike in the train are superimposed for comparison.

b. Relationship between AP peak (p=0.88, df=21) or width (p<0.0001, df=21) in WT mice and AP # during spike trains elicited with a 12 pA/pF current injection.

3165   **c.** Summary data of AP properties. LEC PV interneurons after hAPP injection 1st AP peak (p=0.94,

3166   t=0.08) and half-width remains unchanged (p=0.51, t=0.67, df=21).

3167   **d.** Summary data of AP properties. LEC PV interneurons after hAPP injection AP threshold

3168   (p=0.85, t=0.20), dV/dt max (p=0.12, t=1.6), and AHP (0.63, t=0.49) (df=21) remained unchanged.

3169   **e.** Summary data of AP properties. LEC PV interneurons after hAPP injection show unchanged

3170   Resting Membrane Potential (p=0.09, t=1.79) and Accommodation Ratio (p=0.66, t=0.44), but a

3171   reduction in Membrane Tau(p=0.0008, t=3.93) (df=21).

3172   For all summary graphs, data are expressed as mean ($\pm$ SEM). For **b**: Statistical significance is

3173   denoted as *=p<0.05, as determined by Two-way ANOVA with Sidak's multiple comparison test.

3174   For c, d, e: Individual data points and box plots are displayed. Statistical significance is denoted

3175   as *=p<0.05, as determined by two-tailed unpaired t-test.

3176

3177

3178

3179

3180

3181

3182

3183

Chapter 5. Supplementary Figure 5. Passive and active properties of SS Ctx interneurons after hAPP injection

(Extended Data Figure 5)

a. Graphical summary of AAV.E2.tdTom and AAV.EF1a.hAPP (or for Ctrl, saline) stereotactic injection in the SS Cortex. tdTom+ PV interneurons were fluorescently targeted for whole-cell current-clamp recordings. AP waveforms of tdTom+ PV interneurons were compared at 12 pA/pF square pulse injections in WT mice from Ctrl and hAPP injected. Aps from the 1st spike in the train are superimposed for comparison.

b. Relationship between AP peak (p=0.17, t=1.42 df=23) or width (p=0.15, t=1.49 df=23) for in WT mice and AP # during spike trains elicited with a 12 pA/pF current injection.

c. Summary data of AP properties. SS PV interneurons after hAPP injection 1st AP peak (p=0.17, t=1.42) and half-width (p=0.15, t=1.49) (df=23) remain unchanged.

d. Summary data of AP properties. SS PV interneurons after hAPP injection dV/dt max remains unchanged (p=0.32, t=1.01). AP Threshold (p=0.001, t=3.84) and AHP (p=0.02, t=2.42)(df=23) significantly increase after hAPP injection.

e. Summary data of AP properties. SS PV interneurons after hAPP injection show unchanged Resting Membrane Potential (p=0.40, t=0.85), Accommodation Ratio (p=0.08, t=1.84), and Membrane Tau (p=0.81, t=0.24) (df=23).

For all summary graphs, data are expressed as mean (± SEM). For **b**: Statistical significance is denoted as *=p<0.05, as determined by Two-way ANOVA with Sidak's multiple comparison test. For c, d, e: Individual data points and box plots are displayed. Statistical significance is denoted as *=p<0.05, as determined by two-tailed unpaired t-test.
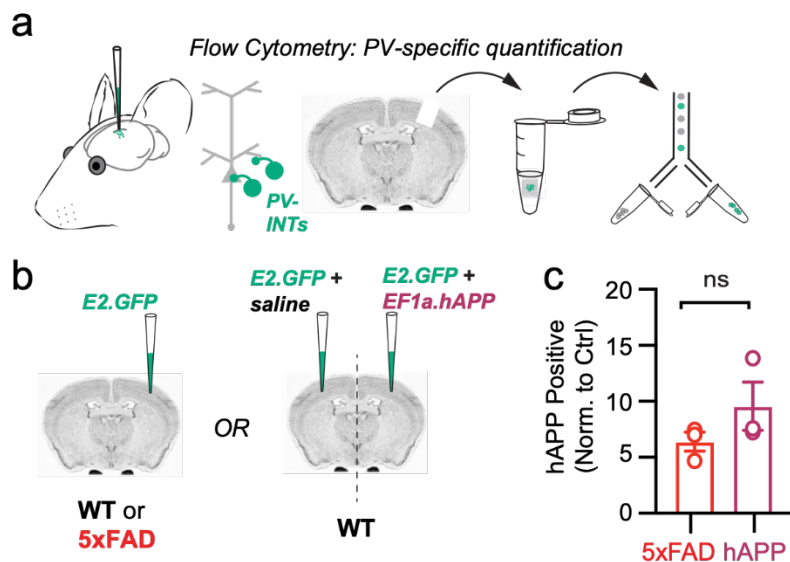
3218

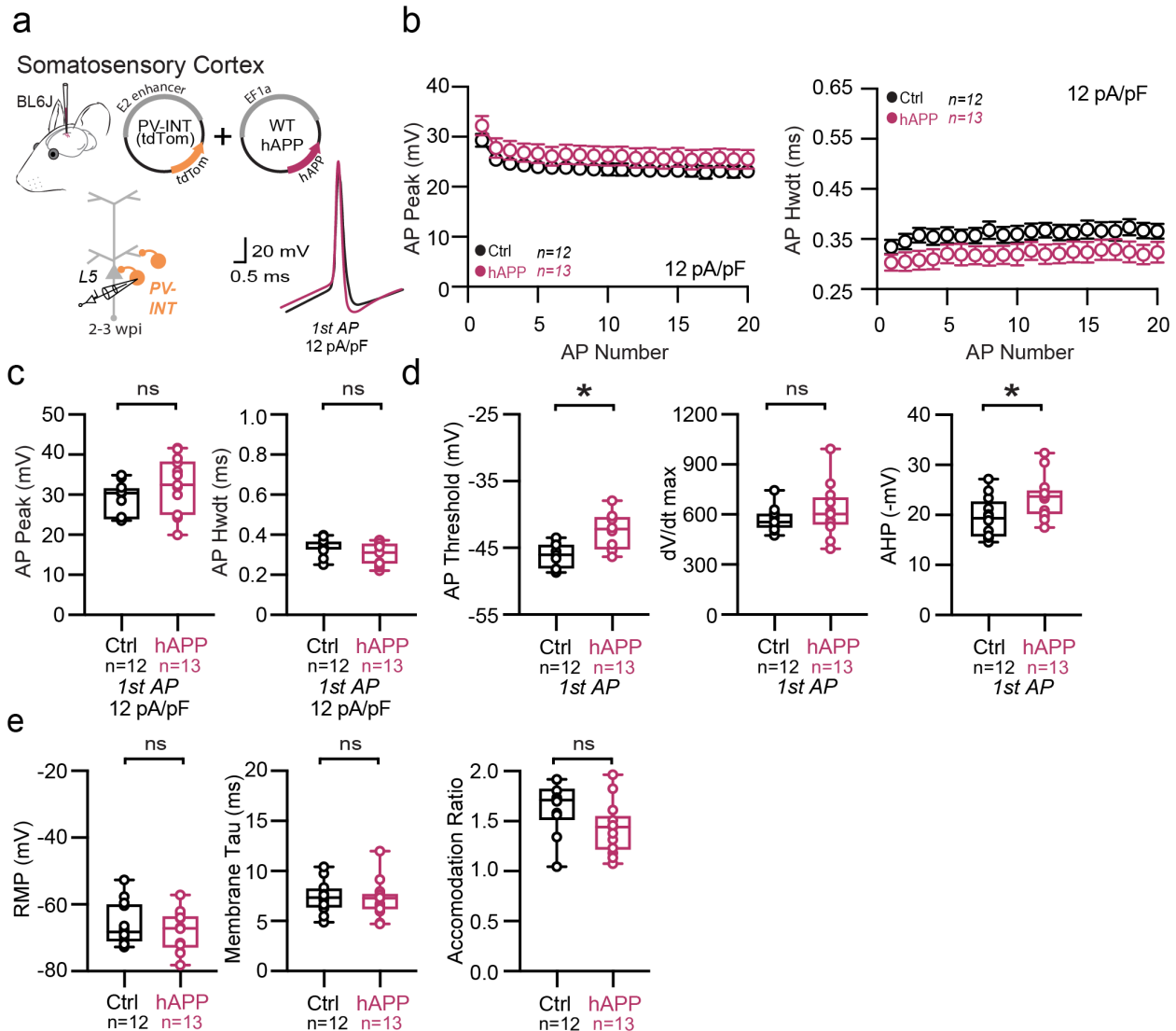*Chapter 5. Supplementary Figure 6. Confirmation of hAPP protein in PV interneurons using PV-specific flow cytometry*

(Extended Data Figure 6)

a. Graphical summary of PV-specific flow cytometry workflow. Region containing fluorescent PV interneurons after AAV.E2.GFP stereotactic injection in the SS Cortex was microdissected, triturated, and sorted based on GFP+ signal. Subsequent confirmation specifically for human APP was completed.

b. WT and 5xFAD mice (~ 2 months) were injected with AAV.E2.GFP and sorted using flow cytometry. WT mice were also used to compare AAV.E2.GFP + EF1a.hAPP injected SS Ctx to the contralateral hemisphere where EF1a was replaced with an equal volume of saline.

 c. Both groups were normalized to their control groups (WT littermates for 5xFAD; contralateral hemi for the hAPP control). The number hAPP expressing PV interneurons did not significantly differ between 5xFAD and hAPP injected (p=0.24, t=1.37, df=4).
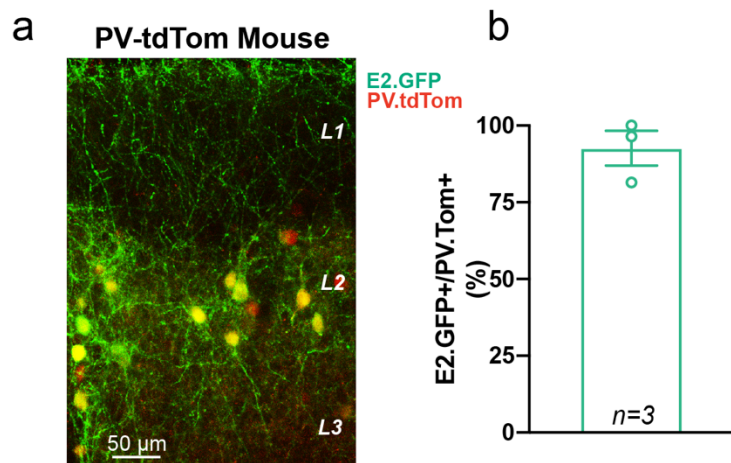
3237

3238

3239 *Chapter 5. Supplementary Figure 7. Specificity of AAV.pHP-eB.E2.GFP in the Lateral*
3240 *Entorhinal Cortex for stereotactic and retro-orbital injections*

3241 (Extended Data Figure 7)

3242 **a.** Stereotactic injection of AAV.pHP-eB.E2.GFP into the LEC of a PV-tdTom transgenic mouse.

3243 **b.** For three animals, three slices were analyzed for E2.GFP+ cells which were also PV.tdTom+

3244 (Mean: $92.62 \pm 5.7\%$ for three biological replicates).

3245

Features	Average±SEM Ctrl PV	Average±SEM mAPP PV	p-value	t-value	Degrees of Freedom
AHP (mV)	23.88±0.98	20.96±1.07	0.06	2.01	19
Threshold (mV)	-43.80±1.82	-42.68±1.68	0.66	0.45	19
dV/dt Max	494.30±30.21	567.00±28.11	0.09	1.76	19
Input Resistance (MΩ)	111.90±15.59	149.20±17.96	0.14	1.53	19
Resting Membrane Potential (mV)	-59.41±2.33	-63.80±1.27	0.12	1.66	19
Membrane Capacitance (pF)	71.04±7.65	71.02±6.67	0.99	0.002	19
Membrane Tau (ms)	8.78±0.60	10.52±0.91	0.15	1.52	19
Accomodation Ratio	1.67±0.23	2.14±0.22	0.17	1.43	19

3246

Chapter 5. Supplementary Figure 8. Passive and active properties of LEC PV interneurons after mAPP injection

(Extended Data Figure 8)

a. Graphical summary of AAV.E2.tdTom and AAV.EF1a.mAPP (or for Ctrl, saline) stereotactic injection in the SS Cortex. tdTom+ PV interneurons were fluorescently targeted for whole-cell

current-clamp recordings. AP waveforms of tdTom+ PV interneurons were compared at 12 pA/pF square pulse injections in WT mice from Ctrl and mAPP injected. Aps from the 1st spike in the train are superimposed for comparison.

b. Relationship between AP peak (p=0.61) or width (p=0.35) in WT mice and AP # during spike trains elicited with a 12 pA/pF current injection.

c. Summary table of AP properties.

d. RNAscope representative images at 40x magnification for Ctrl (top) and mAPP (bottom) injected mice: mAPP mRNA (cyan), Parvalbumin mRNA (gold), human APP mRNA (magenta), and a final merged image.

e. RNAscope quantification for mAPP copies per DAPI+ cell comparing mAPP injected to the contralateral hemisphere endogenous mAPP expression. mAPP injected show a significant increase in mAPP copies in the injected hemisphere (p=0.03, t=2.57, df=9; two-tailed paired t-test).

For all summary graphs, data are expressed as mean (± SEM). For **b**: Statistical significance is denoted as *=p<0.05, as determined by Two-way ANOVA with Sidak's multiple comparison test. For c, e: statistical significance is denoted as *=p<0.05, as determined by two-tailed unpaired t-test.

a Lateral Entorhinal Cortex

BL6J

E2 enhancer
PV-INT (tdTom)
tdTom

+

EF1a
APP Chimera
mAPP/hAβ

LII
PV-INT

20 mV
0.5 ms

2-3 wpi

1st AP
12 pA/pF

b

Ctrl *n=14*
Chimera *n=16*

12 pA/pF

c

1st AP
ns

Ctrl Chimera
n=14 n=16

d

Ctrl *n=24*
Chimera *n=16*
hAPP *n=13*

e

Ctrl *n=14*
Chimera *n=16*

12 pA/pF

f

*

Ctrl Chimera
n=14 n=16

unpaired t-test

g
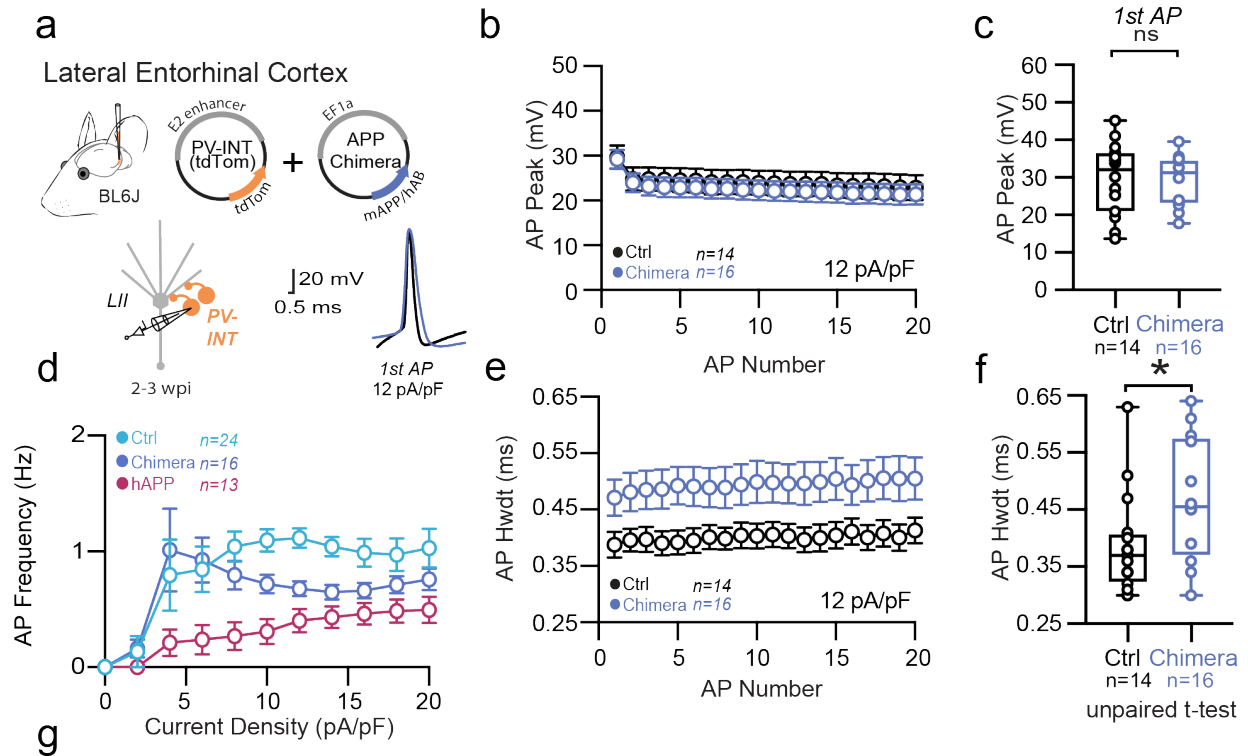
Features	Average±SEM Ctrl	Average±SEM APP Chimera	p-value	t-value	Degrees of Freedom
AHP (mV)	24.54±1.16	23.21±0.97	0.39	0.88	29
Threshold (mV)	-44.17±1.53	-43.29±1.08	0.64	0.48	29
dV/dt Max	518.10±40.35	456.00±36.29	0.26	1.15	29
Input Resistance (MΩ)	141.50±12.70	156.30±23.50	0.60	0.50	29
Resting Membrane Potential (mV)	-69.38±1.38	-70.57±2.06	0.65	0.47	29
Membrane Capacitance (pF)	66.96±8.06	72.59±4.21	0.53	0.64	29
Membrane Tau (ms)	8.28±0.70	10.29±1.12	0.15	1.47	29
Accomodation Ratio	1.13±0.03	1.16±0.02	0.50	0.68	29

Chapter 5. Supplementary Figure 9. Passive and active properties of LEC PV interneurons after mAPP/hAβ Chimera injection

(Extended Data Figure 9)

a. Graphical summary of AAV.E2.tdTom and AAV.EF1a.mAPP/hAβ Chimera (or for Ctrl, saline) stereotactic injection in the SS Cortex. tdTom+ PV interneurons were fluorescently targeted for whole-cell current-clamp recordings. AP waveforms of tdTom+ PV interneurons were compared

3278 at 12 pA/pF square pulse injections in WT mice from Ctrl and mAPP injected. Aps from the 1st

3279 spike in the train are superimposed for comparison.

3280 **b,e.** Relationship between AP peak (b) or width (e) in WT mice and AP # during spike trains

3281 elicited with a 12 pA/pF current injection.

3282 **c.** Summary data of AP properties. LEC PV cells after Chimera injection 1st AP peak (29.74 $\pm$ 2.61

3283 mV, 29.18 $\pm$ 2.08 mV, hAPP and Ctrl respectively, p=0.87, t=0.17, df=24) remains unchanged.

3284 **d.** Group data summary of AP firing frequency in L2 LEC from mAPP injected (blue), Chimera

3285 injected (purple), and hAPP injected mice (magenta), all normalized to their dataset controls.

3286 **f.** AP half-width displays a significant decrease in the chimera group (0.39$\pm$ 0.02 ms, 4.80 $\pm$ 0.03

3287 ms, hAPP and Ctrl respectively, p=0.04, t=2.14, df=24).

3288 **g.** Summary table of AP properties.

3289

3290 For all summary graphs, data are expressed as mean ($\pm$ SEM). For c, f, g: statistical significance

3291 is denoted as *=p<0.05, as determined by two-tailed unpaired t-test.

3292

3293
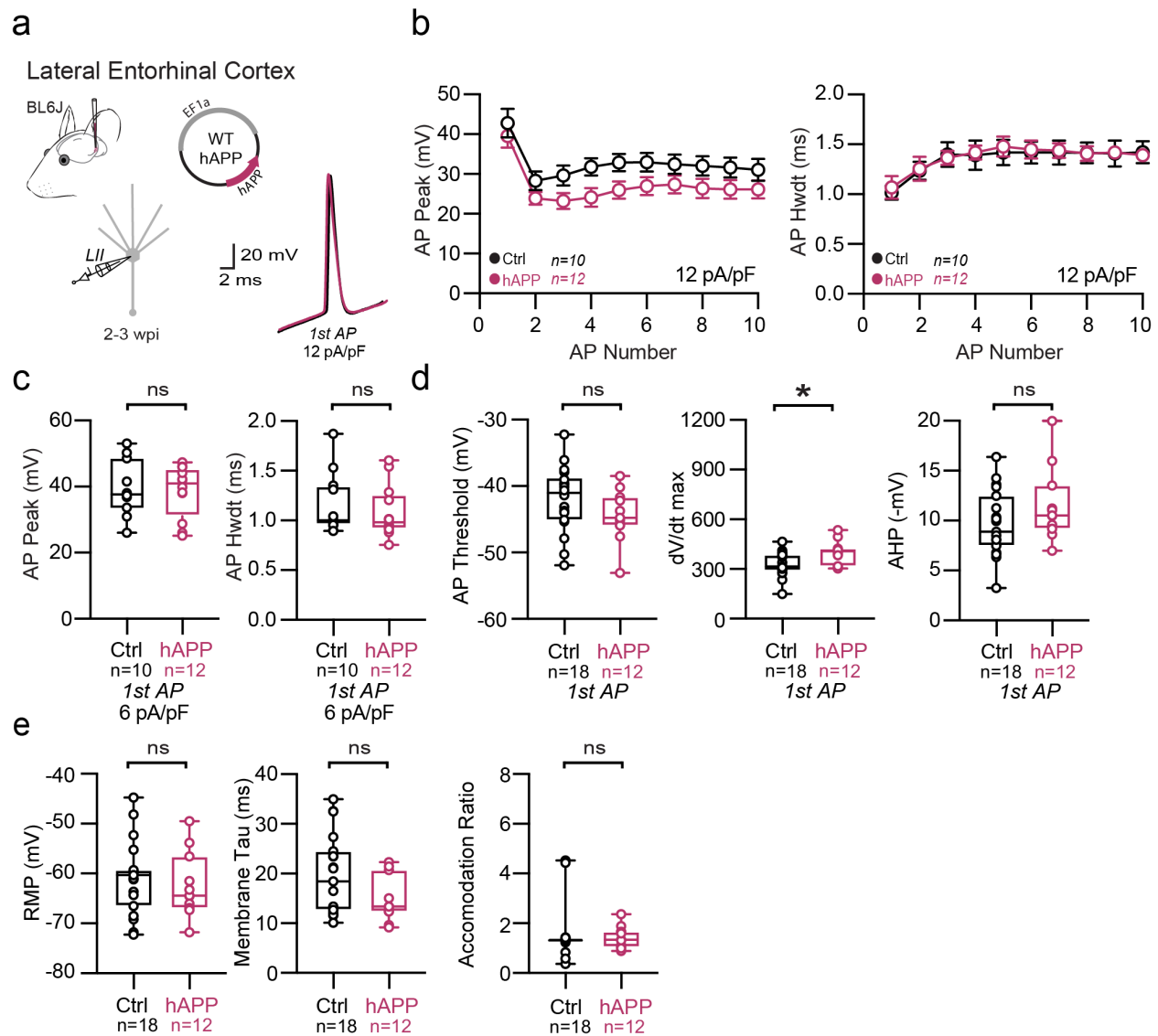
Chapter 5. Supplementary Figure 10. Passive and active properties of LEC excitatory neurons after hAPP injection

(Extended Data Figure 10)

a. Graphical summary of AAV.EF1a.hAPP (or for Ctrl, saline) stereotactic injection in the LEC. Excitatory cells were targeted for whole-cell current-clamp recordings. AP waveforms of excitatory cells were compared at 12 pA/pF square pulse injections in WT mice from Ctrl and hAPP injected. Aps from the 1st spike in the train are superimposed for comparison.

b. Relationship between AP peak or width in WT mice and AP # during spike trains elicited with a 12 pA/pF current injection.

c. Summary data of AP properties. LEC excitatory cells after hAPP injection 1st AP peak (29.36 ± 4.14 mV, 28.62 ± 2.34 mV, hAPP and Ctrl respectively, p=0.87, t=0.17, df=28) and half-width remains unchanged (1.26 ± 0.10 ms, 1.50 ± 0.13 ms, hAPP and Ctrl respectively, p=0.23, t=1.28, df=28).

d. Summary data of AP properties. LEC excitatory cells after hAPP injection AP threshold (p=0.18, t= 1.38, df = 28) and AHP remain unchanged (p=0.16, t=1.46, df=28), but dV/dt max shows a significance increase (399.7 ± 21.82, 331.0 ± 16.71) , hAPP and Ctrl respectively, p=0.02, t=2.49, df=28).

e. Summary data of AP properties. LEC excitatory cells after hAPP injection show unchanged Resting Membrane Potential (p=0.60, t=0.53, df=28), Accommodation Ratio (p=0.69, t=0.40, df=28), and Membrane Tau (p=0.08, t=1.84, df=28).

For all summary graphs, data are expressed as mean (± SEM). For **b**: Statistical significance is denoted as *=p<0.05, as determined by Two-way ANOVA with Sidak's multiple comparison test. For c, d, e: Individual data points and box plots are displayed. Statistical significance is denoted as *=p<0.05, as determined by two-tailed unpaired t-test.
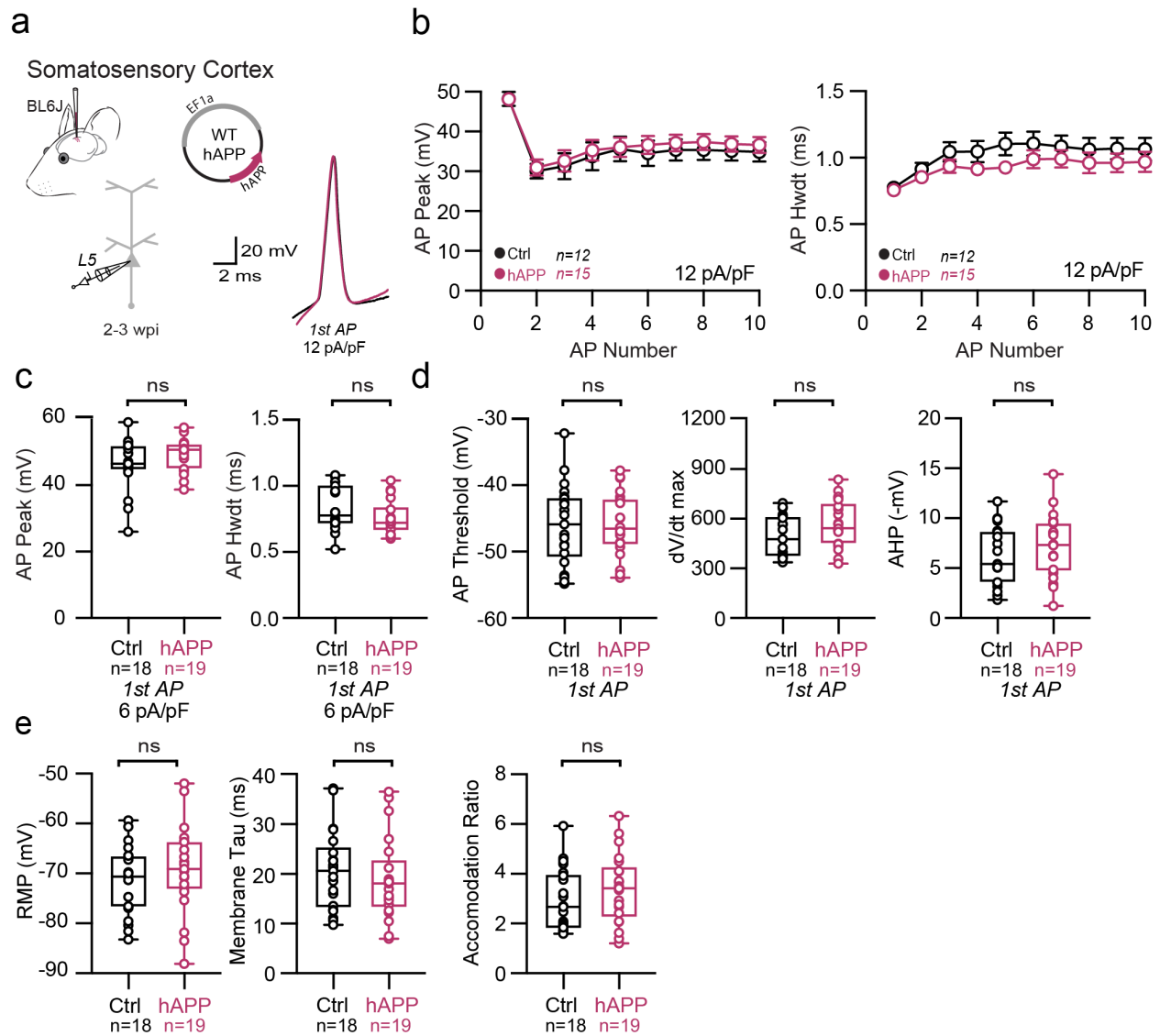
Chapter 5. Supplementary Figure 11. Passive and active properties of SS Ctx excitatory neurons after hAPP injection

(Extended Data Figure 11)

a. Graphical summary of AAV.EF1a.hAPP (or for Ctrl, saline) stereotactic injection in the SS Ctx. Excitatory cells were targeted for whole-cell current-clamp recordings. AP waveforms of excitatory cells were compared at 12 pA/pF square pulse injections in WT mice from Ctrl and hAPP injected. Aps from the 1st spike in the train are superimposed for comparison.

b. Relationship between AP peak or width in WT mice and AP # during spike trains elicited with a 12 pA/pF current injection.

c. Summary data of AP properties. SS Ctx excitatory cells after hAPP injection 1st AP peak (p=0.19, t=1.34) and half-width (p=0.17, t=1.41) (df=40) remains unchanged.

3333   **d.** Summary data of AP properties. SS Ctx excitatory cells after hAPP injection AP threshold

3334   ($p=0.97$, $t=0.04$, $df=40$), dV/dt max ($p=0.08$, $t=1.79$, $df=40$), and AHP remain unchanged ($p=0.32$,

3335 $t=1.00$, $df=40$).

3336   **e.** Summary data of AP properties. SS Ctx excitatory cells after hAPP injection show unchanged

3337   Resting Membrane Potential ($p=0.37$, $t=0.90$, $df=40$), Accommodation Ratio ($p=0.25$, $t=1.16$,

3338 $df=40$), and Membrane Tau($p=0.48$, $t=0.71$, $df=40$).

3339   For all summary graphs, data are expressed as mean ($\pm$ SEM). For **b**: Statistical significance is

3340   denoted as *=$p<0.05$, as determined by Two-way ANOVA with Sidak's multiple comparison test.

3341   For c, d, e: Individual data points and box plots are displayed. Statistical significance is denoted

3342   as *=$p<0.05$, as determined by two-tailed unpaired t-test.

3343

a LEC Excitatory (LII)

b LEC PV interneuron
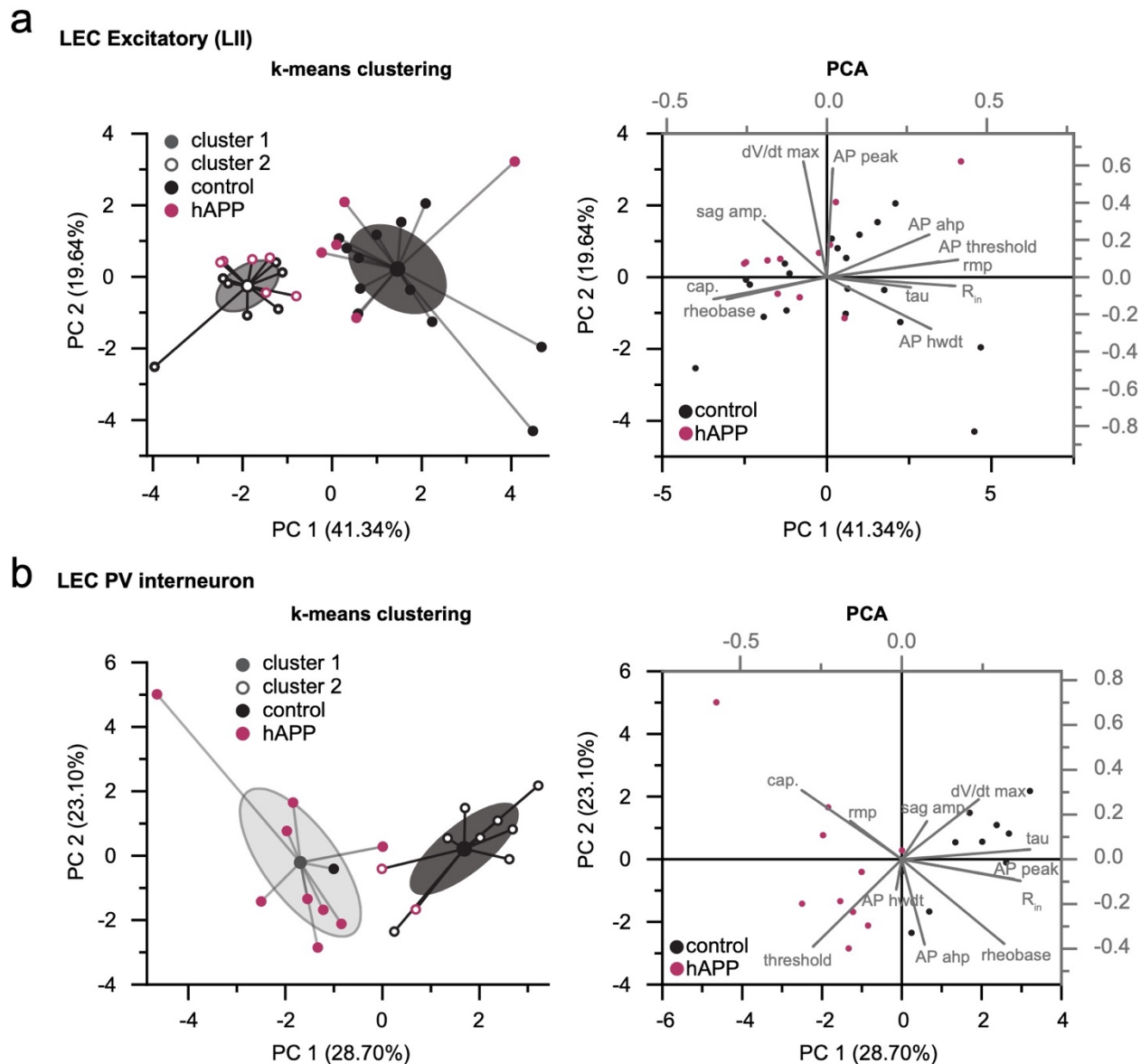
3344

Chapter 5. Supplementary Figure 12. PCA analysis of LEC cell populations after hAPP injection

(Extended Data Figure 12)

K-means clustering and Principal component analysis (PCA) plot performed on all cells based on active and passive properties for (a) excitatory cells and (b) PV interneurons.

a. K-mean clustering fails to separate LEC excitatory cells based on hAPP identity (left), due to largely homogeneous active and passive properties, suggesting differences along different axes.

b. Unsupervised clustering preserves hAPP identity in LEC PV interneurons.
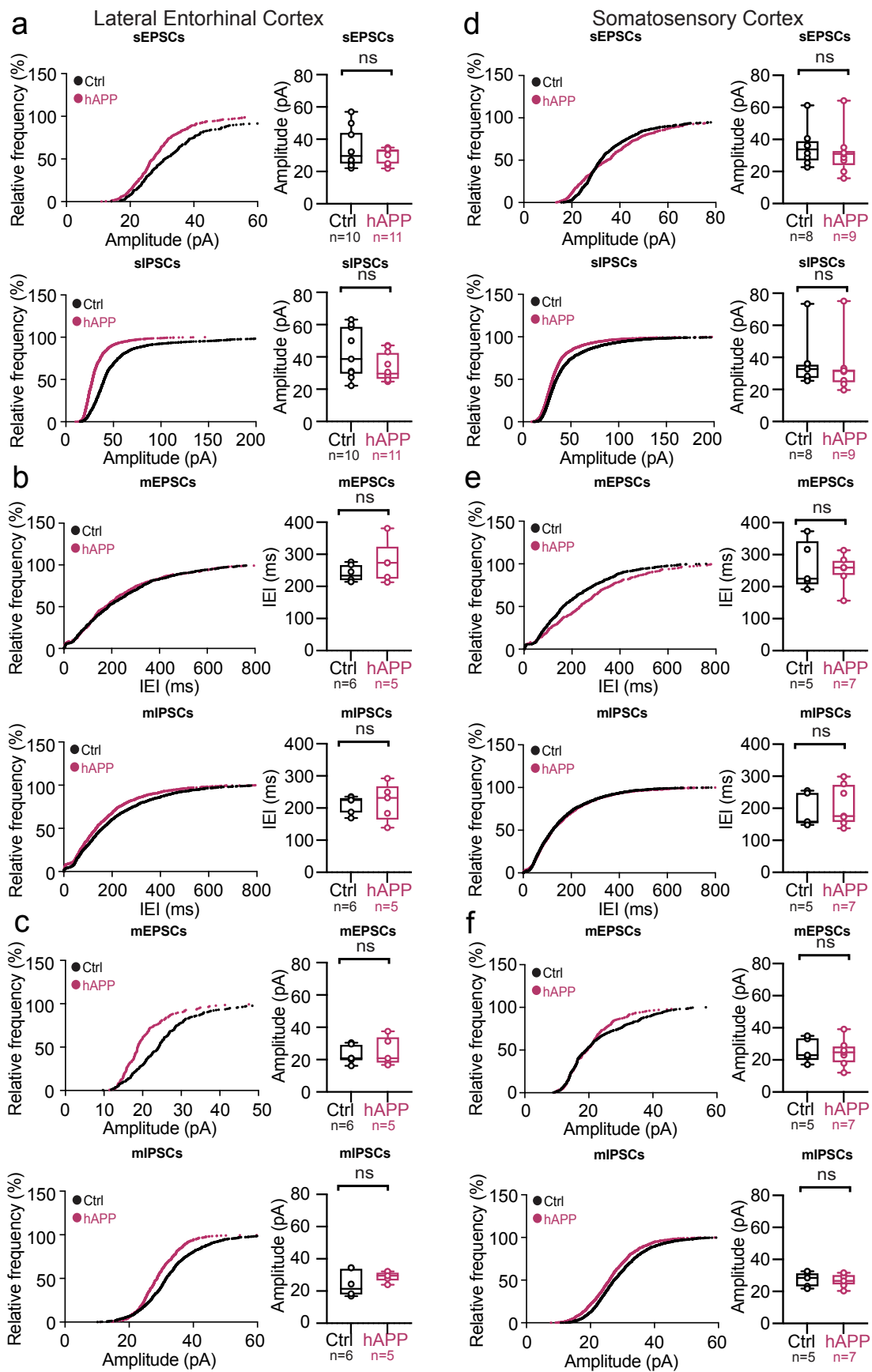
3353 *Chapter 5. Supplementary Figure 13. Adult-onset human APP does not alter mini frequencies or*
3354 *event kinetics in the LEC or SS Ctx*

3355 (Extended Data Figure 13)

3356 **a. Top:** Cumulative distribution curve for spontaneous EPSCs in the LEC showing the relationship
3357 of relative frequency of events to the amplitude (left). Quantified averages of event amplitude are
3358 displayed for each cell as individual data points and compared between Ctrl (black) and hAPP
3359 injected (magenta) conditions (right). L2 LEC sEPSCs showed no amplitude change (p=0.34,
3360 t=0.97, df=19). **Bottom:** Cumulative distribution curve for spontaneous IPSCs in the LEC showing
3361 the relationship of relative frequency of events to the amplitude (left). Quantified averages of event
3362 amplitude are displayed for each cell as individual data points and compared between Ctrl (black)
3363 and hAPP injected (magenta) conditions (right). L2 LEC sIPSCs show an unchanged amplitude
3364 (p=0.11, t=1.66, df=19).

3365 **b. Top:** Cumulative distribution curve for miniature EPSCs in the LEC showing the relationship
3366 of relative frequency of events to the inter-event interval (left). Quantified averages of IEIs are
3367 displayed for each cell as individual data points and compared between Ctrl (black) and hAPP
3368 injected (magenta) conditions (right). L2 LEC mEPSCs show no change in the IEIs (p=0.28,
3369 t=1.16, df=9). **Bottom:** Cumulative distribution curve for miniature IPSCs in the LEC showing
3370 the relationship of relative frequency of events to the IEIs (left). Quantified averages of IEIs are
3371 displayed for each cell as individual data points and compared between Ctrl (black) and hAPP
3372 injected (magenta) conditions (right). L2 LEC mIPSCs show no change in the IEIs (p=0.80, t=0.27,
3373 df=9).

3374 **c. Top:** Cumulative distribution curve for miniature EPSCs in the LEC showing the relationship
3375 of relative frequency of events to the amplitude (left). Quantified averages of event amplitude are
3376 displayed for each cell as individual data points and compared between Ctrl (black) and hAPP
3377 injected (magenta) conditions (right). L2 LEC mEPSCs no amplitude change (p=0.67, 0.45, df=9).
3378 **Bottom:** Cumulative distribution curve for miniature IPSCs in the LEC showing the relationship
3379 of relative frequency of events to the amplitude (left). Quantified averages of event amplitude are
3380 displayed for each cell as individual data points and compared between Ctrl (black) and hAPP
3381 injected (magenta) conditions (right). L2 LEC mIPSCs show an unchanged amplitude (p=0.27,
3382 t=1.18, df=9).

d. Top: Cumulative distribution curve for spontaneous EPSCs in the SS Ctx showing the relationship of relative frequency of events to the amplitude (left). Quantified averages of event amplitude are displayed for each cell as individual data points and compared between Ctrl (black) and hAPP injected (magenta) conditions (right). L5 SS Ctx sEPSCs no amplitude change (p= 0.57, t=0.59, df=15). **Bottom:** Cumulative distribution curve for spontaneous IPSCs in the SS Ctx showing the relationship of relative frequency of events to the amplitude (left). Quantified averages of event amplitude are displayed for each cell as individual data points and compared between Ctrl (black) and hAPP injected (magenta) conditions (right). L5 SS Ctx sIPSCs show an unchanged amplitude (p=0.75, t=0.33, df=15).

e. Top: Cumulative distribution curve for miniature EPSCs in the SS Ctx showing the relationship of relative frequency of events to the IEIs (left). Quantified averages of IEIs are displayed for each cell as individual data points and compared between Ctrl (black) and hAPP injected (magenta) conditions (right). L2 LEC mEPSCs show no change in the IEIs (p=0.74, t=0.35, df=10). **Bottom:** Cumulative distribution curve for miniature IPSCs in the SS Ctx showing the relationship of relative frequency of events to the IEIs (left). Quantified averages of IEIs are displayed for each cell as individual data points and compared between Ctrl (black) and hAPP injected (magenta) conditions (right). L5 SS Ctx mIPSCs show no change in the IEIs (p=0.65, t=0.47, df=10; mEPSC: p=0.74, t=0.35, df=10).

f. Top: Cumulative distribution curve for miniature EPSCs in the SS Ctx showing the relationship of relative frequency of events to the amplitude (left). Quantified averages of event amplitude are displayed for each cell as individual data points and compared between Ctrl (black) and hAPP injected (magenta) conditions (right). L5 SS Ctx mEPSCs no amplitude change (p=0.77, t=0.31, df=10). **Bottom:** Cumulative distribution curve for miniature IPSCs in the SS Ctx showing the relationship of relative frequency of events to the amplitude (left). Quantified averages of event amplitude are displayed for each cell as individual data points and compared between Ctrl (black) and hAPP injected (magenta) conditions (right). L5 SS Ctx mIPSCs show an unchanged amplitude (p=0.78, t=0.29, df=10).

For a, b, c, d, e, f: Individual data points and box plots are displayed. Statistical significance is denoted as *=p<0.05, as determined by two-tailed unpaired t-test
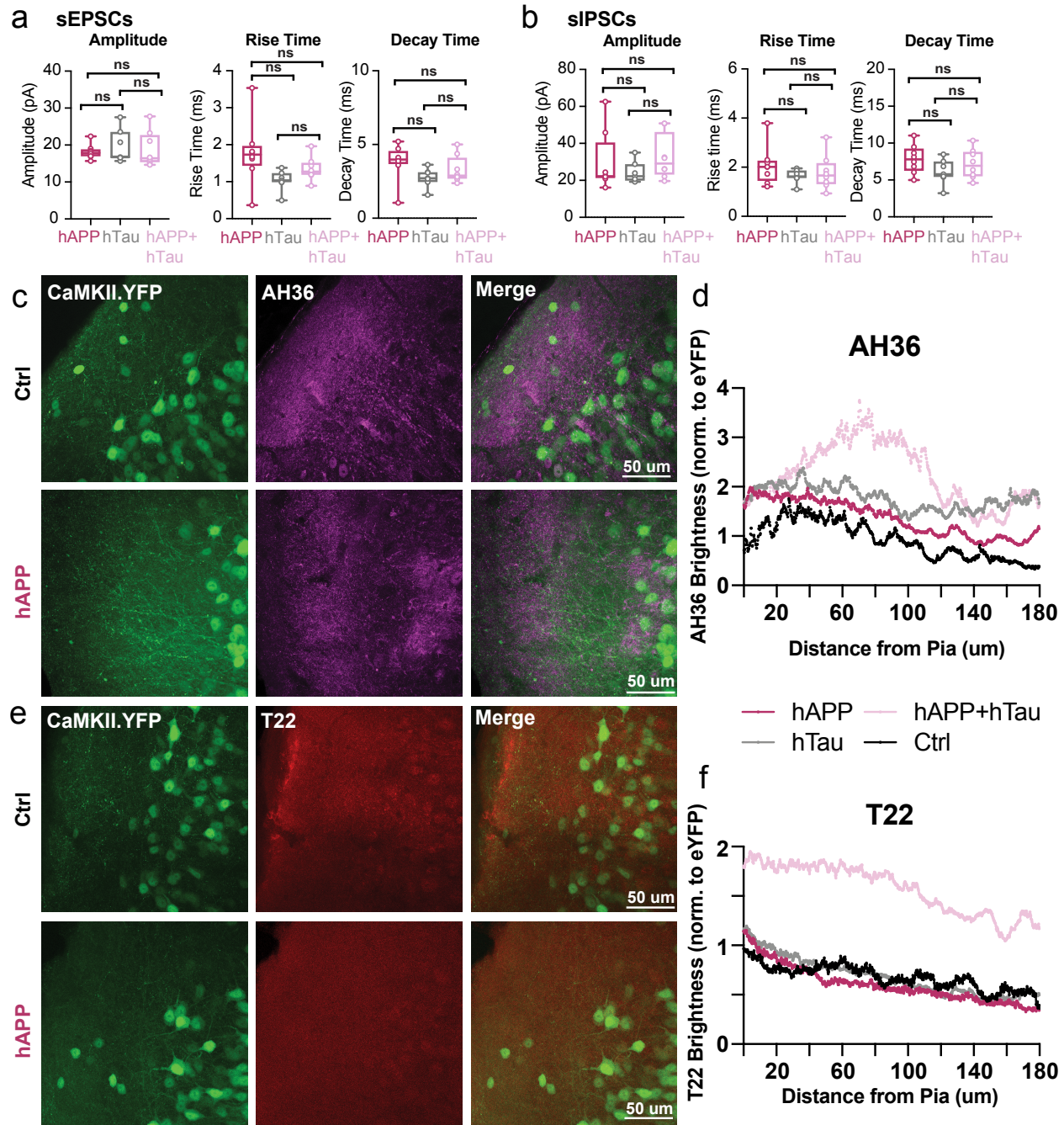
Chapter 5. Supplementary Figure 14. hTau co-injection with hAPP spontaneous properties and Ctrl IHC images

(Extended Data Figure 14)

a. Summary data of sEPSC properties. sEPSC properties between hAPP injection, hTau injection, or hAPP+hTau injection are not significantly different (Amplitude: hAPP vs. hTau p=0.75, hAPP vs. hAPP+hTau p=0.94, hTau vs. hAPP +hTau p=0.92; Rise Time: hAPP vs. hTau p=0.05, hAPP vs. hAPP+hTau p=0.31, hTau vs. hAPP +hTau p=0.55; Decay Time: hAPP vs. hTau p=0.11, hAPP

3420   vs. hAPP+hTau p=0.54, hTau vs. hAPP +hTau p=0.55; df=20, One-way ANOVA with Multiple

3421   Comparisons).

3422   **b.** Summary data of sIPSC properties. sIPSC amplitudes between hAPP injection, hTau injection,

3423   or hAPP+hTau injection are not significantly different (Amplitude: hAPP vs. hTau p=0.69, hAPP

3424   vs. hAPP+hTau p=0.88, hTau vs. hAPP +hTau p=0.41; Rise Time: hAPP vs. hTau p=0.39, hAPP

3425   vs. hAPP+hTau p=0.65, hTau vs. hAPP +hTau p=0.88; Decay Time: hAPP vs. hTau p=0.21, hAPP

3426   vs. hAPP+hTau p=0.76, hTau vs. hAPP +hTau p=0.53; df=20, One-way ANOVA with Multiple

3427   Comparisons).

3428   **c,e.** IHC representative images at 60x magnification for Ctrl (top) or hAPP (bottom) injected mice

3429   with staining for either AH36 (c) or T22 (e).

3430   **d.** Ctrl, hAPP, hTau, and hAPP+hTau were analyzed for AH36 brightness using four line scans in

3431   each slice. AH36 brightness was normalized to CaMKII.eYFP brightness to control for any

3432   potential variability in viral expression. hAPP+hTau showed the highest level of AH36 brightness,

3433   most notably between 40-120 μm from the pia.

3434   **f.** hAPP, hTau, and hAPP+hTau were analyzed for T22 brightness using four line scans in each

3435   slice. AH36 brightness was normalized to CaMKII.eYFP brightness to control for any potential

3436   variability in viral expression. hAPP+hTau showed a higher level of T22 brightness, above all

3437   other groups which displayed only background levels of T22 positivity.

3438

3439

3440
3441

3442

Chapter 6: Discussion

Clearly, future experiments are needed, aimed at determining how interneuronal population variance is altered under various conditions, and the results will likely provide us with important clues regarding the nature of the underlying regulatory mechanisms as well.

-Dr. Ivan Soltesz (2006)

6.1 Summary

While it has taken thousands of years to recognize the brain as the seat of our intelligence and self, the last 100 years of neuroscience research has experienced exponential growth. From discovering neurons are not only connected by synapses, but that they also communicate to one another through electrical means, to which voltage-gated channel subunits are imperative for a specific action potential waveform of unique cell types.

All niches within the field of neuroscience continue to grow rapidly, as it is still unclear how circuits maintain homeostasis while exhibiting the bandwidth to observe an important incoming stimulus. It is, however, blatantly apparent, that a major determinant of this circuit ability is the function of the 'short axon cells' as observed by Ramón y Cajal over a century ago. These short axon cells, or GABAergic interneurons, have the capacity to assist in the excitatory/inhibitory balance required for circuit homeostasis. They are also actively involved in signal propagation as well as facilitating many of the oscillations observed in the brain.

In the cortex, one of the most common and critical regulators of the E/I balance are the parvalbumin+ (PV) interneurons. PV interneurons are often characterized by the fast-spiking phenotype which considered to be mediated by specific voltage-gated channels, such as Kv3 and Nav1.1[22,23]. Furthermore, wild-type PV interneurons are stereotyped by specific intrinsic properties, including a low input resistance (75-90 MΩ), high rheobase (330-400 pA), high firing frequency at 2-3x threshold (130-180 Hz), a narrow action potential half-width (0.40-0.44 ms), and minimal spike frequency adaptation (0.75-0.85)[31]. Of course, it is important to note that the same firing phenotype may be recapitulated by vastly different conductances of the same ion channels[32]. Furthermore, there have multiple observations of PV+ interneurons which fall outside of the canonical 'fast-spiking' phenotype and corresponding intrinsic properties, while still spiking

3472   at a frequency higher than most other cell types of the brain. These have been observed in the

3473   subiculum (quasi fast-spiking interneurons)[33], the striatum (fast-spiking-like cells)[34], and the CA1

3474   region of the hippocampus (non-fast-spiking PV+ interneurons, NFS)[31]. The subgroup of NFS

3475   PV+ interneurons displayed varied intrinsic properties from those canonical FS interneurons,

3476   including a low-firing frequency (~96.1 Hz at 3x threshold), high input resistance, and low

3477   rheobase[31]. Here we demonstrate that PV interneurons within the LEC are biophysically distinct

3478   from other neocortical PV interneurons. However, where these cells represent a small subset of the

3479   PV+ interneurons of these regions (~20% in CA1)[31], the majority of our recorded PV+

3480   interneurons displayed this low-firing phenotype. Although the WT PV firing frequency in our

3481   LEC recordings is consistent with previous observations[340], the striking biophysical differences

3482   (i.e., AP waveform) with respect to PV cells in other cortical regions had not been systematically

3483   evaluated. Whether the baseline low-firing frequency of PV+ interneurons in the LEC confers

3484   vulnerability to hAPP-induced pathophysiology remains unclear.

3485   This dissertation includes multiple studies which explore baseline variability of PV

3486   interneurons between regions, and how they differentially become perturbed in disease models,

3487   dysregulating their ability to regulate the E/I balance within the circuit. This understanding

3488   required the development of a multitude of novel PV interneuron-specific methods, which are

3489   outlined below.

3490   6.2 Development of PV Interneuron-specific Methods

3491   Previously, characterizing PV interneurons in health and disease has relied on either

3492   recognition of their fast-spiking phenotype, post-hoc staining of the Parvalbumin protein, or mouse

3493   models which utilize parvalbumin as a promoter to identify PV interneurons. Understandably,

3494   these techniques observe the canonical FS PV interneurons, and intentionally exclude cells which

3495   may exist outside of the average for this cell type. These techniques also make it difficult for real-

3496   time assessment of transcriptional and translational alterations of PV interneurons between regions

3497   and in disease, without dedicating extensive time and funds for the creation of double- or triple-

3498   transgenic crosses.

3499   With the recent development of highly versatile enhancer-AAVs[254], including tools

3500   targeting inhibitory interneurons[255,256], it has become feasible to compare PV interneuron

3501   characteristics across regions and mouse without the need for laborious techniques. Particularly,

3502   the 'E2' enhancer, which has been shown to specifically target fast-spiking interneurons allows

3503   further dissection of PV interneurons in health and disease[175]. This dissertation wields the E2

3504   enhancer to measure PV-specific alterations in models of health of disease in a multitude of novel

3505   techniques.

3506   One of the modern goals of cellular neuroscience is to elucidate how the molecular

3507   signatures of unique neuronal subtypes translate to their functional diversity in intact circuits.

3508   Single-neuron transcriptomic studies have recently provided unparalleled access to the genetic

3509   diversity of dozens of unique brain cell classes[7]. Although effective, single neuron transcriptomics

3510   is limited by the number of cells which can be acquired and assessed. Alternatively, other methods

3511   of RNA expression detect transcripts from numerous cells, such as quantitative Polymerase Chain

3512   Reaction, or qPCR. However, this method often measures specific RNA transcripts from many cell

3513   types at once, rather than an individual cell class. To circumnavigate this issue, we combined the

3514   E2 enhancer[175] with a recently described technique of fluorescent-targeted cell isolation[7]. We

3515   performed PV interneuron-specific (low-input) qPCR[7] by isolating and pooling AAV.E2.GFP$^+$

3516   neurons from dissected somatosensory cortex following AAV retro-orbital injection[138] in 5xFAD

3517   and control mice. Although incredibly useful, this technique required only complemented more

3518 thorough studies of PV alterations in the model using patch-clamp to assess biophysical alterations

3519 of the voltage-gated ion channels. This unique combination of methods represented the beginning

3520 of a cell-type-specific analysis of PV alterations in health and disease in real-time, which was

3521 followed by the utilization of retro-orbitally injected E2 enhancer for similar analyses.

3522 Functional information is nonetheless limited in transcriptomic studies, due to substantial

3523 discordance between mRNA and protein levels, especially in neurons[131-133]. Thus, our next attempt

3524 at PV-specific assessment of alterations turned to measuring protein levels. In chapter 5

3525 (Supplemental Information), we again utilize the E2 enhancer coupled with a GFP protein to

3526 measure human APP levels in PV interneurons after expressing either the EF1a.hAPP virus or a

3527 control virus. Rather than hand-picking fluorescent cells as our method of cell isolation[7], we

3528 utilized flow cytometry to detect hAPP levels in our AAV.E2.GFP[+] interneurons in our wild-type

3529 animals either injected with a control virus or EF1a.hAPP, or a positive control of 5xFAD which

3530 highly expresses human APP. Using this unique combination of methods, we were able to confirm

3531 human APP protein expression specifically in PV interneurons. While an imperative experiment

3532 for this study, we required a different technique to assess many functional alterations specifically

3533 in PV interneurons across health and disease.

3534 Importantly, proteomic studies relying on physical isolation of individual neuron types are

3535 inadequate, as physical isolation of individual neurons is poorly tolerated, and of those that do

3536 survive, the vast majority of their functional surface area (i.e., dendrites and axons) is lost[135,136].

3537 To overcome these limitations, we recently developed an *in vivo* strategy called cell type-specific

3538 in vivo biotinylation of proteins (CIBOP). When coupled with mass spectrometry, CIBOP can

3539 resolve native state proteomes from physically unaltered cell subtypes *in vivo*[2]. Key technical

3540 advancements, especially relating to neuronal subtype-specific targeting across different disease

3541 models, are also necessary to fully realize the potential of this method via extension to distinct

3542 classes of excitatory and inhibitory neurons.

3543 As discussed throughout this dissertation, PV interneurons represent a vulnerable cell class

3544 in the early stages of the progression of Alzheimer's disease. Thus, to enhance future therapeutic

3545 efficacy, high-resolution native state proteomic signatures of individual cell classes in wild type

3546 and disease models are required. Therefore, we implemented a versatile, systemic AAV-CIBOP

3547 intersectional approach[2,138,255] to characterize and compare native state *in vivo* PV interneuron

3548 proteomes from both wild type mice and in a mouse model of early AD pathology. We utilized the

3549 E2-AAV targeting method to express Cre recombinase specifically in PV neurons throughout the

3550 cortex and hippocampus of Rosa26[TurboID] mice[2]. Upon Cre-mediated recombination, TurboID was

3551 expressed selectively in PV interneurons, leading to robust cellular proteomic biotinylation. This

3552 PV CIBOP approach identified over 600 proteins enriched in PV interneurons, including canonical

3553 proteins as well as over 200 novel PV interneuron proteins. The PV interneuron proteome was

3554 enriched in mitochondrial, metabolic, ribosomal, synaptic, and a large number of

3555 neurodegeneration genetic risk and cognitive resilience-related proteins, suggesting unique

3556 vulnerabilities of PV interneurons in AD. This intersectional method[2,138,255] allows quantitative *in*

3557 *vivo* neuron-type-specific proteomics. We leveraged this approach to isolate the *first* native-state

3558 PV interneuron-specific proteome.

3559 We then took this approach one step further, to assess variability in cortical PV interneurons

3560 between regions. This was achieved through systemic AAV injections to achieve whole-cortex

3561 expression of a PV-specific, Cre-expressing enhancer-AAV in Flex.TurboID mice[142] followed by

3562 region-specific microdissection. Over 800 proteins were biotinylated in PV interneurons in each

3563 region, of which nearly two hundred proteins showed region-specific differential abundances.

3564   Generally, LEC PV interneuron proteomes showed biased enrichment in transmembrane and

3565   synaptic ion channels and transporters, while SS PV interneuron proteomes showed biased

3566   enrichment in microtubule binding, glycolysis, and fatty acid metabolism-related proteins.

3567   Thorough cross-comparison of these non-overlapping cell-type specific alterations with alterations

3568   observed across AD mouse model and human AD bulk-tissue staging (some of these analyses will

3569   be addressed later in this discussion) may provide specific targets for therapeutics to halt disease

3570   progression.

3571   <u>6.3 Pathophysiology of PV interneurons in AD</u>

3572   As an example of this comparison, in Chapter 5, we assessed whether PV interneuron proteins

3573   differentially expressed by region were representative of proteins associated with cognitive

3574   stability during aging. To achieve this, we used data from a protein-wide association study of

3575   cognitive resilience from human brain samples (Religious Orders Study and the Rush Memory and

3576   Aging Project; 'ROSMAP'[146]). In this study, rate of cognitive decline (cognitive slope) was

3577   correlated with post-mortem brain protein levels quantified by mass spectrometry, identifying

3578   proteins positively associated with cognitive stability (pro-resilience proteins) and those negatively

3579   associated with cognitive stability (anti-resilience proteins). Our findings revealed that wild-type

3580   LEC PV interneurons displayed significantly more 'pro-resilience'-associated proteins as

3581   compared to SS Ctx PV interneurons. As nearly all the LEC PV interneuron enriched proteins

3582   associated with cognitive stability during aging, we next explored whether expression of these

3583   enriched proteins was perturbed throughout stages of AD pathology.

3584   In our subsequent exploration, we investigated whether expression of these enriched proteins

3585   was perturbed throughout stages of AD pathology in humans. While several proteomics surveys

3586   of post-mortem brain tissues from AD and control brain have been performed, few studies have

3587   published data comparing the entorhinal cortex (EC) to neocortical regions, such as the frontal

3588   cortex (FC). This is true particularly regarding disease staging. In a recent study[342], EC and FC

3589   regions from post-mortem brains of control and AD cases (BRAAK stages I-III [early] and IV-VI

3590   [late]) were analyzed by quantitative MS. This yielded 737 differentially enriched proteins

3591   comparing AD to control, at either early (BRAAK I-III) or late (BRAAK IV-VI) stages, which

3592   were significant in either EC or FC regions. Among these, 93 human DEPs were observed in our

3593   PV-CIBOP proteome. Of these, 23 proteins showed differential levels in SS Ctx PV interneurons

3594   as compared to LEC PV interneurons. Surprisingly, of the regional PV interneuron proteins that

3595   were altered in human AD brain, many were pro-resilience proteins. Importantly, the LEC-

3596   enriched PV interneuron proteins (including pro-resilience proteins) showed decreased levels in

3597   the EC of human AD cases. Thus, resilience factors in PV interneuron of the entorhinal cortex may

3598   be lost as AD pathology increases.

3599   Although the identified proteins provide specific targets for therapeutics, it is unlikely that

3600   they are ubiquitously expressed across the brain or individual cell types. An elegant treatment

3601   which hopes to be successful at early phases of the disease must consider the regions and cell types

3602   which are vulnerable at that time, as we have shown above. Furthermore, comparison of cell-type-

3603   specific proteomics to ongoing alterations in early phases of the disease including circuit

3604   excitability (*e.g.* hyperexcitability observed in AD patients) may provide such targets at a unique

3605   point of intervention, particularly in regions which are vulnerable at early timepoints.

3606   Although brain regions of early vulnerability have been known for over 30 years[90], our

3607   understanding of what makes certain areas more susceptible remains unknown. The first cortical

3608   region to display pathology and degeneration in AD is the Lateral Entorhinal Cortex

3609   (LEC)[90,94,105,117]. Notably, landmark studies identified Layer II (LII) neurons as highly vulnerable

3610 to early neurodegeneration with up to 60% cell death in mild AD patients and up to 90% in severe

3611 cases[105]. More recently, LII LEC principal neurons were also characterized as a cell population

3612 exhibiting amyloid pathology[94]. However, the distinctive features which impart vulnerability to

3613 neurons in the LEC AD remain unclear. Uncovering region-specific cellular mechanisms could

3614 improve our understanding of the initiating factors in the AD cascade and are imperative in

3615 determining potential interventions at a time when subsequent cognitive decline and

3616 neurodegeneration might still be prevented.

3617   Hyperexcitability is one of the earliest pathophysiological biomarkers in the human AD

3618 brain, and its emergence correlates with severity of cognitive decline in individuals[106].

3619 Hyperexcitability is also observed in recordings from *in vivo* and *in vitro* models of AD

3620 pathology[75,107-112], arising prior to amyloid plaque deposition[113] and likely contributing to spine

3621 degeneration[114]. Interestingly, hypermetabolism[115] and hyperexcitability[109,116] emerged in the LEC

3622 of a sporadic AD mouse model before spreading to other regions[117]. It has previously been unclear

3623 whether cell-intrinsic changes in principal neuron excitability or other forms of circuit dysfunction

3624 are responsible for aberrant LEC activity in early AD. Hyperexcitability may also arise due to

3625 changes in local circuit inhibition from GABAergic interneurons, with several lines of evidence

3626 demonstrating impaired inhibitory tone[107,109,115], most notably from fast-spiking parvalbumin+

3627 (PV) interneurons[108,110,113]. Whether the unique baseline properties of PV interneurons in the LEC

3628 observed here confer functional vulnerability with respect to PV cells in other regions is unknown.

3629   In this dissertation, we report novel mechanisms contributing to cortical circuit dysfunction

3630 multiple early-stage AD mouse models. While Layer II[105] excitatory cells[94] are commonly

3631 considered the most vulnerable cortical cell type in early AD, our study suggests that hAPP-

3632 induced hyperexcitability in the LEC arises not from alterations in the intrinsic or synaptic

3633 properties of AD-vulnerable LII excitatory cells, but rather from an initial alteration in intrinsic

3634 excitability of surrounding PV interneurons. Furthermore, we observed this phenomenon only in

3635 the LEC PV interneurons and corresponding circuit, but not in a comparable cortical circuit, such

3636 as layer 5 of the somatosensory cortex. These two circuits are comparable as they are comprised

3637 of a projecting excitatory cell which is locally inhibited by SST and PV interneurons. However, as

3638 previously discussed, while the excitatory cells of these cortical circuits exhibited high similarity

3639 in their physiological features, the PV interneurons did not. SS Ctx and PV interneuron molecular

3640 markers were also highly distinct. Whether LEC PV interneurons are more susceptible to firing

3641 dysfunction due to their low baseline firing or molecular makeup is unclear.

3642   Remarkably, though the SS Ctx circuit remained stable, the PV interneurons did not go

3643 untouched. Although they did not exhibit intrinsic alterations in their firing, they still exhibited

3644 dysfunction. After 2-3 weeks of hAPP expression, PV interneuron to pyramidal cell

3645 neurotransmission in the SS Ctx was significantly reduced (Chapter 4, Supplementary Figure 11).

3646 This perturbation is likely pre-synaptic (PV bouton), rather than mediated by post-synaptic

3647 alterations of $GABA_C$ receptors (Added to Chapter 4, Supplementary Figure 11, unpublished data).

3648 Furthermore, in the canonical circuit which requires feedforward inhibition from PV interneurons

3649 onto pyramidal cells, pyramidal cells did not display marked hyperexcitability (Unpublished Data

3650 Figure 1). Whether this reduction in PV transmission is a mechanism which arises prior to intrinsic

3651 alterations in firing or a region-specific PV vulnerability to APP is unclear.

3652   Interestingly, we observed a similar significant reduction of PV interneuron to pyramidal

3653 cell neurotransmission in the SS Ctx of another model of AD pathology, 5xFAD. However, in this

3654 study the reduction in neurotransmission does not represent the only perturbation to PV

3655 interneuron or circuit dysfunction. Although previous publications had observed physiological

3656   phenotypes including altered AP firing[108,110], the alteration of PV interneuron firing prior to the

3657   development of severe pathology (as was shown in Chapter 3) had not been observed.

3658   Furthermore, in a circuit model (established by VJO), our specific mechanism of disrupted firing

3659   was sufficient to also result in network hyperexcitability. Although both Chapter 3 and Chapter 5

3660   display hyperexcitability, as is observed in AD patients, the mechanism of PV dysfunction and

3661   specifically how it relates to Alzheimer's related pathologies is not ubiquitous. Although it is

3662   tempting to attribute this solely to 'differences in mouse models', it is imperative to thoroughly

3663   explore what those differences are and how they may arrive at remarkably similar dysfunction.

3664   In Chapter 3, we explore PV interneuron and circuit physiology in the 5xFAD model of

3665   AD pathology at 7-8 weeks of age. Although these mice are slightly younger or similar in age to

3666   those studied in Chapter 5 using the increased hAPP model, the length of human APP expression

3667   is remarkably different. The 5xFAD mouse model is under the promoter of *Thy1* which initiates

3668   expression at post-natal day 7. Thus, studies conducted on 7-8 week old mice represent 6-7 weeks

3669   of transgene expression, rather than the 2-3 weeks represented in Chapter 5 experiments.

3670   Furthermore, while Chapter 3 experiments utilize wild-type human APP, 5xFAD exhibits five

3671   mutations associated with early-onset Alzheimer's Disease, three of which are in the APP protein.

3672   It is possible, that if left longer, the WT hAPP expression in SS Ctx would result in a clear

3673   reduction of PV interneuron firing. Remarkably, this idea follows the progression of AD-related

3674   pathologies through the cortex[90], where it appears in the entorhinal cortex long before neocortical

3675   areas such as the SS Ctx. However, it is similarly possible that left however long – SS Ctx PV

3676   interneurons would never develop an impairment to wild-type human APP and are impaired in

3677   5xFAD only due to the severe mutations associated with the model. This idea is unlikely, however,

3678   as the SS Ctx PV interneurons display variability in the presence of WT hAPP (reduced

3679 neurotransmission). However, this brings about a similar question: What within APP causes the

3680 reduction in PV interneuron firing?

3681 In Chapter 5, we began to address this question – but made it slightly more complicated

3682 than simple. After a short-term expression of WT hAPP (an isoform which does not increase

3683 significantly until AD[54,55] or the onset of risk factors for AD) [56 57 58 59-62], we observed a significant

3684 reduction in PV interneuron firing. Interestingly, this hAPP-induced pathophysiology could not be

3685 recapitulated following expression of the full-length mouse mAPP gene analogue. Of the 26 amino

3686 acids differentiating our hAPP and mAPP proteins, only 3 are situated within the amyloid-beta

3687 region. Of note, of the 'wild-type' versions of newly designed hAPP knock-in mouse models[357,358]

3688 now in wide use, only the 3 amino acids within the amyloid region are humanized. It has been

3689 shown that increasing expression of WT hAPP does result in a substantial increase in amyloid-

3690 beta[359], which may suggest that this phenotype is a result of increased amyloid-beta. Thus, we

3691 investigated if humanizing only the 3 amino acids could recapitulate our findings of hAPP-induced

3692 impaired PV interneuron physiology. Interestingly, the mAPP/hAβ Chimera did result in impaired

3693 PV interneuron firing but was not sufficient to fully replicate the drastic alterations seen after full-

3694 length hAPP expression. These findings suggest that amyloid-beta may not be the sole cause for

3695 early phase interneuron dysfunction, hinting at potential roles for full-length APP or its other

3696 cleavage products in this stage of the neurodegenerative cascade.

3697 GABAergic interneurons require homeostatic APP levels for proper physiological function

3698 and circuit activity control[360]. Recent work shows that APP expression moves outside of normal

3699 homeostatic levels in models of late-onset AD risk alleles[355,356]. The ratio of different APP isoforms

3700 also shifts in human AD, from mainly APP 695 to increasing levels of APP 770 and 751[54,55].

3701 Furthermore, APP[361], as well its cleavage proteins[362-364] and products[233,365], can modulate neuronal

3702   biophysics and alter the expression of ion channels, many of which are essential for maintaining

3703   the 'fast-spiking' phenotype of PV interneurons.

3704   In a hallmark set of studies, differential expression of voltage gated Na^+ channels in PV

3705   neurons was linked with network hyperexcitability in hAPP-expressing AD mice[108,125]. It is

3706   unclear whether other channel types are regulated and contribute to PV neuron dysfunction in AD.

3707   Our findings (combining Chapters 3 and 5) indicate that modulation of K^+ channels contribute to

3708   cortical PV interneuron dysfunction in early AD.

3709   In Chapter 3, we observed physiological changes in 7-8 week old 5xFAD mice, however,

3710   few proteomic changes are predicted until ~4 months of age in this model[174]. In keeping with this

3711   finding, we did not observe differences in Na_v1 or K_v3 mRNA levels in 7-8 week old mice.

3712   However, steady-state mRNA and protein levels are not always well correlated[191,192]. Therefore,

3713   we compared a significant subset of the relevant cortical voltage-gated channel proteome from

3714   5xFAD and wild-type mice, using mass spectrometry across several ages.

3715   In general, the number of channels showing genotype-associated changes increased with

3716   age in 5xFAD mice[174]. Similar to K_v3 mRNA, K_v3 protein levels ($K_v3.1-3.3$) were unchanged in

3717   ~7 week old mice. Interestingly, $K_v3.3$ protein expression was reduced in more aged 5xFAD mice,

3718   displaying progressive depletion with age. Along with other K_v3 subunits[190], $K_v3.3$ expression is

3719   relatively high in PV neurons[228] and alternative splicing of $K_v3.3$ is associated with temporal lope

3720   epilepsy[229]. Thus network hyperexcitability in intermediate-late AD could be associated with

3721   altered $K_v3.3$ expression.

3722   Unfortunately, $K_v3.4$ protein was not isolated in our mass spec analysis. As $K_v3.4$

3723   upregulation has been shown in humans and animal models[230,231] or following Aβ treatment[232],

3724   future studies should focus on evaluating regional $K_v3.4$ mRNA and protein expression in different

3725 AD models and disease stages, including well before extensive amyloid plaque deposition.

3726 Although K_v3 channels are highly expressed in PV cells, our proteomic analysis was from bulk

3727 homogenates. Thus cell-type-specific proteomic approaches in 5xFAD and other AD models

3728 should be a major focus for future work.

3729 Rather than changes in expression levels, our results indicate that biophysical modulation

3730 of K_v3 channels was responsible for reduced AP firing and AP width in young 5xFAD mice.

3731 Interestingly, reduced AP width was observed in PV cells before other intrinsic alterations in

3732 APP/PS1 mice[110] suggesting that K_v3 modulation could precede that of other channels or

3733 homeostatic responses. Several APP-related cellular processes could explain the biophysical

3734 modulation of K_v3 observed here. The intermediate APP transmembrane protein product C99,

3735 produced following β-Secretase (BACE1)-directed cleavage, can regulate K_v channel activity[233].

3736 One or more of these APP-related interactions could contribute to the K_v3 channel dysregulation

3737 observed in 5xFAD mice here.

3738 Biophysical modulation of K_v3 could also arise through several other well-described

3739 mechanisms without direct hAPP interactions. Changes in K_v3 phosphorylation via PKC, PKA,

3740 nitric oxide phosphatase[203,234-238], or casein kinases[239] as well via K_v3 glycosylation[240] can impart

3741 changes in K_v3 conductance, voltage dependence, or kinetics. Future work to characterize the

3742 phosphorylation and glycosylation state of K_v3 in AD models will be necessary. Differential

3743 surface expression of K_v3 subunits or splice variants could also explain the K_v3 phenotype

3744 described here. For example, $K_v3.4$ subunits can increase K_v3 activation kinetics while also

3745 hyperpolarizing their activation voltage in cerebellar interneurons[24,241]. However, of three $K_v3.4$

3746 splice variants (Kv3.4a-c) only one ($K_v3.4a$) could impart these features *in vitro[24]*. Intriguingly,

3747 increased BACE1 activity in AD[242] may promote surface expression of $K_v3.4$ subunits. BACE1

3748   may also physically associate with K_v3 channel proteins in a beta-subunit-like fashion to modify

3749   their gating properties[243]. Additionally, changes in ancillary protein (*e.g.,* K_v beta subunit *Kcne*)

3750   expression or activity represent another avenue for modulation of K_v3 biophysics. For example,

3751   co-expression of K_v3 channels with *Kcne3* hyperpolarized their activation voltage[244]. While not

3752   well characterized in PV interneurons to date, *Kcne* subunits may be differentially regulated in

3753   AD[232,245]. Cortical single-cell RNAseq datasets from the Allen institute[246] show no expression of

3754   *Kcne*1-3 in cortical PV interneurons, and a variable level of *Kcne4* expression (our analysis).

3755   Intriguingly, the APP cleavage product C99 displays significant sequence homology with *Kcne[233]*

3756   suggesting that K_v3 channels could be biophysically regulated via C99 in a similar manner as with

3757   *Kcne*. Implementing the PV-type-specific viral approach utilized in this study in various AD

3758   models will allow for a deeper evaluation of the possible mechanisms responsible for K_v3

3759   modulation in future work. Additional longitudinal studies at multiple stages of the disease will be

3760   necessary to parse out the emergence of cell-type-specific biophysical mechanisms during the

3761   disease.

3762   In Chapter 5, although short-term full-length hAPP expression in this study could

3763   significantly reduce PV firing, we observed no biophysical indicators implicating changes to either

3764 Na_v1 or K_v3 availability which may underlie altered PV firing in the LEC. Although the SS Ctx

3765   PV interneurons did not observe reduced firing, we did note alterations in their AP threshold and

3766   AHP, which could be attributed to alterations in Na_v1 or K_v3 availability, respectively. It is possible

3767   that if left longer, hAPP expression in the SS Ctx may result in impaired PV interneuron

3768   excitability[108,113]. Thus, alternative biophysical mechanisms must be responsible for our

3769   observations following more short-term hAPP expression in adult mice. Notably, we observed a

3770   substantial decrease in input resistance in LEC PV cells expressing hAPP. This could be due to

3771 enhanced availability of leak channels or potentially low-voltage activating K^+ conductances, such

3772 as KCNQ (K_v7), which curiously have been shown to be regulated by APP cleaving proteins[362]

3773 and cleavage products[233,366]. However, the reduction in PV interneuron firing after expression of

3774 the mAPP/hAβ chimera is likely due to the widening AP half-width, which may similarly be due

3775 to Kv3 alterations. Whether these differences in mechanisms underlying altered PV firing is related

3776 to model systems, different cleavage product and accompanying protein effects, or different time

3777 points through the disease will be necessary to further understand mechanisms of PV and

3778 excitatory cell dysfunction. We cannot rule out that longer hAPP expression times *in vivo* may

3779 induce other changes through distinct pathological or homeostatic processes. Notably, we did

3780 observe reductions in Na_v1 channel expression in bulk brain tissue in later stages of the 5xFAD

3781 mouse model (6 mo.+) as has been described previously as a mechanism for PV interneuron

3782 dysfunction in AD[108]. Whether this represents another distinct phase of PV interneuron dysfunction

3783 and hyperexcitability after the onset of severe amyloid pathology is unclear. Further

3784 disentanglement of the mechanisms of interneuron dysfunction in distinct AD models is necessary.

3785 Specifically, the relationship of hAPP, amyloid[111,252], and its intermediate products to PV-related

3786 dysfunction and abnormal circuit function.

3787 6.4 Circuit response to PV Interneuron Dysfunction

3788   Overall, despite the severe dysfunction observed in PV interneurons across models, there

3789 is evidence suggesting the feasibility of restoring circuit homeostasis. However, it appears this

3790 restoration may come at a cost.

3791   In Chapter 4, when we assessed the SS Ctx PV interneuron intrinsic firing and circuit

3792 excitability at 2-3 months of age (1-2 months after Chapter 3), we observed both phenomena return

3793 to a homeostatic set point. However, as we have observed consistently, the reduction of

3794 neurotransmission from PV interneurons to pyramidal cells persisted. Notably, this sequence of

3795 events, characterized by reduced intrinsic firing and neurotransmission, followed by normalization

3796 of the circuit and intrinsic firing with a persistent reduction in neurotransmission, has also been

3797 previously observed in early stages of devastating epilepsy models[374]. However, the precise

3798 mechanism behind this circuit normalization in AD models remains unclear – whether it arises

3799 from PV intrinsic excitability homeostasis, circuit reorganization involving recruitment of

3800 inhibition from other interneurons (*e.g.,* SST interneurons[375]), intrinsic regulation of excitatory

3801 neuron excitability, or a combination of all these factors.

3802 To compensate for this early circuit dysfunction, PV interneurons are well-suited to

3803 homeostatically respond[334], but this process could impose a higher metabolic demand to sustain

3804 this compensation. Indeed, mitochondrial impairments have been observed prior to extensive

3805 pathology in APP/Aβ model mice[335,336]. In our PV-CIBOP proteomes, we found a signature of

3806 stress-responsive proteins (Armt1, Rhob, Gstm1, RhoA, Tmco1, Akr1b3, Gcn1, Hras, Cul3, Pdk2,

3807 Rap2a, Flot1) in 5xFAD as compared to WT. Of note, RhoA activation increases Aβ and tau

3808 pathology and co-localizes with NFTs in human brain[337,338]. In contrast to the overall synaptic

3809 effects of early AD pathology in PV interneurons, we observed a marked increase in mitochondrial

3810 and metabolic proteins in PV interneurons. This increase could be reflective of a protective or

3811 compensatory responses (via increased mitochondrial biogenesis to sustain higher metabolic

3812 demand). Other compensatory signatures observed in 5xFAD PV interneurons included increased

3813 Dhcr7 for de-novo cholesterol biosynthesis in neurons, increased Apeh to process Aβ oligomers

3814 along with increased autophagy as supported by increased levels of positive regulators of

3815 autophagy and increased lipidated form of LC3 (LC3-II). Conversely, a detrimental/dysfunctional

3816 response (*e.g.,* accumulation of dysfunction mitochondria) is also possible. We noted that

3817   mitochondrial functional proteins and Complex I, III, IV, V proteins were selectively increased in

3818   5xFAD PV interneurons while a smaller group of mitochondrial structural, dogma, and Complex

3819   II proteins were not. Therefore, follow-up studies focusing on mitochondrial structure and function

3820   specifically in PV interneurons are warranted to better understand the basis and consequences of

3821   these mitochondrial alterations. Taken together, the molecular phenotype of 5xFAD PV

3822   interneurons is indicative of a significant cellular stress response occurring in 3 month old PV

3823   interneurons, comprising both compensatory and maladaptive events, which is not evident in the

3824   bulk proteome at this age. Therefore, although PV interneurons undergo intrinsic homeostatic

3825   changes to improve their firing, their neurotransmission remains reduced, and thus PV intrinsic

3826   excitability may not be the sole mechanism underlying the circuit's return to homeostasis.

3827   It is possible that without sufficient inhibition from PV interneurons, the circuit may recruit

3828   other inhibitory interneurons to restore the E/I balance. Recently, it has been shown that the other

3829   highly common cortical interneuron, the SST interneuron, may play a role. In fact, SST

3830   interneurons have been shown to display hyperexcitability with a corresponding reduction of

3831   excitatory neuron activity in the SS Ctx[375]. The only data we have which assessed SST activity at

3832   this time is in the context of SST protein levels. Somatostatin (Sst), a protein primarily expressed

3833   in cortical dendrite-targeting (non-PV fast spiking)[324,325] inhibitory interneurons, was reduced

3834   starting at 3 months of age. As both Pvalb and Sst expression are linked to the level of circuit

3835   activity[38,326] these changes may reflect a differential dysregulation of interneuron activity levels at

3836   a stage where substantial plaque formations are just arising in 5xFAD mice. At the histological

3837   level, no measurable differences in PV interneuron density were observed between 3 month old

3838   wild-type and 5xFAD mice, arguing against early overall cell loss of PV interneurons at this early

3839   stage, but rather suggesting changes to their proteomic profile. Thus, whether SST interneurons

3840   are underlying maintenance of E/I balance at this time is unclear.

3841   One other potential mechanism to restore E/I balance is intrinsic homeostasis of excitability

3842   by excitatory neurons. Although this may be achieved through many mechanisms, we suggest one

3843   such way may involve the other major pathology involved in Alzheimer's disease, the Tau protein.

3844   Interestingly, the LEC is also the first cortical region to develop tau pathology[90,91,347-349].

3845   Yet, the relationship between hAPP, hyperexcitability, and Tau remains unclear. It has previously

3846   been established that artificially increasing neuronal activity can accelerate tau pathology[163,350,351].

3847   However, the expression of hTau has been suggested to strongly dampen circuit

3848   excitability[116,165,352] (but see[353]). Here we observed that hTau co-expressed with hAPP results in an

3849   intermediate circuit excitability level when compared to hAPP or hTau injected alone. Thus, hTau

3850   may act to normalize circuit excitability, restoring the E/I balance.

3851   However, even if hTau normalizes the circuit, the outcome of its expression may not be

3852   benign. Trans-synaptic spread of tau has been shown from the entorhinal cortex to other brain

3853   regions[367,368], and most recently this spread has been suggested to occur in human patients via the

3854   oligomeric tau species (T22+)[354]. Remarkably, here we show that although hTau co-injection with

3855   hAPP somewhat normalized circuit excitability, it also caused a significant increase in this

3856   oligomeric tau species. Further research is necessary to determine if this resultant oligomeric

3857   species displays a similar trans-synaptic spread to downstream regions, such as the dentate gyrus

3858   (DG).

3859   Although we cannot currently conclude (based on the data presented here) that oligomeric

3860   tau has spread at this point to the dentate gyrus, it is clear that communication from the LEC to the

3861   DG is perturbed. In a series of unpublished experiments, we explored the neurotransmission from

3862 LEC boutons to DG granule cells with and without the expression of WT hAPP + WT hTau. While

3863 LEC somas in both Control and 'AD' conditions are excitable through optogenetics to a

3864 suprathreshold level, firing an AP in response to each stimulus, those expressing WT hAPP + WT

3865 hTau display reduced neurotransmission (Unpublished Data Figure 2). This may potentially be

3866 explained as axonal failure of the action potential. However, at this time, the DG Granule Cells in

3867 receiving reduced neurotransmission from the LEC do not display altered intrinsic firing

3868 (Unpublished Data Figure 2). This experiment series represents only the beginning of a long line

3869 of investigation necessary to further explore the propagation of AD-related pathophysiology

3870 outside of the LEC.

3871 Thus, an individual circuit such as the LEC may induce mechanisms in early AD to restore

3872 its excitability to a homeostatic set point. However, the mechanisms utilized to do so may

3873 ultimately result in further network-wide and brain dysfunction, alongside increasing pathology.

3874 If circuit re-organization is also involved, it may ultimately impair the ability for regions such as

3875 the LEC to perform their required tasks, such as contextualizing memory. Perhaps interventional

3876 treatments which restore PV interneuron firing and neurotransmission prior to re-organization

3877 might prevent further pathology and impairment.

3878 6.5 Potential Therapeutic Strategies and Intervention Points for AD

3879 Circuit hyperexcitability is likely an influential factor in the neurodegenerative cascade, as

3880 it has been shown to exacerbate release of amyloid-beta[371], and also promotes tau pathology and

3881 subsequent trans-synaptic tau spreading[163], which ultimately induces spine degeneration[114] and cell

3882 death[372]. Ultimately, regions that first undergo hyperexcitability may also be among the earliest to

3883 display these pathological markers as the disease progresses[163,373].

3884   While this dissertation has showcased clear points for intervention in AD models, it has not

3885 proposed any potential therapeutic strategies. Part of this stems from a missing link in the

3886 mechanistic cause of the dysfunction – how APP or its processing units truly perturb ion channels

3887 within PV interneurons. In Chapter 3, our findings suggest an opportunity for implementation of

3888 novel targeted therapies to improve cortical circuit hyperexcitability in AD. Our biophysical,

3889 dynamic clamp, and modeling experiments here indicate that a specific K_v3 biophysical parameter,

3890 altered in 5xFAD mice (hyperpolarized activation voltage), can strongly alter PV firing and overall

3891 circuit activity. Our data suggest that strategies to increase expression of wild-type K_v3 are unlikely

3892 to rescue the AD firing phenotype, as supplementation of wild-type gK_v3 did not affect near-

3893 threshold PV excitability. However, drugs that depolarize the activation voltage of endogenous

3894 K_v3 channels, or PV-specific genetic therapies[175] to modify K_v3 activation voltage dependence[24,241]

3895 present promising avenues for therapeutic intervention. Firing in our PV model was not highly

3896 sensitive to changes in other K_v3 properties, such as inactivation kinetics. Thus some off-target

3897 K_v3 effects of pilot therapeutics may be acceptable. To better understand the translational scope of

3898 our findings, future work should focus on understanding whether biophysical K_v modifications are

3899 shared across other AD models at early stages of the disease. However, other approved clinical

3900 studies may circumnavigate this specific detail to improve network balance at this stage, such as

3901 exogenous modulation of circuits to reduce epileptiform activity[376]. How this phenomenon occurs

3902 and its longevity, however, are unclear.

3903   In Chapter 4, our results indicate early dysregulation of mTOR signaling in PV

3904 interneurons as a potential upstream mechanism for mitochondrial and metabolic alterations as

3905 well as synaptic dysfunction occurring selectively in PV interneurons in early stages of AD

3906 pathology in 5xFAD mice. Comparison of PV-CIBOP proteomic signatures with human post-

3907   mortem data suggests selective synaptic and metabolic PV interneuron vulnerabilities in early AD

3908   pathogenesis that may be linked to cognitive dysfunction. These findings provide a strong rationale

3909   to investigate and target early proteomic changes occurring in PV interneurons and other inhibitory

3910   neuron types in mouse models of AD and other neurological diseases.

3911   In Chapter 5, our results indicate that one of the potential mechanisms to restore circuit

3912   homeostasis may initiate severe tau pathology – resulting in further problems to be encountered as

3913   the disease progresses. When the circuit is rearranged or altered to achieve balance, it may become

3914   vulnerable to subsequent insults. Ultimately, the circuit may stray so far past its 'original'

3915   homeostatic set-point, that it will be unable to return[160].

3916   Thus, from this dissertation it is evident that PV interneurons may provide an effective

3917   intervention point in the progression of early Alzheimer's Disease to prevent hyperexcitability and

3918   potentially, subsequent neurodegeneration and cognitive decline.

Unpublished Data

And if you don't know, now you know
-The Notorious B.I.G.
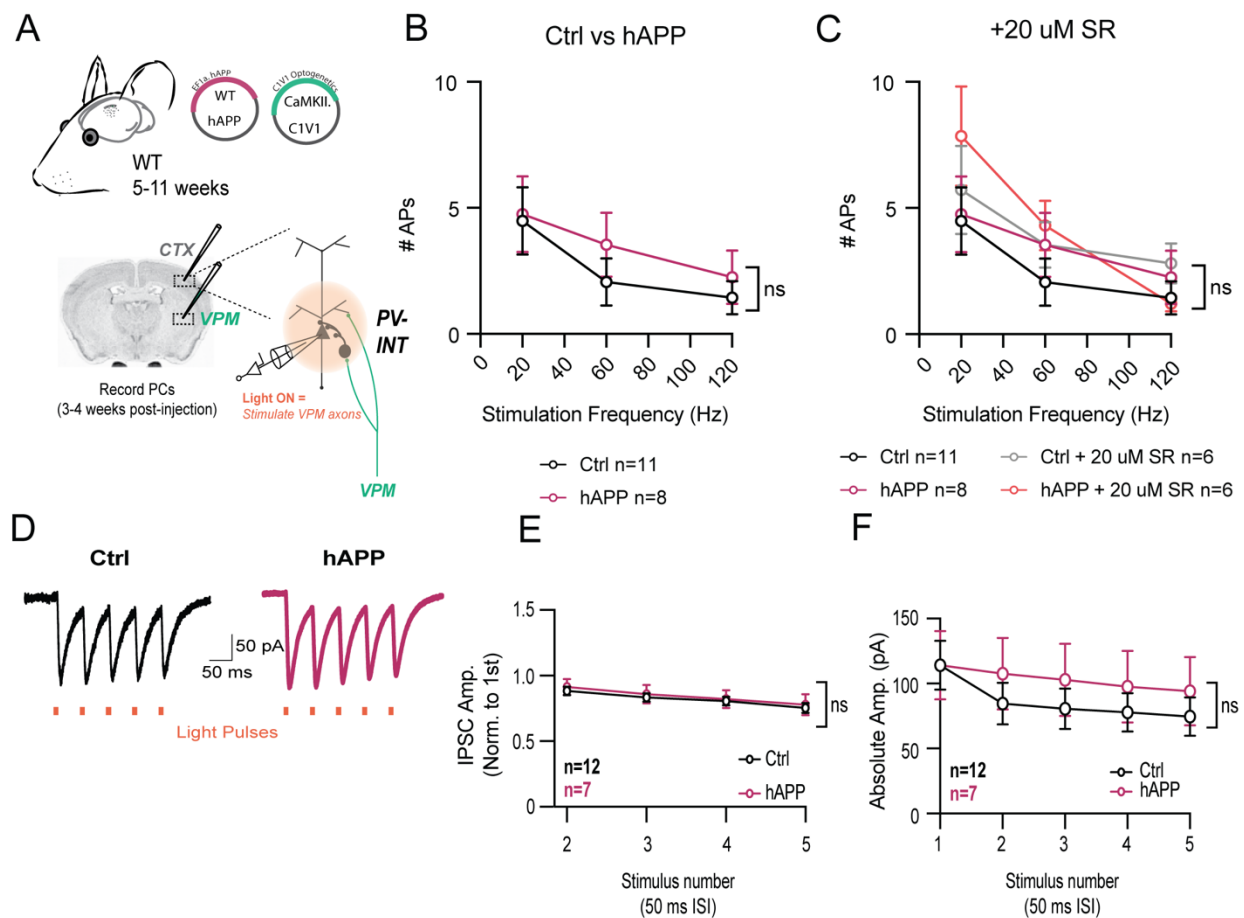
Unpublished Data Figure 1. VPM stimulation to assess SS Ctx PV interneuron neurotransmission in the naturalistic circuit

A. Experimental outline: BL6J mice were injected with AAV.CaMKIIa.C1V1 in the Ventral posteromedial nucleus and with or without AAV.EF1a.hAPP in the somatosensory cortex at 5-11 weeks of age.

B. Three weeks post-injection, VPM axons were stimulated in L5 SS Ctx and stimulated across frequencies at to determine how many APs were fired by post-synaptic pyramidal cells. For **B-F**, 1.5mM external Ca^{2+} was used.

C. With the same experimental setup as B, 20 uM SR was added to determine the role of inhibition on pyramidal cell output.

D. Example traces of optogenetically-evoked VPM excitatory post-synaptic currents on pyramidal cells for saline-injected (left) and hAPP-AAV injected (right) cortices using 1.5mM external Ca^{2+}.

E, F. EPSCs in AAV-hAPP injected mice displayed no significant change in amplitude as measured using MPR and (F) absolute amplitude across all measured stimuli at 20 Hz. (*$p<0.05$ Two-way ANOVA with Sidak's posthoc comparisons for each stimulus between hAPP and saline control experiments).
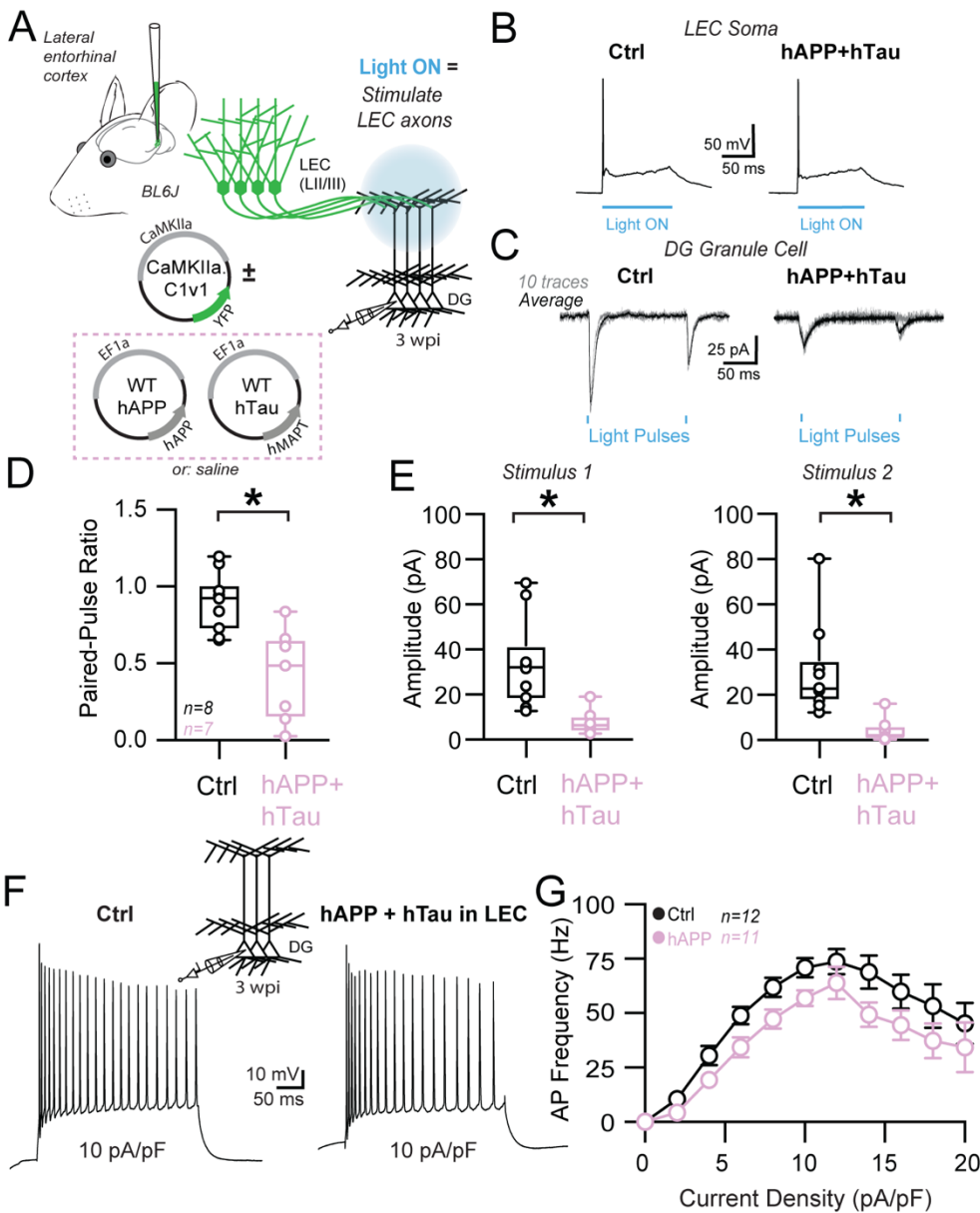
Unpublished Data Figure 2. Impact of WT hAPP+ WT hTau on LEC to DG neurotransmission and DG GC firing properties.

A. Experimental outline: BL6J mice were injected with AAV.CaMKIIa.C1V1 in the LEC with or without AAV.EF1a.hAPP + AAV.EF1a.hMAPT in the at 6-8 weeks of age.

B. Confirmation of LEC somas expressing AAV.CaMKIIa.C1V1firing in response to 100 ms bar of light in both conditions.

C. Example traces of optogenetically-evoked excitatory post-synaptic currents on pyramidal cells for saline-injected (left) and hAPP/hTau-AAV injected (right) mice.

3945   **D.** Three weeks post-injection, LEC axons were stimulated in the DG outer molecular layer and

3946   stimulated at 20 Hz to PPR from LEC to DG GCs. hAPP/hTau condition shows a significant

3947   reduction in LEC to DG PPR. For **B-G**, 1.5mM external Ca^{2+} was used with KGlu internal.

3948   **E.** hAPP/hTau condition shows a significantly lower absolute EPSC amplitude for both stimuli.

3949   **F.** Example traces DG Granule Cell action potential trains of Ctrl (left) and hAPP+hTau in the

3950   LEC (right). No viruses were expressed in the DG.

3951   **G.** Quantification of DG GC action potential firing frequency in response to increasing current

3952   density injections (normalized to capacitance). Despite LEC neurotransmission being reduced,

3953   DG GC intrinsic features in the 'AD' condition remain insignificantly changed at this time.

3954   (p>0.05, Two-way ANOVA with Sidak's posthoc).

Ancillary Documents

There's no losing, only learning.
-Pitbull

Songs I patched the best cell of the day to throughout the PhD (in no particular order):
1. Bad Moon Rising - Creedence Clearwater Revival
2. Band On The Run – Paul McCartney, Wings
3. More Than A Woman – Bee Gees
4. This Must Be the Place (Naïve Melody) – Talking Heads
5. Isn't She Lovely – Stevie Wonder
6. Big Poppa – The Notorious B.I.G.
7. Time of Our Lives – Pitbull, Ne-Yo
8. The Spins – Mac Miller
9. Dancing Queen – ABBA
10. Doses & Mimosas – Cherub
11. Bohemian Rhapsody – Queen
12. Lost – Frank Ocean
13. The Devil Went Down to Georgia – The Charlie Daniels Band
14. You & Me – Disclosure, Eliza Doolittle, Flume
15. Still Into You – Paramore
16. 6's to 9's – Big Wild, Rationale
17. Weekend Friend – Goth Babe
18. Good Days – SZA
19. Jackie and Wilson – Hozier
20. Wouldn't It Be Nice – The Beach Boys

Ancillary Figure 1.

Playlist entitled 'Best Patch O' The Day'.

Ancillary Figure 2.

'Awoken in the Night.' (Chalk on Chalkboard, 2022)

Ancillary Figure 3.

The Rowan Lab hearth at Christmastime – complete with the *Mattalisa* atop the mantel (2022).

Citations

1   Johnson, E. C. B. *et al.* Large-scale deep multi-layer analysis of Alzheimer's disease brain reveals strong proteomic disease-related changes not observed at the RNA level. *Nat Neurosci* **25**, 213-225, doi:10.1038/s41593-021-00999-y (2022).

2   Rayaprolu, S. *et al.* Cell type-specific biotin labeling in vivo resolves regional neuronal and astrocyte proteomic differences in mouse brain. *Nat Commun* **13**, 2927, doi:10.1038/s41467-022-30623-x (2022).

3   Ramón y Cajal, S. *Textura del Sistema Nervioso del Hombre y de los Vertebrados.* (1899).

4   Cole, K. S. & Curtis, H. J. Electric Impedance of the Squid Giant Axon during Activity. *J Gen Physiol* **22**, 649-670, doi:10.1085/jgp.22.5.649 (1939).

5   Hodgkin, A. L. & Huxley, A. F. A quantitative description of membrane current and its application to conduction and excitation in nerve. *J Physiol* **117**, 500-544, doi:10.1113/jphysiol.1952.sp004764 (1952).

6   Katz, B. & Miledi, R. A study of synaptic transmission in the absence of nerve impulses. *J Physiol* **192**, 407-436, doi:10.1113/jphysiol.1967.sp008307 (1967).

7   Tasic, B. *et al.* Shared and distinct transcriptomic cell types across neocortical areas. *Nature* **563**, 72-78, doi:10.1038/s41586-018-0654-5 (2018).

8   Greig, L. C., Woodworth, M. B., Galazo, M. J., Padmanabhan, H. & Macklis, J. D. Molecular logic of neocortical projection neuron specification, development and diversity. *Nat Rev Neurosci* **14**, 755-769, doi:10.1038/nrn3586 (2013).

9   Lowel, S. & Singer, W. Selection of intrinsic horizontal connections in the visual cortex by correlated neuronal activity. *Science* **255**, 209-212, doi:10.1126/science.1372754 (1992).

10   Turrigiano, G. Too many cooks? Intrinsic and synaptic homeostatic mechanisms in cortical circuit refinement. *Annu Rev Neurosci* **34**, 89-103, doi:10.1146/annurev-neuro-060909-153238 (2011).

11   LeMasson, G., Marder, E. & Abbott, L. F. Activity-dependent regulation of conductances in model neurons. *Science* **259**, 1915-1917, doi:10.1126/science.8456317 (1993).

12   Miller, K. D. Synaptic economics: competition and cooperation in synaptic plasticity. *Neuron* **17**, 371-374, doi:10.1016/s0896-6273(00)80169-5 (1996).

13   Turrigiano, G. G. & Nelson, S. B. Homeostatic plasticity in the developing nervous system. *Nat Rev Neurosci* **5**, 97-107, doi:10.1038/nrn1327 (2004).

14   Zhang, W. & Linden, D. J. The other side of the engram: experience-driven changes in neuronal intrinsic excitability. *Nat Rev Neurosci* **4**, 885-900, doi:10.1038/nrn1248 (2003).

15   Somogyi, P., Tamas, G., Lujan, R. & Buhl, E. H. Salient features of synaptic organisation in the cerebral cortex. *Brain Res Brain Res Rev* **26**, 113-135, doi:10.1016/s0165-0173(97)00061-1 (1998).

16   Rudy, B., Fishell, G., Lee, S. & Hjerling-Leffler, J. Three groups of interneurons account for nearly 100% of neocortical GABAergic neurons. *Dev Neurobiol* **71**, 45-61, doi:10.1002/dneu.20853 (2011).

17   Petilla Interneuron Nomenclature, G. *et al.* Petilla terminology: nomenclature of features of GABAergic interneurons of the cerebral cortex. *Nat Rev Neurosci* **9**, 557-568, doi:10.1038/nrn2402 (2008).

18   Klausberger, T. & Somogyi, P. Neuronal diversity and temporal dynamics: the unity of hippocampal circuit operations. *Science* **321**, 53-57, doi:10.1126/science.1149381 (2008).

19   Fukuda, T., Aika, Y., Heizmann, C. W. & Kosaka, T. Dense GABAergic input on somata of parvalbumin-immunoreactive GABAergic neurons in the hippocampus of the mouse. *Neurosci Res* **26**, 181-194, doi:10.1016/s0168-0102(96)01102-9 (1996).

20   Katsumaru, H., Kosaka, T., Heizmann, C. W. & Hama, K. Immunocytochemical study of GABAergic neurons containing the calcium-binding protein parvalbumin in the rat hippocampus. *Exp Brain Res* **72**, 347-362, doi:10.1007/BF00250256 (1988).

21   Somogyi, P., Nunzi, M. G., Gorio, A. & Smith, A. D. A new type of specific interneuron in the monkey hippocampus forming synapses exclusively with the axon initial segments of pyramidal cells. *Brain Res* **259**, 137-142, doi:10.1016/0006-8993(83)91076-4 (1983).

22   Martina, M., Schultz, J. H., Ehmke, H., Monyer, H. & Jonas, P. Functional and molecular differences between voltage-gated K+ channels of fast-spiking interneurons and pyramidal neurons of rat hippocampus. *J Neurosci* **18**, 8111-8125, doi:10.1523/JNEUROSCI.18-20-08111.1998 (1998).

23   Rudy, B. & McBain, C. J. Kv3 channels: voltage-gated K+ channels designed for high-frequency repetitive firing. *Trends Neurosci* **24**, 517-526, doi:10.1016/s0166-2236(00)01892-0 (2001).

24   Baranauskas, G., Tkatch, T., Nagata, K., Yeh, J. Z. & Surmeier, D. J. Kv3.4 subunits enhance the repolarizing efficiency of Kv3.1 channels in fast-spiking neurons. *Nat Neurosci* **6**, 258-266, doi:10.1038/nn1019 (2003).

25   Catterall, W. A., Kalume, F. & Oakley, J. C. NaV1.1 channels and epilepsy. *J Physiol* **588**, 1849-1859, doi:10.1113/jphysiol.2010.187484 (2010).

26   Cheah, C. S. *et al.* Specific deletion of NaV1.1 sodium channels in inhibitory interneurons causes seizures and premature death in a mouse model of Dravet syndrome. *Proc Natl Acad Sci U S A* **109**, 14646-14651, doi:10.1073/pnas.1211591109 (2012).

27   Erisir, A., Lau, D., Rudy, B. & Leonard, C. S. Function of specific K(+) channels in sustained high-frequency firing of fast-spiking neocortical interneurons. *J Neurophysiol* **82**, 2476-2489, doi:10.1152/jn.1999.82.5.2476 (1999).

28   Goldberg, E. M. *et al.* K+ channels at the axon initial segment dampen near-threshold excitability of neocortical fast-spiking GABAergic interneurons. *Neuron* **58**, 387-400, doi:10.1016/j.neuron.2008.03.003 (2008).

29   Gu, Y. *et al.* Balanced Activity between Kv3 and Nav Channels Determines Fast-Spiking in Mammalian Central Neurons. *iScience* **9**, 120-137, doi:10.1016/j.isci.2018.10.014 (2018).

30   Wang, L. Y., Gan, L., Forsythe, I. D. & Kaczmarek, L. K. Contribution of the Kv3.1 potassium channel to high-frequency firing in mouse auditory neurones. *J Physiol* **509 (Pt 1)**, 183-194, doi:10.1111/j.1469-7793.1998.183bo.x (1998).

31   Ekins, T. G. *et al.* Emergence of non-canonical parvalbumin-containing interneurons in hippocampus of a murine model of type I lissencephaly. *Elife* **9**, doi:10.7554/eLife.62373 (2020).

32   Golowasch, J., Goldman, M. S., Abbott, L. F. & Marder, E. Failure of averaging in the construction of a conductance-based neuron model. *J Neurophysiol* **87**, 1129-1131, doi:10.1152/jn.00412.2001 (2002).

33   Nassar, M. *et al.* Diversity and overlap of parvalbumin and somatostatin expressing interneurons in mouse presubiculum. *Front Neural Circuits* **9**, 20, doi:10.3389/fncir.2015.00020 (2015).

34   Munoz-Manchado, A. B. *et al.* Diversity of Interneurons in the Dorsal Striatum Revealed by Single-Cell RNA Sequencing and PatchSeq. *Cell Rep* **24**, 2179-2190 e2177, doi:10.1016/j.celrep.2018.07.053 (2018).

35   Schwaller, B., Meyer, M. & Schiffmann, S. 'New' functions for 'old' proteins: the role of the calcium-binding proteins calbindin D-28k, calretinin and parvalbumin, in cerebellar physiology. Studies with knockout mice. *Cerebellum* **1**, 241-258, doi:10.1080/147342202320883551 (2002).

36   Arif, S. H. A Ca(2+)-binding protein with numerous roles and uses: parvalbumin in molecular biology and physiology. *Bioessays* **31**, 410-421, doi:10.1002/bies.200800170 (2009).

37   Kamphuis, W., Huisman, E., Wadman, W. J., Heizmann, C. W. & Lopes da Silva, F. H. Kindling induced changes in parvalbumin immunoreactivity in rat hippocampus and its relation to long-term decrease in GABA-immunoreactivity. *Brain Res* **479**, 23-34, doi:10.1016/0006-8993(89)91331-0 (1989).

38   Patz, S., Grabert, J., Gorba, T., Wirth, M. J. & Wahle, P. Parvalbumin expression in visual cortical interneurons depends on neuronal activity and TrkB ligands during an Early period of postnatal development. *Cereb Cortex* **14**, 342-351, doi:10.1093/cercor/bhg132 (2004).

39   Taniguchi, H., Lu, J. & Huang, Z. J. The spatial and temporal origin of chandelier cells in mouse neocortex. *Science* **339**, 70-74, doi:10.1126/science.1227622 (2013).

40   Courcelles, E. J. *et al.* Association cortical areas in the mouse contain a large population of fast-spiking GABAergic neurons that do not express parvalbumin. *Eur J Neurosci*, doi:10.1111/ejn.16341 (2024).

41   Ruden, J. B., Dugan, L. L. & Konradi, C. Parvalbumin interneuron vulnerability and brain disorders. *Neuropsychopharmacology* **46**, 279-287, doi:10.1038/s41386-020-0778-9 (2021).

42   Hu, H., Roth, F. C., Vandael, D. & Jonas, P. Complementary Tuning of Na(+) and K(+) Channel Gating Underlies Fast and Energy-Efficient Action Potentials in GABAergic Interneuron Axons. *Neuron* **98**, 156-165 e156, doi:10.1016/j.neuron.2018.02.024 (2018).

43   Degenhardt, E. K. *et al.* Florbetapir F18 PET Amyloid Neuroimaging and Characteristics in Patients With Mild and Moderate Alzheimer Dementia. *Psychosomatics* **57**, 208-216, doi:10.1016/j.psym.2015.12.002 (2016).

44   Alzheimer, A., Stelzmann, R. A., Schnitzlein, H. N. & Murtagh, F. R. An English translation of Alzheimer's 1907 paper, "Uber eine eigenartige Erkankung der Hirnrinde". *Clin Anat* **8**, 429-431, doi:10.1002/ca.980080612 (1995).

45   Lacor, P. N. *et al.* Abeta oligomer-induced aberrations in synapse composition, shape, and density provide a molecular basis for loss of connectivity in Alzheimer's disease. *J Neurosci* **27**, 796-807, doi:10.1523/JNEUROSCI.3501-06.2007 (2007).

46   Hardy, J. A. & Higgins, G. A. Alzheimer's disease: the amyloid cascade hypothesis. *Science* **256**, 184-185, doi:10.1126/science.1566067 (1992).

47   Haass, C. & Selkoe, D. J. Soluble protein oligomers in neurodegeneration: lessons from the Alzheimer's amyloid beta-peptide. *Nat Rev Mol Cell Biol* **8**, 101-112, doi:10.1038/nrm2101 (2007).

48   Mucke, L. *et al.* Synaptotrophic effects of human amyloid beta protein precursors in the cortex of transgenic mice. *Brain Res* **666**, 151-167, doi:10.1016/0006-8993(94)90767-6 (1994).

49   Zheng, H. & Koo, E. H. Biology and pathophysiology of the amyloid precursor protein. *Mol Neurodegener* **6**, 27, doi:10.1186/1750-1326-6-27 (2011).

50   Allinquant, B. *et al.* Downregulation of amyloid precursor protein inhibits neurite outgrowth in vitro. *J Cell Biol* **128**, 919-927, doi:10.1083/jcb.128.5.919 (1995).

51   Lee, S. H. *et al.* APP Family Regulates Neuronal Excitability and Synaptic Plasticity but Not Neuronal Survival. *Neuron* **108**, 676-690 e678, doi:10.1016/j.neuron.2020.08.011 (2020).

52   O'Brien, R. J. & Wong, P. C. Amyloid precursor protein processing and Alzheimer's disease. *Annu Rev Neurosci* **34**, 185-204, doi:10.1146/annurev-neuro-061010-113613 (2011).

53   Bayer, T. A., Cappai, R., Masters, C. L., Beyreuther, K. & Multhaup, G. It all sticks together--the APP-related family of proteins and Alzheimer's disease. *Mol Psychiatry* **4**, 524-528, doi:10.1038/sj.mp.4000552 (1999).

54   Koo, E. H. *et al.* Differential expression of amyloid precursor protein mRNAs in cases of Alzheimer's disease and in aged nonhuman primates. *Neuron* **4**, 97-104, doi:10.1016/0896-6273(90)90446-m (1990).

55   Matsui, T. *et al.* Expression of APP pathway mRNAs and proteins in Alzheimer's disease. *Brain Res* **1161**, 116-123, doi:10.1016/j.brainres.2007.05.050 (2007).

56   Thakur, M. K. & Mani, S. T. Estradiol regulates APP mRNA alternative splicing in the mice brain cortex. *Neurosci Lett* **381**, 154-157, doi:10.1016/j.neulet.2005.02.014 (2005).

57   Bjelik, A. *et al.* Human apoB overexpression and a high-cholesterol diet differently modify the brain APP metabolism in the transgenic mouse model of atherosclerosis. *Neurochem Int* **49**, 393-400, doi:10.1016/j.neuint.2006.01.026 (2006).

58   Bjelik, A. *et al.* APP mRNA splicing is upregulated in the brain of biglycan transgenic mice. *Neurochem Int* **50**, 1-4, doi:10.1016/j.neuint.2006.07.009 (2007).

59   Dubal, D. B., Broestl, L. & Worden, K. Sex and gonadal hormones in mouse models of Alzheimer's disease: what is relevant to the human condition? *Biol Sex Differ* **3**, 24, doi:10.1186/2042-6410-3-24 (2012).

60   Notkola, I. L. *et al.* Serum total cholesterol, apolipoprotein E epsilon 4 allele, and Alzheimer's disease. *Neuroepidemiology* **17**, 14-20, doi:10.1159/000026149 (1998).

61   Kivipelto, M. *et al.* Apolipoprotein E epsilon4 allele, elevated midlife total cholesterol level, and high midlife systolic blood pressure are independent risk factors for late-life Alzheimer disease. *Ann Intern Med* **137**, 149-155, doi:10.7326/0003-4819-137-3-200208060-00006 (2002).

62   Honig, L. S., Kukull, W. & Mayeux, R. Atherosclerosis and AD: analysis of data from the US National Alzheimer's Coordinating Center. *Neurology* **64**, 494-500, doi:10.1212/01.WNL.0000150886.50187.30 (2005).

63   Lee, J. *et al.* Adaptor protein sorting nexin 17 regulates amyloid precursor protein trafficking and processing in the early endosomes. *J Biol Chem* **283**, 11501-11508, doi:10.1074/jbc.M800642200 (2008).

64   Fukumori, A. *et al.* Presenilin-dependent gamma-secretase on plasma membrane and endosomes is functionally distinct. *Biochemistry* **45**, 4907-4914, doi:10.1021/bi052412w (2006).

65   Meziane, H. *et al.* Memory-enhancing effects of secreted forms of the beta-amyloid precursor protein in normal and amnestic mice. *Proc Natl Acad Sci U S A* **95**, 12683-12688, doi:10.1073/pnas.95.21.12683 (1998).

66   Roch, J. M. *et al.* Increase of synaptic density and memory retention by a peptide representing the trophic domain of the amyloid beta/A4 protein precursor. *Proc Natl Acad Sci U S A* **91**, 7450-7454, doi:10.1073/pnas.91.16.7450 (1994).

67   Kinoshita, A. *et al.* Demonstration by FRET of BACE interaction with the amyloid precursor protein at the cell surface and in early endosomes. *J Cell Sci* **116**, 3339-3346, doi:10.1242/jcs.00643 (2003).

68   Parvathy, S., Hussain, I., Karran, E. H., Turner, A. J. & Hooper, N. M. Cleavage of Alzheimer's amyloid precursor protein by alpha-secretase occurs at the surface of neuronal cells. *Biochemistry* **38**, 9728-9734, doi:10.1021/bi9906827 (1999).

69   Koo, E. H. & Squazzo, S. L. Evidence that production and release of amyloid beta-protein involves the endocytic pathway. *J Biol Chem* **269**, 17386-17389 (1994).

70   Barger, S. W. & Harmon, A. D. Microglial activation by Alzheimer amyloid precursor protein and modulation by apolipoprotein E. *Nature* **388**, 878-881, doi:10.1038/42257 (1997).

71   Furukawa, K. *et al.* Increased activity-regulating and neuroprotective efficacy of alpha-secretase-derived secreted amyloid precursor protein conferred by a C-terminal heparin-binding domain. *J Neurochem* **67**, 1882-1896, doi:10.1046/j.1471-4159.1996.67051882.x (1996).

72   Freude, K. K., Penjwini, M., Davis, J. L., LaFerla, F. M. & Blurton-Jones, M. Soluble amyloid precursor protein induces rapid neural differentiation of human embryonic stem cells. *J Biol Chem* **286**, 24264-24274, doi:10.1074/jbc.M111.227421 (2011).

73   Chasseigneaux, S. *et al.* Secreted amyloid precursor protein beta and secreted amyloid precursor protein alpha induce axon outgrowth in vitro through Egr1 signaling pathway. *PLoS One* **6**, e16301, doi:10.1371/journal.pone.0016301 (2011).

74   Lauritzen, I. *et al.* Intraneuronal aggregation of the beta-CTF fragment of APP (C99) induces Abeta-independent lysosomal-autophagic pathology. *Acta Neuropathol* **132**, 257-276, doi:10.1007/s00401-016-1577-6 (2016).

75   Mondragon-Rodriguez, S., Gu, N., Manseau, F. & Williams, S. Alzheimer's Transgenic Model Is Characterized by Very Early Brain Network Alterations and beta-CTF Fragment Accumulation: Reversal by beta-Secretase Inhibition. *Front Cell Neurosci* **12**, 121, doi:10.3389/fncel.2018.00121 (2018).

76   Passer, B. *et al.* Generation of an apoptotic intracellular peptide by gamma-secretase cleavage of Alzheimer's amyloid beta protein precursor. *J Alzheimers Dis* **2**, 289-301, doi:10.3233/jad-2000-23-408 (2000).

77   Kamenetz, F. *et al.* APP processing and synaptic function. *Neuron* **37**, 925-937, doi:10.1016/s0896-6273(03)00124-7 (2003).

78   Abramov, E. *et al.* Amyloid-beta as a positive endogenous regulator of release probability at hippocampal synapses. *Nat Neurosci* **12**, 1567-1576, doi:10.1038/nn.2433 (2009).

79   Cirrito, J. R. *et al.* Synaptic activity regulates interstitial fluid amyloid-beta levels in vivo. *Neuron* **48**, 913-922, doi:10.1016/j.neuron.2005.10.028 (2005).

80   Kang, J. E. *et al.* Amyloid-beta dynamics are regulated by orexin and the sleep-wake cycle. *Science* **326**, 1005-1007, doi:10.1126/science.1180962 (2009).

81   Walsh, D. M. & Selkoe, D. J. A beta oligomers - a decade of discovery. *J Neurochem* **101**, 1172-1184, doi:10.1111/j.1471-4159.2006.04426.x (2007).

82   Rice, H. C. *et al.* Contribution of GABAergic interneurons to amyloid-beta plaque pathology in an APP knock-in mouse model. *Mol Neurodegener* **15**, 3, doi:10.1186/s13024-019-0356-y (2020).

83   Pelkey, K. A. *et al.* Hippocampal GABAergic Inhibitory Interneurons. *Physiol Rev* **97**, 1619-1747, doi:10.1152/physrev.00007.2017 (2017).

84   Eikelenboom, P., Zhan, S. S., van Gool, W. A. & Allsop, D. Inflammatory mechanisms in Alzheimer's disease. *Trends Pharmacol Sci* **15**, 447-450, doi:10.1016/0165-6147(94)90057-4 (1994).

85   Kinney, J. W. *et al.* Inflammation as a central mechanism in Alzheimer's disease. *Alzheimers Dement (N Y)* **4**, 575-590, doi:10.1016/j.trci.2018.06.014 (2018).

86   Bai, R., Guo, J., Ye, X. Y., Xie, Y. & Xie, T. Oxidative stress: The core pathogenesis and mechanism of Alzheimer's disease. *Ageing Res Rev* **77**, 101619, doi:10.1016/j.arr.2022.101619 (2022).

87   Perry, G. *et al.* Is oxidative damage the fundamental pathogenic mechanism of Alzheimer's and other neurodegenerative diseases? *Free Radic Biol Med* **33**, 1475-1479, doi:10.1016/s0891-5849(02)01113-9 (2002).

88   Hickman, S. E., Allison, E. K. & El Khoury, J. Microglial dysfunction and defective beta-amyloid clearance pathways in aging Alzheimer's disease mice. *J Neurosci* **28**, 8354-8360, doi:10.1523/JNEUROSCI.0616-08.2008 (2008).

89   Herrup, K. The case for rejecting the amyloid cascade hypothesis. *Nat Neurosci* **18**, 794-799, doi:10.1038/nn.4017 (2015).

90   Braak, H. & Braak, E. Neuropathological stageing of Alzheimer-related changes. *Acta Neuropathol* **82**, 239-259, doi:10.1007/BF00308809 (1991).

91   Braak, H., Braak, E., Bohl, J. & Bratzke, H. Evolution of Alzheimer's disease related cortical lesions. *J Neural Transm Suppl* **54**, 97-106, doi:10.1007/978-3-7091-7508-8_9 (1998).

92   Buckner, R. L., Andrews-Hanna, J. R. & Schacter, D. L. The brain's default network: anatomy, function, and relevance to disease. *Ann N Y Acad Sci* **1124**, 1-38, doi:10.1196/annals.1440.011 (2008).

93   Greicius, M. D., Srivastava, G., Reiss, A. L. & Menon, V. Default-mode network activity distinguishes Alzheimer's disease from healthy aging: evidence from functional MRI. *Proc Natl Acad Sci U S A* **101**, 4637-4642, doi:10.1073/pnas.0308627101 (2004).

94   Kobro-Flatmoen, A., Nagelhus, A. & Witter, M. P. Reelin-immunoreactive neurons in entorhinal cortex layer II selectively express intracellular amyloid in early Alzheimer's disease. *Neurobiol Dis* **93**, 172-183, doi:10.1016/j.nbd.2016.05.012 (2016).

95   Lipton, P. A. & Eichenbaum, H. Complementary roles of hippocampus and medial entorhinal cortex in episodic memory. *Neural Plast* **2008**, 258467, doi:10.1155/2008/258467 (2008).

96   Ward, A. M. *et al.* The parahippocampal gyrus links the default-mode cortical network with the medial temporal lobe memory system. *Hum Brain Mapp* **35**, 1061-1073, doi:10.1002/hbm.22234 (2014).

97   Kahn, I., Andrews-Hanna, J. R., Vincent, J. L., Snyder, A. Z. & Buckner, R. L. Distinct cortical anatomy linked to subregions of the medial temporal lobe revealed by intrinsic functional connectivity. *J Neurophysiol* **100**, 129-139, doi:10.1152/jn.00077.2008 (2008).

98   Lacy, J. W. & Stark, C. E. Intrinsic functional connectivity of the human medial temporal lobe suggests a distinction between adjacent MTL cortices and hippocampus. *Hippocampus* **22**, 2290-2302, doi:10.1002/hipo.22047 (2012).

99   Libby, L. A., Ekstrom, A. D., Ragland, J. D. & Ranganath, C. Differential connectivity of perirhinal and parahippocampal cortices within human hippocampal subregions revealed by high-resolution functional imaging. *J Neurosci* **32**, 6550-6560, doi:10.1523/JNEUROSCI.3711-11.2012 (2012).

100   Delacourte, A. *et al.* The biochemical pathway of neurofibrillary degeneration in aging and Alzheimer's disease. *Neurology* **52**, 1158-1165, doi:10.1212/wnl.52.6.1158 (1999).

101   Hanseeuw, B. J. *et al.* Association of Amyloid and Tau With Cognition in Preclinical Alzheimer Disease: A Longitudinal Study. *JAMA Neurol* **76**, 915-924, doi:10.1001/jamaneurol.2019.1424 (2019).

102   Jack, C. R. *et al.* The bivariate distribution of amyloid-beta and tau: relationship with established neurocognitive clinical syndromes. *Brain* **142**, 3230-3242, doi:10.1093/brain/awz268 (2019).

103   Ossenkoppele, R. *et al.* Tau PET patterns mirror clinical and neuroanatomical variability in Alzheimer's disease. *Brain* **139**, 1551-1567, doi:10.1093/brain/aww027 (2016).

104   Tomlinson, B. E., Blessed, G. & Roth, M. Observations on the brains of demented old people. *J Neurol Sci* **11**, 205-242, doi:10.1016/0022-510x(70)90063-8 (1970).

105   Gomez-Isla, T. *et al.* Profound loss of layer II entorhinal cortex neurons occurs in very mild Alzheimer's disease. *J Neurosci* **16**, 4491-4500, doi:10.1523/JNEUROSCI.16-14-04491.1996 (1996).

106   Vossel, K. A. *et al.* Incidence and impact of subclinical epileptiform activity in Alzheimer's disease. *Ann Neurol* **80**, 858-870, doi:10.1002/ana.24794 (2016).

107   Palop, J. J. *et al.* Aberrant excitatory neuronal activity and compensatory remodeling of inhibitory hippocampal circuits in mouse models of Alzheimer's disease. *Neuron* **55**, 697-711, doi:10.1016/j.neuron.2007.07.025 (2007).

108   Verret, L. *et al.* Inhibitory interneuron deficit links altered network activity and cognitive dysfunction in Alzheimer model. *Cell* **149**, 708-721, doi:10.1016/j.cell.2012.02.046 (2012).

109   Petrache, A. L. *et al.* Aberrant Excitatory-Inhibitory Synaptic Mechanisms in Entorhinal Cortex Microcircuits During the Pathogenesis of Alzheimer's Disease. *Cereb Cortex* **29**, 1834-1850, doi:10.1093/cercor/bhz016 (2019).

110   Hijazi, S. *et al.* Early restoration of parvalbumin interneuron activity prevents memory loss and network hyperexcitability in a mouse model of Alzheimer's disease. *Mol Psychiatry* **25**, 3380-3398, doi:10.1038/s41380-019-0483-4 (2020).

111   Johnson, E. C. B. *et al.* Behavioral and neural network abnormalities in human APP transgenic mice resemble those of App knock-in mice and are modulated by familial Alzheimer's disease mutations but not by inhibition of BACE1. *Mol Neurodegener* **15**, 53, doi:10.1186/s13024-020-00393-5 (2020).

112   Zhang, Z. *et al.* Hyper-excitability of corticothalamic PT neurons in mPFC promotes irritability in the mouse model of Alzheimer's disease. *Cell Rep* **41**, 111577, doi:10.1016/j.celrep.2022.111577 (2022).

113   Olah, V. J. *et al.* Biophysical K(v)3 channel alterations dampen excitability of cortical PV interneurons and contribute to network hyperexcitability in early Alzheimer's. *Elife* **11**, doi:10.7554/eLife.75316 (2022).

114   Siskova, Z. *et al.* Dendritic structural degeneration is functionally linked to cellular hyperexcitability in a mouse model of Alzheimer's disease. *Neuron* **84**, 1023-1033, doi:10.1016/j.neuron.2014.10.024 (2014).

115   Nuriel, T. *et al.* Neuronal hyperactivity due to loss of inhibitory tone in APOE4 mice lacking Alzheimer's disease-like pathology. *Nat Commun* **8**, 1464, doi:10.1038/s41467-017-01444-0 (2017).

116   Angulo, S. L. *et al.* Tau and amyloid-related pathologies in the entorhinal cortex have divergent effects in the hippocampal circuit. *Neurobiol Dis* **108**, 261-276, doi:10.1016/j.nbd.2017.08.015 (2017).

117   Khan, U. A. *et al.* Molecular drivers and cortical spread of lateral entorhinal cortex dysfunction in preclinical Alzheimer's disease. *Nat Neurosci* **17**, 304-311, doi:10.1038/nn.3606 (2014).

118   Chen, L., Saito, T., Saido, T. C. & Mody, I. Novel Quantitative Analyses of Spontaneous Synaptic Events in Cortical Pyramidal Cells Reveal Subtle Parvalbumin-Expressing Interneuron Dysfunction in a Knock-In Mouse Model of Alzheimer's Disease. *eNeuro* **5**, doi:10.1523/ENEURO.0059-18.2018 (2018).

119   Palop, J. J. & Mucke, L. Network abnormalities and interneuron dysfunction in Alzheimer disease. *Nat Rev Neurosci* **17**, 777-792, doi:10.1038/nrn.2016.141 (2016).

120   Zhou, S. & Yu, Y. Synaptic E-I Balance Underlies Efficient Neural Coding. *Front Neurosci* **12**, 46, doi:10.3389/fnins.2018.00046 (2018).

121   Arroyo-Garcia, L. E. *et al.* Impaired spike-gamma coupling of area CA3 fast-spiking interneurons as the earliest functional impairment in the App(NL-G-F) mouse model of Alzheimer's disease. *Mol Psychiatry* **26**, 5557-5567, doi:10.1038/s41380-021-01257-0 (2021).

122   Li, Y. *et al.* Reversible GABAergic dysfunction involved in hippocampal hyperactivity predicts early-stage Alzheimer disease in a mouse model. *Alzheimers Res Ther* **13**, 114, doi:10.1186/s13195-021-00859-8 (2021).

123   Sederberg, P. B. *et al.* Hippocampal and neocortical gamma oscillations predict memory formation in humans. *Cereb Cortex* **17**, 1190-1196, doi:10.1093/cercor/bhl030 (2007).

124   Caccavano, A. *et al.* Inhibitory Parvalbumin Basket Cell Activity is Selectively Reduced during Hippocampal Sharp Wave Ripples in a Mouse Model of Familial Alzheimer's Disease. *J Neurosci* **40**, 5116-5136, doi:10.1523/JNEUROSCI.0425-20.2020 (2020).

125   Martinez-Losa, M. *et al.* Nav1.1-Overexpressing Interneuron Transplants Restore Brain Rhythms and Cognition in a Mouse Model of Alzheimer's Disease. *Neuron* **98**, 75-89 e75, doi:10.1016/j.neuron.2018.02.029 (2018).

126   Park, K. *et al.* Optogenetic activation of parvalbumin and somatostatin interneurons selectively restores theta-nested gamma oscillations and oscillation-induced spike timing-dependent long-term potentiation impaired by amyloid beta oligomers. *BMC Biol* **18**, 7, doi:10.1186/s12915-019-0732-7 (2020).

127   Kim, C. K. *et al.* Alzheimer's Disease: Key Insights from Two Decades of Clinical Trial Failures. *J Alzheimers Dis* **87**, 83-100, doi:10.3233/JAD-215699 (2022).

128   Jack, C. R., Jr. *et al.* NIA-AA Research Framework: Toward a biological definition of Alzheimer's disease. *Alzheimers Dement* **14**, 535-562, doi:10.1016/j.jalz.2018.02.018 (2018).

129   Kunkle, B. W. *et al.* Genetic meta-analysis of diagnosed Alzheimer's disease identifies new risk loci and implicates Abeta, tau, immunity and lipid processing. *Nat Genet* **51**, 414-430, doi:10.1038/s41588-019-0358-2 (2019).

130   Tosches, M. A. & Lee, H. J. Cellular atlases of the entire mouse brain. *Nature* **624**, 253-255, doi:10.1038/d41586-023-03781-1 (2023).

131   Moritz, C. P., Muhlhaus, T., Tenzer, S., Schulenborg, T. & Friauf, E. Poor transcript-protein correlation in the brain: negatively correlating gene products reveal neuronal polarity as a potential cause. *J Neurochem* **149**, 582-604, doi:10.1111/jnc.14664 (2019).

132   Tasaki, S. *et al.* Inferring protein expression changes from mRNA in Alzheimer's dementia using deep neural networks. *Nat Commun* **13**, 655, doi:10.1038/s41467-022-28280-1 (2022).

133   Wei, Y. N. *et al.* Transcript and protein expression decoupling reveals RNA binding proteins and miRNAs as potential modulators of human aging. *Genome Biol* **16**, 41, doi:10.1186/s13059-015-0608-2 (2015).

134   Johnson, E. C. B. *et al.* Cerebrospinal fluid proteomics define the natural history of autosomal dominant Alzheimer's disease. *Nat Med* **29**, 1979-1988, doi:10.1038/s41591-023-02476-4 (2023).

135   Chalatsi, T. *et al.* Autophagy in parvalbumin interneurons is required for inhibitory transmission and memory via regulation of synaptic proteostasis. *bioRxiv*, 2022.2010.2010.511533, doi:10.1101/2022.10.10.511533 (2022).

136   Joseph, D. J. *et al.* Protocol for isolating young adult parvalbumin interneurons from the mouse brain for extraction of high-quality RNA. *STAR Protoc* **2**, 100714, doi:10.1016/j.xpro.2021.100714 (2021).

137   Taylor, A. L. What we talk about when we talk about capacitance measured with the voltage-clamp step method. *J Comput Neurosci* **32**, 167-175, doi:10.1007/s10827-011-0346-8 (2012).

138   Chan, K. Y. *et al.* Engineered AAVs for efficient noninvasive gene delivery to the central and peripheral nervous systems. *Nat Neurosci* **20**, 1172-1179, doi:10.1038/nn.4593 (2017).

139   Caballero, A., Flores-Barrera, E., Thomases, D. R. & Tseng, K. Y. Downregulation of parvalbumin expression in the prefrontal cortex during adolescence causes enduring prefrontal disinhibition in adulthood. *Neuropsychopharmacology* **45**, 1527-1535, doi:10.1038/s41386-020-0709-9 (2020).

140   Madisen, L. *et al.* A robust and high-throughput Cre reporting and characterization system for the whole mouse brain. *Nat Neurosci* **13**, 133-140, doi:10.1038/nn.2467 (2010).

141   Oakley, H. *et al.* Intraneuronal beta-amyloid aggregates, neurodegeneration, and neuron loss in transgenic mice with five familial Alzheimer's disease mutations: potential factors in amyloid plaque formation. *J Neurosci* **26**, 10129-10140, doi:10.1523/JNEUROSCI.1202-06.2006 (2006).

142   Kumar, P. *et al.* Native-state proteomics of Parvalbumin interneurons identifies unique molecular signatures and vulnerabilities to early Alzheimer's pathology. *Nat Commun* **15**, 2823, doi:10.1038/s41467-024-47028-7 (2024).

143   Perez-Riverol, Y. *et al.* The PRIDE database resources in 2022: a hub for mass spectrometry-based proteomics evidences. *Nucleic Acids Res* **50**, D543-D552, doi:10.1093/nar/gkab1038 (2022).

144   Rangaraju, S. *et al.* Quantitative proteomics of acutely-isolated mouse microglia identifies novel immune Alzheimer's disease-related proteins. *Mol Neurodegener* **13**, 34, doi:10.1186/s13024-018-0266-4 (2018).

145   Rayaprolu, S. *et al.* Flow-cytometric microglial sorting coupled with quantitative proteomics identifies moesin as a highly-abundant microglial protein with relevance to Alzheimer's disease. *Mol Neurodegener* **15**, 28, doi:10.1186/s13024-020-00377-5 (2020).

146   Yu, L. *et al.* Cortical Proteins Associated With Cognitive Resilience in Community-Dwelling Older Persons. *JAMA Psychiatry* **77**, 1172-1180, doi:10.1001/jamapsychiatry.2020.1807 (2020).

147   Kavanagh, T., Halder, A. & Drummond, E. Tau interactome and RNA binding proteins in neurodegenerative diseases. *Mol Neurodegener* **17**, 66, doi:10.1186/s13024-022-00572-6 (2022).

148   Szklarczyk, D. *et al.* The STRING database in 2023: protein-protein association networks and functional enrichment analyses for any sequenced genome of interest. *Nucleic Acids Res* **51**, D638-D646, doi:10.1093/nar/gkac1000 (2023).

149   Hanzelmann, S., Castelo, R. & Guinney, J. GSVA: gene set variation analysis for microarray and RNA-seq data. *BMC Bioinformatics* **14**, 7, doi:10.1186/1471-2105-14-7 (2013).

150   Galea, E. *et al.* Multi-transcriptomic analysis points to early organelle dysfunction in human astrocytes in Alzheimer's disease. *Neurobiol Dis* **166**, 105655, doi:10.1016/j.nbd.2022.105655 (2022).

151   Wingo, A. P. *et al.* Shared proteomic effects of cerebral atherosclerosis and Alzheimer's disease on the human brain. *Nat Neurosci* **23**, 696-700, doi:10.1038/s41593-020-0635-5 (2020).

152   Hodge, R. D. *et al.* Conserved cell types with divergent features in human versus mouse cortex. *Nature* **573**, 61-68, doi:10.1038/s41586-019-1506-7 (2019).

153   Cai, M. *et al.* Robust and accurate estimation of cellular fraction from tissue omics data via ensemble deconvolution. *Bioinformatics* **38**, 3004-3010, doi:10.1093/bioinformatics/btac279 (2022).

154   Barbie, D. A. *et al.* Systematic RNA interference reveals that oncogenic KRAS-driven cancers require TBK1. *Nature* **462**, 108-112, doi:10.1038/nature08460 (2009).

155   Hurst, C. *et al.* Integrated Proteomics to Understand the Role of Neuritin (NRN1) as a Mediator of Cognitive Resilience to Alzheimer's Disease. *Mol Cell Proteomics*, 100542, doi:10.1016/j.mcpro.2023.100542 (2023).

156   Seyfried, N. T. *et al.* A Multi-network Approach Identifies Protein-Specific Co-expression in Asymptomatic and Symptomatic Alzheimer's Disease. *Cell Syst* **4**, 60-72 e64, doi:10.1016/j.cels.2016.11.006 (2017).

157   He, M. *et al.* Cell-type-based analysis of microRNA profiles in the mouse brain. *Neuron* **73**, 35-48, doi:10.1016/j.neuron.2011.11.010 (2012).

158   Shimojo, M. *et al.* Selective Disruption of Inhibitory Synapses Leading to Neuronal Hyperexcitability at an Early Stage of Tau Pathogenesis in a Mouse Model. *J Neurosci* **40**, 3491-3501, doi:10.1523/JNEUROSCI.2880-19.2020 (2020).

159   De Strooper, B. & Karran, E. The Cellular Phase of Alzheimer's Disease. *Cell* **164**, 603-615, doi:10.1016/j.cell.2015.12.056 (2016).

160   Frere, S. & Slutsky, I. Alzheimer's Disease: From Firing Instability to Homeostasis Network Collapse. *Neuron* **97**, 32-58, doi:10.1016/j.neuron.2017.11.028 (2018).

161   Davis, K. E., Fox, S. & Gigg, J. Increased hippocampal excitability in the 3xTgAD mouse model for Alzheimer's disease in vivo. *PLoS One* **9**, e91203, doi:10.1371/journal.pone.0091203 (2014).

162   Pooler, A. M. *et al.* Propagation of tau pathology in Alzheimer's disease: identification of novel therapeutic targets. *Alzheimers Res Ther* **5**, 49, doi:10.1186/alzrt214 (2013).

163   Wu, J. W. *et al.* Neuronal activity enhances tau propagation and tau pathology in vivo. *Nat Neurosci* **19**, 1085-1092, doi:10.1038/nn.4328 (2016).

164   Lamoureux, L., Marottoli, F. M., Tseng, K. Y. & Tai, L. M. APOE4 Promotes Tonic-Clonic Seizures, an Effect Modified by Familial Alzheimer's Disease Mutations. *Front Cell Dev Biol* **9**, 656521, doi:10.3389/fcell.2021.656521 (2021).

165   Minkeviciene, R. *et al.* Amyloid beta-induced neuronal hyperexcitability triggers progressive epilepsy. *J Neurosci* **29**, 3453-3462, doi:10.1523/JNEUROSCI.5215-08.2009 (2009).

166   Bai, Y. *et al.* Abnormal dendritic calcium activity and synaptic depotentiation occur early in a mouse model of Alzheimer's disease. *Mol Neurodegener* **12**, 86, doi:10.1186/s13024-017-0228-2 (2017).

167   Busche, M. A. & Konnerth, A. Neuronal hyperactivity--A key defect in Alzheimer's disease? *Bioessays* **37**, 624-632, doi:10.1002/bies.201500004 (2015).

168   Dickerson, B. C. *et al.* Increased hippocampal activation in mild cognitive impairment compared to normal aging and AD. *Neurology* **65**, 404-411, doi:10.1212/01.wnl.0000171450.97464.49 (2005).

169   Hamalainen, A. *et al.* Increased fMRI responses during encoding in mild cognitive impairment. *Neurobiol Aging* **28**, 1889-1903, doi:10.1016/j.neurobiolaging.2006.08.008 (2007).

170   Miller, S. L. *et al.* Hippocampal activation in adults with mild cognitive impairment predicts subsequent cognitive decline. *J Neurol Neurosurg Psychiatry* **79**, 630-635, doi:10.1136/jnnp.2007.124149 (2008).

171   Sperling, R. A. *et al.* Amyloid deposition is associated with impaired default network function in older persons without dementia. *Neuron* **63**, 178-188, doi:10.1016/j.neuron.2009.07.003 (2009).

172   Quiroz, Y. T. *et al.* Hippocampal hyperactivation in presymptomatic familial Alzheimer's disease. *Ann Neurol* **68**, 865-875, doi:10.1002/ana.22105 (2010).

173   Sepulveda-Falla, D., Glatzel, M. & Lopera, F. Phenotypic profile of early-onset familial Alzheimer's disease caused by presenilin-1 E280A mutation. *J Alzheimers Dis* **32**, 1-12, doi:10.3233/JAD-2012-120907 (2012).

174   Bundy, J. L., Vied, C., Badger, C. & Nowakowski, R. S. Sex-biased hippocampal pathology in the 5XFAD mouse model of Alzheimer's disease: A multi-omic analysis. *J Comp Neurol* **527**, 462-475, doi:10.1002/cne.24551 (2019).

175   Vormstein-Schneider, D. *et al.* Viral manipulation of functionally distinct interneurons in mice, non-human primates and humans. *Nat Neurosci* **23**, 1629-1636, doi:10.1038/s41593-020-0692-9 (2020).

176   Jawhar, S., Trawicka, A., Jenneckens, C., Bayer, T. A. & Wirths, O. Motor deficits, neuron loss, and reduced anxiety coinciding with axonal degeneration and intraneuronal Abeta aggregation in the 5XFAD mouse model of Alzheimer's disease. *Neurobiol Aging* **33**, 196 e129-140, doi:10.1016/j.neurobiolaging.2010.05.027 (2012).

177   Chow, A. *et al.* K(+) channel expression distinguishes subpopulations of parvalbumin- and somatostatin-containing neocortical interneurons. *J Neurosci* **19**, 9332-9345, doi:10.1523/JNEUROSCI.19-21-09332.1999 (1999).

178   Ogiwara, I. *et al.* Nav1.1 localizes to axons of parvalbumin-positive inhibitory interneurons: a circuit basis for epileptic seizures in mice carrying an Scn1a gene mutation. *J Neurosci* **27**, 5903-5914, doi:10.1523/JNEUROSCI.5270-06.2007 (2007).

179   Saito, T., Matsuba, Y., Yamazaki, N., Hashimoto, S. & Saido, T. C. Calpain Activation in Alzheimer's Model Mice Is an Artifact of APP and Presenilin Overexpression. *J Neurosci* **36**, 9933-9936, doi:10.1523/JNEUROSCI.1907-16.2016 (2016).

180   Kole, M. H. *et al.* Action potential generation requires a high sodium channel density in the axon initial segment. *Nat Neurosci* **11**, 178-186, doi:10.1038/nn2040 (2008).

181   Li, T. *et al.* Action potential initiation in neocortical inhibitory interneurons. *PLoS Biol* **12**, e1001944, doi:10.1371/journal.pbio.1001944 (2014).

182   Platkiewicz, J. & Brette, R. A threshold equation for action potential initiation. *PLoS Comput Biol* **6**, e1000850, doi:10.1371/journal.pcbi.1000850 (2010).

183   Escayg, A. & Goldin, A. L. Sodium channel SCN1A and epilepsy: mutations and mechanisms. *Epilepsia* **51**, 1650-1658, doi:10.1111/j.1528-1167.2010.02640.x (2010).

184   Yu, F. H. *et al.* Reduced sodium current in GABAergic interneurons in a mouse model of severe myoclonic epilepsy in infancy. *Nat Neurosci* **9**, 1142-1149, doi:10.1038/nn1754 (2006).

185   Barry, J. *et al.* Activation of conventional kinesin motors in clusters by Shaw voltage-gated K+ channels. *J Cell Sci* **126**, 2027-2041, doi:10.1242/jcs.122234 (2013).

186   Rowan, M. J., Tranquil, E. & Christie, J. M. Distinct Kv channel subtypes contribute to differences in spike signaling properties in the axon initial segment and presynaptic boutons of cerebellar interneurons. *J Neurosci* **34**, 6611-6623, doi:10.1523/JNEUROSCI.4208-13.2014 (2014).

187   Song, P. *et al.* Acoustic environment determines phosphorylation state of the Kv3.1 potassium channel in auditory neurons. *Nat Neurosci* **8**, 1335-1342, doi:10.1038/nn1533 (2005).

188   Lien, C. C., Martina, M., Schultz, J. H., Ehmke, H. & Jonas, P. Gating, modulation and subunit composition of voltage-gated K(+) channels in dendritic inhibitory interneurones of rat hippocampus. *J Physiol* **538**, 405-419, doi:10.1113/jphysiol.2001.013066 (2002).

189   Fernandez, F. R., Morales, E., Rashid, A. J., Dunn, R. J. & Turner, R. W. Inactivation of Kv3.3 potassium channels in heterologous expression systems. *J Biol Chem* **278**, 40890-40898, doi:10.1074/jbc.M304235200 (2003).

190   Weiser, M. *et al.* Differential expression of Shaw-related K+ channels in the rat central nervous system. *J Neurosci* **14**, 949-972, doi:10.1523/JNEUROSCI.14-03-00949.1994 (1994).

191   Vogel, C. & Marcotte, E. M. Insights into the regulation of protein abundance from proteomic and transcriptomic analyses. *Nat Rev Genet* **13**, 227-232, doi:10.1038/nrg3185 (2012).

192   de Sousa Abreu, R., Penalva, L. O., Marcotte, E. M. & Vogel, C. Global signatures of protein and mRNA expression levels. *Mol Biosyst* **5**, 1512-1526, doi:10.1039/b908315d (2009).

193   Lien, C. C. & Jonas, P. Kv3 potassium conductance is necessary and kinetically optimized for high-frequency action potential generation in hippocampal interneurons. *J Neurosci* **23**, 2058-2068, doi:10.1523/JNEUROSCI.23-06-02058.2003 (2003).

194   Bean, B. P. The action potential in mammalian central neurons. *Nat Rev Neurosci* **8**, 451-465, doi:10.1038/nrn2148 (2007).

195   Dodson, P. D., Barker, M. C. & Forsythe, I. D. Two heteromeric Kv1 potassium channels differentially regulate action potential firing. *J Neurosci* **22**, 6953-6961, doi:10.1523/JNEUROSCI.22-16-06953.2002 (2002).

196   Pathak, D., Guan, D. & Foehring, R. C. Roles of specific Kv channel types in repolarization of the action potential in genetically identified subclasses of pyramidal neurons in mouse neocortex. *J Neurophysiol* **115**, 2317-2329, doi:10.1152/jn.01028.2015 (2016).

197   Coetzee, W. A. *et al.* Molecular diversity of K+ channels. *Ann N Y Acad Sci* **868**, 233-285, doi:10.1111/j.1749-6632.1999.tb11293.x (1999).

198   Alle, H., Kubota, H. & Geiger, J. R. Sparse but highly efficient Kv3 outpace BKCa channels in action potential repolarization at hippocampal mossy fiber boutons. *J Neurosci* **31**, 8001-8012, doi:10.1523/JNEUROSCI.0972-11.2011 (2011).

199   Casale, A. E., Foust, A. J., Bal, T. & McCormick, D. A. Cortical Interneuron Subtypes Vary in Their Axonal Action Potential Properties. *J Neurosci* **35**, 15555-15567, doi:10.1523/JNEUROSCI.1467-13.2015 (2015).

200   Goldberg, E. M. *et al.* Specific functions of synaptically localized potassium channels in synaptic transmission at the neocortical GABAergic fast-spiking cell synapse. *J Neurosci* **25**, 5230-5235, doi:10.1523/JNEUROSCI.0722-05.2005 (2005).

201   Guan, D., Higgs, M. H., Horton, L. R., Spain, W. J. & Foehring, R. C. Contributions of Kv7-mediated potassium current to sub- and suprathreshold responses of rat layer II/III neocortical pyramidal neurons. *J Neurophysiol* **106**, 1722-1733, doi:10.1152/jn.00211.2011 (2011).

202   Sekulic, V., Chen, T. C., Lawrence, J. J. & Skinner, F. K. Dendritic distributions of I h channels in experimentally-derived multi-compartment models of oriens-lacunosum/moleculare (O-LM) hippocampal interneurons. *Front Synaptic Neurosci* **7**, 2, doi:10.3389/fnsyn.2015.00002 (2015).

203   Desai, R., Kronengold, J., Mei, J., Forman, S. A. & Kaczmarek, L. K. Protein kinase C modulates inactivation of Kv3.3 channels. *J Biol Chem* **283**, 22283-22294, doi:10.1074/jbc.M801663200 (2008).

204   Yao, Y., Wu, M., Wang, L., Lin, L. & Xu, J. Phase Coupled Firing of Prefrontal Parvalbumin Interneuron With High Frequency Oscillations. *Front Cell Neurosci* **14**, 610741, doi:10.3389/fncel.2020.610741 (2020).

205   Yu, J., Hu, H., Agmon, A. & Svoboda, K. Recruitment of GABAergic Interneurons in the Barrel Cortex during Active Tactile Behavior. *Neuron* **104**, 412-427 e414, doi:10.1016/j.neuron.2019.07.027 (2019).

206   Jouhanneau, J. S., Kremkow, J. & Poulet, J. F. A. Single synaptic inputs drive high-precision action potentials in parvalbumin expressing GABA-ergic cortical neurons in vivo. *Nat Commun* **9**, 1540, doi:10.1038/s41467-018-03995-2 (2018).

207   Jaeger, D. Mini-review: synaptic integration in the cerebellar nuclei--perspectives from dynamic clamp and computer simulation studies. *Cerebellum* **10**, 659-666, doi:10.1007/s12311-011-0248-3 (2011).

208   Xu-Friedman, M. A. & Regehr, W. G. Dynamic-clamp analysis of the effects of convergence on spike timing. II. Few synaptic inputs. *J Neurophysiol* **94**, 2526-2534, doi:10.1152/jn.01308.2004 (2005).

209   Rowan, M. J. M. & Christie, J. M. Rapid State-Dependent Alteration in K(v)3 Channel Availability Drives Flexible Synaptic Signaling Dependent on Somatic Subthreshold Depolarization. *Cell Rep* **18**, 2018-2029, doi:10.1016/j.celrep.2017.01.068 (2017).

210   Hu, H., Martina, M. & Jonas, P. Dendritic mechanisms underlying rapid synaptic activation of fast-spiking hippocampal interneurons. *Science* **327**, 52-58, doi:10.1126/science.1177876 (2010).

211   Cardin, J. A. *et al.* Driving fast-spiking cells induces gamma rhythm and controls sensory responses. *Nature* **459**, 663-667, doi:10.1038/nature08002 (2009).

212   Fuchs, E. C. *et al.* Recruitment of parvalbumin-positive interneurons determines hippocampal function and associated behavior. *Neuron* **53**, 591-604, doi:10.1016/j.neuron.2007.01.031 (2007).

213 Sohal, V. S., Zhang, F., Yizhar, O. & Deisseroth, K. Parvalbumin neurons and gamma rhythms enhance cortical circuit performance. *Nature* **459**, 698-702, doi:10.1038/nature07991 (2009).

214 Bock, D. D. *et al.* Network anatomy and in vivo physiology of visual cortical neurons. *Nature* **471**, 177-182, doi:10.1038/nature09802 (2011).

215 Galarreta, M. & Hestrin, S. Electrical and chemical synapses among parvalbumin fast-spiking GABAergic interneurons in adult mouse neocortex. *Proc Natl Acad Sci U S A* **99**, 12438-12443, doi:10.1073/pnas.192159599 (2002).

216 Hofer, S. B. *et al.* Differential connectivity and response dynamics of excitatory and inhibitory neurons in visual cortex. *Nat Neurosci* **14**, 1045-1052, doi:10.1038/nn.2876 (2011).

217 Markram, H. *et al.* Reconstruction and Simulation of Neocortical Microcircuitry. *Cell* **163**, 456-492, doi:10.1016/j.cell.2015.09.029 (2015).

218 Perin, R., Berger, T. K. & Markram, H. A synaptic organizing principle for cortical neuronal groups. *Proc Natl Acad Sci U S A* **108**, 5419-5424, doi:10.1073/pnas.1016051108 (2011).

219 Wang, X. J. & Buzsaki, G. Gamma oscillation by synaptic inhibition in a hippocampal interneuronal network model. *J Neurosci* **16**, 6402-6413, doi:10.1523/JNEUROSCI.16-20-06402.1996 (1996).

220 Bartos, M., Vida, I. & Jonas, P. Synaptic mechanisms of synchronized gamma oscillations in inhibitory interneuron networks. *Nat Rev Neurosci* **8**, 45-56, doi:10.1038/nrn2044 (2007).

221   Morgan, R. J., Santhakumar, V. & Soltesz, I. Modeling the dentate gyrus. *Prog Brain Res* **163**, 639-658, doi:10.1016/S0079-6123(07)63035-0 (2007).

222   Paz, J. T. & Huguenard, J. R. Microcircuits and their interactions in epilepsy: is the focus out of focus? *Nat Neurosci* **18**, 351-359, doi:10.1038/nn.3950 (2015).

223   Cannon, R. C., O'Donnell, C. & Nolan, M. F. Stochastic ion channel gating in dendritic neurons: morphology dependence and probabilistic synaptic activation of dendritic spikes. *PLoS Comput Biol* **6**, doi:10.1371/journal.pcbi.1000886 (2010).

224   Lemay, M., de Lange, E. & Kucera, J. P. Effects of stochastic channel gating and distribution on the cardiac action potential. *J Theor Biol* **281**, 84-96, doi:10.1016/j.jtbi.2011.04.019 (2011).

225   Olah, V. J. *et al.* Functional specification of CCK+ interneurons by alternative isoforms of Kv4.3 auxiliary subunits. *Elife* **9**, doi:10.7554/eLife.58515 (2020).

226   Yu, F. H., Yarov-Yarovoy, V., Gutman, G. A. & Catterall, W. A. Overview of molecular relationships in the voltage-gated ion channel superfamily. *Pharmacol Rev* **57**, 387-395, doi:10.1124/pr.57.4.13 (2005).

227   Tremblay, R., Lee, S. & Rudy, B. GABAergic Interneurons in the Neocortex: From Cellular Properties to Circuits. *Neuron* **91**, 260-292, doi:10.1016/j.neuron.2016.06.033 (2016).

228   Chang, S. Y. *et al.* Distribution of Kv3.3 potassium channel subunits in distinct neuronal populations of mouse brain. *J Comp Neurol* **502**, 953-972, doi:10.1002/cne.21353 (2007).

229   Heinzen, E. L. *et al.* Alternative ion channel splicing in mesial temporal lobe epilepsy and Alzheimer's disease. *Genome Biol* **8**, R32, doi:10.1186/gb-2007-8-3-r32 (2007).

230   Angulo, E. *et al.* Up-regulation of the Kv3.4 potassium channel subunit in early stages of Alzheimer's disease. *J Neurochem* **91**, 547-557, doi:10.1111/j.1471-4159.2004.02771.x (2004).

231   Boscia, F. *et al.* The expression and activity of K(V)3.4 channel subunits are precociously upregulated in astrocytes exposed to Abeta oligomers and in astrocytes of Alzheimer's disease Tg2576 mice. *Neurobiol Aging* **54**, 187-198, doi:10.1016/j.neurobiolaging.2017.03.008 (2017).

232   Pannaccione, A. *et al.* Up-regulation and increased activity of KV3.4 channels and their accessory subunit MinK-related peptide 2 induced by amyloid peptide are involved in apoptotic neuronal death. *Mol Pharmacol* **72**, 665-673, doi:10.1124/mol.107.034868 (2007).

233   Manville, R. W. & Abbott, G. W. The Amyloid Precursor Protein C99 Fragment Modulates Voltage-Gated Potassium Channels. *Cell Physiol Biochem* **55**, 157-170, doi:10.33594/000000397 (2021).

234   Atzori, M. *et al.* H2 histamine receptor-phosphorylation of Kv3.2 modulates interneuron fast spiking. *Nat Neurosci* **3**, 791-798, doi:10.1038/77693 (2000).

235   Beck, E. J., Sorensen, R. G., Slater, S. J. & Covarrubias, M. Interactions between multiple phosphorylation sites in the inactivation particle of a K+ channel. Insights into the molecular mechanism of protein kinase C action. *J Gen Physiol* **112**, 71-84, doi:10.1085/jgp.112.1.71 (1998).

236   Kaczmarek, L. K. & Zhang, Y. Kv3 Channels: Enablers of Rapid Firing, Neurotransmitter Release, and Neuronal Endurance. *Physiol Rev* **97**, 1431-1468, doi:10.1152/physrev.00002.2017 (2017).

237   Macica, C. M. *et al.* Modulation of the kv3.1b potassium channel isoform adjusts the fidelity of the firing pattern of auditory neurons. *J Neurosci* **23**, 1133-1141, doi:10.1523/JNEUROSCI.23-04-01133.2003 (2003).

238   Moreno, H., Vega-Saenz de Miera, E., Nadal, M. S., Amarillo, Y. & Rudy, B. Modulation of Kv3 potassium channels expressed in CHO cells by a nitric oxide-activated phosphatase. *J Physiol* **530**, 345-358, doi:10.1111/j.1469-7793.2001.0345k.x (2001).

239   Macica, C. M. & Kaczmarek, L. K. Casein kinase 2 determines the voltage dependence of the Kv3.1 channel in auditory neurons and transfected cells. *J Neurosci* **21**, 1160-1168, doi:10.1523/JNEUROSCI.21-04-01160.2001 (2001).

240   Hall, M. K. *et al.* Membrane Distribution and Activity of a Neuronal Voltage-Gated K+ Channel is Modified by Replacement of Complex Type N-Glycans with Hybrid Type. *J Glycobiol* **6**, doi:10.4172/2168-958X.1000128 (2017).

241   Rowan, M. J., DelCanto, G., Yu, J. J., Kamasawa, N. & Christie, J. M. Synapse-Level Determination of Action Potential Duration by K(+) Channel Clustering in Axons. *Neuron* **91**, 370-383, doi:10.1016/j.neuron.2016.05.035 (2016).

242   Rossner, S., Sastre, M., Bourne, K. & Lichtenthaler, S. F. Transcriptional and translational regulation of BACE1 expression--implications for Alzheimer's disease. *Prog Neurobiol* **79**, 95-111, doi:10.1016/j.pneurobio.2006.06.001 (2006).

243   Hessler, S. *et al.* beta-Secretase BACE1 regulates hippocampal and reconstituted M-currents in a beta-subunit-like fashion. *J Neurosci* **35**, 3298-3311, doi:10.1523/JNEUROSCI.3127-14.2015 (2015).

244   Abbott, G. W. *et al.* MiRP2 forms potassium channels in skeletal muscle with Kv3.4 and is associated with periodic paralysis. *Cell* **104**, 217-231, doi:10.1016/s0092-8674(01)00207-0 (2001).

245   Sachse, C. C. *et al.* BACE1 and presenilin/gamma-secretase regulate proteolytic processing of KCNE1 and 2, auxiliary subunits of voltage-gated potassium channels. *FASEB J* **27**, 2458-2467, doi:10.1096/fj.12-214056 (2013).

246   Gouwens, N. W. *et al.* Classification of electrophysiological and morphological neuron types in the mouse visual cortex. *Nat Neurosci* **22**, 1182-1195, doi:10.1038/s41593-019-0417-0 (2019).

247   Busche, M. A. *et al.* Clusters of hyperactive neurons near amyloid plaques in a mouse model of Alzheimer's disease. *Science* **321**, 1686-1689, doi:10.1126/science.1162844 (2008).

248   Palop, J. J. & Mucke, L. Amyloid-beta-induced neuronal dysfunction in Alzheimer's disease: from synapses toward neural networks. *Nat Neurosci* **13**, 812-818, doi:10.1038/nn.2583 (2010).

249   Picard, N., Takesian, A. E., Fagiolini, M. & Hensch, T. K. NMDA 2A receptors in parvalbumin cells mediate sex-specific rapid ketamine response on cortical activity. *Mol Psychiatry* **24**, 828-838, doi:10.1038/s41380-018-0341-9 (2019).

250   Wang, J. *et al.* Enhanced Gamma Activity and Cross-Frequency Interaction of Resting-State Electroencephalographic Oscillations in Patients with Alzheimer's Disease. *Front Aging Neurosci* **9**, 243, doi:10.3389/fnagi.2017.00243 (2017).

251   Carlen, M. *et al.* A critical role for NMDA receptors in parvalbumin interneurons for gamma rhythm induction and behavior. *Mol Psychiatry* **17**, 537-548, doi:10.1038/mp.2011.31 (2012).

252   Rodgers, S. P., Born, H. A., Das, P. & Jankowsky, J. L. Transgenic APP expression during postnatal development causes persistent locomotor hyperactivity in the adult. *Mol Neurodegener* **7**, 28, doi:10.1186/1750-1326-7-28 (2012).

253   Kim, J. Y. *et al.* Viral transduction of the neonatal brain delivers controllable genetic mosaicism for visualising and manipulating neuronal circuits in vivo. *Eur J Neurosci* **37**, 1203-1220, doi:10.1111/ejn.12126 (2013).

254   Graybuck, L. T. *et al.* Enhancer viruses for combinatorial cell-subclass-specific labeling. *Neuron* **109**, 1449-1464 e1413, doi:10.1016/j.neuron.2021.03.011 (2021).

255   Vormstein-Schneider, D. *et al.* Viral manipulation of functionally distinct interneurons in mice, non-human primates and humans. *Nat Neurosci* **23**, 1629-1636, doi:10.1038/s41593-020-0692-9 (2020).

256   Hrvatin, S. *et al.* A scalable platform for the development of cell-type-specific viral drivers. *Elife* **8**, doi:10.7554/eLife.48089 (2019).

257   Vossel, K. *et al.* Effect of Levetiracetam on Cognition in Patients With Alzheimer Disease With and Without Epileptiform Activity: A Randomized Clinical Trial. *JAMA Neurol* **78**, 1345-1354, doi:10.1001/jamaneurol.2021.3310 (2021).

258   Shu, S. *et al.* Prefrontal parvalbumin interneurons deficits mediate early emotional dysfunction in Alzheimer's disease. *Neuropsychopharmacology* **48**, 391-401, doi:10.1038/s41386-022-01435-w (2023).

259   Oblak, A. L. *et al.* Comprehensive Evaluation of the 5XFAD Mouse Model for Preclinical Testing Applications: A MODEL-AD Study. *Front Aging Neurosci* **13**, 713726, doi:10.3389/fnagi.2021.713726 (2021).

260   Sommeijer, J. P. & Levelt, C. N. Synaptotagmin-2 is a reliable marker for parvalbumin positive inhibitory boutons in the mouse visual cortex. *PLoS One* **7**, e35323, doi:10.1371/journal.pone.0035323 (2012).

261   Stevens, S. R. *et al.* Ankyrin-R regulates fast-spiking interneuron excitability through perineuronal nets and Kv3.1b K(+) channels. *Elife* **10**, doi:10.7554/eLife.66491 (2021).

262   Akgul, G. & McBain, C. J. Diverse roles for ionotropic glutamate receptors on inhibitory interneurons in developing and adult brain. *J Physiol* **594**, 5471-5490, doi:10.1113/JP271764 (2016).

263   Kim, H. *et al.* The small GTPase ARF6 regulates GABAergic synapse development. *Mol Brain* **13**, 2, doi:10.1186/s13041-019-0543-3 (2020).

264   Lucas, E. K. *et al.* PGC-1alpha provides a transcriptional framework for synchronous neurotransmitter release from parvalbumin-positive interneurons. *J Neurosci* **34**, 14375-14387, doi:10.1523/JNEUROSCI.1222-14.2014 (2014).

265   Stevens, S. R. *et al.* Ankyrin-R Links Kv3.3 to the Spectrin Cytoskeleton and Is Required for Purkinje Neuron Survival. *J Neurosci* **42**, 2-15, doi:10.1523/JNEUROSCI.1132-21.2021 (2022).

266   Yao, Z. *et al.* A taxonomy of transcriptomic cell types across the isocortex and hippocampal formation. *Cell* **184**, 3222-3241 e3226, doi:10.1016/j.cell.2021.04.021 (2021).

267   Wingo, A. P. *et al.* Brain microRNAs are associated with variation in cognitive trajectory in advanced age. *Transl Psychiatry* **12**, 47, doi:10.1038/s41398-022-01806-3 (2022).

268   Fu, H., Hardy, J. & Duff, K. E. Selective vulnerability in neurodegenerative diseases. *Nat Neurosci* **21**, 1350-1358, doi:10.1038/s41593-018-0221-2 (2018).

269   de Leeuw, C. A., Mooij, J. M., Heskes, T. & Posthuma, D. MAGMA: generalized gene-set analysis of GWAS data. *PLoS Comput Biol* **11**, e1004219, doi:10.1371/journal.pcbi.1004219 (2015).

270   Umoh, M. E. *et al.* A proteomic network approach across the ALS-FTD disease spectrum resolves clinical phenotypes and genetic vulnerability in human brain. *EMBO Mol Med* **10**, 48-62, doi:10.15252/emmm.201708202 (2018).

271   Ping, L. *et al.* Global Quantitative Analysis of the Human Brain Proteome in Alzheimer's and Parkinson's Disease. *Scientific Data* **in press** (2018).

272   Higginbotham, L. *et al.* Integrated proteomics reveals brain-based cerebrospinal fluid biomarkers in asymptomatic and symptomatic Alzheimer's disease. *Science Advances* **6**, eaaz9360, doi:10.1126/sciadv.aaz9360 (2020).

273   Rayaprolu, S. *et al.* Systems-based proteomics to resolve the biology of Alzheimer's disease beyond amyloid and tau. *Neuropsychopharmacology* **46**, 98-115, doi:10.1038/s41386-020-00840-3 (2021).

274   Bishof, I. *et al.* RNA-binding proteins with basic-acidic dipeptide (BAD) domains self-assemble and aggregate in Alzheimer's disease. *J Biol Chem* **293**, 11047-11066, doi:10.1074/jbc.RA118.001747 (2018).

275   Dai, J. *et al.* Effects of APOE Genotype on Brain Proteomic Network and Cell Type Changes in Alzheimer's Disease. *Front Mol Neurosci* **11**, 454, doi:10.3389/fnmol.2018.00454 (2018).

276   Higginbotham, L. *et al.* Network Analysis of a Membrane-Enriched Brain Proteome across Stages of Alzheimer's Disease. *Proteomes* **7**, doi:10.3390/proteomes7030030 (2019).

277   Wingo, A. P. *et al.* Large-scale proteomic analysis of human brain identifies proteins associated with cognitive trajectory in advanced age. *Nat Commun* **10**, 1619, doi:10.1038/s41467-019-09613-z (2019).

278   Johnson, E. C. B. *et al.* Large-scale proteomic analysis of Alzheimer's disease brain and cerebrospinal fluid reveals early changes in energy metabolism associated with microglia and astrocyte activation. *Nat Med* **26**, 769-780, doi:10.1038/s41591-020-0815-6 (2020).

279   Bennett, D. A. *et al.* Religious Orders Study and Rush Memory and Aging Project. *J Alzheimers Dis* **64**, S161-S189, doi:10.3233/JAD-179939 (2018).

280   Benamer, N., Vidal, M., Balia, M. & Angulo, M. C. Myelination of parvalbumin interneurons shapes the function of cortical sensory inhibitory circuits. *Nat Commun* **11**, 5151, doi:10.1038/s41467-020-18984-7 (2020).

281   Ueno, H. *et al.* Age-dependent and region-specific alteration of parvalbumin neurons and perineuronal nets in the mouse cerebral cortex. *Neurochem Int* **112**, 59-70, doi:10.1016/j.neuint.2017.11.001 (2018).

282   Reichelt, A. C., Hare, D. J., Bussey, T. J. & Saksida, L. M. Perineuronal Nets: Plasticity, Protection, and Therapeutic Potential. *Trends Neurosci* **42**, 458-470, doi:10.1016/j.tins.2019.04.003 (2019).

283 Celio, M. R., Spreafico, R., De Biasi, S. & Vitellaro-Zuccarello, L. Perineuronal nets: past and present. *Trends Neurosci* **21**, 510-515, doi:10.1016/s0166-2236(98)01298-3 (1998).

284 Carceller, H., Guirado, R., Ripolles-Campos, E., Teruel-Marti, V. & Nacher, J. Perineuronal Nets Regulate the Inhibitory Perisomatic Input onto Parvalbumin Interneurons and gamma Activity in the Prefrontal Cortex. *J Neurosci* **40**, 5008-5018, doi:10.1523/JNEUROSCI.0291-20.2020 (2020).

285 Sahara, S., Yanagawa, Y., O'Leary, D. D. & Stevens, C. F. The fraction of cortical GABAergic neurons is constant from near the start of cortical neurogenesis to adulthood. *J Neurosci* **32**, 4755-4761, doi:10.1523/JNEUROSCI.6412-11.2012 (2012).

286 Jiang, Y. *et al.* COX5A over-expression protects cortical neurons from hypoxic ischemic injury in neonatal rats associated with TPI up-regulation. *BMC Neurosci* **21**, 18, doi:10.1186/s12868-020-00565-5 (2020).

287 Luu, W., Hart-Smith, G., Sharpe, L. J. & Brown, A. J. The terminal enzymes of cholesterol synthesis, DHCR24 and DHCR7, interact physically and functionally. *J Lipid Res* **56**, 888-897, doi:10.1194/jlr.M056986 (2015).

288 Yamin, R., Zhao, C., O'Connor, P. B., McKee, A. C. & Abraham, C. R. Acyl peptide hydrolase degrades monomeric and oligomeric amyloid-beta peptide. *Mol Neurodegener* **4**, 33, doi:10.1186/1750-1326-4-33 (2009).

289 Glasgow, S. D., McPhedrain, R., Madranges, J. F., Kennedy, T. E. & Ruthazer, E. S. Approaches and Limitations in the Investigation of Synaptic Transmission and Plasticity. *Front Synaptic Neurosci* **11**, 20, doi:10.3389/fnsyn.2019.00020 (2019).

290   Eggermann, E., Bucurenciu, I., Goswami, S. P. & Jonas, P. Nanodomain coupling between Ca(2)(+) channels and sensors of exocytosis at fast mammalian synapses. *Nat Rev Neurosci* **13**, 7-21, doi:10.1038/nrn3125 (2011).

291   Hefft, S., Kraushaar, U., Geiger, J. R. & Jonas, P. Presynaptic short-term depression is maintained during regulation of transmitter release at a GABAergic synapse in rat hippocampus. *J Physiol* **539**, 201-208, doi:10.1113/jphysiol.2001.013455 (2002).

292   Muller, M., Felmy, F., Schwaller, B. & Schneggenburger, R. Parvalbumin is a mobile presynaptic Ca2+ buffer in the calyx of Held that accelerates the decay of Ca2+ and short-term facilitation. *J Neurosci* **27**, 2261-2271, doi:10.1523/JNEUROSCI.5582-06.2007 (2007).

293   Mackenzie-Gray Scott, C. A. *et al.* Resilient Hippocampal Gamma Rhythmogenesis and Parvalbumin-Expressing Interneuron Function Before and After Plaque Burden in 5xFAD Alzheimer's Disease Model. *Front Synaptic Neurosci* **14**, 857608, doi:10.3389/fnsyn.2022.857608 (2022).

294   Rath, S. *et al.* MitoCarta3.0: an updated mitochondrial proteome now with sub-organelle localization and pathway annotations. *Nucleic Acids Res* **49**, D1541-D1547, doi:10.1093/nar/gkaa1011 (2021).

295   Morita, M. *et al.* mTORC1 controls mitochondrial activity and biogenesis through 4E-BP-dependent translational regulation. *Cell Metab* **18**, 698-711, doi:10.1016/j.cmet.2013.10.001 (2013).

296   Ma, T. *et al.* Dysregulation of the mTOR pathway mediates impairment of synaptic plasticity in a mouse model of Alzheimer's disease. *PLoS One* **5**, doi:10.1371/journal.pone.0012845 (2010).

297   Hoeffer, C. A. & Klann, E. mTOR signaling: at the crossroads of plasticity, memory and disease. *Trends Neurosci* **33**, 67-75, doi:10.1016/j.tins.2009.11.003 (2010).

298   Deleyto-Seldas, N. & Efeyan, A. The mTOR-Autophagy Axis and the Control of Metabolism. *Front Cell Dev Biol* **9**, 655731, doi:10.3389/fcell.2021.655731 (2021).

299   Murakoshi, H., Wang, H. & Yasuda, R. Local, persistent activation of Rho GTPases during plasticity of single dendritic spines. *Nature* **472**, 100-104, doi:10.1038/nature09823 (2011).

300   Ma, X. M. & Blenis, J. Molecular mechanisms of mTOR-mediated translational control. *Nat Rev Mol Cell Biol* **10**, 307-318, doi:10.1038/nrm2672 (2009).

301   Zhao, J., Zhai, B., Gygi, S. P. & Goldberg, A. L. mTOR inhibition activates overall protein degradation by the ubiquitin proteasome system as well as by autophagy. *Proc Natl Acad Sci U S A* **112**, 15790-15797, doi:10.1073/pnas.1521919112 (2015).

302   Fornasiero, E. F. *et al.* Precisely measured protein lifetimes in the mouse brain reveal differences across tissues and subcellular fractions. *Nat Commun* **9**, 4230, doi:10.1038/s41467-018-06519-0 (2018).

303   Mich, J. K. *et al.* Functional enhancer elements drive subclass-selective expression from mouse to primate neocortex. *Cell Rep* **34**, 108754, doi:10.1016/j.celrep.2021.108754 (2021).

304   Banks, E., Zheng, J.Q., Eaton, A., Oláh, V.J., Rowan, M.J.M. A novel enhancer-AAV approach selectively targeting dentate granule cells. *bioRxiv*, doi:https://doi.org/10.1101/2023.02.03.527045 (2023).

305   Sharma, K. *et al.* Cell type- and brain region-resolved mouse brain proteome. *Nat Neurosci* **18**, 1819-1831, doi:10.1038/nn.4160 (2015).

306   Alvarez-Castelao, B., Schanzenbacher, C. T., Langer, J. D. & Schuman, E. M. Cell-type-specific metabolic labeling, detection and identification of nascent proteomes in vivo. *Nat Protoc* **14**, 556-575, doi:10.1038/s41596-018-0106-6 (2019).

307   Alvarez-Castelao, B. *et al.* Cell-type-specific metabolic labeling of nascent proteomes in vivo. *Nat Biotechnol* **35**, 1196-1201, doi:10.1038/nbt.4016 (2017).

308   Sunna, S. *et al.* Advances in proteomic phenotyping of microglia in neurodegeneration. *Proteomics*, e2200183, doi:10.1002/pmic.202200183 (2023).

309   Sunna, S. *et al.* Cellular proteomic profiling using proximity labelling by TurboID-NES in microglial and neuronal cell lines. *bioRxiv*, 2022.2009.2027.509765, doi:10.1101/2022.09.27.509765 (2022).

310   Dimidschstein, J. *et al.* A viral strategy for targeting and manipulating interneurons across vertebrate species. *Nat Neurosci* **19**, 1743-1749, doi:10.1038/nn.4430 (2016).

311   Kann, O., Huchzermeyer, C., Kovacs, R., Wirtz, S. & Schuelke, M. Gamma oscillations in the hippocampus require high complex I gene expression and strong functional performance of mitochondria. *Brain* **134**, 345-358, doi:10.1093/brain/awq333 (2011).

312   Antoine, M. W., Langberg, T., Schnepel, P. & Feldman, D. E. Increased Excitation-Inhibition Ratio Stabilizes Synapse and Circuit Excitability in Four Autism Mouse Models. *Neuron* **101**, 648-661 e644, doi:10.1016/j.neuron.2018.12.026 (2019).

313   Hanson, J. E. *et al.* GluN2A NMDA Receptor Enhancement Improves Brain Oscillations, Synchrony, and Cognitive Functions in Dravet Syndrome and Alzheimer's Disease Models. *Cell Rep* **30**, 381-396 e384, doi:10.1016/j.celrep.2019.12.030 (2020).

314   Perdigao, C., Barata, M. A., Burrinha, T. & Guimas Almeida, C. Alzheimer's disease BIN1 coding variants increase intracellular Abeta levels by interfering with BACE1 recycling. *J Biol Chem* **297**, 101056, doi:10.1016/j.jbc.2021.101056 (2021).

315   Strang, K. H., Golde, T. E. & Giasson, B. I. MAPT mutations, tauopathy, and mechanisms of neurodegeneration. *Lab Invest* **99**, 912-928, doi:10.1038/s41374-019-0197-x (2019).

316   McCann, H., Stevens, C. H., Cartwright, H. & Halliday, G. M. alpha-Synucleinopathy phenotypes. *Parkinsonism Relat Disord* **20 Suppl 1**, S62-67, doi:10.1016/S1353-8020(13)70017-8 (2014).

317   Barba, L. *et al.* Alpha and Beta Synucleins: From Pathophysiology to Clinical Application as Biomarkers. *Mov Disord* **37**, 669-683, doi:10.1002/mds.28941 (2022).

318   Kang, J. Q. Epileptic Mechanisms Shared by Alzheimer's Disease: Viewed via the Unique Lens of Genetic Epilepsy. *Int J Mol Sci* **22**, doi:10.3390/ijms22137133 (2021).

319   Berkel, S. *et al.* Mutations in the SHANK2 synaptic scaffolding gene in autism spectrum disorder and mental retardation. *Nat Genet* **42**, 489-491, doi:10.1038/ng.589 (2010).

320   Leblond, C. S. *et al.* Genetic and functional analyses of SHANK2 mutations suggest a multiple hit model of autism spectrum disorders. *PLoS Genet* **8**, e1002521, doi:10.1371/journal.pgen.1002521 (2012).

321   Kilinc, M. *et al.* Species-conserved SYNGAP1 phenotypes associated with neurodevelopmental disorders. *Mol Cell Neurosci* **91**, 140-150, doi:10.1016/j.mcn.2018.03.008 (2018).

322   Del Pino, I. *et al.* Erbb4 deletion from fast-spiking interneurons causes schizophrenia-like phenotypes. *Neuron* **79**, 1152-1168, doi:10.1016/j.neuron.2013.07.010 (2013).

323   Batista-Brito, R. *et al.* Developmental loss of ErbB4 in PV interneurons disrupts state-dependent cortical circuit dynamics. *Mol Psychiatry*, doi:10.1038/s41380-023-02066-3 (2023).

324   Jang, H. J. *et al.* Distinct roles of parvalbumin and somatostatin interneurons in gating the synchronization of spike times in the neocortex. *Sci Adv* **6**, eaay5333, doi:10.1126/sciadv.aay5333 (2020).

325   Kleinjan, M. S. *et al.* Dually innervated dendritic spines develop in the absence of excitatory activity and resist plasticity through tonic inhibitory crosstalk. *Neuron* **111**, 1517, doi:10.1016/j.neuron.2023.04.003 (2023).

326   Hou, Z. H. & Yu, X. Activity-regulated somatostatin expression reduces dendritic spine density and lowers excitatory synaptic transmission via postsynaptic somatostatin receptor 4. *J Biol Chem* **288**, 2501-2509, doi:10.1074/jbc.M112.419051 (2013).

327   Ulrich, D. Amyloid-beta Impairs Synaptic Inhibition via GABA(A) Receptor Endocytosis. *J Neurosci* **35**, 9205-9210, doi:10.1523/JNEUROSCI.0950-15.2015 (2015).

328   Limon, A., Reyes-Ruiz, J. M. & Miledi, R. Loss of functional GABA(A) receptors in the Alzheimer diseased brain. *Proc Natl Acad Sci U S A* **109**, 10071-10076, doi:10.1073/pnas.1204606109 (2012).

329   Sos, K. E. *et al.* Amyloid beta induces interneuron-specific changes in the hippocampus of APPNL-F mice. *PLoS One* **15**, e0233700, doi:10.1371/journal.pone.0233700 (2020).

330   Gainey, M. A. & Feldman, D. E. Multiple shared mechanisms for homeostatic plasticity in rodent somatosensory and visual cortex. *Philos Trans R Soc Lond B Biol Sci* **372**, doi:10.1098/rstb.2016.0157 (2017).

331   Mattis, J. *et al.* Corticohippocampal circuit dysfunction in a mouse model of Dravet syndrome. *Elife* **11**, doi:10.7554/eLife.69293 (2022).

332   Busche, M. A. & Konnerth, A. Impairments of neural circuit function in Alzheimer's disease. *Philos Trans R Soc Lond B Biol Sci* **371**, doi:10.1098/rstb.2015.0429 (2016).

333   Chen, C. *et al.* Early impairment of cortical circuit plasticity and connectivity in the 5XFAD Alzheimer's disease mouse model. *Transl Psychiatry* **12**, 371, doi:10.1038/s41398-022-02132-4 (2022).

334   Gainey, M. A., Aman, J. W. & Feldman, D. E. Rapid Disinhibition by Adjustment of PV Intrinsic Excitability during Whisker Map Plasticity in Mouse S1. *J Neurosci* **38**, 4749-4761, doi:10.1523/JNEUROSCI.3628-17.2018 (2018).

335   Yao, J. *et al.* Mitochondrial bioenergetic deficit precedes Alzheimer's pathology in female mouse model of Alzheimer's disease. *Proc Natl Acad Sci U S A* **106**, 14670-14675, doi:10.1073/pnas.0903563106 (2009).

336   Hauptmann, S. *et al.* Mitochondrial dysfunction: an early event in Alzheimer pathology accumulates with age in AD transgenic mice. *Neurobiol Aging* **30**, 1574-1586, doi:10.1016/j.neurobiolaging.2007.12.005 (2009).

337   Huesa, G. *et al.* Altered distribution of RhoA in Alzheimer's disease and AbetaPP overexpressing mice. *J Alzheimers Dis* **19**, 37-56, doi:10.3233/JAD-2010-1203 (2010).

338   Cai, R. *et al.* Role of RhoA/ROCK signaling in Alzheimer's disease. *Behav Brain Res* **414**, 113481, doi:10.1016/j.bbr.2021.113481 (2021).

339   Goettemoeller, A. M. *et al.* Entorhinal cortex vulnerability to human APP expression promotes hyperexcitability and tau pathology. *Res Sq*, doi:10.21203/rs.3.rs-3370607/v1 (2023).

340   Nilssen, E. S. *et al.* Inhibitory Connectivity Dominates the Fan Cell Network in Layer II of Lateral Entorhinal Cortex. *J Neurosci* **38**, 9712-9727, doi:10.1523/JNEUROSCI.1290-18.2018 (2018).

341   Titlow, J. S. *et al.* Systematic analysis of YFP traps reveals common mRNA/protein discordance in neural tissues. *J Cell Biol* **222**, doi:10.1083/jcb.202205129 (2023).

342   Mendonca, C. F. *et al.* Proteomic signatures of brain regions affected by tau pathology in early and late stages of Alzheimer's disease. *Neurobiol Dis* **130**, 104509, doi:10.1016/j.nbd.2019.104509 (2019).

343   Lehmann, L., Lo, A., Knox, K. M. & Barker-Haliski, M. Alzheimer's Disease and Epilepsy: A Perspective on the Opportunities for Overlapping Therapeutic Innovation. *Neurochem Res* **46**, 1895-1912, doi:10.1007/s11064-021-03332-y (2021).

344   Chen, L. *et al.* Progressive excitability changes in the medial entorhinal cortex in the 3xTg mouse model of Alzheimer's disease pathology. *bioRxiv*, doi:10.1101/2023.05.30.542838 (2023).

345   Tahvildari, B. & Alonso, A. Morphological and electrophysiological properties of lateral entorhinal cortex layers II and III principal neurons. *J Comp Neurol* **491**, 123-140, doi:10.1002/cne.20706 (2005).

346   Varga, C., Lee, S. Y. & Soltesz, I. Target-selective GABAergic control of entorhinal cortex output. *Nat Neurosci* **13**, 822-824, doi:10.1038/nn.2570 (2010).

347   Desikan, R. S. *et al.* Amyloid-beta--associated clinical decline occurs only in the presence of elevated P-tau. *Arch Neurol* **69**, 709-713, doi:10.1001/archneurol.2011.3354 (2012).

348   Lue, L. F. *et al.* Soluble amyloid beta peptide concentration as a predictor of synaptic change in Alzheimer's disease. *Am J Pathol* **155**, 853-862, doi:10.1016/s0002-9440(10)65184-x (1999).

349   Naslund, J. *et al.* Correlation between elevated levels of amyloid beta-peptide in the brain and cognitive decline. *JAMA* **283**, 1571-1577, doi:10.1001/jama.283.12.1571 (2000).

350   Schultz, M. K., Jr. *et al.* Pharmacogenetic neuronal stimulation increases human tau pathology and trans-synaptic spread of tau to distal brain regions in mice. *Neurobiol Dis* **118**, 161-176, doi:10.1016/j.nbd.2018.07.003 (2018).

351   Yamada, K. *et al.* Neuronal activity regulates extracellular tau in vivo. *J Exp Med* **211**, 387-393, doi:10.1084/jem.20131685 (2014).

352   Busche, M. A. *et al.* Tau impairs neural circuits, dominating amyloid-beta effects, in Alzheimer models in vivo. *Nat Neurosci* **22**, 57-64, doi:10.1038/s41593-018-0289-8 (2019).

353   Hall, A. M. *et al.* Tau-dependent Kv4.2 depletion and dendritic hyperexcitability in a mouse model of Alzheimer's disease. *J Neurosci* **35**, 6221-6230, doi:10.1523/JNEUROSCI.2552-14.2015 (2015).

354   Colom-Cadena, M. *et al.* Synaptic oligomeric tau in Alzheimer's disease - A potential culprit in the spread of tau pathology through the brain. *Neuron* **111**, 2170-2183 e2176, doi:10.1016/j.neuron.2023.04.020 (2023).

355   Huang, Y. A., Zhou, B., Wernig, M. & Sudhof, T. C. ApoE2, ApoE3, and ApoE4 Differentially Stimulate APP Transcription and Abeta Secretion. *Cell* **168**, 427-441 e421, doi:10.1016/j.cell.2016.12.044 (2017).

356   Lee, S. I. *et al.* APOE4-carrying human astrocytes oversupply cholesterol to promote neuronal lipid raft expansion and Abeta generation. *Stem Cell Reports* **16**, 2128-2137, doi:10.1016/j.stemcr.2021.07.017 (2021).

357   Saito, T. *et al.* Single App knock-in mouse models of Alzheimer's disease. *Nat Neurosci* **17**, 661-663, doi:10.1038/nn.3697 (2014).

358   Baglietto-Vargas, D. *et al.* Generation of a humanized Abeta expressing mouse demonstrating aspects of Alzheimer's disease-like pathology. *Nat Commun* **12**, 2421, doi:10.1038/s41467-021-22624-z (2021).

359   Mucke, L. *et al.* High-level neuronal expression of abeta 1-42 in wild-type human amyloid protein precursor transgenic mice: synaptotoxicity without plaque formation. *J Neurosci* **20**, 4050-4058, doi:10.1523/JNEUROSCI.20-11-04050.2000 (2000).

360   Mehr, A. *et al.* Lack of APP and APLP2 in GABAergic Forebrain Neurons Impairs Synaptic Plasticity and Cognition. *Cereb Cortex* **30**, 4044-4063, doi:10.1093/cercor/bhaa025 (2020).

361   Yamamoto, K., Yamamoto, R. & Kato, N. Amyloid beta and Amyloid Precursor Protein Synergistically Suppress Large-Conductance Calcium-Activated Potassium Channel in Cortical Neurons. *Front Aging Neurosci* **13**, 660319, doi:10.3389/fnagi.2021.660319 (2021).

362   Agsten, M. *et al.* BACE1 modulates gating of KCNQ1 (Kv7.1) and cardiac delayed rectifier KCNQ1/KCNE1 (IKs). *J Mol Cell Cardiol* **89**, 335-348, doi:10.1016/j.yjmcc.2015.10.006 (2015).

363   Lehnert, S. *et al.* Ion channel regulation by beta-secretase BACE1 - enzymatic and non-enzymatic effects beyond Alzheimer's disease. *Channels (Austin)* **10**, 365-378, doi:10.1080/19336950.2016.1196307 (2016).

364   Wong, H. K. *et al.* beta Subunits of voltage-gated sodium channels are novel substrates of beta-site amyloid precursor protein-cleaving enzyme (BACE1) and gamma-secretase. *J Biol Chem* **280**, 23009-23017, doi:10.1074/jbc.M414648200 (2005).

365   Furukawa, K., Barger, S. W., Blalock, E. M. & Mattson, M. P. Activation of K+ channels and suppression of neuronal activity by secreted beta-amyloid-precursor protein. *Nature* **379**, 74-78, doi:10.1038/379074a0 (1996).

366   Mayordomo-Cava, J., Yajeya, J., Navarro-Lopez, J. D. & Jimenez-Diaz, L. Amyloid-beta(25-35) Modulates the Expression of GirK and KCNQ Channel Genes in the Hippocampus. *PLoS One* **10**, e0134385, doi:10.1371/journal.pone.0134385 (2015).

367   Harris, J. A. *et al.* Human P301L-mutant tau expression in mouse entorhinal-hippocampal network causes tau aggregation and presynaptic pathology but no cognitive deficits. *PLoS One* **7**, e45881, doi:10.1371/journal.pone.0045881 (2012).

368   Pickett, E. K. *et al.* Spread of tau down neural circuits precedes synapse and neuronal loss in the rTgTauEC mouse model of early Alzheimer's disease. *Synapse* **71**, doi:10.1002/syn.21965 (2017).

369   Cope, Z. A., Murai, T. & Sukoff Rizzo, S. J. Emerging Electroencephalographic Biomarkers to Improve Preclinical to Clinical Translation in Alzheimer's Disease. *Front Aging Neurosci* **14**, 805063, doi:10.3389/fnagi.2022.805063 (2022).

370   Kelberman, M. A. *et al.* Age-dependent dysregulation of locus coeruleus firing in a transgenic rat model of Alzheimer's disease. *Neurobiol Aging* **125**, 98-108, doi:10.1016/j.neurobiolaging.2023.01.016 (2023).

371   Bero, A. W. *et al.* Neuronal activity regulates the regional vulnerability to amyloid-beta deposition. *Nat Neurosci* **14**, 750-756, doi:10.1038/nn.2801 (2011).

372   Olney, J. W. Brain lesions, obesity, and other disturbances in mice treated with monosodium glutamate. *Science* **164**, 719-721, doi:10.1126/science.164.3880.719 (1969).

373   Rodriguez, G. A., Barrett, G. M., Duff, K. E. & Hussaini, S. A. Chemogenetic attenuation of neuronal activity in the entorhinal cortex reduces Abeta and tau pathology in the hippocampus. *PLoS Biol* **18**, e3000851, doi:10.1371/journal.pbio.3000851 (2020).

374   Kaneko, K. *et al.* Developmentally regulated impairment of parvalbumin interneuron synaptic transmission in an experimental model of Dravet syndrome. *Cell Rep* **38**, 110580, doi:10.1016/j.celrep.2022.110580 (2022).

375   Algamal, M. *et al.* Reduced excitatory neuron activity and interneuron-type-specific deficits in a mouse model of Alzheimer's disease. *Commun Biol* **5**, 1323, doi:10.1038/s42003-022-04268-x (2022).

376   Blanpain, L. T., Cole, E.R., Chen, E., Park, J.K., Walelign, M.Y., Gross, R.E., Cabaniss, B.T., Willie, J.T., Singer, A.C. Multisensory flicker modulates widespread brain networks and reduces interictal epileptiform discharges. *Nature Communications* **15**, doi:10.1038/s41467-024-47263-y (2024).